IMT School for Advanced Studies, Lucca
Lucca, Italy

New methods to assess the performance of structural joints with microstructures

PhD Program in Institutions, Markets and Technologies

Curriculum in Computer Science and Systems Engineering

XXXIII Cycle

By

Maria Rosaria Marulli

2021

The dissertation of Maria Rosaria Marulli is approved.

PhD Program Coordinator: Mirco Tribastone, IMT School for Advanced Studies Lucca

Advisor: Prof. Marco Paggi, IMT School for Advanced Studies Lucca

Co-Advisor: Prof. Jose Antonio Reinoso Cuevas, Universidad de Sevilla

The dissertation of Maria Rosaria Marulli has been reviewed by:

Prof. Sonia Marfia, Università Roma Tre

Prof. Paolo Sebastiano Valvo, Università di Pisa

IMT School for Advanced Studies Lucca
2021

To my family

Contents

List of Figures

List of Tables

Acknowledgements

First of all, I would like to express my gratitude to Prof. Marco Paggi and Dr. José Reinoso Cuevas for their supervision during my doctoral period, for the opportunity of this research work, their research directions, guidance, and support.

Part of the present Thesis is based on the articles published and listed in the Publications Section. Chapters 5 and 4 are taken from papers in preparation.

I also would like to acknowledge funding from the MIUR-DAAD Joint Mobility Program 2017 to the project "Multi-scale modelling of friction for large scale engineering problems," which has been granted by the Italian Ministry of Education, University and Research (MIUR) and by the Deutscher Akademischer Austausch Dienst (DAAD) through funds of the German Federal Ministry of Education and Research (BMBF). This funding allowed me to spend two visiting periods at the University of Bundeswehr Universität, M "unchen (Germany) in September 2018 and in January 2019.

The work presented in Chapter 2 is based on the article co-authored by Prof. Marco Paggi, Prof. Alexander Popp, Dr. Jacopo Bonari, Dr. Nora Hagmeyer, and Dr. Matthias Mayr, and it is the result of the above-presented funding. I want to thank all the co-authors for their contributions which enriched me as a researcher and person. Among them, my special gratitude goes to Dr. Jacopo Bonari for have been an intellectually stimulating colleague and, above all, a great friend since the beginning of the doctoral period.

Chapter 3 is based on two articles co-authored by Dr. Hamed Zarei, Prof. Marco Paggi, Dr. Riccardo Pietrogrande, Dr.

Christoph Üffing and Dr. Philipp Weißgraber. My gratitude goes to Dr. Hamed Zarei for the scientific and personal support and the other co-authors for the opportunity of this collaboration and their expert guidance.

Moreover, I would like to acknowledge the funding from the Erasmus+ program of the European Union for the traineeship having the title "Modelling of adhesive/cohesive failure of structural adhesives," which have been used for three months visiting period at the University of Seville (Spain) started in January 2020. The funding led to the investigation described in Chapter 5 for which I would like to thank Dr. Adrià Quintanas Corominas, always available and supporting.

I am very grateful to my colleagues and friends from IMT Lucca, who have become my family in these almost four years. Studying for the Ph.D. would have been much more complicated and tedious without all the people I met on the campus. Someone wrote that *"The best beers are the ones we drink with friends"*, and I want to add that after all, canteen food was not so bad when we were all sharing the table.

A special thank you goes to my hometown friends that have been constantly by my side, even from far away. We did not have much time to be together but every time was like I never really left. Moreover, words alone cannot express my gratitude to Giuseppe, who has always encouraged me to do my best. Finally, I want to thank all my family, especially my parents and my brother, for their love, patience, and support during these years. I could have never achieved the Ph.D. title without them.

Publications

1. J. Bonari, M. R. Marulli, N. Hagmeyer, M. Mayr, A. Popp, and M. Paggi, "A multi-scale FEM-BEM formulation for contact mechanics between rough surfaces," Comput. Mech., 2019.
2. H. Zarei, M. R. Marulli, M. Paggi, R. Pietrogrande, C. Üffing, and P. Weißgraeber, "Mechanical characterization and failure modes in the peeling of adhesively bonded strips from a plastic substrate," Mech. Adv. Mater. Struct., pp. 1–6, Oct. 2020.
3. H. Zarei, M. Rosaria Marulli, M. Paggi, R. Pietrogrande, C. Üffing, and P. Weißgraeber, "Adherend surface roughness effect on the mechanical response of silicone-based adhesive joints," Eng. Fract. Mech., vol. 240, p. 107353, Dec. 2020.

Abstract

The reliability of structural joints plays a crucial role in our daily life since the most recent innovations in engineering and structural materials have exponentially increased the usage of advanced products, multi- components, and structures. Hence, it is necessary to introduce new methods to assess the bonding strengths of adhesive joints, especially in complex interfaces, as in the presence of micro-structured or rough surfaces, since the morphology of the interface highly influences the overall performance of a structural joint.

The present thesis explores the role of complex interfaces and functional surfaces in the overall performance of multi- components products, intending to understand the mechanical phenomena that may take place at the interface between different materials, simply in contact or joined through an adhesive.

Different topics have been analyzed through experimental and numerical analyses. The research deals with rough interface contact simulations proposing a novel multi-scale approach in the context of computational contact mechanics. Furthermore, the surface morphology influence on adhesive joints has been investigated through peeling tests and numerical models. Moreover, a computational framework for micro-structured adhesives has been proposed. The final topic regards the failure simulation of bilayer structural joints with rubber-like materials.

Chapter 1

Introduction

The permanent assembly of individual components is an important technological issue in many fields of engineering, from buildings construction to industrial production and bio-medical applications. A structural joint can be defined as a connection between two or more components able to assure a certain load-bearing capacity.

There are many different technologies for joining two or more components, including fastening methods like bolts and rivets, the use of adhesives, and welding techniques. Since the most recent innovations in engineering and structural materials are based on combining different types of materials to obtain advanced products, the reliability of the mechanical joining of different materials plays a very important role in our daily life.

The design of a structural joint can be very different according to the nature of materials to be assembled and to the mechanical role of the connection in the whole structure. Material characteristics as flexibility, thermal expansion, optical and electrical properties must be taken into account together with service conditions, environment influence, fracture behavior, fatigue, and degradation process. Moreover, the features of the surfaces in contact at the joining interface can also affect the mechanical performance of the structural joint.

With respect to other binding techniques such as mechanical fasten-

ings or welding, the use of adhesives has acquired greater importance through the years, supported also by the increased production and usage of synthetic materials in the industrial sector.

Total weight reduction is of primary importance in the aerospace, automotive, and shipbuilding industry. With this aim, traditional materials have been replaced by composites materials, and the traditional fastened joining methods have been substituted by the use of adhesives for composite-composite, metal-metal, and metal-composite connections (Figure 1). In fact, adhesive bonding offers the advantages of weight saving and extending fatigue-life because of the elimination of fasteners and fastener holes [1, 2].

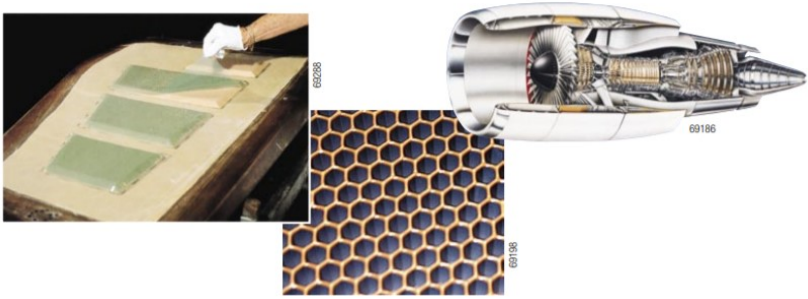

Figure 1: Adhesive film for metal to honeycomb components for aerospace application. Adapted from [3].

Regarding civil engineering, common applications of structural adhesives are represented by external reinforcements to existing buildings. For this method, steel and carbon fiber-reinforced polymers (CFRP) are commonly bonded to the existing concrete using different methods of attachment from solely adhesive bonding to hybrid jointing techniques, for example adhesive bonding in combination with bolting. Remaining in the civil engineering sector, mechanical fixation devices between glass panels and metallic structures used in facade buildings are being progressively substituted by adhesive connections. An example is the huge glass facade of the Charlemagne Building in Brussels, realized using adhesively bonded joints during the renovation of the skyscraper between

1994 and 1998, see Figure 2. Another common application in civil engineering is the laminated glass, a composite material consisting of one or more sheets of glass or synthetic polymers like acrylic glass joined together with one or more interlayers, simultaneously acting as adhesive and separator [4]. Special safety requirements have to be full-filled by the Laminated Safety Glass (LSG), since the adhesive layer is must guarantee residual carrying capacity and avoid dropping out after breakage. In steel construction, adhesive bonding is less common. Even though in 1955 a bridge based on hybrid bonding technology (adhesive bonding backed up with screws) was raised in Marl (Germany), the adhesive bonding applications are mostly limited to research projects, due to to the progressive development of welding technology, and to the lack of statements on the durability of adhesive connections in structural steel for the service life.

Figure 2: Facade of the Charlemagne Building in Brussels, Belgium. Source [5].

In everyday life objects many other applications can be found because of the adhesive's higher strengths, lower weights, lesser expenses, and ease of fabrication compared to other methods of joining. There is hardly any product in our surroundings that does not contain at least one adhesive, be it the label on a beverage bottle, impermeable packaging materials, computer screen, the shoes that we wear.

It is hence necessary to establish methods to guarantee the performance of adhesive joints, especially for structural application. Their mechanical behavior is influenced, in general, by the choice of the adhesive, the joined components properties, the geometry of the joints, and the service environments. The present work considers mostly the influence of the mechanical properties of the joint parts, with special attention to the geometrical properties of the surfaces at the interface.

The surface characteristics, in fact, play an important role in multi-component products, with or without adhesives. Load transfer, friction, adhesion, and wear are all phenomena highly dependent on the surface morphology. Hence, joint design needs to consider the interface characteristics.

Many surfaces that appear smooth at the naked eye, present a much more complex geometry using a microscope, as in the case of crystal surface (Figure 3). The presence of irregularities on the surface can results in unique characteristic so that many different surfaces treatment have been developed to optimize the surface topology.

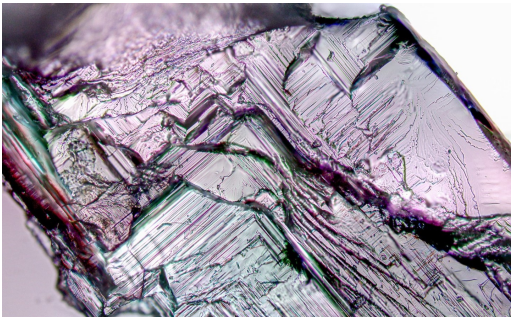

Figure 3: Irregularities of a crystal surface. The approximate dimension of the picture is $150\,\mu\mathrm{m}$. Taken from [6].

The design of new functional surfaces often brings amazing results: for example, windows having surfaces not perfectly smooth, but having a particular roughness are easier to clean; special suits for swimmers allowed to break the world records because of the lower resistance offered by the water; adhesives with three-dimensional surface patterns

have better performance; lenses with a specific rough surface produce better pictures because of the different reflection of light. Most of these technologies are inspired by nature and mimic animals' and vegetables' surface characteristics.

1.1 Surface roughness

All the surfaces of macroscopic solids, even the one that appears smooth to the naked eye, present irregularities and deviations from the ideal geometrical form, on many different length scales, starting from the macroscopic scale to the inter-atomic distance scale. These deviations from the ideal shape can be classified in form errors, which may derive from an inaccurate production process, for example, surface textures or waviness, when the deviations are periodically repeated on the surface, or microscale irregularities.

This finer scale component is called roughness and even the smoothest surface contains microscopical irregularities that no machining method can remove, no matter how precise. These irregularities, which appear like hills and valleys on the surface using a certain magnification (an example is given in Figure 4), might be a natural characteristic of the surface solid, result from interaction with the environment, or derive from the production or machining process.

Properties of solids surfaces are important for technological applications, since phenomena like contact mechanics, friction, wear, lubrication, and adhesion are affected by surface topology. For example, if we consider two bodies brought in contact, the percentage of the surface that we can see in contact at the macro-scale, called *nominal contact area*, will be much bigger than the area that is really in contact, since this latter area, defined as *real contact area*, includes only tiny parts of the surface where the "hills" (asperities) from one solid are squeezed against the asperities of the other solid [8]. The real contact area assumes great importance in many practical applications involving heat transfer and contact resistivity.

Furthermore, special macroscopic features, like hydrophobicity of self-

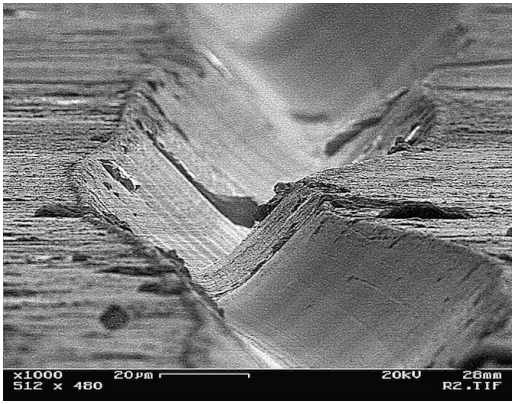

Figure 4: Magnification of a vinyl disk surface. Taken from [7].

cleaning, are related to the presence of particular micro-structures on many plants surfaces, which cause the liquid drop to remain suspended on the tips of the asperities, with some air trapped between the liquid and the substrate. The well-known hydrophobic micro-structures on the lotus leaf are depicted in Figure 5. Hence, the drop easily rolls off, explaining the so-called *lotus effect* which is nowadays used in many applications like self-cleaning glass and paints [9].

Roughness influence is a matter of discussion also within the research area dealing with adhesion, at different length scales, since the adhesive strength is enhanced or reduced according to the surface topography. Some animal species exploit the surface characteristics for special abilities that have been studied by researchers for new technologies applications: the peculiar structure of gecko's feet allow them to climb vertically on a wall, or the texture of the shark's skin is the secret for their speed inside the water.

1.1.1 Profilometric acquisition and statistical analysis

Surface morphology can be analyzed using the topographical data of the surface obtained using specific instruments, called profilometers, which associate to the points on the surface, the value of height with respect to a

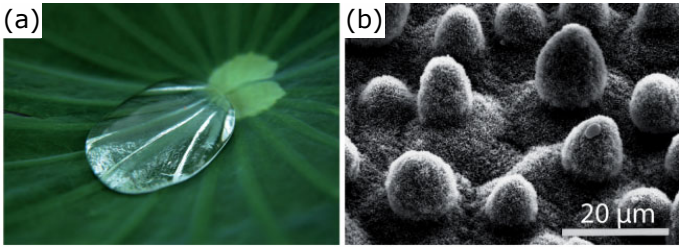

Figure 5: Photograph of a lotus leaf with some drops of water (a) and Scanning electron micrograph of the surface (b). The droplet touches the leaf only a few points and forms a ball that easily rolls off even for small inclinations. Source [10] for (a) and [11] for (b).

reference plane. The measurement may involve only a line on the surface (profile) or it can be repeated along multiple lines in a perpendicular grid, obtaining a three-dimensional scan.

The different available measurement methods can be distinguished in contact or non-contact methods. In the first case, the height values are obtained using a stylus moved across the surface. The probe is directly in contact with the surface and the instrument records the vertical displacement of the probe as it scans along the surface to obtain the surface profile (see Figure 6). This technique has some disadvantages since the probe can damage the surface or be contaminated. Soft plastic and rubber materials, for example, cannot be measured with contact profilometers, as their surface will deform when a force is applied. The contact method results can be also affected by the size and the shape of the stylus, which are directly related to the limiting lateral resolution that can be achieved by the instrument.

Non-contact methods, on the other hand, are based on different physical principles and exploit the light instead of a physical stylus, using optical techniques. One of these tools is the confocal profilometer which works by using a small aperture, known as a confocal aperture (see Figure 7). A highly focused light is projected through the aperture and the detection of the light reflected by the sample allows the evaluation of the surface texture. The reflected signals that are out of focus are cut off

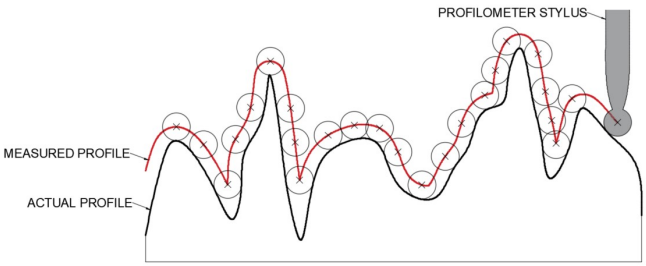

Figure 6: The stylus tip of a contact profilometer physically senses the sample surface. Its geometry affects the measured profile.

using a pinhole inside the optical pathway, thus allowing only the signals from the illuminated spot to enter the light detector. The confocal profilometer scans different planes of the surface moving vertically and only the points of the surface within the focal plane will provide a useful signal. These points will have a known height since the position of the focal plane is also known.

A confocal profilometer (Leica DCM-3D) is available in the laboratory of the Research Unit MUSAM (Multi-scale Analysis of Materials). It has been used to scan the surfaces taken into account in chapter 3. This contactless confocal profilometer is equipped with three lenses providing various sample magnification (10x, 20x, 100x) and it allows different spatial resolutions (which correspond to the distance between two consequent points of which the height is evaluated) in x, y, z directions depending on the adopted lens.

The topographical data acquired through the profilometric scanning of the surface can be analyzed using quantitative parameters to compare different samples, control the quality of the manufacturing process, and to link the surface characteristic to the above-mentioned phenomena (wear, friction, adhesion,...). A variety of parameters have been identified over the years, some of them are very specific to certain applications especially in the industry sector, others are more related to the research activity. Dozens of reference standards exist to describe measurement techniques and desired surface characteristics, such as ASME B46 [13],

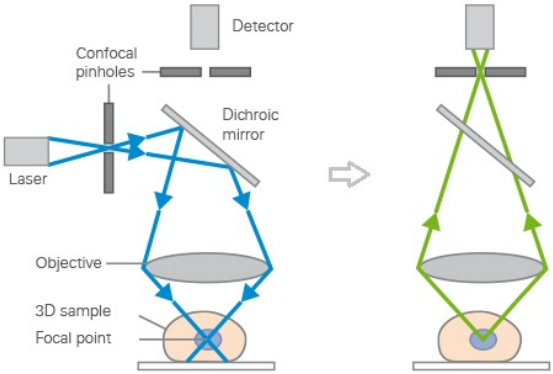

Figure 7: Working principle of a confocal profilometer: a laser ray is used to enlighten a specific plane of the sample surface; then, the light is reflected back to the profilometer through a confocal pinholes which allows to detect only the signal coming from the focal plane. Adapted from [12].

ISO 4287 [14] and ISO 25178 [15] and SEMI MF1811 [16], however an exhausting list of surface parameters is above the goal of this thesis. Hence, the attention will be limited to those parameters relevant for the following chapters.

The amplitude parameters are defined in the ISO 4287 [14] considering a roughness profile $z(x)$ with evaluation length l_r (profile length). The proposed parameters are summarised in Table 1. Note that some parameters are evaluated over profile segments (called sampling length) and then averaged along the profile length; in this case, n is the chosen number of segments. Among them, the parameter R_z evaluates the average peak-to-valley distance over the profile length (see Figure 8), and it will be used to classify the different samples analyzed in chapter 3. The corresponding definitions can be found also for areal data (instead of for profile data), using the notation $S_\square$ instead of $R_\square$.

If the surface or profile heights are considered as random variables, the statistical distribution of the profile (or surface) heights can be reconstructed starting from the histogram data of the digitized points over the evaluation length, by plotting the number or fraction of surface heights

Symbol	Description	Definition
R_a	Average roughness = arithmetical mean deviation	$R_a = \frac{1}{l_r}\int_0^{l_r} \lvert z(x)\rvert \, dx$
R_q	Root mean square roughness	$Rq = \sqrt{\frac{1}{l_r}\int_0^{l_r} z(x)^2 dx}$
R_{vi}	Maximum valley depth below the mean line	$R_{vi} = \lvert \min z(x)\rvert$
R_v	Average of R_{vi} values over evaluation length	$R_v = \frac{\sum_{i=1}^{n} R_{vi}}{n}$
R_{pi}	Maximum peak height above the mean line	$R_{pi} = \max z(x)$
R_p	Average of R_{pi} values over evaluation length	$R_p = \frac{\sum_{i=1}^{n} Rp_i}{n}$
R_{zi}	Maximum peak to valley height of the profile	$R_{zi} = R_{ip} + R_{vi}$
R_z	Average of R_{zi} values over evaluation length	$R_z = \frac{\sum_{i=1}^{n} R_{zi}}{n}$

Table 1: Roughness amplitude parameters as defined in ISO 4287 [14]

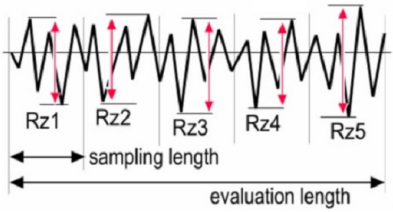

Figure 8: Evaluation of the peak-to-valley distance, R_{zi}, of different profile segments (sampling length). The average value R_z over the evaluation length is obtained as $R_z = \frac{1}{5}\sum_{i=1}^{5} R_{zi}$. Adapted from [17].

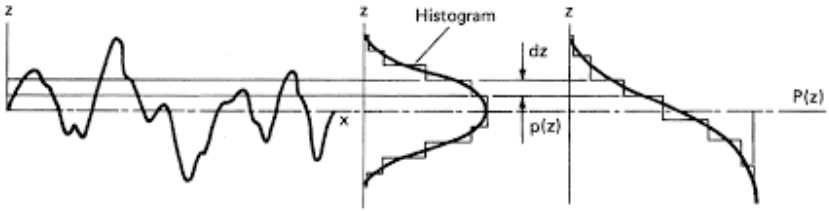

Figure 9: Histogram and cumulative distribution function derived from a profile. Taken from [19].

lying between two specific heights as a function of height (see Figure 9). The height distribution of many natural surfaces, such as surfaces prepared by fracture, or surfaces prepared with sandblasting or ion sputtering, are usually nearly Gaussian [18]. Other types of rough surfaces, for example, prepared by fracture and then (slightly) polished, display a non-symmetric and non-Gaussian height distribution since the asperity tops have been polished [18]. For a Gaussian distribution of the heights field, the probability density of surface height, $p(z)$, is defined as:

$$p(z) = \frac{1}{\sigma(2\pi)^{0.5}} exp\left[-\frac{(z-\mu)^2}{2\sigma^2}\right] \tag{1.1}$$

where μ is the mean and σ is the standard deviation.

The heights field can be represented also considering the cumulative distribution function $P(z)$, which is obtained by plotting the cumulative number or portion of the surface height lying at or below a specific height as a function of that height (see Figure 9) [19].

1.1.2 Fractal surfaces

In contact mechanics, as in other research fields, the statistical description of rough surfaces has been used to model the contact interactions between rough bodies (for the related literature, see Chapter 2), involving statistical parameters as mean and variance of the surface elevations, slopes, and curvatures. However, these statistical quantities are strongly

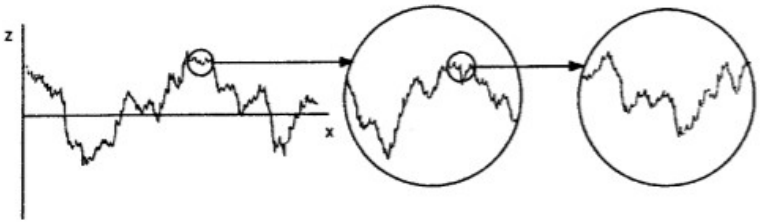

Figure 10: Sketch of the self-affinity characteristic of a profile. Taken from [19]

dependent on the resolution of the measuring instrument, and their values change according to the magnification [20].

If we observe a rough profile (or surface) at increasing magnification, increasing details can be recognized right down to the nano-scale. Furthermore, the rough profile appears quite similar in the structure at all magnifications, as in the sketch of Figure 10. Due to this multi-scale nature of the surface, it is known that the variance of surface height and its derivatives and other roughness parameters depend strongly on the resolution of the roughness measuring instrument or any other form of filter [19]. Hence, it is necessary to introduce a scale-independent characterization of roughness.

For this purpose, the surface multi-scale properties can be characterized by fractal geometry [21]. The morphology of natural interface as metallic components, rock joints, asphalt road, fracture surfaces, are very well reproduced by fractal models and show the property of invariance by scale transformation: the parts of a structure are similar in successive ranges of view (magnification or reduction) in all directions (self-similarity) or at least one direction (self-affinity). The scaling relation of a self-affine surface $z(x, y)$ can be mathematically described as [22]:

$$f(x, y, z) \rightarrow f(rx, ry, r^H z) \tag{1.2}$$

where r is a scaling coefficient and $H < 1$ is called *Hurst exponent* and it varies between 0.5 and 1 for most natural surfaces.

The *fractal dimension* D is related to the Hurst exponent as $D = 3 - H$

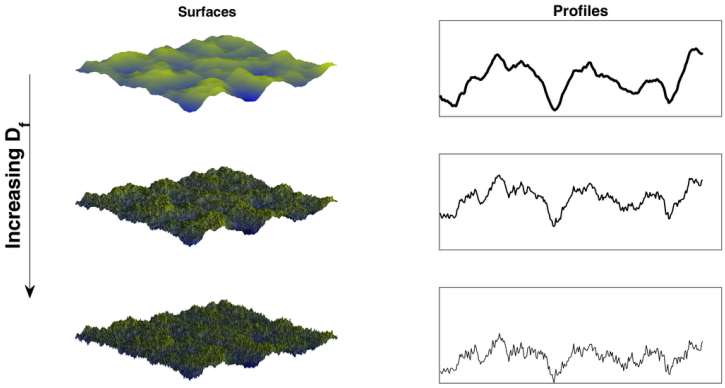

Figure 11: Illustration of surface fractality. Self-affine surfaces (left) and surface profiles (right) showing increasing fractal dimension. Taken from [23].

and it is used as a general descriptor of the surface characteristic. In ordinary geometry shapes, the fractal dimension has integer values (0 for sets describing points, 1 for lines, 2 for surfaces, and 3 for volumes). In the case of fractal dimensions, D has non-integer values, it can vary between 2 and 3 for fractal surfaces. An example of increasing fractal dimension is shown in Figure 11.

Starting from the pioneering work of Majumdar and Bhushan [20], fractal geometry has been applied to predict the behavior of surface phenomena at different length scales; moreover, numerically generate synthetic rough surfaces started to be used as surface simulation methods. Notable examples of algorithms that provide artificial surfaces data for numerical simulations are the Weierstrass-Mandelbrot function [24], the spectral synthesis method [25] and the Random Midpoint Displacement method which will be treated more exhaustively since it will be used later in the thesis.

1.1.3 Random Midpoint Displacement algorithm for fractal surfaces

The Random Midpoint Displacement (RMD) algorithm is one of the methods used to generate the heights field of fractal surfaces, and it is extensively used in computer graphics to generate 2D and 3D landscapes and height-maps, an example is in Figure 12.

Figure 12: Example of a landscape generated with the Random Midpoint Displacement algorithm. Taken from [26].

The method was first introduced by Fournier, Fussell, and Carpenter in 1982 [27] and different variants have been proposed during the years. A review of the algorithm, also known as the diamond-square algorithm, and the different modifications that have followed one another over the years can be found in [28]. The input parameters necessary for this method are: the lateral dimension of the desired surface L, the nodal spacing δ, the fractal dimension D, and the initial variance σ_0^2 of the Gaussian random number extraction. The surface is generated starting from a rectangular cell whose corners have heights extracted by a Gaussian random distribution with variance σ_0 (See Figure 13 (a)). A central node is then added computing its height equal to the average of the four corners heights, plus a random number taken from a random Gaussian variable with reduced variance $\sigma_1^2 = \sigma_0^2(1/\sqrt{2})^{3-D}$ (Figure 13 (b)). Subsequently, the heights of the four intermediate points along the boundaries are computed considering the three neighboring nodes heights and

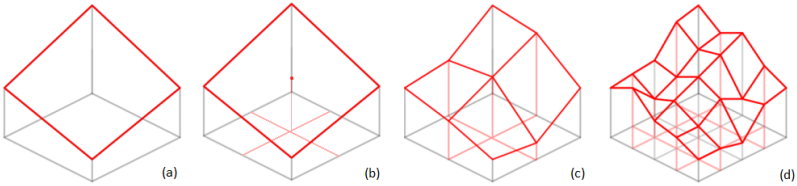

Figure 13: First steps of the Random Midpoint Displacement algorithm to generate a fractal surface. Adapted from [29].

adding a random value from a Gaussian distribution with a scaled variance $\sigma_2^2 = \sigma_1^2(1/\sqrt{2})^{3-D}$, as in Figure 13 (c). The process is repeated for each new square, and so on, until the desired level of detail is reached (Figure 13 (c)).

It is worth noticing that, at each step, the heights previously computed are no longer modified, so that at the k-th step, the surface includes all the height fields generated at the previous step. As explained in [30], the surfaces obtained with this algorithm generally contains a random waviness effect that is related mostly to the first step, when the heights of the four corner are set to four random numbers and no longer modified. The longest wavelength contained in the surface power spectrum will be then related to this initial geometry since the following steps only enrich the spectrum without modification to the low-frequency range.

In many simulations including numerical generated rough surfaces, it is important to distinguish the roughness effect from the waviness and form component, a modified algorithm is proposed in [30] to reduce this undesired waviness effect, and it is used later in this thesis. First of all, the height of the corners is set equal to zero, and the surface is obtained by the composition of n x n patches generated using the RMD with different random seeds. Each patch will have a lateral size, and the associated longest wavelength, significantly smaller than the total length size of L. Hence, the final surface will be composed of a n x n grid of RMD patch, and each of them will consequently have a different average value. This latter characteristic can be another source of waviness and it has been removed by scaling the height field of each patch to match the average

plane of the one including the tallest asperity.

1.2 Structural Adhesives

Adhesives are defined as non-metallic substances that allow to bind two or more separate items together and resist their separation. Adhesive-like substances, commonly referred also as glue, are known for a very long time in human history: remains of adhesives made in prehistory were discovered in different archaeological sites, in the form or resins or natural substance used for flint ceramic vessels or tar-hafted stone tools [31], [32].

In general, adhesives can be natural substances or produced synthetically; they usually have a polymeric structure, meaning that the chemical structure is a long molecule composed of repeated units chemically bonded together. An example is the epoxy polymer adhesive used in several everyday applications, including glue sticks for glue guns and a variety of craft glues.

The formation of the joint is the results of physical and chemical phenomena within the adhesive and between the adhesive and the components (called *adherends*). The joint strength is the result of *adhesive* and *cohesive* forces which develop respectively at the interfaces and inside the adhesive (see Figure 14).

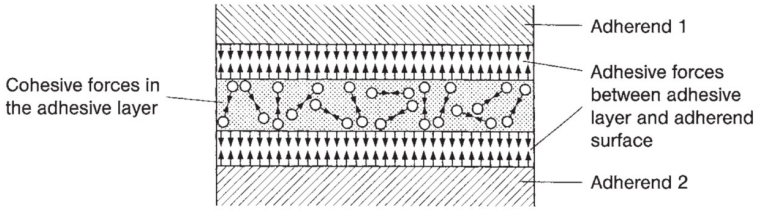

Figure 14: Adhesive and cohesive forces in a adhesive bonded joint. Source [33].

Adhesives can be classified according to the process necessary to develop the cohesive forces inside the adhesive layer. One class of adhe-

sives is liquid at the beginning of the application and becomes solid at the final stage due to a chemical reaction in the adhesive layer. These types of adhesives are classified as *chemical reactive* and the bonding process is called *curing*. Temperature and time affect the chemical reaction necessary for the adhesive layer formation. Multi-component adhesives belong to this class because they harden by mixing two or more components that are not adhesive by nature, but they chemically react when they are mixed.

In other types of polymeric adhesive, the bonding process happens because of a physical reaction, called *setting* process. It is the case of solvent-based adhesives, for which the solid-state is reached when the solvent evaporates, and of pressure-sensitive adhesive. Post-it is a common example of pressure-sensitive adhesives, which form a bond with the surface where are applied when a certain pressure is applied (see Figure 15).

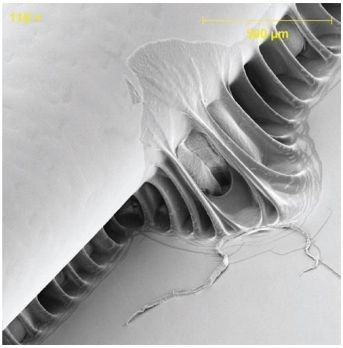

Figure 15: Re-adherable glue of a post-it, example of pressure-sensitive adhesive. Source [34].

The most important contributions at the interface level the formation of adhesive forces between the adhesive and the substrate are presented in Figure 16.

The molecular contact at the surface of the substrate is the seat of chemical bonding and diffusion between the molecules of the involved parts. Intermolecular van der Walls forces, which develop because of the

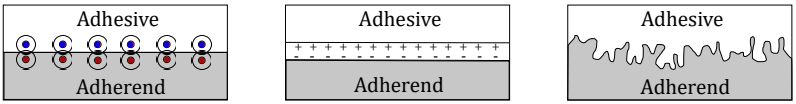

(a) Chemical bond **(b)** Static electricity **(c)** Mechanical interlocking

Figure 16: Sketch of different factors involved in the adhesion between surfaces.

temporary formation of opposite dipoles on the surfaces, are responsible for the adhesive abilities of hair-like attachment systems of some animals feet [35].

Polymers molecules can also interdiffuse into the other polymer in contact, binding the two components together. Electrostatic (Coulomb) and magnetic attraction are other well-known interface phenomena exploited in semiconductor and robotic industries.

Finally, the surface irregularities play an important role because of the mechanical interlocking between the adhesive and the surface pores and asperities. The irregularities increase the surface area, increasing total contact between adhesive and substrate and it also provides a physical impediment to crack propagation at the interface.

According to the application, many different types of adhesives are available. The present thesis focus on the *structural adhesive* which can be described as 'high-strength glue' that binds together components in a connection capable of transmitting structural stress without loss of structural integrity within design limits (Figure 17).

Structural adhesives are used extensively for bonding metallic, polymeric, and composite parts [37]. There are many types of structural adhesive, including epoxy, silicone, urethane, and acrylic. The thesis aims to assess the structural integrity of adhesively bonded joints.

Figure 17: Example of application of a structural adhesive in the industrial sector. Source [36].

1.2.1 Hyperelastic constitutive model

As stated before, adhesive materials usually have a polymeric structure. Their chemical composition is characterized by long molecular chains composed of repeated units, called monomers, and arranged in a three-dimensional structure. The macroscopic physical properties of a polymer depend on the interactions between the chains: for examples, if the polymeric chains are linked together to form a three-dimensional network, the polymer is brittle and stiff, on the contrary, if the chains are connected through weak intermolecular forces, the polymer has a rubber-like behavior. Moreover, many factors as temperature, pressure, and phase change can modify the chemical structures and the macroscopic properties.

Aside from the adhesives, other natural polymeric materials are wool, silk, and natural rubber. The list of synthetic polymers is even longer and includes synthetic rubber, nylon, silicone, polyethylene, polystyrene, and polypropylene among others.

From a mechanical point of view, this class of materials, defined elastic material, can experience large deformations and return to the initial state once their load disappears. In other words, the work done during the loading process is recovered during the unloading process [38]. While for linear elastic materials, stress varies linearly with respect to strain, other linear solids manifest a nonlinear elastic response, see Figure 18, defined *hyperelasticity*. The hyperelastic constitutive laws account both for nonlinear material behavior and large shape changes.

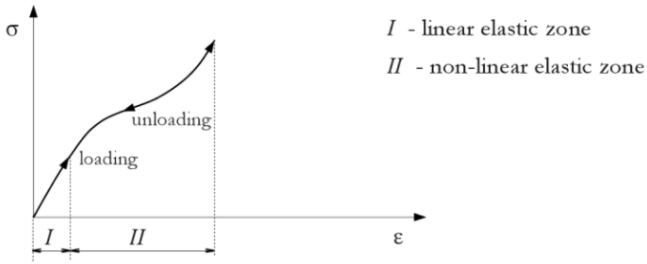

Figure 18: Stress-strain response for elastic material. Source [38].

Many researchers have studied the hyperelastic constitutive model, producing phenomenological or empirical laws, or based on the microstructure of the solid. Among the others laws, we can cite Mooney-Rivlin [39], Ogden [40], Arruda-Boice [41] and Neo-Hookean models.

Often the hyperelastic components are used together with other types of materials, with different mechanical behaviors in many technological solutions: structural joints, where the adhesives connect stiffer adherends, fibers-reinforced rubber, bio-mimetic structures, and stretchable electronic devices.

Flexible electronic devices, for example, combine metallic layers (or islands) with a linear elastic behavior to polymeric substrates that assure large deformations to the final product.

1.2.2 Adhesive bonded joints

Adhesive bonding offers different possibilities for joint geometry design (see Figure 19). Apart from the realization of layered components, where the adhesive represents simply a relatively thin layer, one of the simplest join types is the so-called *butt joint* realized by applying the adhesive at two components extremities. The geometry of the *scarf joint* differs for the slope of the interface. Other configurations overlap the lateral surface of the parts, in the geometry defined as *single-lap* and *double lap*. Moreover, different geometries are used to realize corner assemblies.

The broad use of adhesive for the realization of structural joints is

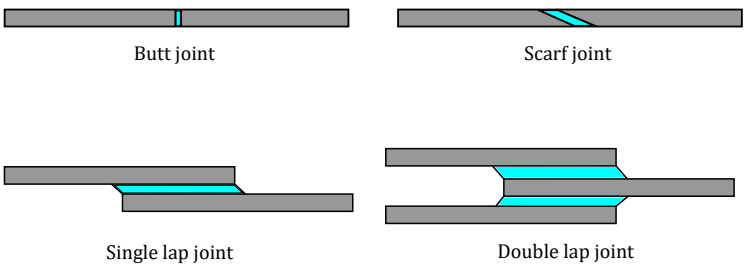

Figure 19: Adhesive bonded joints geometries.

justified because of the advantages offered by this technology compared to welding and fastening techniques. A great advantage is represented also by a good strength/weight ratio. The adhesive allows connecting both similar and dissimilar materials, and various types of geometries. Besides the weight reduction, this bonding technique, in fact, allows uniform load transfer, reduces the stress concentration, and enhances the energy efficiency of the structure [42]. Because of the large number of available adhesives, the chemical and physical properties can be tuned according to the adherends and service condition, for example sealing joints against different environments, insulating against heat transfer and electrical conductance, damping vibration, and absorbing shock.

However, adhesive bonded joints present some disadvantages:

- extensive surface preparation;
- difficult disassemble of the joint;
- degradation from moisture, humidity, and temperature.

Regarding the first point, bond strength and joint durability can be significantly improved by treating the adherend surface before the bonding. Typical surface pretreatment techniques include solvent cleaning, surface chemistry alteration, and abrasion, and other topographical changes [43].

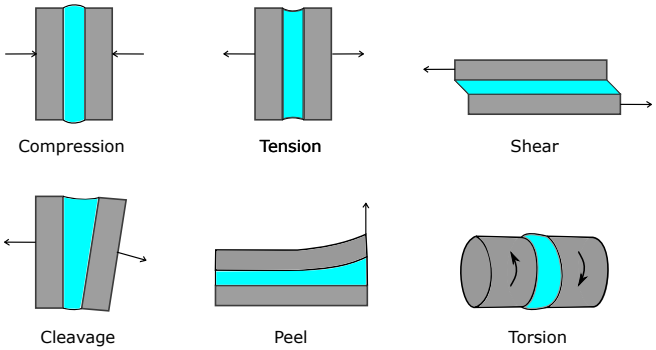

Figure 20: Sketch of different types of loading cases for adhesive bonded joints.

The adhesive joints can experience different types of loading conditions, depending on the joint geometry and the mechanical properties of adhesive and adherend, as depicted in Figure 20.

The failure of the adhesive joint can be classified into two different types: (i) the first mechanism is called *adhesive* failure and regards the interfacial bond failure between the adhesive and the adherend; (ii) the second one is called *cohesive* failure and occurs when a fracture allows a layer of adhesive to remain on both surfaces. A sketch of the different failure modes is shown in Figure 21. Another situation occurs when the adherend fails before the adhesive, this case is known as a cohesive failure of the substrate. Combinations of the two mechanisms may also occur if the crack propagates at some spots in a cohesive way and at others in an interfacial manner.

Different standards have been established for the assessment of adhesive joint strength. To evaluate the viscosity, tensile strength, bulk modulus, shear strength, and shear modulus, ASTM (American Society for Testing and Materials) standards describe different experimental tests according to the bonded materials (metals, plastic, and wood). One of the most used is the peeling test where the strength required to detach (peel) an adherend (usually a flexible stripe) from the substrate is recorded and

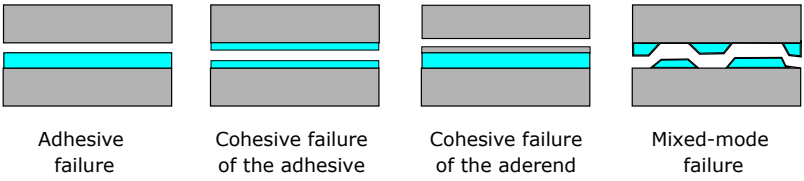

Figure 21: Sketch of different types of adhesive bond failure.

used to characterize the adhesive.

As will be described later in Chapter 3, peeling test is a useful tool to analyze also the influence of the substrate characteristics on the strength of the adhesive. The joint strength is, in fact, the result of the characteristics of the components and of the interface features. The presence of geometric discontinuities, material mismatch, and property jumps introduce more complexity than the simple evaluation of the single component performance, in the adhesive joints, as well as other multi-component assemblies.

1.2.3 Bio-inspired adhesives

As already introduced in Section 1.1, the natural abilities to climb vertically, developed by many animal species derive from the special characteristic of their feet surface. Geckos, spiders, and some insects, for example, are very well known for their ability to run up any walls and ceilings. They rely on the unique distribution of micro-structures on their feet skin which creates multiple contact elements. This adhesive mechanism has been investigated to produce new bio-inspired adhesives, which surface reproduce the natural micro-structures on animal skins.

In the specif case of geckos, their foot-pads are covered by a huge number of keratin hairs, called *setae* and visible at a certain magnification as in Figure 22. Each hair has a sub-micrometer dimension and branches at the tip into hundreds of projections, called *spatulae* [35]. These micro-structures produce a sufficient adhesive force, thanks to van der Walls attraction forces (more recent studies have shown the contribution of elec-

trostatic interaction [44]), to allows geckos to climb most surfaces [45].

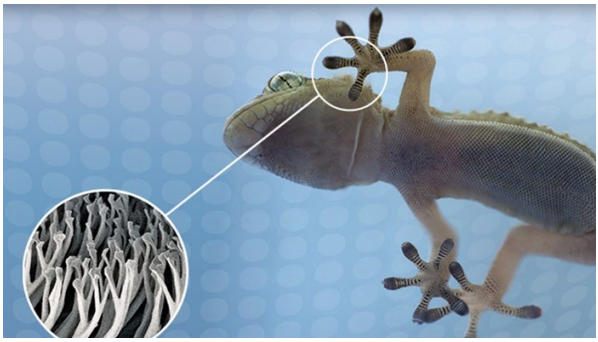

Figure 22: Spatulae microstructures on geckos feet, responsible for their ability of climb vertically. Source [46].

Spatula-shaped contacts are also known from other biological systems and therefore seem to represent the optimized geometry for multiple contact formation and rupture with the substrate [35]. The spatula-shaped system can generate adhesion only when a shear force is applied, which is possible because of muscle force express by geckos while running or walking.

Contact elements in biological attachment systems can also assume a mushroom-shaped geometry, which assures a long-term temporary adhesion, compared to the dynamic adhesive system of the spatula shape (see Figure 23). The mushroom-shaped geometry adhesion is independent of applied shear and can remain attached without the external support of muscle force. A relatively high pull-off force is needed for the contact breakage. These characteristics make the mushroom-shaped geometry more suitable for the realization of bio-inspired adhesive since a long term attachment without the constant external load application is required. Moreover, it has been demonstrated that in dry adhesives, mushroom shapes are much more efficient than flat-punch contact elements [47].

Mushroom-Shaped Adhesive Microstructures (MSAMSs) are usually

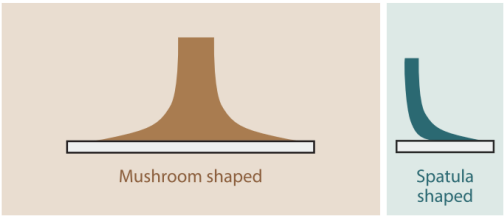

Figure 23: Contact shapes of biological attachment systems. Adapted from [35].

produced using polymers as polyurethane, PDMS, or polyvinylsiloxane (PVS) through soft molding technique. The result is shown in Figure 24. A sketch of the singular pillar, which is the singular mushroom-shape unity that composes the texture of the adhesive, is shown in Figure 25.

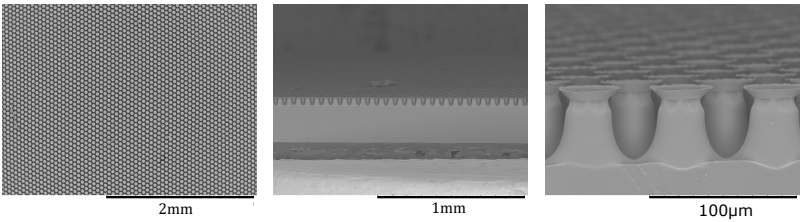

(a) Top view **(b)** Side view **(c)** Side view, close up

Figure 24: Mushroom-shaped fibrillar adhesive micro-structures made of PVS.

The pillar geometry needs to be optimised considering the stress distribution dependence on the stalk radius (R_i) and contact plate radius (R_e) and thickness (s) in order to avoid stress singularities [35], because stress peak does not guarantee the correct adhesion between the substrate and the pillar.

In the case of an optimized geometry, if a tensile load acts on a pillar of the MSAMSs, the detachment is governed by two types of debonding mechanisms: (i) crack nucleation in the middle of the contact interface, known as mode II, and crack propagation toward the outer edge and

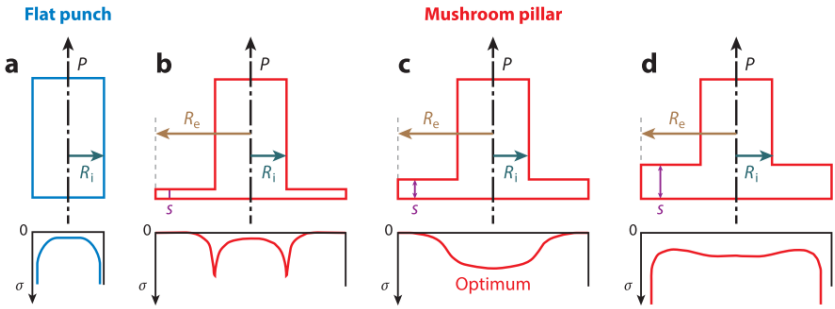

Figure 25: Interfacial stress distribution of different pillars stress. Source [35].

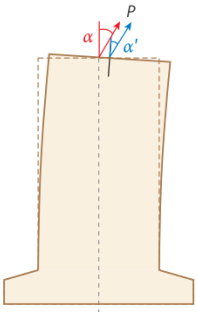

Figure 26: Single mushroom-shaped pillar upon the action of a pull-off force P tilted by an angle α. Adapted from [35].

(ii) homogeneous separation due to the achievement of the theoretical contact strength of intermolecular van der Waals interactions. Moreover, the pull-off force required for the detachment of the pillar depends on the tilt angle (α) (see Figure 26). Hence, the contact rupture can then be controlled by increasing the tilt angle.

Mushroom-shaped technology has several advantages compared to conventional pressure-sensitive adhesives since it is glue-free, and switchable, reversible, and can be used underwater [35]. MSAMSs are also resistant to many attachment cycles and the contamination can be easily removed by washing. They have been used to allows robots to climb

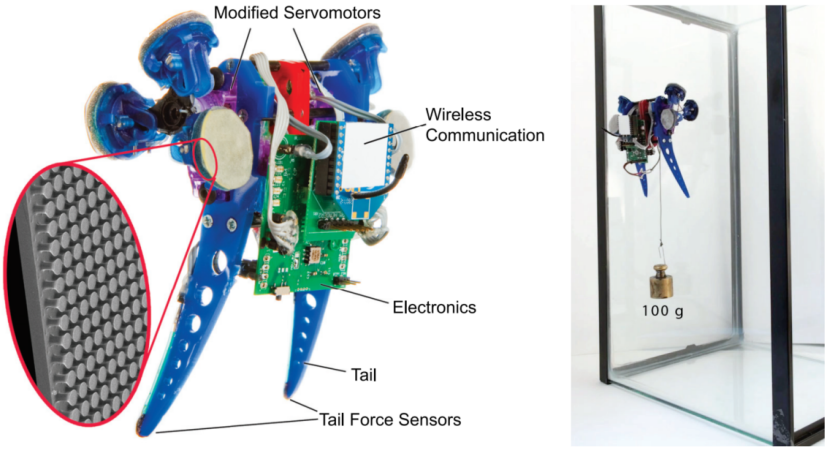

Figure 27: (a) Components of the climbing robot Waalbot II with labeled components and an inset of a SEM image of the MSAMSs adhesive used in the footpads. (b) Climbing payload capacity of Waalbot on smooth vertical surfaces. Adapted from [48].

vertical glass walls [48] (Figure 27) and as skin patch for health monitoring [49] (Figure 28).

1.3 Objectives and outline of the thesis

Intending to understand the mechanical phenomena that may take place at the interface between different materials, simply in contact or joined through an adhesive, the present research project explores the role of complex interfaces and functional surfaces in the overall performance of a multi-component product, focusing on different topics and applications.

Firstly, the thesis examines the influence of the morphological properties of the surface on the stress transfer between components directly in contact in the context of computational contact mechanics. The research focuses on the development of a new variational approach and its

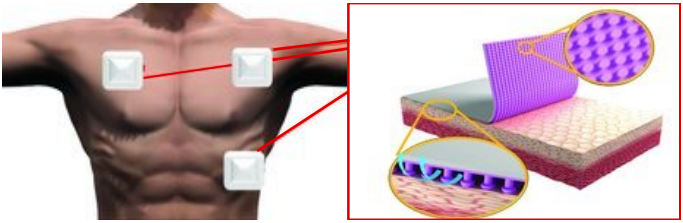

Figure 28: Skin patch for health monitoring systems with MSAMSs adhesive. Adapted from [49].

related finite element formulation that overcomes the issue of requiring an accurate representation of roughness, treating the interface as nominally smooth at the macro-level and embedding, at the micro-level, the actual rough topology. A multi-scale FEM-BEM formulation is proposed in Chapter 2 to address large-scale contact problems without smoothing out the influence of the roughness at the micro-scale. The formulation considers a 2D frictionless normal contact problem and the coupling between the micro- and macro-scale has been implemented by exploiting three alternative approaches for accelerating the computations.

The second topic of the thesis, developed in Chapter 3, aims at studying the mechanical behavior of structural adhesives. In this chapter, the effect of roughness and adhesive thickness on the peeling response of a silicone-based adhesive bonded to a polymeric substrate has been experimentally investigated through peeling tests. The effect of the surface morphology on the cohesive failure of the adhesive has been modeled starting from the collected experimental data. The simulation of the joint has been performed using standard finite elements for the adherends and zero-thickness interface finite elements for the adhesive, using a cohesive zone model approach.

Moreover, the research project focuses on the simulation of biologically inspired adhesives with mushroom-shaped micro-structures, using a computational model to reproduce experimental data and evaluate the adhesive performance on more complex applications. This topic has been explored in Chapter 4.

Finally, in Chapter 5, the failure of bilayer structures with material mismatch has been analyzed to assess the reliability of layered structures used, for example, in stretchable devices. The polymeric nature of adhesives and flexible substrates has been considered coding a phase-field finite element with a hyperelastic constitutive model to simulate crack initiation and propagation in bilayer structural joints.

Finally, Chapter 6 discusses the conclusion of this investigation and future developments.

Chapter 2

Multi-scale FEM-BEM model for rough mechanical joint

In this chapter, a multi-scale method for contact mechanics problems is presented to address the simulation of rough contact interfaces between two bodies considering the presence of roughness at the interacting surfaces. Since industrial products have a size-scale usually much bigger than the microscopical size-scale of roughness, an effective approach is needed to take into account both the bulk properties of the components coming into contact and the surface topography influence on the overall performance. A multi-scale approach that combines the Finite Element Method (FEM) for the mechanics of the bulk components and the Boundary Element Method (BEM) at the microscopic scale for solving the rough contact problem has been developed.

Rough contact has been widely studied in contact mechanics to compute contact variables, such as contact pressure, contact stiffness and real contact area, and deformation and stress states of the bodies considering the presence of roughness. In particular, an overview of the different approaches available in the literature for simulating the effect of roughness is provided in Section 2.1. In Section 2.2 the variational formulation

of the problem is introduced together with the micro- and macro-scale models, afterwards their coupling is presented in Section 2.3. Section 2.3.4 is devoted to numerical examples and discussion of the computational advantages of the proposed approach.

Nomenclature

Ω_i	i-th body domain
$\delta\Omega_i^{\mathrm{D}}$	Dirichlet boundary of the i-th body
$\delta\Omega_i^{\mathrm{N}}$	Neumann boundary of the i-th body
Γ	Interface between the two bodies
Γ_i	Interface boundary of the i-th body
Γ^*	Macro-scale smooth representation of Γ
Γ_i^*	Macro-scale smooth representation of Γ_i
x, y, z	Coordinates at the macro-scale
$\mathbf{u}_i$	Displacement field of the i-th body
$\mathbf{x}$	Position vector
$\boldsymbol{\epsilon}_i$	Small Deformation strain vector of the i-th body
$\boldsymbol{\sigma}_i$	Cauchy stress tensor vector of the i-th body
$\Psi(\epsilon_i)$	Helmholtz free-energy
$\mathbb{C}$	Constitutive operator for the i-th solid
$e_{i,max}$	Maximum peak to valley distance for Γ_i
L	Characteristic length for Ω_i
$\Delta\mathbf{u} = \mathbf{u}_1 - \mathbf{u}_2$	Relative displacement field
$\mathbf{n}_i, \mathbf{t}_i$	Normal and tangential vectors of Γ_i^*
$\mathbf{n}, \mathbf{t}$	Normal and tangential vectors of Γ^*
$\mathbf{g} = (g_{\mathrm{n}}, g_{\mathrm{t}})^{\mathrm{T}}$	Gap field across the interface
$\mathbf{p} = (p_{\mathrm{n}}, p_{\mathrm{t}})^{\mathrm{T}}$	Contact pressure vector at the interface
$\mathbf{M}$	Averaging operator
w_i	Gauss quadrature weight for the i-th integration point
$\det J$	Determinant of the Jacobian of the element coordinates transformation
$g_{\mathrm{n,i}}, p_{\mathrm{n,i}}$	Normal gap and the normal contact pressure at the i-th Gauss Point
$\mathbf{d}$	Nodal displacement vector
$\mathbf{R}$	Rotation matrix
$\mathbf{N}$	Shape function matrix
$\mathbf{L}$	Matrix operator
r	Coordinate of the natural reference system
$\mathbf{R}^{(k)}$,	Residual vector at the k Newton-Rapson iteration
$\mathbf{K}^{(k)}$	Tangent stiffness matrix at the k Newton-Rapson iteration
$\mathbb{C}$	Interface constitutive matrix
$\boldsymbol{\xi} = (\xi_1, \xi_2)^T$	Position vector at the micro-scale
$e_i(\boldsymbol{\xi})$	Elevations field of Γ_i measured from Γ^*
$e^*(\boldsymbol{\xi})$	Elevation of the composite topography
$e^*_{\max}$	Maximum peak-to-valley distance for the composite topography
E_i, ν_i, G_i	Young's module, Poisson ratio and Shear modulus of the i-th body
E, ν, G	Composite elastic parameters
$u(\boldsymbol{\xi})$	Normal displacement of the half-space
$\overline{u}(\boldsymbol{\xi}, g_{\mathrm{n}})$	Indentation of the half-space

Nomenclature

$w(\boldsymbol{\xi}, g_{\mathrm{n}})$	Half-space displacement elastic correction
$p(\boldsymbol{\xi})$	Normal contact pressure at the micro-scale
P	Total contact force
l	Lateral size of the discretized rough surface
n	Resolution paramenters
NxN	Number of grid cells, $N = 2^n + 1$
a	Lateral size of a cell
$e^*_{i,j}, u_{i,j}, \bar{u}_i, j$	Height, half-space displacement and indentation of the i, j cell
w_i, j	Displacement elastic correction of the i, j cell
$\bar{e}^*$	Mean elevation of the discretized rough field
s	Root mean square of the discretized rough field
$H(\boldsymbol{\xi}, \eta), \mathbf{H}$	Green's function continuous and discretized forms
$\mathbf{C}$	Cholesky factorization of $\mathbf{H}$
$\mathbf{u}^*, \mathbf{p}^*$	optimal normal displacement and optimal contact force vectors
$\overline{p}$	Averaged contact pressure
α	Coefficient depending on the mesh size of the surface grid
w_0	Elastic uniform displacement for the body elastic compliance
δ_t, δ_r	Total displacement and roughness related displacement
δ_c	Augmented displacement for the BEM algorithm
p^i	p_{n} value at the iteration i of the pressure correction procedure
err	Relative error for the pressure correction procedure
a, b	Power-law fitting function coefficients
$g^t_{\mathrm{n,k}}, p^t_{\mathrm{n,k}}$	p_{n} and g_{n} at the k-th Newton-Rapson iteration at timestep t
$\Delta g^t_{\mathrm{n,k}}$	g_{n} pertubation at the k-th Newton-Rapson iteration at timestep t
$g^t_{\mathrm{n,k+1}}, p^t_{\mathrm{n,k+1}}$	Perturbed g_{n} and p_{n} at the k-th Newton-Rapson iteration at timestep t
Δ	Imposed displacement in the benchmark test
$h^*(g_{\mathrm{n}})$	Distance between the smooth reference plane and the mean plane of the rough surface

2.1 Contact of rough surfaces

The performance and reliability of a mechanical joint are heavily influenced by the geometrical/topological features of the interacting surfaces. Any local imperfections and deviations from the ideal flatness of the surface can play a crucial role in stress transfer between the bodies, friction, wear, and lubrication. Besides the mechanical properties, also thermal and electrical conductance, optical properties, and fluid-solid interactions are influenced by the presence of roughness.

In fact, the inevitable roughness on the contacting surfaces causes intimate contact to be restricted to a few microscopic actual contact areas constituting a small percentage of the nominal contact area, as firstly in-

troduced by Bowden and Tabor in [50].

Subsequently, starting from one of the best-known results in mechanics, the Hertzian analysis of the elastic contact between two spheres, in 1966 Greenwood and Williamson [51] extended the Hertz's result to rough surfaces and giving the base for many subsequent theories used in tribology [52, 53, 54]. In the Greenwood and Williamson's theory, the rough surface is described through an exponential distributions function of the surface heights and it is assumed that the asperities have the same radius of curvature, behave independently and deform as a Hertzian sphere. A more complex statistical distribution of the elevations and curvatures are introduced in [55], while the interaction between the asperities has been later analyzed in [56]. Based on a fractal description of the rough surfaces, in the 1990s, different models exploited the multi-scale features of roughness as in [20, 22, 8].

The mentioned efforts focused mostly on the characterization of the interface interactions between the contacting surfaces, neglecting the mechanics of the bulk. Moreover, the analytical methods can deal with a limited number of cases, in other more complex situations numerical methods are needed. A numerical formulation of a contact problem reduces the contact interface to a set of discrete nodes and to a finite set of algebraic equations [57]. Mathematically, the discrete problem differs from the continuum problem, though the value of the numerical method depends on the assumption that, with appropriate mesh refinement, the predicted physical relations will approach those of the continuum problem asymptotically.

In the literature, the most common approaches are (i) the Boundary Element Methods, where, on the same line of semi-analytical approaches, only the surface of the bodies is examined, and (ii) Finite Element Methods in which also the surrounding continuum is considered.

The boundary element method, first introduced in 1977 [58] and applied to contact mechanics within the work of Andersson and Allan-Persson [59], has been historically preferred because of the minor computational effort than the finite element one, since the discretization of both rough surface and bulk increases the dimension of the problem. In

the boundary element method, the deformable body beneath the rough surface is commonly assumed as a half-space or a half-plan. For a linear elastic problem, the methods lead to an integral equation, the so-called Green's function, that relate the displacement at a generic point to the action of a concentrated force on the surface caused by the contact interaction. Discretizing the half-plane with a grid of boundary elements, performing the numerical integration over each boundary element, and assembling the solution matrix, the unknown quantities (either the surface displacement or traction per node) can be solved numerically from the set of linear equalities and inequalities stemming from the contact conditions using constrained optimization methods. Different algorithms are available in the literature, Bemporad and Paggi [60], provided an overview of different available solution algorithms. Within the same publication, a warm-started Non-Negative Least Squares (NNLS) algorithm is proposed and it will be used and described later in this chapter.

The generalization of BEM to finite-size geometries and inhomogeneous material is not straightforward and it has been attempted in [61] and [62]. In this framework, the finite element methods demonstrate better capabilities and it has been applied in the case of interface constitutive nonlinearities as in [63], and material nonlinearities. For examples, the elastoplastic behavior is considered in [64], and viscoelastic materials involving frictional dissipation are exploited in [65].

Remarkable applications of the FEM can be found in the case of multifield problems, involving heat-transfer [66, 67] or in reaction-diffusion problems [68], where the BEM has not been applied so far.

The size-scale of the components involved in industrial products still constitute an open problem because the above mentioned finite element techniques are designed only for micro-scale computations, comparable with the roughness scale. To overcome this issue, multi-scale approaches can be considered. In this regard, large-scale finite elements simulations of contact problems using a refined constitutive model for including roughness effects can be found in [69] and in [70], where a finite element contact model with a fine mesh at the interface has been proposed exploiting local refinement techniques. In the already cited

[66], the authors developed a modified nonlinear penalty formulation at the macro-scale using a micro-mechanical model solution in closed form, with the drawback of introducing some assumptions on the statistics of the heights field. Moreover, a multi-scale FEM approach using surface interpolation techniques and micro-scale off-line computations for frictional contact has been proposed in [65], mentioned also above for the viscoelastic material model.

As compared to the previous methods proposed in the literature, the approach presented in this thesis does not rely on a closed-form solution at the micro-scale associated with a specific microscopical contact model, which implies assumptions on roughness statistics. The proposed method, in fact, allows using directly any kind of height fields, available from profilometric acquisitions or numerically generated, simply as input data for the problem. Furthermore, the macro-scale model benefits from the advantages of the FEM, that can simulate more complex geometries than the half-plane assumed for the BEM, and can be extended to frictional and multi-field contact problems.

The next sections present the variational formulation of the mechanical problem and clarifies the coupling between the FEM and BEM at the different scales, exploiting a new interface finite element.

2.2 Variational formulation

This section delineates the variational formulation for the contact problem between two solids with a rough interface. Firstly, the strong differential form describing the mechanics of the bodies and the contact conditions at the interface is presented. Then, the corresponding weak form is derived, providing the basis for the interface finite element formulation.

2.2.1 Strong form of the governing equations

Consider two deformable bodies occupying the domains $\Omega_i \in \mathbb{R}^2$ $(i = 1, 2)$ in the undeformed configuration, where a point position is defined by the reference system $Oxyz$ or Oxz in the case of a two-dimensional

setting, which is used in the following presentation for the sake of simplicity (see Figure 29).

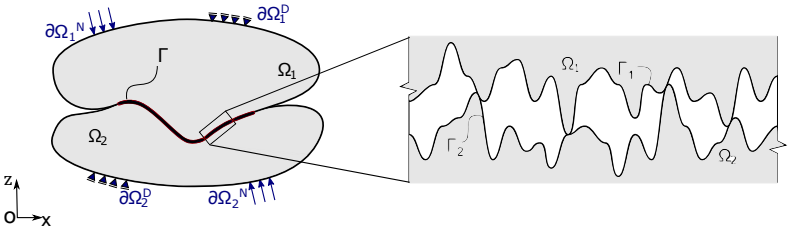

Figure 29: The solid domains Ω_i $(i = 1, 2)$ and the interfaces Γ_i $(i = 1, 2)$.

In the most general case, let us introduce, for each body, a displacement field $\mathbf{u}_i = (u_i, v_i)^{\mathrm{T}}$, that maps the transformation from the undeformed configuration to the deformed ones, and vice versa. Such functions are thereby assumed to be continuous, invertible, and differentiable functions of the position vector $\mathbf{x} = (x, z)^{\mathrm{T}}$ within each body [71]. As customary [63], inside each deformable solid, the small deformation strain tensor $\boldsymbol{\epsilon}_i$ $(i = 1, 2)$, defined as the symmetric part of the displacement gradient: $\boldsymbol{\epsilon}_i = \nabla^s \mathbf{u}_i$, is introduced. In the sequel, using the standard Voigt notation, the strain tensor components are collected in the vector $\boldsymbol{\epsilon}_i = (\epsilon_{xx}, \epsilon_{zz}, \gamma_{xz})_i^{\mathrm{T}}$. In the same way, the Cauchy stress tensor components are defined in the vector $\sigma_i = (\sigma_{xx}, \sigma_{zz}, \tau_{xz})_i^{\mathrm{T}}$.

The two solids are separated by an interface Γ defined by the opposite boundaries Γ_i $(i = 1, 2)$ of the two domains, viz. $\Gamma = \bigcup_{i=1,2} \Gamma_i$, where contact takes place. The whole boundary of the i-th body, $\partial\Omega_i$, can be divided into three sections:

- the Dirichlet boundary $\partial\Omega_i^D$ where displacements are imposed;
- the Neumann boundary $\partial\Omega_i^N$ where tractions are specified;
- the interface Γ_i where the contact is described by imposing specific boundary conditions.

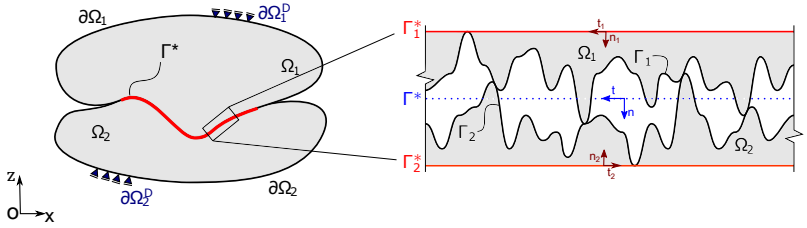

Figure 30: Smoother representations of the interface Γ_1^* and Γ_2^* and respective normal and tangent unit vectors.

Here, we assume that Γ_i is nominally smooth but microscopically rough, thus introducing a scale separation. A smoother representation of each interface, Γ_i^*, is then introduced by considering a surface parallel to the average one of the rough surface Γ_i and passing through its lowest point, i.e. the deepest valley (see Figure 30).

The formulation is not restricted to macroscopically flat surfaces, but it has general validity, and includes curved surfaces. In this latter case, it is possible to distinguish the roughness from the form of the solid. The lowest point of the rough surfaces would be hence determined considering the maximum distance with respect to the surface of the form along the normal direction to this latter surface. Another possible approach considers the surface to be macroscopically flat and includes the form in the rough description at the micro-scale. The reference surface for defining the lowest point would be represented in any case by the smooth macroscopic description. The scale separation holds if the following hypotheses are satisfied:

- $e_{i,max} << L$, where $e_{i,max}$ is the maximum peak-to-valley distance for the i-th rough surface and L is a characteristic length for Ω_i;
- $e_{i,max} << R$ for every point of Γ_i^*, where R is the local radius of curvature of Γ_i^*.

The two reference curves Γ_1^* and Γ_2^* are distinct lines separated by a distance t, which defines the interface thickness at the micro-scale, while

at the macro-scale such a distance is negligible, thus allowing to consider them distinct but coincident lines which concur to define Γ^*. Hence, the smooth representation of the interface Γ^* is used to solve the problem at the macro-scale and for the definition of the governing equations of the system.

Moreover, as a result of the scale separation, at the macro-scale level, conforming contact takes place over the nominal contact area *apriori* defined by Γ^*, while at the micro-scale, non conforming contact between the two opposite rough surfaces holds. At the initial condition, the actual contact area between the undeformed surfaces Γ_i can be determined by their geometry.

Consider, also, the tangential and normal unit vectors $\mathbf{t}_i(x,z)$ and $\mathbf{n}_i(x,z)$ at any point of Γ_i^*, with $\mathbf{n}_i$ pointing outwards from the domain Ω_i. The two coincident smoother surfaces are parallel to each other because we assumed that two non-conformal profiles are microscopically rough but nominally smooth, and therefore $\mathbf{n}_1(x,z) = -\mathbf{n}_2(x,z)$ and $\mathbf{t}_1(x,z) = -\mathbf{t}_2(x,z)$, $\forall x,z$ on Γ^*. As a result, unique tangential and normal unit vectors $\mathbf{n}$ and $\mathbf{t}$ (assumed to be coincident with $\mathbf{n}_1$ and $\mathbf{t}_1$) can be defined, and Γ^* can be described by a zero-thickness interface model.

At the interface Γ^*, the configuration of the system is described by the gap field across the interface $\mathbf{g} = (g_\mathrm{n}, g_\mathrm{t})^\mathrm{T}$, which is mathematically defined as the projection of the relative displacement field $\Delta\mathbf{u} = \mathbf{u}_1 - \mathbf{u}_2$ onto the normal and tangential directions of the interface. The mathematical expression for the $\mathbf{g}$ is described later in Eq. (2.8) with more details.

Supposing the absence of body forces, the linear momentum equation of the system provides the strong (differential) form of equilibrium for each body, equipped with the Dirichlet and the Neumann boundary conditions acting respectively on $\partial\Omega_i^D$ and $\partial\Omega_i^N$, where $i = 1, 2$. Furthermore, the interaction between the two bodies is described by the contact conditions on Γ^*, so that the strong form of equilibrium reads:

$$\nabla \cdot \boldsymbol{\sigma}_i = \mathbf{0} \ \text{ in}\,\Omega_i, \tag{2.1a}$$

$$\mathbf{u}_i = \hat{\mathbf{u}} \ \text{ on}\,\partial\Omega_i^D, \tag{2.1b}$$

$$\boldsymbol{\sigma}_i \cdot \mathbf{n} = \mathbf{T} \ \text{ on}\,\partial\Omega_i^N, \tag{2.1c}$$

$$g_{\mathrm{n}} > 0,\ p_{\mathrm{n}} > 0 \ \text{ on}\,\Gamma^* \tag{2.1d}$$

$$g_{\mathrm{n}} \leq 0,\ p_{\mathrm{n}} = 0 \ \text{ on}\,\Gamma^* \tag{2.1e}$$

where $\hat{\mathbf{u}}$ and $\mathbf{T}$ denote, respectively, the imposed displacement and the applied traction vector, while p_{n} is the nominal pressure at the contact interface, and depends on the normal component of the relative displacement, g_{n}. The sign convention adopted in this Chapter considers the gap g_{n} to be zero at the initial condition, and to be positive-valued when the initial distance between Γ_1^* and Γ_2 reduces (the bodies are getting closer), corresponding to a positive contact pressure p_{n}. Since the adhesion between the bodies is neglected, a negative gap represents the detachment of the bodies and corresponds to $p_{\mathrm{n}} = 0$. The nominal pressure $p_{\mathrm{n}}(g_{\mathrm{n}})$ is an unknown variable for the macro-scale problem and it is computed using the boundary element method at the micro-scale level, as described in the Section 2.3.2.

In order to solve the Eq. 2.1, recalling standard thermodynamics arguments, a general constitutive stress-strain relation is considered for the i-th material domain: $\boldsymbol{\sigma}_i := \partial_{\boldsymbol{\epsilon}_i}\Psi(\boldsymbol{\epsilon}_i)$ and $\mathbb{C}_i := \partial^2_{\boldsymbol{\epsilon}_i\boldsymbol{\epsilon}_i}\Psi(\boldsymbol{\epsilon}_i)$, whereby $\Psi(\boldsymbol{\epsilon}_i)$ is the Helmholtz free-energy function for body i, whereas $\boldsymbol{\sigma}_i$ and $\mathbb{C}_i$ are, respectively, the Cauchy stress tensor and the constitutive operator. In the present formulation, a linear elastic material law has been considered. However, the given framework can be adopted also for the nonlinear case.

The constitutive response of the interface should be introduced by distinguishing between the normal and the tangential directions. Although the present formulation can encompass any type of interface interactions, we restrict our attention to the frictionless normal contact problem and we neglect the influence of adhesion.

2.2.2 Weak form of the equilibrium equations

According to the principle of virtual work, a virtual displacement field $\mathbf{v}_i$ and a virtual normal gap $g_{\mathrm{n}}(\Delta\mathbf{v})$ at the interface Γ^* are introduced in order to compute the weak form of the equilibrium equations associated with the strong form in Eq. (2.1):

$$\begin{aligned}\delta\Pi = \int_{\Omega_1} \boldsymbol{\sigma}_1(\mathbf{u}_1)^{\mathrm{T}}\boldsymbol{\epsilon}_1(\mathbf{v}_1)\mathrm{d}\Omega + \int_{\Omega_2} \boldsymbol{\sigma}_2(\mathbf{u}_2)^{\mathrm{T}}\boldsymbol{\epsilon}_2(\mathbf{v}_2)\mathrm{d}\Omega - \\ \int_{\partial\Omega_1^{\mathrm{N}}} \mathbf{T}^{\mathrm{T}}\mathbf{v}_1 \,\mathrm{d}\partial\Omega - \int_{\partial\Omega_2^{\mathrm{N}}} \mathbf{T}^{\mathrm{T}}\mathbf{v}_2 \,\mathrm{d}\partial\Omega - \int_{\Gamma^*} p_{\mathrm{n}}(\Delta\mathbf{u}) g_{\mathrm{n}}(\Delta\mathbf{v})\mathrm{d}\Gamma = 0\end{aligned} \tag{2.2}$$

The test function in the i-th body fulfills the condition $\mathbf{v}_i = \mathbf{0}$ on $\partial\Omega_i^D$, whereas the contact conditions on Γ^* can be formulated as:

$$p_{\mathrm{n}}(g_{\mathrm{n}}) = \begin{cases} p_{\mathrm{n}} & \text{if } g_{\mathrm{n}} > 0, \\ 0, & \text{if } g_{\mathrm{n}} \leq 0. \end{cases} \tag{2.3}$$

The contact conditions on Γ^* impose that the corresponding integral is greater or equal to zero everywhere on Γ^*. Thus, the solution of the problem implies the solution of the following variational inequality:

$$\begin{aligned}\int_{\Omega_1} \boldsymbol{\sigma}_1(\mathbf{u}_1)^{\mathrm{T}}\boldsymbol{\epsilon}_1(\mathbf{v}_1)\mathrm{d}\Omega + \int_{\Omega_2} \sigma_2(\mathbf{u}_2)^{\mathrm{T}}\boldsymbol{\epsilon}_2(\mathbf{v}_2)\mathrm{d}\Omega - \\ \int_{\partial\Omega_1^{N}} \mathbf{T}^{\mathrm{T}}\mathbf{v}_1 \,\mathrm{d}\partial\Omega - \int_{\partial\Omega_2^{N}} \mathbf{T}^{\mathrm{T}}\mathbf{v}_2 \,\mathrm{d}\partial\Omega \geq 0.\end{aligned} \tag{2.4}$$

The displacement field $\mathbf{u}_i$ solution of the weak form in Eq. (2.2) is such that it corresponds to the minimum of Π for any choice of the test functions $\mathbf{v}_i$.

2.3 Multi-scale contact formulation

The present Section introduces the discretization of system with main focus on the interface model. In fact, for the bulk, standard linear quadrilateral or triangular isoparametric finite elements can be invoked, while, at the interface, the solution of the presented contact problem is treated

at two different levels. At the macro-scale, a zero-thickness interface finite element is employed to model interface interactions. The integral expressions for the stiffness operator and the residual vector are approximated via a Gaussian integration, as explained in detail in Section 2.3.1, using the values of the contact pressure evaluated by solving, for each Gauss point, the micro-scale problem. The latter is solved considering an equivalent contact problem between the rough surface and an elastic half plane exploiting the boundary element method, see Section 2.3.2.

The macro-scale interface discretization is treated under 2D plane strain assumption, while the micro-scale is 3D, and deals with two surfaces coming into contact. As stated in the previous section, the nominal pressure computed at the micro-scale is used at the macro-scale into the interface finite element. For guaranteeing the consistency between the two scales, the average pressure acting on the surfaces and evaluated using the BEM is multiplied by a unit depth before passing it to the FEM model. The same approach can be developed considering a 3D model also for the macro-scale discretization.

2.3.1 Finite element discretization of the interface at the macro-scale

The macro-scale discretization of the interface exploits the formulation of interface elements used in non-linear fracture mechanics for cohesive crack growth which is further specialized to account for the effect of roughness at a microscopical level. This 4 node isoparametric interface finite element is characterized by nodes 1 and 2, belonging to Γ_2^*, and by nodes 3 and 4, which belong to Γ_1^*, see Figure 31.

Using the described interface finite elements, the integral on Γ^* in Eq. (2.2) can be evaluated as:

$$\int_{\Gamma^*} p_{\mathrm{n}}(g_{\mathrm{n}}) g_{\mathrm{n}} \, \mathrm{d}\Gamma \cong \int_{\Gamma_h^*} p_{\mathrm{n}}(g_{\mathrm{n}}) g_{\mathrm{n}} \, \mathrm{d}\Gamma = \sum_{e=1}^{n_{el}} \left\{ \int_{\Gamma_e^*} p_{\mathrm{n}}(g_{\mathrm{n}}) g_{\mathrm{n}} \, \mathrm{d}\Gamma \right\} \tag{2.5}$$

where the subscript h refers to the discretised geometrical features of the interface, the subscript e denotes a single interface element contribution (with $e = 1, ..., n_{el}$).

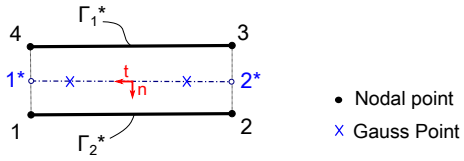

Figure 31: Sketch of the interface finite element topology.

The element formulation is related to a middle line obtained by averaging the position vectors of the two sides of the interface. The position vector of a generic point on the middle line, $\hat{\mathbf{x}}$, can be computed using an averaging operator $\mathbf{M}$:

$$\hat{\mathbf{x}} = \mathbf{M}\mathbf{x} \tag{2.6}$$

The latter equation allows to determine the nodal points 1^* and 2^* along the middle line of the interface. Each interface element is mapped into a natural reference system, having origin in the center of the element, such that the position of a point along the middle line can be specified by a dimensionless parameter,r, whose absolute magnitude never exceeds unity. The introduction of the middle line of the element allows also the definition of the normal and tangential unit vectors $\mathbf{n}$ and $\mathbf{t}$ representing the local reference system of the element.

Each element contribution is then computed using the two points Gauss quadrature formula:

$$\int_{\Gamma_e^*} p(g_\mathrm{n}) g_\mathrm{n} \, \mathrm{d}\Gamma = \det J \sum_{i=1,2} w_i \; p_{\mathrm{n,i}} \; g_{\mathrm{n,i}} \tag{2.7}$$

where $g_{\mathrm{n,i}}$ and $p_{\mathrm{n,i}}$ are the normal gap and the normal contact pressure at the i-th Gauss Point, w_i is the weight for the i-th integration point, and $\det J$ is the standard determinant of the Jacobian of the element coordinates transformation from its global reference frame (Oxz) to the natural reference system.

In the latter equation, both the normal gap g_n and the nominal pressure $p_\mathrm{n}(g_\mathrm{n})$ are required. The gap at any point inside the interface finite

element, $\mathbf{g} = (g_{\mathrm{t}}, g_{\mathrm{n}})^{\mathrm{T}}$, is derived from the nodal displacement vector $\mathbf{d} = (u_1, v_1, \ldots, u_4, v_4)^{\mathrm{T}}$, which collects the displacements components u and v of the four interface finite element nodes. The relative displacements of the nodes 1-4 and 2-3 can be computed applying a matrix operator $\mathbf{L}$ which calculates the difference between the displacements of nodes 1 and 2 with respect to those of nodes 4 and 3.

At this point, the relative displacements at any points of the interface finite element are evaluated by the multiplication of the nodal values with the matrix $\mathbf{N}$ that collects the standard linear shape functions at the element level.

Finally, we need to get the projections of the relative displacements on the local coordinate system of the interface finite element (normal and tangential gap). For this purpose, the rotation matrix $\mathbf{R}$, defined by the components of the unit vectors $\mathbf{t}$ and $\mathbf{n}$, is introduced.

In formulae, we have:

$$\mathbf{g} = -\mathbf{RNLd}, \tag{2.8}$$

where the operators present the following matrix form:

$$\mathbf{L} = \begin{bmatrix} -1 & 0 & 0 & 0 & 0 & 0 & 1 & 0 \\ 0 & -1 & 0 & 0 & 0 & 0 & 0 & 1 \\ 0 & 0 & -1 & 0 & 1 & 0 & 0 & 0 \\ 0 & 0 & 0 & -1 & 0 & 1 & 0 & 0 \end{bmatrix}, \tag{2.9a}$$

$$\mathbf{N} = \begin{bmatrix} N_1 & 0 & N_2 & 0 \\ 0 & N_1 & 0 & N_2 \end{bmatrix} \tag{2.9b}$$

$$\text{with } N_1 = \frac{1}{2}(1-r)\ N_2 = \frac{1}{2}(1-r), \tag{2.9c}$$

$$\mathbf{R} = \begin{bmatrix} t_x & t_z \\ n_x & n_z \end{bmatrix}, \tag{2.9d}$$

where n_x, n_z, t_x and t_z are the components of the unit vectors $\mathbf{n}$ and $\mathbf{t}$ along the x and z directions.

Since we restricted our attention on the frictionless normal problem, only the normal component of $\mathbf{g}$, g_{n}, is used in Eq. 2.7. The other unknown value in that equation is the normal contact pressure p_{n} that, as anticipated before, is computed according to the boundary element

method accounting for micro-scale contact interactions as explained in the following subsection.

Supposed that the nominal pressure has been evaluated, the interface finite element formulation provides, after the assembly operation, a non-linear algebraic system of equations, due to the intrinsic non-linearity introduced by the contact conditions. A Newton-Raphson scheme is herein adopted to solve the implicit non-linear set of equations:

$$\mathbf{K}^{(k)}\Delta\mathbf{d}^{(k)} = -\mathbf{R}^{(k)}, \tag{2.10a}$$

$$\mathbf{d}^{(k+1)} = \mathbf{d}^{(k)} + \Delta\mathbf{d}^{(k)}, \tag{2.10b}$$

where the superscript k denotes the iteration inside the Newton-Raphson loop.

At the element level, the residual vector $\mathbf{R}_e^{(k)}$ and the tangent stiffness matrix $\mathbf{K}_e^{(k)}$ associated with the $e-$th interface finite element, read:

$$\mathbf{R}_e^{(k)} = -\int_{\Gamma_e^*} \mathbf{L}^{\mathrm{T}}\mathbf{N}^{\mathrm{T}}\mathbf{R}^{\mathrm{T}}\mathbf{p}\,\mathrm{d}\Gamma, \tag{2.11a}$$

$$\mathbf{K}_e^{(k)} = \int_{\Gamma_e^*} \mathbf{L}^{\mathrm{T}}\mathbf{N}^{\mathrm{T}}\mathbf{R}^{\mathrm{T}}\mathbb{C}\mathbf{R}\mathbf{N}\mathbf{L}\,\mathrm{d}\Gamma, \tag{2.11b}$$

where $\mathbf{p} = (p_{\mathrm{t}}, p_{\mathrm{n}})^{\mathrm{T}} = (0, p_{\mathrm{n}})^{\mathrm{T}}$ and $\mathbb{C}$ is the linearized interface constitutive matrix:

$$\mathbb{C} = \begin{bmatrix} \dfrac{\partial p_{\mathrm{t}}}{\partial g_{\mathrm{t}}} & \dfrac{\partial p_{\mathrm{t}}}{\partial g_{\mathrm{n}}} \\ \dfrac{\partial p_{\mathrm{n}}}{\partial g_{\mathrm{t}}} & \dfrac{\partial p_{\mathrm{n}}}{\partial g_{\mathrm{n}}} \end{bmatrix}, \tag{2.12}$$

that, for the frictionless normal contact problem, reads:

$$\mathbb{C} = \begin{bmatrix} 0 & 0 \\ 0 & \dfrac{\partial p_{\mathrm{n}}}{\partial g_{\mathrm{n}}} \end{bmatrix} \tag{2.13}$$

The formulation requires herein to specify $\partial p_{\mathrm{n}}/\partial g_{\mathrm{n}}$, depending on the sign of the normal gap.

2.3.2 Boundary element method for micro-scale interactions

The computation of p_{n} at each Gauss Point, left pending in the previous subsection, is here explained starting from the formulation of the contact problem at the micro-scale, which involves, in general, two deformable rough surfaces.

The equations governing the micro-scale contact problem of two deformable rough surfaces, whose heights field has been previously acquired through profilometric analysis or numerically generated, can be solved, for simplicity, using an equivalent system as demonstrated in [72]. The two deformable rough surfaces can be substituted with a rigid rough surface indenting an elastic half-plane with composite elastic parameters.

The heights field of the rigid rough surface is obtained considering a composition of the topography of the two original surfaces. Let $e_1(\boldsymbol{\xi})$ and $e_2(\boldsymbol{\xi})$ be the elevations of the rough surfaces measured from their macro-scale smooth representation,where $\boldsymbol{\xi} = (\xi_1, \xi_2)^T$ is a position vector referring to the surfaces local reference system, as in Figure 32(a). As already stated, the smooth reference surfaces (dashed lines) are sketched in Figure 32(a) where they are represented as flat profiles for the sake of simplicity, even though the formulation can be applied also to curved surfaces.

The elevation of the composite topography can be evaluated as:

$$e^*(\boldsymbol{\xi}) = e_1(\boldsymbol{\xi}) + e_2(\boldsymbol{\xi}) - \min[e_1(\boldsymbol{\xi}) + e_2(\boldsymbol{\xi})] \tag{2.14}$$

measured from a new datum set in correspondence of the lowest point, with distance $e^*_{\max}$ from the reference surfaceas shown in Figure 32(b).

As illustrated in [57, 73], the composite elastic parameters of the flat half-space can be computed as:

$$E = \left(\frac{1-\nu_1^2}{E_1} + \frac{1-\nu_2^2}{E_2} \right)^{-1}, \tag{2.15a}$$

$$G = \left(\frac{2-\nu_1}{4G_1} + \frac{2-\nu_2}{4G_2} \right)^{-1}, \tag{2.15b}$$

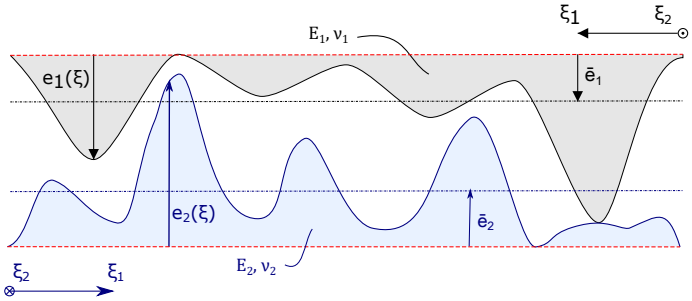

(a) Rough profiles identified by $e_1(\boldsymbol{\xi})$ and $e_2(\boldsymbol{\xi})$.

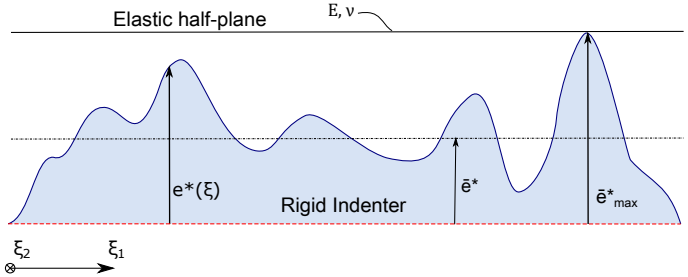

(b) Composite topography described by $e^*(\boldsymbol{\xi})$.

Figure 32: Transformation of two rough profiles (a) into a flat line, the elastic part, and a profile with composite topography (b), *i.e.* the rigid indenter.

where E_i, ν_i, and $G_i = E_i/[2(1+\nu_i)]$ denote, respectively, the Young's Modulus, the Poisson ratio and the shear modulus of the original bodies. In the same way, the composite Poisson ratio ν is related to G and E via $\nu = E/(2G) - 1$.

The micro-scale contact problem of the described equivalent system is solved under displacement control, for each Gauss point of the interface finite elements, considering a far-field displacement in the direction perpendicular to the undeformed half-space, equal to g_{n} computed at the macro-scale. At the initial condition, when $g_{\mathrm{n}} = 0$, the assumption that only the tallest height of the composite topography touches the half-plane, with a resulting zero normal traction, has been made. For each value of $g_{\mathrm{n}} > 0$, a non-zero contact area and a corresponding total normal force, P, can be computed. The total normal force, represented by the surface integral of the contact tractions over the interface, is evaluated using the BEM implementation proposed in [60]. The average nominal pressure p_{n}, needed at the macro-scale, can be herein computed as the ratio between the total normal force and the nominal contact area.

According to the boundary element method, the deformation of the half-space at any point can be described by the normal displacement $u(\boldsymbol{\xi})$, where $\boldsymbol{\xi}$ is the position vector related to the point, with respect to the underformed state. A 2D sketch of the micro-scale contact problem is shown in Figure 33. For a given far-displacement g_{n} imposed to the flat half-space, its rigid body motion is represented by the black dashed lines, whereas the deformed configuration is represented by the black solid line.

The displacement is related to the pressure $p(\boldsymbol{\eta})$ through the so-called Green's function, noted as $H(\boldsymbol{\xi}, \boldsymbol{\eta})$, that relates the displacement of a generic point of the half-space to the action of a concentrated force on the surface due to the contact interactions, according to the equation:

$$u(\boldsymbol{\xi}) = \int_S H(\boldsymbol{\xi}, \boldsymbol{\eta}) p(\boldsymbol{\eta}) \, \mathrm{d}\boldsymbol{\eta} \tag{2.16}$$

where S is the half-space.

For homogeneous, isotropic, linear elastic materials, the Green's func-

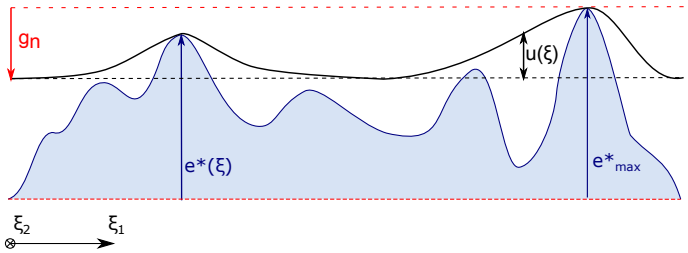

Figure 33: Illustration of the contact problem between a rigid rough surface, solid blue line, and an elastic half-plane, for a given far-field displacement g_{n}. The rigid body motion of the half-plane is indicated by the dashed black lines, while its deformed boundary by the solid black one.

tion has been chosen as ([52], [73]):

$$H(\boldsymbol{\xi}, \boldsymbol{\eta}) = \frac{1}{\pi E} \frac{1}{||\boldsymbol{\xi} - \boldsymbol{\eta}||} \tag{2.17}$$

where $||\cdot||$ represents the Euclidean norm. As already mentioned, the total contact force P can be evaluated by integrating the pressure field over the whole interface.

$$P = \int_S p(\boldsymbol{\xi}) \, \mathrm{d}\boldsymbol{\xi} \tag{2.18}$$

As shown in Figure 34, the deformed configuration of the half-space makes the points to be of three types:

- not in contact from the beginning (a), because the far-field displacement is not enough to fill the gap to the corresponding elevation of the rough surface;
- losing contact due to elastic interactions (b);
- in contact after taking into account elastic interactions (c).

At each point in contact, the indentation of the half-space is given by $\overline{u}(\boldsymbol{\xi}, g_{\mathrm{n}})$. Introducing the quantity $w(\boldsymbol{\xi}, g_{\mathrm{n}}) = u(\boldsymbol{\xi}) - \overline{u}(\boldsymbol{\xi}, g_{\mathrm{n}})$ (Figure 34b), the unilateral conditions that describes the contact interaction

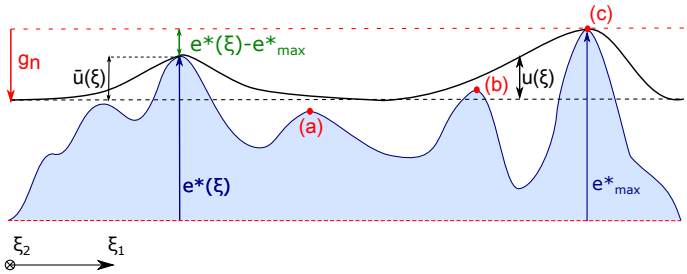

(a) Different types of points of the rigid rough surface according to the deformation of the half-space: (a) not in contact, (b) not in contact due to elastic interaction, (c) in contact.

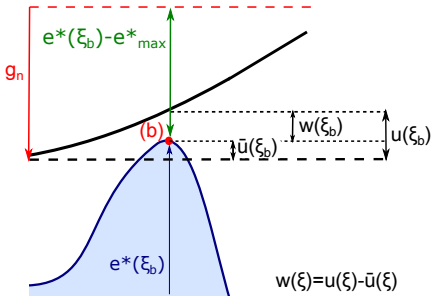

(b) Magnification of the point (b) and sketch of the quantities $u(\boldsymbol{\xi})$, $w(\boldsymbol{\xi})$ and $\bar{u}(\boldsymbol{\xi})$.

Figure 34: Deformed configuration of the half-space at a given far-field displacement g_n.

can be written as:

$$w(\boldsymbol{\xi}, g_\mathrm{n}) \geq 0, \tag{2.19a}$$

$$p(\boldsymbol{\xi}) \geq 0, \tag{2.19b}$$

$$w(\boldsymbol{\xi}, g_\mathrm{n}) p(\boldsymbol{\xi}) = 0, \tag{2.19c}$$

The solution of the normal contact problem for the micro-scale model

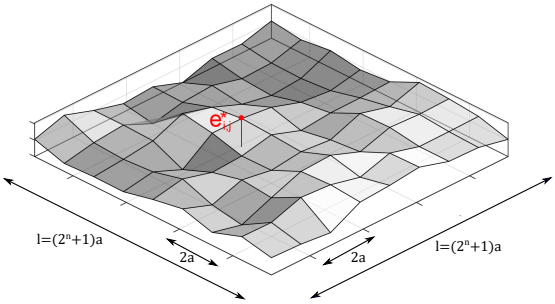

Figure 35: Example of the discretization of the rough surface in a square grid.

is then represented by the couple of the values $u(\boldsymbol{\xi})$ and $p(\boldsymbol{\xi})$ that satisfies Eq. (2.16) together with (2.19). This infinite dimensional problem can be solved numerically by discretizing the rough surface.

A square grid with lateral size l and resolution parameter n has been considered, such that the grid is composed of $N \times N$ cells with $N = 2^n + 1$ boundary elements per side. The lateral size of each boundary element is $a = l/(2^n + 1)$. In the examples proposed in the next section, a random midpoint displacement algorithm has been used to generate the height field $e^*_{i,j}$ (with $i = 1, ..., N$, $j = 1, ..., N$) of the rough surface, although any data field obtained from experiments can be used as input, without any restriction (see Figure 35). To compare the results of the method, different microscopically rough surfaces have been considered and, for each of them, a preliminary statistical characterization gives the mean elevation $\bar{e}^*$, the maximum elevation $e^*_{\max}$, and the root mean square roughness s.

A unit cell of the surface grid is denoted with $S_{i,j}$, while its central coordinate is defined as $\xi_{i,j} \triangleq \int_{\xi \in S_{i,j}} \xi d\xi$, the displacement and the re-

sultant of the contact pressures on the surface element are:

$$u_{i,j} \triangleq \int_{\xi \in S_{i,j}} u(\xi) d\xi \tag{2.20a}$$

$$p_{i,j} \triangleq \int_{\xi \in S_{i,j}} p(\xi) d\xi \tag{2.20b}$$

The discretised form of Eq. (2.16) reads:

$$u_{i,j} = \sum_{k=1}^{N} \sum_{l=1}^{N} H_{i-k,j-l} p_{k,l} \tag{2.21}$$

In the same way, the discretised form of $\overline{u}$ can be defined as:

$$\overline{u}_{i,j} \triangleq g_{\mathrm{n}} - e^*_{max} + e^*_{i,j} \tag{2.22}$$

Each term of the matrix $\mathbf{H}$ represents the Green's function in Eq. (2.17) averaged on an elementary cell of the surface grid and corresponds to the displacement induced by a uniformly loaded square. The matrix form is obtained using an approximation as in [22]:

$$H_{i-k,j-l} = \begin{cases} \frac{1}{\pi E} & \text{if } i = k \text{ and } j = l, \\ \frac{1}{\pi E} \arcsin \frac{1}{\|\boldsymbol{\xi}_{i,j} - \boldsymbol{\xi}_{k,l}\|} & \text{if } i \neq k,\, j \neq l, \end{cases} \tag{2.23}$$

The discretized matrix form of the problem thus reads:

$$\mathbf{w} = \mathbf{H} \cdot \mathbf{p} - \overline{\mathbf{u}}, \tag{2.24a}$$

$$\mathbf{w} \geq \mathbf{0}, \quad \mathbf{p} \geq \mathbf{0}, \quad \mathbf{w} \cdot \mathbf{p} = 0, \tag{2.24b}$$

where $w_{i,j} \triangleq u_{i,j} - \overline{u}_{i,j}$ is the vector of elastic corrections to the displacements.

The problem has a unique solution for any $g_{\mathrm{n}} \geq 0$ since $\mathbf{H}$ is symmetric and positive definite because of the property of linear elasticity. The problem can be also recast as a convex quadratic program:

$$\min_{p} \ \frac{1}{2} \mathbf{p}^T \mathbf{H} \mathbf{p} - \overline{\mathbf{u}}^T \mathbf{p}, \tag{2.25a}$$

$$\text{s.t. } \mathbf{p} \geq \mathbf{0}. \tag{2.25b}$$

for which the equations in (2.24) represent the Karash-Kuhn-Tucker optimality conditions.

Moreover, the problem can be written effectively as a non-negative least squares problem introducing a Cholesky factorization of the compliance coefficients matrix: $\mathbf{H} = \mathbf{C}'\mathbf{C}$. The Non-Negative Least Squares (NNLS) problem reads:

$$\min_{p} \ \frac{1}{2}\|\mathbf{C}\mathbf{p} - \mathbf{C}^{-T}\overline{\mathbf{u}}\|_2^2, \tag{2.26a}$$

$$\text{s.t. } \mathbf{p} \geq \mathbf{0}. \tag{2.26b}$$

An active-set method has been implemented in the interface finite element as proposed in [60], together with the proposed warm-start technique that takes advantage of the monotonic increasing (or decreasing) of pressure by increasing the far-field displacement. In a quasi-static simulation, the contact forces determined for a certain value of g_{n} can be saved in a history variable and used as an initial value for the optimization of the next step. The algorithm converges to the normal displacement vector $\mathbf{u}^*$ and the optimal contact force vector $\mathbf{p}^*$ from which we can derive the normal pressure p_{n} required at the macro-scale.

The evaluation of p_{n} from the computed contact pressure requires a further step since the boundary element method accounts for both the half-place deformation and the surface roughness effect. Since the elastic compliance of the bulk is already included at the macro-scale within the FEM framework, the contribution of the elastic compliance of the half-space has to be removed from the BEM result. It is necessary to evaluate the elastic deformation associated with the micro-scale problem and apply a correction to the obtained pressure field.

For this purpose, let us consider the problem of a flat rigid indenter, with dimension lxl over an elastic half-plane. An averaged nominal pressure equal to $\overline{p}$ will cause a uniform displacement w_0 equal to:

$$w_0(\overline{p}) = \frac{\alpha\, \overline{p}\, l}{E}, \tag{2.27}$$

where the coefficient α depends on the mesh size used for the surface grid. In our problem, starting from a given w_0, $\overline{p}$ is derived through the

above-explained BEM algorithm for the flat rigid indenter, to compute in advance the value of α for different surface resolution n. The values are given in Table 3, whereas different methods to obtain the limit value of α when the mesh size approaches the continuum description can be found in [57, 74, 75].

n	1	2	3	4	5	6	7	8
α	0.778	0.806	0.826	0.841	0.852	0.858	0.862	0.865

Table 3: Values of the coefficient α computed by solving the problem of a rigid flat indenter in contact with an elastic half-plane with the BEM algorithm, for different values of the surface resolution parameter n.

Known the value of α, for a set of far-field displacement δ and the corresponding nominal pressure p, the effect of roughness can be isolated applying the Eq. (2.27), so that the roughness related displacement is $\delta_r = \delta_t - w_0(p_t)$ and the corrected curve is obtained by subtracting the BEM curve to the linear elastic contribution. In Figure 36, the qualitative representation of the subtracting procedure is shown, and we can notice that the identified roughness contribution is stiffer than the one resulting from the overall system.

It must be underlined that this subtracting procedure is not directly applicable in the interface element routine, since the macro-model provides to the micro-model a single displacement g_n for each Newton-Raphson iteration at each Gauss point, instead of a series of displacement δ which are the necessary input for the above-mentioned procedure.

In other words, the subtracting procedure requires the knowledge of the entire total contribution curve, while the implemented formulation provides only a point of the curve, as depicted in Figure 37, where the result of the BEM algorithm for a given displacement g_n is noted as point (a). The desired value of pressure would be p_c (point (b)) cannot be evaluated directly through the subtracting procedure, since it corresponds to the point (c) on the total contribution curve that is also unknown. It corresponds to an augmented input displacement for the BEM algorithm $\delta_c = g_\mathrm{n} + w_0(p_c)$ where the elastic displacement w_0 would require the knowledge of p_c itself. To compute this augmented displacement, an it-

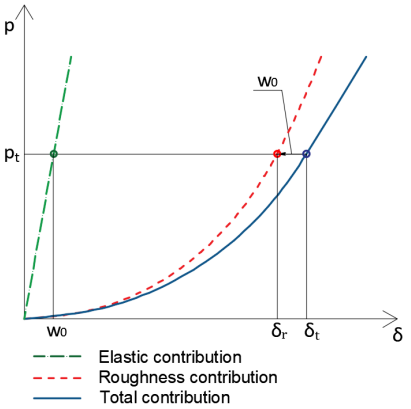

Figure 36: Qualitative representation of pressure vs. imposed displacement curve considering the elastic contribution (green dashed line), the roughness contribution (red dashed curve), and their combined effect (blue solid curve) as obtained by the BEM algorithm.

erative procedure has been established.

The iterative approach starts from the evaluation of the pressure $p^1(g_\mathrm{n})$, and the corresponding displacement correction $w_0^1(p^1)$. Using the augmented displacement $\delta_c^1 = g_\mathrm{n} + w_0^1$, a new value of nominal pressure $p^2(\delta^1)$ is found. At the i-th generic iteration, the corrected displacement reads:

$$\delta_\mathrm{c}^i = g_\mathrm{n} + w_0^i(p^i). \tag{2.28}$$

At this point, the relative error on the nominal pressure is evaluated, and eventually, the procedure is repeated. The relative error is defined as:

$$\mathrm{err} = \frac{p^i - p^{i-1}}{p^i} \tag{2.29}$$

and, the procedure stops when it is less than an imposed tolerance chosen according to previous convergence studies as shown in the numerical examples section. The resulting average pressure is herein ready to be read by the interface finite element at the macro-scale level.

The algorithm for the solution of the contact problem at the micro-scale is summarized in the box 1.

Algorithm 1: Micro-scale BEM subroutine

Input : Normal gap g_{n}, Number of grid points N, lateral size l, Young's Modulus E, Nominal surface area A, Surface data, Tolerance ϵ, Maximum number of iterations i_{max}, Surface flag $fl = 0$ at the first timestep.

Initialization: Iteration counter $i, w_0, \mathbf{u}^*, \mathbf{p}^*, \mathbf{p}_0, N_0, p, p^{i-1}, \boldsymbol{\xi}_1, \boldsymbol{\xi}_2, \mathbf{e}^*, \delta, \delta_c$, err, History variable $\mathcal{H}_{st}$

if $fl == 0$ **then**
- Read the surface data:
- $\boldsymbol{\xi}_1 \leftarrow$ grid points coordinates in direction 1
- $\boldsymbol{\xi}_2 \leftarrow$ grid points coordinates in direction 2
- $\mathbf{e}^* \leftarrow$ heights field
- $\mathcal{H}_{st} \leftarrow [\boldsymbol{\xi}_1, \boldsymbol{\xi}_2, \mathbf{e}^*]$
- $fl \leftarrow 1$

else
- $[\boldsymbol{\xi}_1, \boldsymbol{\xi}_2, \mathbf{e}^*] \leftarrow \mathcal{H}_{st}$

end

while $err \leq \epsilon$ ***and*** $i \leq i_{max}$ **do**
- $\delta_c \leftarrow g_{\mathrm{n}} + w_0$
- **if** $i > 1$ **then**
  - Call *Warm-Start* procedure:
  - **begin**
    - **Input :** $N, \boldsymbol{\xi}_1, \xi_2$, Coordinates of the points in contact from the previous iteration $\boldsymbol{\xi}_{c,1}, \boldsymbol{\xi}_{c,2}$, Contact pressure from the previous iteration $\mathbf{p}^*$
    - See Reference [60]-Algorithm 4 for the procedure details
    - **Output:** Initial guess for the contact pressure $\mathbf{p}_0$, Initial guess of points in contact N_0 having coordinates $\boldsymbol{\xi}_{0,1}, \boldsymbol{\xi}_{0,2}$
  - **end**
- **end**
- Call *Non-Negative Least Squares (NNLS)* procedure:
- **begin**
  - **Input :** $\delta_c, N, \boldsymbol{\xi}_1, \boldsymbol{\xi}_2, \mathbf{e}^*, \mathbf{p}_0, N_0, \boldsymbol{\xi}_{0,1}, \boldsymbol{\xi}_{0,2}$
  - See Reference [60]-Algorithm 3 for the procedure details
  - **Output:** $\mathbf{p}^*, \mathbf{u}^*, N_c, \boldsymbol{\xi}_{c,1}, \boldsymbol{\xi}_{c,2}$
- **end**
- $p \leftarrow \sum_j^{N_c} p_j^*/A$
- $err \leftarrow \frac{p^{i-1}-p}{p}$
- $p^{i-1} \leftarrow p$
- $w_0 \leftarrow \frac{\alpha\, p\, l}{E}$
- $i \leftarrow i + 1$

end

$p_{\mathrm{n}} \leftarrow p$

Output: Normal contact pressure p_{n}

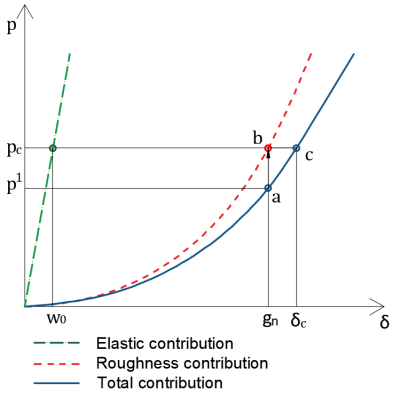

Figure 37: Since point (b) is not directly derivable in the element routine, starting from point (a) the iterative procedure evaluates the pressure in (c) which guarantees equilibrium between w_0, g_n and δ_c and gives the corrected pressure related to g_n.

2.3.3 Implementation details and different approaches for the multi-scale coupling

The interface finite element has been coded as a user element for FEAP, exploiting a Newton-Raphson solution scheme. At each time step and for each Gauss point, the contact pressure $p_\mathrm{n}(g_\mathrm{n})$ is computed by calling the subroutine which contains the explained algorithm for the solution of the BEM model and the pressure correction procedure (Algorithm 1). As seen in the section regarding the micro-scale model, the BEM subroutine is called to compute the nominal pressure p_n. However, the interface finite element requires also the computation of the Jacobian of the element, in particular, it needs the contact stiffness $\partial p_\mathrm{n}/\partial g_\mathrm{n}$. Three coupling approaches have been explored for its evaluation since the computational effort is heavily influenced by the Jacobian computation.

The first approach proposes a full integration of FEM and BEM using an approximation of the Jacobian for the iterative update scheme. For the current k-th Newton-Raphson iteration at the timestep t, the BEM subroutine is called once using $g^t_{\mathrm{n,k}}$ as the far-field displacement

to compute p_{n}^t and then a second time using a small perturbation of g_{n}: $g_{\mathrm{n,k+1}}^t = g_{\mathrm{n,k}}^t + \Delta g_{\mathrm{n,k}}^t$. This latter value corresponds to the pressure indicated with $p_{\mathrm{n,k+1}}^t$. The normal contact stiffness is then computed via a finite difference approximation:

$$\frac{\partial p_{\mathrm{n}}}{\partial g_{\mathrm{n}}} \simeq \frac{p_{\mathrm{n},k+1}^t - p_{\mathrm{n},k}^t}{g_{\mathrm{n},k+1}^t - g_{\mathrm{n},k}^t} \tag{2.30}$$

Since an approximation of the Jacobian is used for the iterative update scheme, this approach is called FEM-BEM Quasi-Newton (FBEM-QN). For this approach, in the following applications, a value of the perturbation $\Delta g_{\mathrm{n},i}^t = 0.01 g_{\mathrm{n},i}^t$ has been chosen.

Since this coupling procedure is computationally demanding, a second approach is also proposed for the numerical evaluation of the normal contact stiffness to save CPU time. In such approach, called FEM-BEM Cheap Quasi-Newton (FBEM-CQN), Eq. (2.30) is used only at the first time step and then for the following step, the finite difference formula uses, as reference values, the displacement and the pressure corresponding to the previous converged time step, stored in an appropriate history variable. The contact stiffness, at the current t step, is evaluated according to the formula:

$$\frac{\partial p_{\mathrm{n}}}{\partial g_{\mathrm{n}}} \simeq \frac{p_{\mathrm{n,k}}^t - p_{\mathrm{n}}^{t-1}}{g_{\mathrm{n,k}}^t - g_{\mathrm{n}}^{t-1}}, \tag{2.31}$$

where $t-1$ denotes the previous time steps variables.

The last approach, which is referred to as FEM-BEM semi-analytical (FBEM-SAN), directly avoids calling the BEM subroutine, using, instead, a closed-form expression for $p_{\mathrm{n}}(g_{\mathrm{n}})$. This expression has been obtained solving off-line the normal contact problem at the micro-scale, for a set of far-field displacements and for the given height field. A power-law continuous function of the type:

$$p_{\mathrm{n}}(g_{\mathrm{n}}) = a g_{\mathrm{n}}^b, \tag{2.32}$$

has been used to fit the solution of the problem in terms of predicted average contact pressure vs. the imposed far-field displacement. The lin-

earized interface stiffness matrix $\mathbb{C}$ in analytical form has been computed as the derivative of the obtained expression for $p_{\mathrm{n}}(g_{\mathrm{n}})$.

The power-law fitting function has been chosen considering the results in [30] where it is shown that the relation between the nominal pressure and the plane separation follows a power-law expression, at least in the range of intermediate situation between two limit regime, the high and the low separations. For very high separation, since only the tallest asperities are in contact, scatter in contact pressures is usually observed, because the contact response is affected by the statistics of the extremes of the lower tail of the asperity elevation distributions. On the opposite, low separations and the consequent high pressures bring the asperities to merge and form a large contact area. To avoid this latter scenario, in the fitting procedure used in the following numerical examples, the maximum allowed far-field displacement corresponds to $3s$, which approximately corresponds to a rigid body motion of the half-plane from the tallest height of the rough surface to the average plane. Apart from the disadvantages related to the extreme cases, the FBEM-SAN approach is the fastest method, as showed in the following paragraphs, especially when the same representative surface is used at all the integration points of the interface macro-scale model, or when the same surface is analyzed for different loading scenarios since it is necessary to compute the fitting-function parameters only once and reused them multiple times.

The three approaches for the multi-scale coupling are summarised in the Algorithm 2, 3, 4 which illustrate also the entire scheme of the FEAP user element.

2.3.4 Benchmark tests and discussion of the results

The capabilities of the numerical framework derived in the previous sections are herein explored considering a benchmark test to compare different solutions strategies and different input surfaces.

The benchmark test is composed by two square blocks of lateral size $L = 10\,\mathrm{mm}$ discretized by a single finite element each and connected by an interface finite element at the common boundary of the two bodies,

Algorithm 2: Interface finite element with FEM-BEM Quasi-Newton Approach

Input : Iteration number inside the Newton-Raphson scheme (k), Nodal coordinates $\mathbf{x}$, Nodal displacement $\mathbf{d}$, Gauss quadrature weights w_{igp}, History variables $\mathcal{H}_{st1}, \mathcal{H}_{st2}$.

Input for the Micro-scale BEM subroutine: Rough Surface data, Material properties, Tolerance ϵ, Maximum number of iterations for the micro-scale i_{max}.

Initialization: Gauss points index igp, $\mathbf{g}_{igp} = [g_{\mathrm{t}}, g_{\mathrm{n}}]^T$, $\mathbf{p}_{igp} = [p_{\mathrm{t}}, p_{\mathrm{n}}]^T$, $\mathbb{C}$

for $igp \leftarrow 1$ **to** 2 **do**

- Compute $detJ$, $\mathbf{N}$, $\mathbf{L}$, $\mathbf{R}$
- $\mathbf{g}_{igp} \leftarrow -\mathbf{RNLd}$
- **if** $g_{\mathrm{n}} < 0$ **then**
  - First call *Micro-scale BEM* Procedure:
  - **begin**
    - **Input :** Normal gap g_{n}, Rough Surface data, Material properties, Tolerance ϵ, Maximum number of iterations for the micro-scale i_{max}
    - See Algorithm 1
    - **Output:** Normal contact pressure p_{n}
  - **end**
  - $g_{\mathrm{n},k+1} \leftarrow g_{\mathrm{n}} + 0.01 g_{\mathrm{n}}$
  - Second call *Micro-scale* Procedure:
  - **begin**
    - **Input :** Normal gap $g_{\mathrm{n},k+1}$, Rough Surface data, Material properties, Tolerance ϵ, Maximum number of iterations for the micro-scale i_{max}
    - See Algorithm 1
    - **Output:** Normal contact pressure $p_{\mathrm{n},k+1}$
  - **end**
  - $\mathbf{p}_{igp} \leftarrow [0, p_{\mathrm{n}}]^T$
  - $\dfrac{\partial p_{\mathrm{n}}}{\partial g_{\mathrm{n}}} \leftarrow \dfrac{p_{\mathrm{n},k+1} - p_{\mathrm{n}}}{g_{\mathrm{n},k+1} - g_{\mathrm{n}}}$
  - $\mathbb{C}_{2,2} \leftarrow \dfrac{\partial p_{\mathrm{n}}}{\partial g_{\mathrm{n}}}$
- **end**
- $\mathbf{R}_e^{(k)} \leftarrow \mathbf{R}_e^{(k)} - \mathbf{L}^T\mathbf{N}^T\mathbf{R}^T\mathbf{p}_{igp} w_{igp} detJ$
- $\mathbf{K}_e^{(k)} \leftarrow \mathbf{K}_e^{(k)} + \mathbf{L}^T\mathbf{N}^T\mathbf{R}^T\mathbb{C}\mathbf{RNL} w_{igp} detJ$

end

Output: Residual vector $\mathbf{R}_e^{(k)}$, Stiffness Matrix $\mathbf{K}_e^{(k)}$

Algorithm 3: Interface finite element with FEM-BEM Cheap Quasi-Newton Approach

Input : Iteration number inside the Newton-Raphson scheme (k), Nodal coordinates $\mathbf{x}$, Nodal displacement $\mathbf{d}$, Gauss quadrature weights w_{igp}, History variables $\mathcal{H}_{st1}, \mathcal{H}_{st2}$.

Input for the micro-scale subroutine: Rough Surface data, Material properties, Tolerance ϵ, Maximum number of iterations for the micro-scale i_{max}.

Initialization: Gauss points index igp, $\mathbf{g}_{igp} = [g_{\mathrm{t}}, g_{\mathrm{n}}]^T$, $\mathbf{p}_{igp} = [p_{\mathrm{t}}, p_{\mathrm{n}}]^T$, $\mathbb{C}$

for $igp \leftarrow 1$ **to** 2 **do**

  Compute $detJ$, $\mathbf{N}$, $\mathbf{L}$, $\mathbf{R}$

  $\mathbf{g}_{igp} \leftarrow -\mathbf{RNLd}$

  if $g_{\mathrm{n}} < 0$ **then**

    Call *Micro-scale* Procedure:

    begin

      Input : Normal gap g_{n}, Rough Surface data, Material properties, Tolerance ϵ, Maximum number of iterations for the micro-scale i_{max}

      See Algorithm 1

      Output: Normal contact pressure p_{n}

    end

    $\mathbf{p}_{igp} \leftarrow [0, p_{\mathrm{n}}]^T$

    $\dfrac{\partial p_{\mathrm{n}}}{\partial g_{\mathrm{n}}} \leftarrow \dfrac{\mathcal{H}_{st1,igp} - p_{\mathrm{n}}}{\mathcal{H}_{st2,igp} - g_{\mathrm{n}}}$

    $\mathbb{C}_{2,2} \leftarrow \dfrac{\partial p_{\mathrm{n}}}{\partial g_{\mathrm{n}}}$

    $\mathcal{H}_{st1,igp} \leftarrow p_{\mathrm{n}}$ (at convergence)

    $\mathcal{H}_{st2,igp} \leftarrow g_{\mathrm{n}}$ (at convergence)

  end

  $\mathbf{R}_e^{(k)} \leftarrow \mathbf{R}_e^{(k)} - \mathbf{L}^T\mathbf{N}^T\mathbf{R}^T\mathbf{p}_{igp}w_{igp}detJ$

  $\mathbf{K}_e^{(k)} \leftarrow \mathbf{K}_e^{(k)} + \mathbf{L}^T\mathbf{N}^T\mathbf{R}^T\mathbb{C}\mathbf{RNL}w_{igp}detJ$

end

Output: Residual vector $\mathbf{R}_e^{(k)}$, Stiffness Matrix $\mathbf{K}_e^{(k)}$

Algorithm 4: Interface finite element with FEM-BEM Semi-Analytical Approach

Input : Iteration number inside the Newton-Raphson scheme (k), Nodal coordinates $\mathbf{x}$, Nodal displacement $\mathbf{d}$, Gauss quadrature weights w_{igp}, Parameters of the power law function a, b.

Initialization: Gauss points index igp, $\mathbf{g}_{igp} = [g_{\mathrm{t}}, g_{\mathrm{n}}]^T$, $\mathbf{p}_{igp} = [p_{\mathrm{t}}, p_{\mathrm{n}}]^T$, $\mathbb{C}$

for $igp \leftarrow 1$ **to** 2 **do**

  Compute $detJ$, $\mathbf{N}$, $\mathbf{L}$, $\mathbf{R}$

  $\mathbf{g}_{igp} \leftarrow -\mathbf{RNLd}$

  if $g_{\mathrm{n}} < 0$ **then**

    $p_{\mathrm{n}} \leftarrow a g_{\mathrm{n}}^b$

    $\mathbf{p}_{igp} \leftarrow [0, p_{\mathrm{n}}]^T$

    $\dfrac{\partial p_{\mathrm{n}}}{\partial g_{\mathrm{n}}} \leftarrow ab g_{\mathrm{n}}^{b-1}$

    $\mathbb{C}_{2,2} \leftarrow \dfrac{\partial p_{\mathrm{n}}}{\partial g_{\mathrm{n}}}$

  end

  $\mathbf{R}_e^{(k)} \leftarrow \mathbf{R}_e^{(k)} - \mathbf{L}^T\mathbf{N}^T\mathbf{R}^T\mathbf{p}_{igp} w_{igp} detJ$

  $\mathbf{K}_e^{(k)} \leftarrow \mathbf{K}_e^{(k)} + \mathbf{L}^T\mathbf{N}^T\mathbf{R}^T\mathbb{C}\mathbf{RNL} w_{igp} detJ$

end

Output: Residual vector $\mathbf{R}_e^{(k)}$, Stiffness Matrix $\mathbf{K}_e^{(k)}$

see Figure 38. The nominal contact area at the interface is $A = 10mm^2$. The two solids are chosen with equal material parameters for simplicity: Young's moduli $E_1 = E_2 = 1\,\mathrm{N}/\mu\mathrm{m}^2$ and Poisson ratios $\nu_1 = \nu_2 = 0.3$, where the subscripts 1 and 2 identify the lower and upper bodies, respectively. Choosing the same elastic properties for the two blocks avoids the coupling between the normal and the tangential contact problems, since a frictional constitutive response for the interface is not specified in this test. Eq.s (2.15a) and (2.15b) allow to compute the composite parameters: composite Young's modulus $E = 0.5495\,\mathrm{N}/\mu\mathrm{m}^2$ and a composite Poisson ratio $\nu = -0.3929$ to be used at the interface.

The imposed Dirichlet boundary conditions consist of vertical constraints onto the lower side of Ω_2 and a single horizontal constraint applied at the top-left nodes of both bodies, to avoid rigid body motion. An imposed downward vertical displacement Δ acts on the upper side of Ω_1, monotonically increasing with a pseudo-time variable to simulate the quasi-static normal contact problem, starting from 0 up to a maxi-

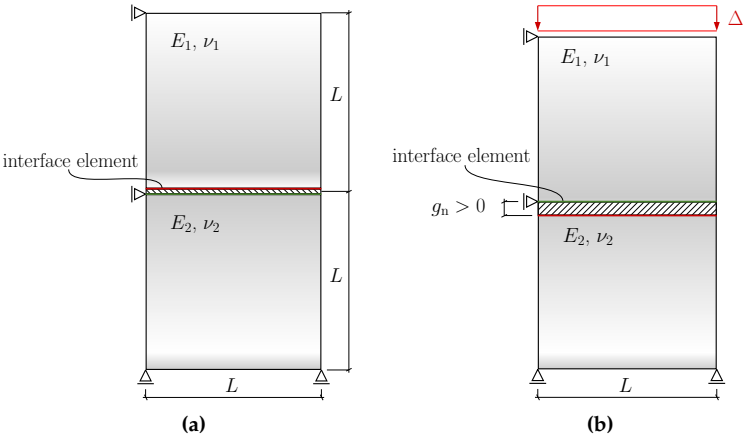

Figure 38: Geometry and boundary conditions of the benchmark test in uniaxial compression.

mum value of $3s$, denoting s the root mean square of the surface roughness used to represent the composite topography.

The assumption of scale-separation between the micro- and the macroscales is essential to the method. Thence, the composite topography chosen as input for the BEM algorithm has a lateral size l much smaller than the macroscopic lateral size L. In the present benchmark, $l = 1$ mm, which leads to a ratio $l/L = 0.1$, and the maximum height of the rough surface is $50\,\mu$m. Moreover, it is assumed that the heights fields used as input, are statistically representative of the surface topography and can be used at both the integration points.

The rough surfaces used in the numerical simulations are generated using the *Random Midpoint Displacement* (RMD) algorithm described in the Introduction in Section 1.1.3. The Hurst exponent has been set equal to $H = 0.7$, while three resolutions corresponding to $n = 6$, 7 and 8 have been considered, which implies having 65, 129, and 257 heights per side, respectively. By increasing the surface resolution, the dimension of the contact problem solved by BEM at each Gauss point increases consequently, and this allows us to explore the capabilities of the FEM-

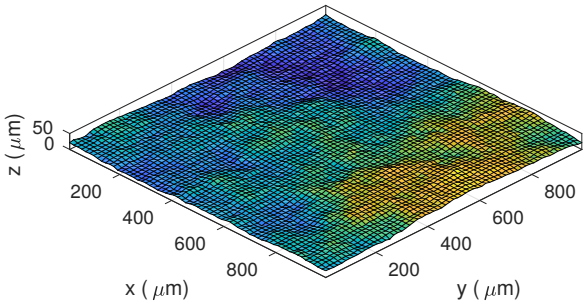

Figure 39: Example of a RMD rough surface ($n = 6$).

BEM approach at different levels of complexity. The goal is to compare the accuracy of the results and the computational effort of the proposed coupling strategies. An example of the generated surface is shown in Figure 39.

In order to apply the correcting procedure on the contact pressure explained in Section 2.3.2, a preliminary convergence study has been carried on to establish the tolerance value used to control the error in Eq. (2.29). A tolerance of 1×10^{-2} results in good accordance with the gap-pressure curves and it has been used in our numerical simulations. An example is given in Figure 40 for the surface with $n = 6$ and for the given dimensionless displacements Δ/s.

In the preliminary analysis for the FBEM-SAN scheme, the fitting procedure as been performed employing MATLAB's built-in `fitnlm` function[1] for performing non-linear regressions. The resulting curve coefficients for the power-law function in Eq. (2.32) are collected in Table 4 and distinguished by the three different value of surface resolution n.

The goodness of the fitting function has been evaluated considering the sum of squares due to error (SSE), the sum of squares of the regression (SSR), the total sum of squares (SST), and finally the R-square (R^2) coefficients. Improvements in all the estimators can be observed as the resolution gets higher. It is important to consider also the CPU re-

[1]See `https://uk.mathworks.com/help/stats/fitnlm.html` for documentation.

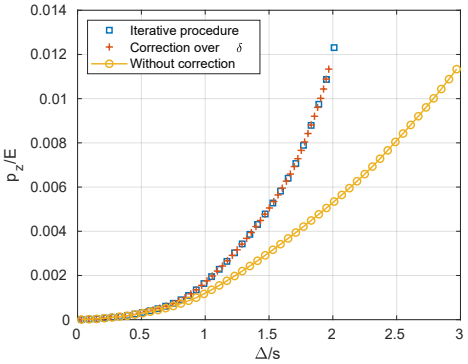

Figure 40: Comparison of the gap-pressure curves evaluated using two different procedures with tolerance sets as 1×10^{-2}.

quired by this off-line stage, which is highly affected by the number of discretization steps in which the imposed displacement Δ is divided for this analysis. Figure 41a and Figure 41b show, respectively, the variation of R^2 and the CPU time required by the off-line stage, with respect to the number of discretization steps. The value of 10^2 steps, used in the present benchmark example, represents a good trade-off between fitting accuracy and computational time spent during the operation.

Table 4: Coefficients of the power-law function $p(g_{\mathrm{n}}) = a g_{\mathrm{n}}^{b}$, together with goodness of fit parameter.

n	**6**	**7**	**8**
a [N/μm^2]	1.416×10^{-06}	1.240×10^{-06}	1.064×10^{-06}
b	2.831	2.862	2.905
SSE	5.677×10^{-07}	4.073×10^{-07}	3.407×10^{-07}
SSR	3.773×10^{-04}	3.576×10^{-04}	3.461×10^{-04}
SST	3.722×10^{-04}	3.537×10^{-04}	3.437×10^{-04}
R^2	0.9985	0.9988	0.9990

In the following analyses, the dimensionless total normal load $P/(EA)$, computed as the sum of the vertical reactions forces at the constrained nodes of the macro-scale model, is plotted to vary dimensionless normal

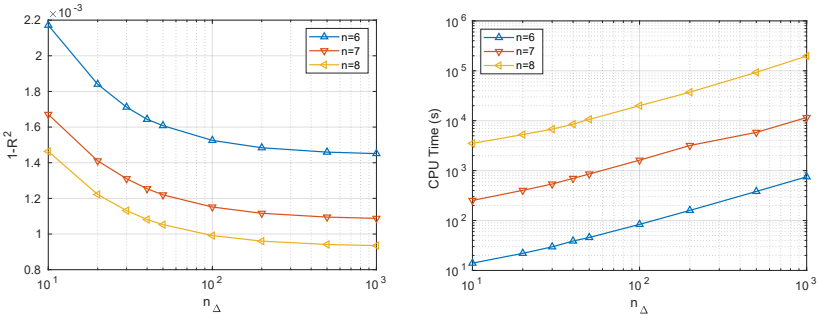

(a) R-square coefficient. **(b)** Computational time.

Figure 41: Parametric study over the number of time steps used in the fitting, for the same imposed far field displacement Δ.

gap h^*/s, where $h^*(g_{\mathrm{n}}) = e^*_{max} - \bar{e}^* - g_{\mathrm{n}}$ is the actual distance between the flat plane and mean plane of the rough surface.

Figure 42 shows the $P/(EA)$ vs. h^*/s contact predictions for different coupling strategies, FBEM-QN, FBEM-CQN and FBEM-SAN, and for increasing resolution parameter $n = 6$, 7 and 8. Overall, it is possible to notice that the three approaches provide almost coincident results for the highest surface resolution (see Figure 42f), while the semi-analytical scheme leads to slightly different predictions for lower resolutions (surfaces with $n = 6$ in Figure 42b and $n = 7$ in Figure 42d). The power-law function used to approximate the contact response in the FBEM-SAN scheme does not exactly reproduce the actual BEM contact response for coarse meshes or large separations, being affected by a scatter induced by statistics of extremes of the asperity height distribution. Moreover, as shown in Figures 42a, 42c and 42e, varying the surface resolution, the curves have the same trend, regardless of the coupling strategy.

The differences between the three approaches are more visible by examining the dimensionless normal contact stiffness $C_{\mathrm{mat}}s/E$ vs. the dimensionless normal gap h^*/s in Figure 43. As expected, the FBEM-SAN predicts a smooth response for all the surface resolutions and all the normal gap values, see Figure 43e, due to the power-law best-fitting equa-

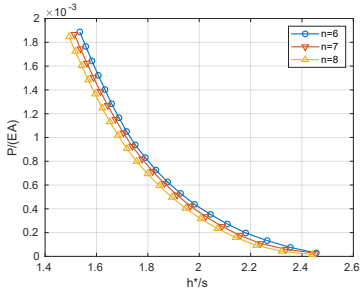

(a) FBEM-QN

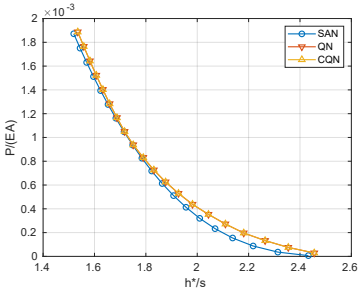

(b) $n = 6$

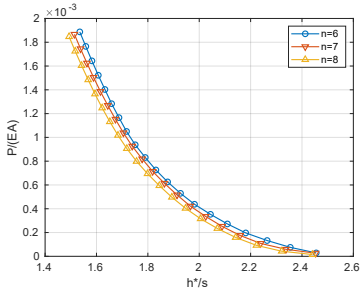

(c) FBEM-CQN

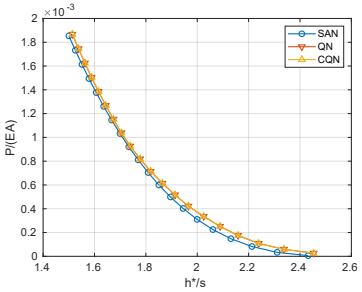

(d) $n = 7$

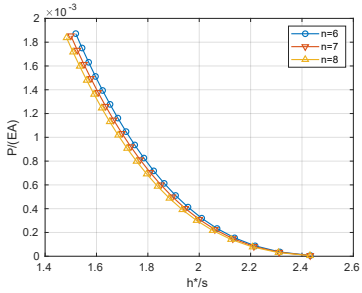

(e) FBEM-SAN

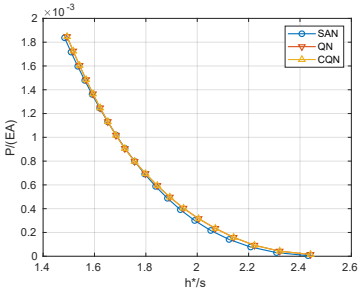

(f) $n = 8$

Figure 42: Dimensionless contact pressure vs. dimensionless normal gap predictions depending on the solution scheme and the surface resolution.

tion, which derivative is used to compute the normal contact stiffness. The other two coupling strategies present a less smooth behavior, especially for the high separation regime, corresponding approximately to $2.2 \leq h^*/s \leq 2.5$. In this regime, the actual contact behavior is governed by few asperities in contact and therefore the contact response should present oscillations and a non-smooth behavior. By reducing the separation between the bodies, the number of contact spots increases, and, consequentially the collective response tends to be much more stable and smoother. It can be noticed that the same happens also at the increase of surface resolutions, as it can be seen in Figures 43b, 43d, and 43f. The power-law best-fit approximation becomes much more reliable and the results are almost coincident for the highest resolution.

The computational effort required for solving the problem using the proposed multi-scale approach is a fundamental aspect since, as explained in Section 2.1, in the literature, the application of the BEM method over the FEM technique has been preferred mainly because computationally less expensive. The following paragraphs examine the convergence rate and the computational time for the presented benchmark test, to show the capabilities of the FEM-BEM approach.

The contact problem has been solved using a convergence tolerance of 1×10^{-9} and the convergence rate of the last time-step ($\Delta = 3s$) is presented in 44, where the evolution of the residual norm is plotted against the number of iterations of the numerical scheme used to solve the set of nonlinear algebraic equations. The Figures 44a, 44c and 44e compare the convergence rate of the three numerical strategies for the same surface resolution. As expected, the FBEM-SAN displays a quadratic convergence, regardless of the resolution, since the tangent stiffness is computed exactly from the derivative of the pressure-separation relation, which is given in the analytic form. The FBEM-QN and FBEM-CQN display a slower convergence rate than FBEM-SAN, requiring at least one iteration more than the semi-analytic approach, due to the numerical approximation of the tangent stiffness matrix. From Figure 44a, 44c and 44e, the influence of the surface resolution can be analyzed: the integrated approaches (FBEM-QN and FBEM-CQN) show an increasing

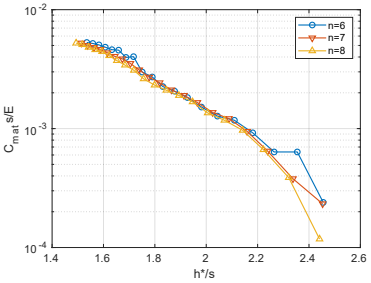

(a) FBEM-QN

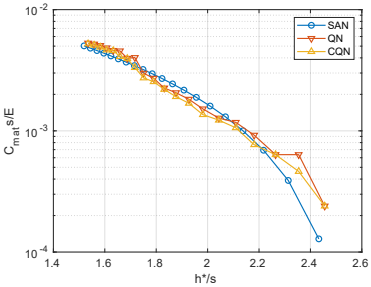

(b) $n = 6$

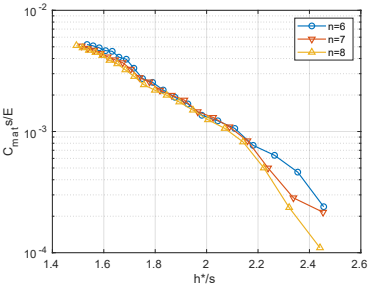

(c) FBEM-CQN

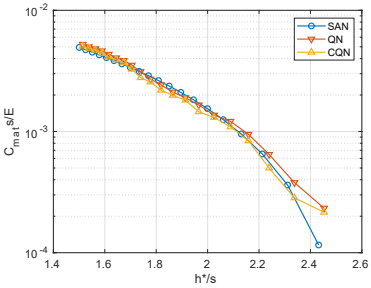

(d) $n = 7$

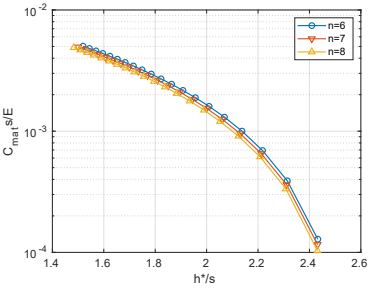

(e) FBEM-SAN

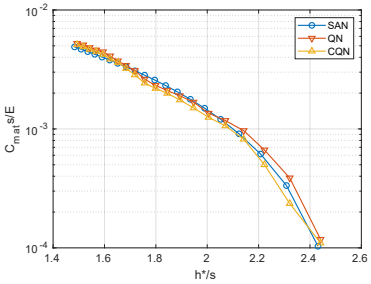

(f) $n = 8$

Figure 43: Dimensionless contact stiffness vs. dimensionless normal gap predictions depending on the solution scheme and the surface resolution.

number of iterations with the increasing n, as expected.

Regarding the CPU time required to solve the benchmark problem, the comparison between the different strategies is reported in Figure 45a, 45c and 45e for the FBEM-QN, FBEM-CQN and FBEM-SAN solution strategies and in Figures 45b, 45d and 45f for the three different resolution parameters. It is visible that the FBEM-SAN is much faster than the other two strategies especially for intermediate and low separations when the time required for the micro-scale BEM computations spent to predict the contact pressure and the contact stiffness in the FBEM-QN and the FBEM-CQN schemes is significant. Moreover, this result is also due to the fact that the CPU time for the FBEM-SAN strategy includes only the time required for FEM to solve the macro-scale contact problem without the time for the off-line execution of BEM since this preparatory step is very case-specific and depends not only on the maximum value of pressure required but also on the accuracy requested to the fitting operation, as already shown in Figure 41b.

Both the integrated strategies show almost the same CPU time, with slight differences: the FBEM-QN is faster at the beginning, for high separation, whereas the FBEM-CQN allows saving time in the low separation range. Both the integrated approaches become more expensive for the low-separation regime when the number of contact points increases. For the same reason, these strategies are also more time consuming for the higher resolutions.

Another advantage of the proposed multi-scale method is the possibility to extract local information about the micro-scale contact problem when the integrated strategies are used. An exemplary use is reported in Figure 46 where the actual contact area has been extracted at different time steps, without additional effort. The same could be done for the pressure field and other variables that may be useful for simulations including wear and friction or for multi-field problems involving heat transfer or reaction-diffusion phenomena where the actual contact variables can be reused in the model. For the FBEM-SAN strategy, the information about the percentage of the actual area or other local variables can be extracted as well but required an additional interpolating function

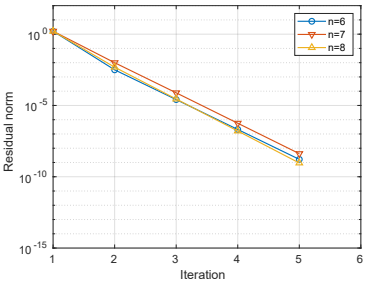

(a) FBEM-QN

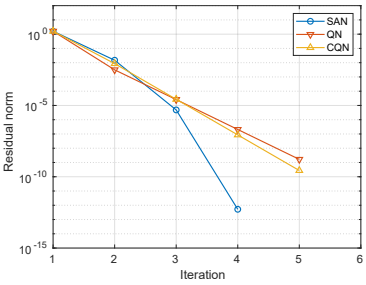

(b) $n = 6$

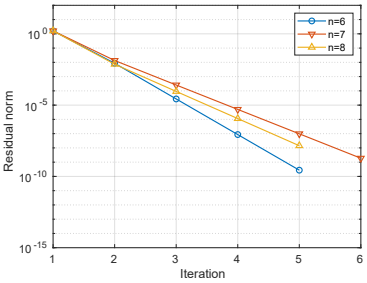

(c) FBEM-CQN

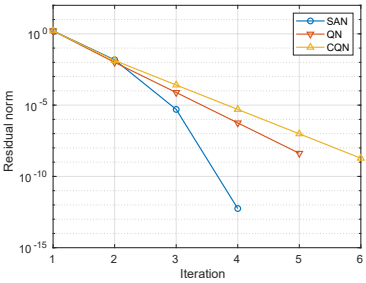

(d) $n = 7$

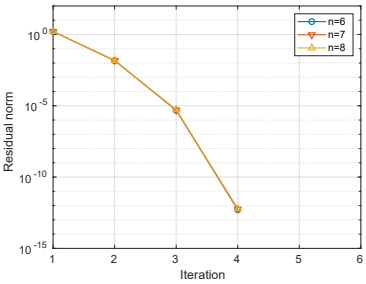

(e) FBEM-SAN

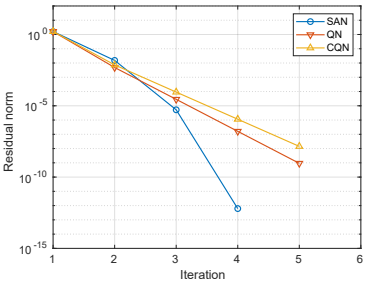

(f) $n = 8$

Figure 44: Residual norm vs. iteration step depending on the solution scheme and the surface resolution.

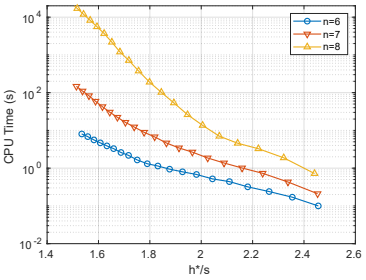

(a) FBEM-QN

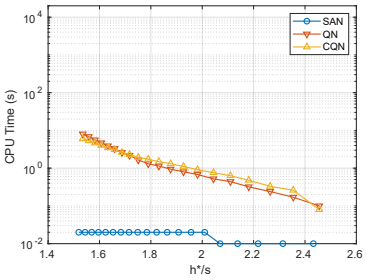

(b) $n = 6$

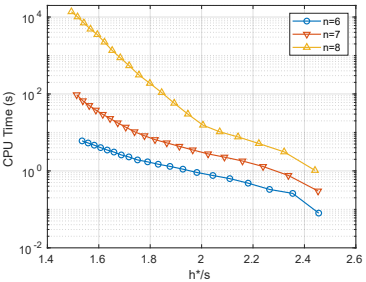

(c) FBEM-CQN

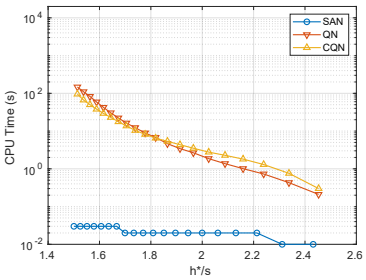

(d) $n = 7$

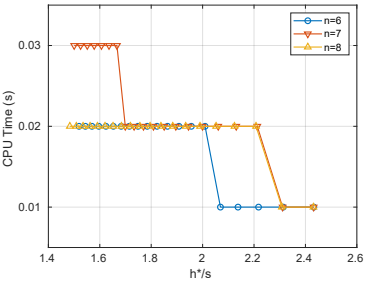

(e) FBEM-SAN

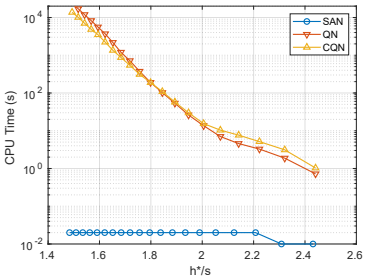

(f) $n = 8$

Figure 45: CPU time (s) vs. dimensionless normal gap predictions depending on the solution scheme and the surface resolution.

during the off-line stage.

Despite the additional computational cost associated with concurrent FEM-BEM coupling compared to a micro-mechanical model, this approach presents the highest versatility since the BEM algorithm is applied at each integration point of the interface finite element using any height field as input data, without introducing any simplifying assumption on the topology. Compared to a microscopical model, in fact, it does not rely on a closed-form solution at the micro-scale associated with a specific microscopical contact model, which implies assumptions on roughness statistics. It can be easily used to solve macroscopic contact problems accounting also for the effect of the rough interface.

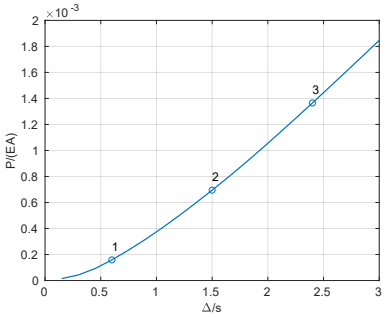

(a) Dimensionless overall reaction force against the imposed displacement.

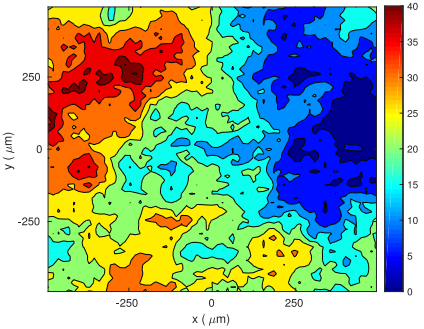

(b) Point 1, $A/A_{\mathrm{n}} = 0.38\%$.

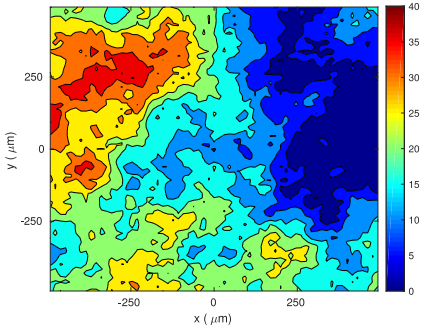

(c) Point 2, $A/A_{\mathrm{n}} = 1.66\%$.

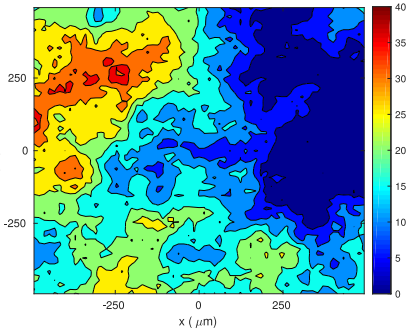

(d) Point 3, $A/A_{\mathrm{n}} = 3.12\%$.

Figure 46: Evolution of the free volume of the real geometry at the micro-scale for three different levels of imposed displacement, for the $n = 7$, FBEM-QN case. For every one of the three contour plots the ratio between the actual contact area A and the nominal one A_{n} is provided, while the dark blue islands show the contact area, the deepest valleys are marked in red.

Chapter 3

Mechanical characterization of silicone-based adhesive joint: roughness influence and failure modes assessment

The previous Chapter considered the influence of the surface roughness at the interface of two bodies directly in contact. This Chapter explores the surface topology influence in adhesive bonded joints, where the components are assembled through an adhesive layer. The roughness of the surface affects locally the adhesion at the interface and the overall joint response.

In the introduction (Chapter 1), the general properties and applications of structural adhesives, defined as load-bearing adhesives, have been already described. Among them, silicone adhesives are used in a wide range of industrial applications also because of the favorable cost-efficiency ratio. In this Chapter, the analysis focuses on the mechanical behavior of silicone adhesives in presence of rough interfaces. The investigation considers the experimental tests of a silicone adhesive applied on

polymeric substrates with different roughness, and the numerical simulation of the bonded joint.

The Chapter introduces the state of the art for roughness dependence in adhesive joints in Section 3.1, describes materials, tools and methods of the experimental campaign in Section 3.2, and finally shows the results in Section 3.3. Moreover, the phenomenon is investigated using a numerical model of the joint which is explored in Section 3.4.

Nomenclature

R_z	Average of peak-to-valley distance values over evaluation length
σ	Root mean square of the surface height field
E_a	Adhesive Young's modulus
t_a	Adhesive thickness
t_b	Peeling strip thickness
t_p	Substrate thickness
d	Peeling extension
F	Peeling force
G_{C}	Adhesive fracture energy
θ	Peeling angle
w	Peeling strip width
G_{IC}	Adhesive fracture energy in Mode I
α	Dimensionless parameter for the roughness influence
Ω_i	i-th body domain
$\mathbf{u}_i$	Displacement field of the i-th body
$\delta\Omega_i$	Boundary of the i-th body
$\delta\Omega_i^{\mathrm{D}}$	Dirichlet boundary of the i-th body
$\delta\Omega_i^{\mathrm{N}}$	Neumann boundary of the i-th body
Γ	Interface between the two bodies
$\mathbf{n}$	Normal unit vector of the interface
$\mathbf{t}$	Tangential unit vector of the interface
$\mathbf{T}$	Interface cohesive traction
$\mathbf{g}_{\mathrm{loc}}$	Gap field across the interface in the local reference system
g_n	Normal component of the gap
g_t	Tangential component of the gap
$\hat{\mathbf{x}}$	Position vector on the middle line of the interface finite element
$\mathbf{M}$	Averaging operator
$\mathbf{N}$	Shape function matrix
$\bar{\mathbf{x}}$	Coordinates vector of the interface finite element nodes
$\mathbf{d}$	displacement vector of the interface finite element nodes
$\mathbf{L}$	Matrix operator for computing the relative displacements
$\mathbf{R}$	Rotation matrix
$\mathbb{C}$	Tangent interface constitutive matrix
k_{p}	Standard penalty parameter
$\sigma(g_n)$	Normal component of the interface traction
σ_c	Critical traction (normal direction)
g_{nc}	Critical crack opening (normal direction)

Nomenclature

g_{nu}	Critical crack opening at the complete decohesion
k_n	Initial Stiffness parameter of the interface law
h	Effective thickness of the adhesive
$\bar{z}$	Average height of the surface
z_{min}	Minimum height of the surface
$\sigma_{\text{c,smooth}}$	Critical traction for the smooth part
$\sigma_{\text{c,rough}}$	Critical traction for the rough part
$G_{\text{IC,smooth}}$	Adhesive fracture energy for the smooth part
$G_{\text{IC,rough}}$	Adhesive fracture energy for the rough part

3.1 Adhesive bonding strength evaluation and surface roughness influence

Increasing the load capacity of a structural joint by optimizing the components' surface properties is of great importance for industrial applications and mechanical joints design. The mechanical response of adhesive joints can be influenced by a wide number of parameters that can be classified into three main groups: (i) intrinsic properties of the adhesive, e.g. chemical structure, visco-elasticity, strength, etc.; (ii) the substrate interaction with the adhesive, including the adhesive application methods and the surface morphology; (iii) environmental factors as temperature, moisture, fatigue, etc [76, 77]. The main topic of this Chapter is establishing the influence of the surface topology of the component on the strength of adhesive joints. Regarding this issue, different contributions can be listed in the specif literature, including experimental results and theoretical predict

The surface roughness effect on adhesive strength has been studied in [78] through the shear tests on single lap joint samples realized using the heat-resistant, silicone-rubber RTV88 adhesive (see Figure 47). Their investigation shows that the surface roughness increases the effective area while decreasing the shear strength due to the decreasing of the cohesive failure area.

The work of Azari et al. [79] focuses on the fatigue and fracture behavior of epoxy adhesive investigated through Double Cantilever Beam (DCB), and Asymmetric Double Cantilever Beam (ADCB) specimens, re-

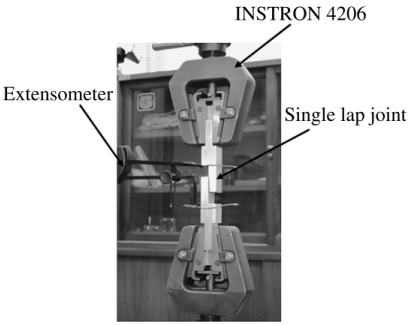

Figure 47: Single lap joint subject to shear test. Source [78].

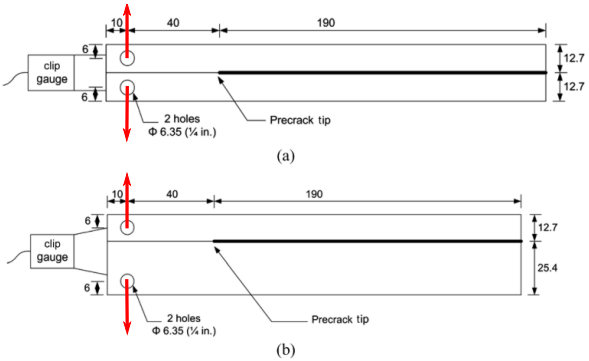

Figure 48: Geometry of DCB (a) and ADCB (b) joints. Adapted from [79].

spectively, as shown in Figure 48. Their results show that for mode I (DBC tests), the roughness increase causes the increase of the fatigue threshold to a certain value, after which further increase of roughness causes a decrease of the fatigue critical value. While for mixed-mode (ADBC) loading, no roughness effects have been observed.

Surface roughness dependence is a matter of research also in the field of Fiber Reinforced Polymer (FRP) used in the reinforcement of concrete structures. Before applying the reinforcement, the concrete surface is commonly prepared by different methods, resulting in different roughness profiles. In [80], profilometric data have been collected on the

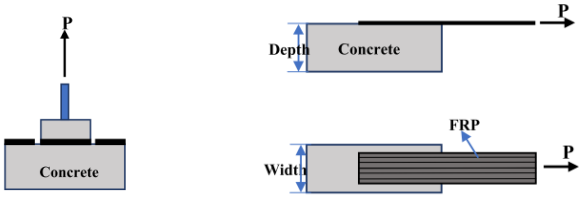

(a) Direct tension pull-off test **(b)** Single shear pull-out test

Figure 49: FRP bonded on concrete specimens experimental tests. Adapted from [81].

concrete roughness resulting from brushing, grinding, bush-hammering, and sandblasting. Empirical correlations have been found between the measured roughness parameters and the bond strength measured through pull-off and single shear pull-out tests (measuring mode I and mode II adhesion strength). A sketch of the two types of experimental tests is shown in Figure 49.

Among the different experimental procedures developed to measure the adhesive bond, the most used is the peel test which involves peeling a thin strip (a film, called peel arm) away from a substrate, previously bonded to each other through an adhesive layer. The peeling extension, corresponding to the length of the detached strip, and the applied peel force are measured during the test.

The possible configurations for this experimental test are depicted in Figure 50, different in the way the load is applied on the peeling strip. Peeling is usually performed in a standard testing machine, at a constant rate of peeling extension and measuring the peel force with a load cell. All the procedures describe the use of rectangular specimens with constant adherend thickness and large ratios of width to thickness.

The focus of this Chapter is the fixed arm peel test, executed with the substrate fixed and the peeling strip detached at different angles, usually in the range 45°–180° [82].

A prediction of the mechanical behavior of a peel test can be achieved using fracture mechanics. Initial analytical models for the peel geome-

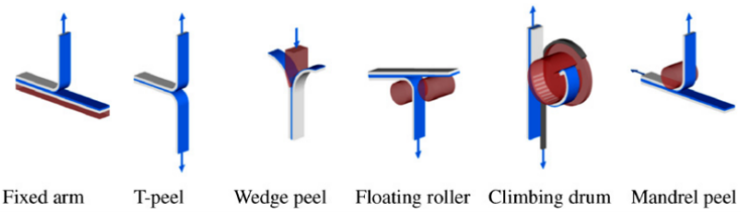

Figure 50: Configurations of different types of peel tests. Source [82].

try treated the film as an elastic beam attached to an elastic foundation, representing the adhesive layer through their interactions. The interface crack is assumed to advance when the maximum stress reaches the value identified with the strength of the adhesive. With the hypothesis of negligible shear stresses in the adhesive, Bikerman [83] computed the peel force at the start of the adhesive rupture, for a 90° peeling test, considering the influence of the adhesive and film thickness.

The condition for fracture of an adhesive joint subject to peeling test had been derived in [84], using an energy-balance approach analogous to the one suggested by Griffith [85] for fracture of brittle solids. Assuming a linear elastic behavior for the elastic film and neglecting the influence of the adhesive layer, the total energy of the joint is computed as the sum of three terms: the interface surface energy, the potential energy term due to the applied force at a given angle of peeling and the elastic energy required to bend and stretch the film. According to Kendall's analysis, the interface surface energy is defined as the work required to separate two surfaces and corresponds to the adhesive fracture energy. The peel force required for the crack propagation is hence computed as a function of the adhesive fracture energy.

Subsequently, [86, 87] model the adhesive joint using Timoshenko's theory for beams on elastic foundation with extensional and rotational stiffness computed considering half of the peel arm thickness and its material properties. With respect to the previous theories, Timoshenko's model includes the shear effect but neglects the effect of the adhesive thickness. Further investigations extended the approach to elastoplastic

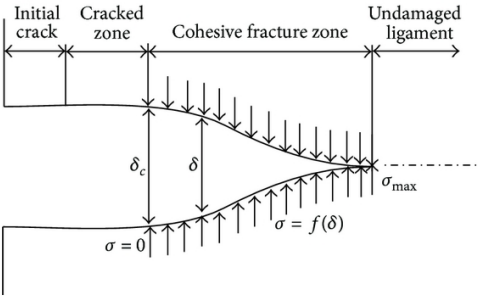

Figure 51: Cohesive zone model process zone. Source [92].

or viscoelastic materials and large deformations [88, 89].

The fixed arm peel test has been modeled also using the Linear Elastic Fracture Mechanics (LEFM) approach in [90], analyzing the crack-tip stress field using the stress intensity factor computed in [91] for interface fracture.

A somewhat different approach towards the same objective is the cohesive zone model (CZM), which adds a zone of vanishing thickness ahead of the crack tip aiming at describing more realistically the fracture process without the use of stress singularity. According to this model, the failure process involves a process zone after the crack tip where the material is damaged but is still able to transfer stress so that the stress decreases slowly as a function of the crack opening (see Figure 51).

Hence, the cohesive zone is idealized as two cohesive surfaces held together by cohesive traction, and the separation process is described by a cohesive interface law that relates the cohesive traction and the relative displacement of the surfaces, till the complete separation when a critical value is reached [93]. The traction-separation is described by three parameters: critical energy release rate (G_C), critical limiting maximum stress (or equivalently the critical separation), and the shape of the traction-separation law.

In the CZM framework, the interface law reproduces the adhesive layer and, in general, the resulting finite element model is composed of

the standard FEM adherends discretization and a single layer of cohesive zone elements at the interface. A comparison of the CZM results with benchmark tests developed with analytical models can be found in [94].

In [95], various cohesive zone traction laws had been incorporated into the beam on elastic foundation model, obtaining an analytical solution for the peeling analysis. In this work, the cohesive zone relationship is not a material property but depends on the thickness of the peel arm, since the initial stiffness of the stress-displacement relationship is proportional to the ratio of the Young's modulus over the thickness [96, 97]. Dynamical and geometrical nonlinearities have been included in finite thickness interface elements in [98] to address layer debonding in 90° peeling tests involving thick adhesive layers.

Finite-thickness contact elements have been recently used to study decohesion problems in layered materials in [99] where the stiffness of the initial linear branch of the interface law is considered to be dependent on the finite thickness of the adhesive. The bond of linearly elastic adherends to quasi-brittle substrates has been modeled using the cohesive zone model also in [100]. In [101], the interface law is coupled with a damage variable that accounts for the degradation of the interface during the test.

3.2 Experimental campaign

In our investigation, the 90° and 180° fixed arm peeling tests have been considered. According to the standard ASTM D1876 for the 90° peeling test, the substrate is kept horizontal, while the strip is bonded to the substrate for only a part of its length, while the free part is gripped and pull vertically with the standard machine, creating an "L" shape. During the test, the 90° angle between the substrate and the free part of the strip remains constant. The 180° configuration is similar but the strip bends to form a tight "U" with the substrate (see Figure 52).

The 90° peeling test measures the adhesive joint strength under pure opening displacements, or mode I, while for a different angle the adhesive undergoes mixed-mode fracture, involving also tangential sliding.

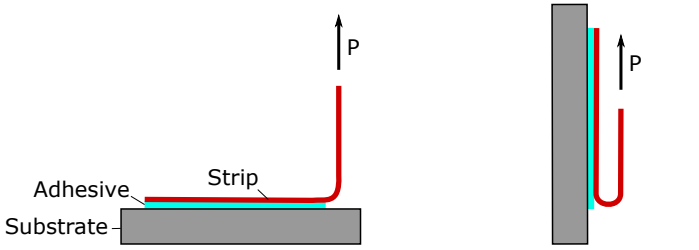

Figure 52: 90° and 180° peeling test geometries.

A detailed description of the sample preparation and the test results are given in the following paragraphs.

3.2.1 Substrates and their roughness characterization

Thermoplastic substrates of dimension $120 \times 25 \times 2\text{mm}^3$ have been fabricated through injection molding as shown in Figure 53, using steel inserts with prescribed roughness to generate a specific rough surface also on the substrate. In particular, the inserts surface has been characterised by R_z (see definition in Table 1) producing five different types of polymeric substrates ($R_z = 0.6, 0.7, 1.8, 3.0, 7.5\mu\text{m}$), to which can be add another class of smooth samples.

The substrate surface appears divided into two areas: a smooth part where the peeling will start, and a rough part that will be used to compare the peeling response to the smooth part (Figure 54). The different rough surfaces obtained on the substrates are shown in Figure 55.

The surface features of the substrates might differ from the used insert and a proper characterization is then necessary. A non-contact confocal profilometer LEICA DCM3D available in the MUSAM-Lab at the IMT School for Advanced Studies Lucca has been used to acquire surface data to define a statistically representative surface of each type of substrate. The statistically representative surface can be defined as the surface size that includes enough valleys and peaks such that the overall

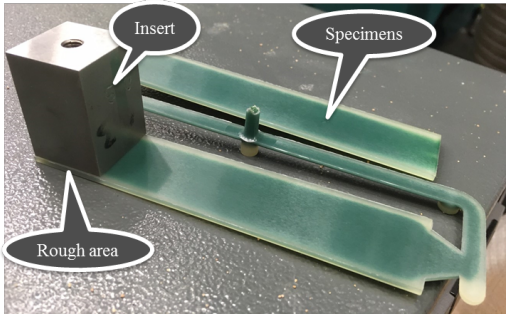

Figure 53: Realization of the substrate using steel inserts of specific roughness.

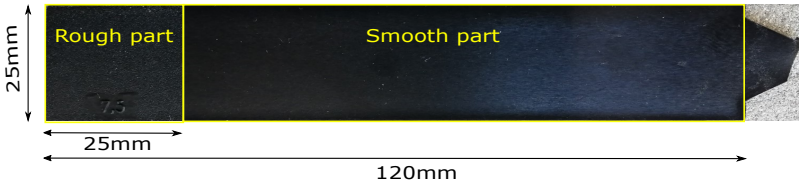

Figure 54: Plastic substrate with rough and smooth part.

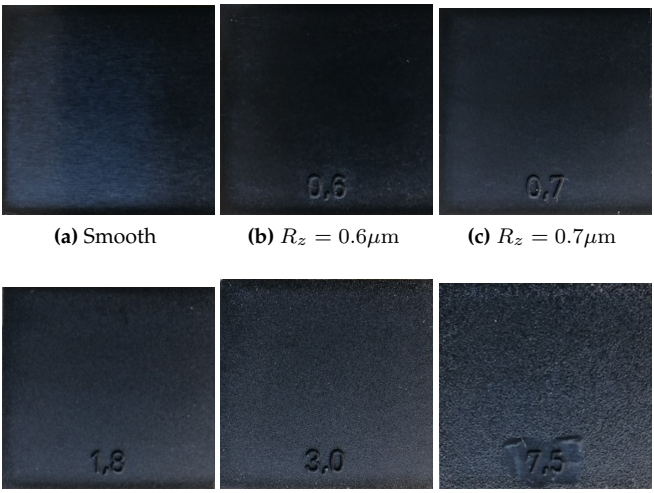

(a) Smooth **(b)** $R_z = 0.6\mu\text{m}$ **(c)** $R_z = 0.7\mu\text{m}$

(d) $R_z = 1.8\mu\text{m}$ **(e)** $R_z = 3.0\mu\text{m}$ **(f)** $R_z = 7.5\mu\text{m}$

Figure 55: Details of the substrates with different R_z values.

ensemble is able to fully characterize the statistical features of the overall surface. For this purpose, the "stitching tool" of the profilometer has been used, increasing the scanned area as needed through the stitching of smaller areas. For the finest rough surface ($R_z = 0.6\mu\text{m}$), the results of the stitching procedure with the 100x magnification is shown in Figure 56 starting from the smallest area to the biggest one obtained by considering a grid of 9×9 individual scans. The dimensions of the acquired topography can be found in Table 6.

Grid Size	**1×1**	**2×2**	**3×3**	**4×4**
Area (μm^2)	127×95	229×172	332×249	434×325
Number of heights	768×576	1382×1036	1996×1496	2610×1956
Grid Size	**5×5**	**6×6**	**7×7**	**8×8**
Area (μm^2)	536×402	638×478	740×555	843×632
Number of heights	3224×2416	3838×2876	4452×3336	2533×1898

Table 6: Grid size of the scanned surface using the profilometer stitching tool.

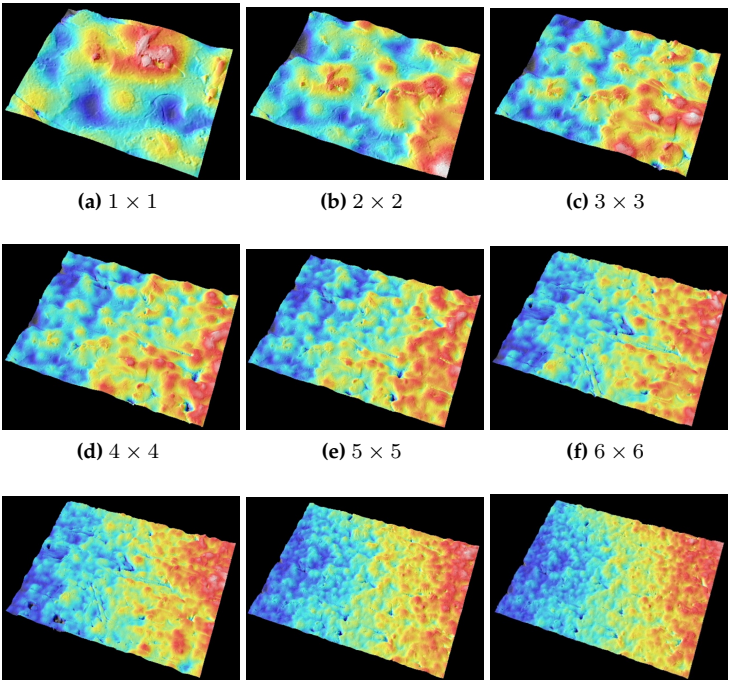

(a) 1×1 **(b)** 2×2 **(c)** 3×3

(d) 4×4 **(e)** 5×5 **(f)** 6×6

(g) 7×7 **(h)** 8×8 **(i)** 9×9

Figure 56: Scanned extended topography of substrate with $R_z = 0.6\mu\text{m}$ obtained by increasing number of individual scans. The elevation range is $\pm 8.0\mu\text{m}$

.

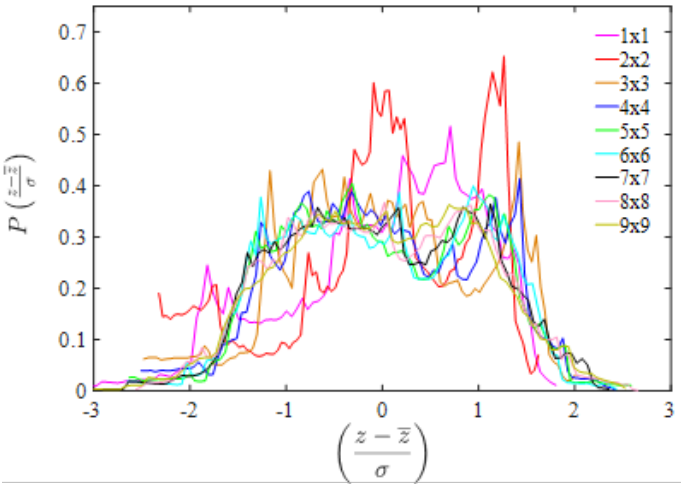

Figure 57: Normalized distributions of the height field for different stitching number for the sample with $R_z = 7.5\mu\text{m}$.

The size of the representative surface has been chosen by analyzing the statistical features of the extended areas. By increasing the scanned area size, the probability distributions of the acquired height fields tend to converge suggesting that the statistical representative surface size has been reached. This effect can be qualitatively spotted in Figure 57, observing the probability density functions obtained for the sample with $R_z = 7.5\mu\text{m}$.

The objective measure of the similarity between two curves has been obtained through Dynamic Space Warping (DSW) algorithm. This algorithm, applied on the normalized probability density function of the surfaces height fields, generates a quantitative indicator of the mismatch between two probability distribution curves, as in Figure 58 which shows that after the size the 8×8 the distance does not vary: this surface portion is hence large enough to be statistically representative of the sample. The test has been repeated for all the roughness types involved in the experimental campaign and the resulting representative surface sizes are reported in Table 7.

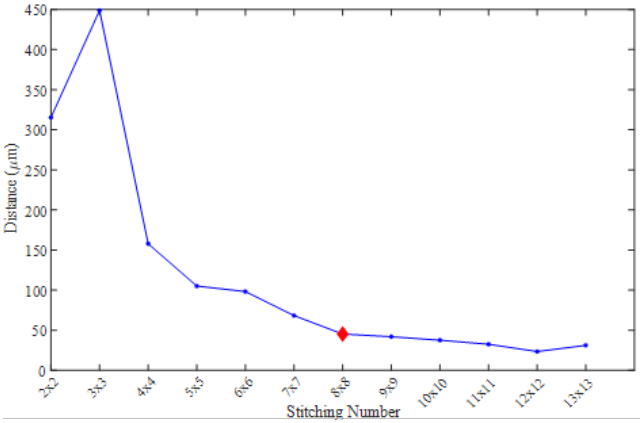

Figure 58: DWS algorithm results showing the similarity value obtained for $R_z = 7.5\mu$m.

$R_z[\mu\text{m}]$	7.5	3.0	1.8	0.7	0.6
Grid size	8×8	7×7	6×6	6×6	5×5
$\sigma[\mu\text{m}]$	11.36	4.03	3.25	2.20	1.14

Table 7: Grid sizes and root mean square values (σ) of the statistically representative surfaces for the different R_z.

As already stated, the substrate roughness may differ from the roughness of the steel insert used for the molding process. However in the following parameters, for the sake of brevity, we will speak about "substrate with R_z equal to a certain value □", meaning that the specific sample has been prepared with the insert having $R_z = \square$.

3.2.2 Sample preparation and peeling tests

The samples have been prepared using:

- the black polymeric substrate (glass fiber reinforced Polybutylene Terephthalate, PBT-GF30) presented above;
- a thin strip of HELIOX PV FERON NEOX CPC 300, flexible and inextensible, having dimensions 5mm wide $\times 0.3\text{mm}$ thick;

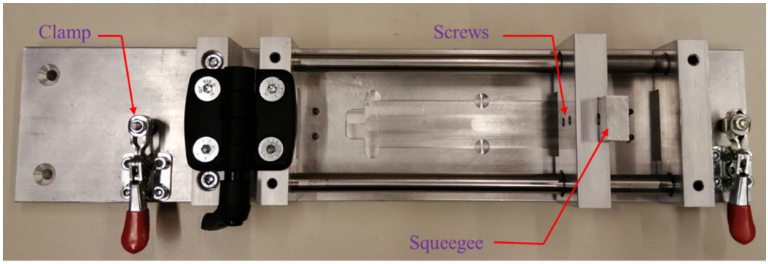

Figure 59: Fixture used to realize the samples with a controlled adhesive thickness.

- a black two-component silicone sealant cured at room temperature.

Both the adherends and dog-bone silicone samples have been previously characterized through tensile tests to obtain mechanical properties. The Young's modulus of the HELIOX strip is equal to 4.9GPa and the tensile strength is 180MPa, the silicone samples have Young's modulus $E_a = 3.30\text{MPa}$, the polymeric substrate has Young's modulus equal to 3.65GPa. The different order of magnitude of the elasticity modulus values allows to consider the strip inextensible compare to the adhesive and the substrate can be considered rigid.

To control the thickness of the adhesive layer bonding the substrate and the peel strip, the samples have been prepared using a specific fixture designed for this experimental campaign (see Figure 59).

The sample preparation requires the following steps: firstly, the substrate is placed in the mold of the fixture and the strip is secured through a clamp at one extremity; then the adhesive is dispensed in a line on the substrate. The last step requires deploying the strip on the adhesive and clamping it at the other extremity. At this point, the squeegee can be manually swiped on the sample to bond together the components. The adhesive thickness can be controlled by adjusting the vertical position of the squeegee, assuring the reproducibility of the final sample, shown in Figure 60.

Peeling tests have been conducted employing the Zwick/Roell universal testing machine on the six different R_z types of substrates and

Figure 60: Sample at the end of the preparation, before the peeling test which will be conducted starting from the smooth part of the sample.

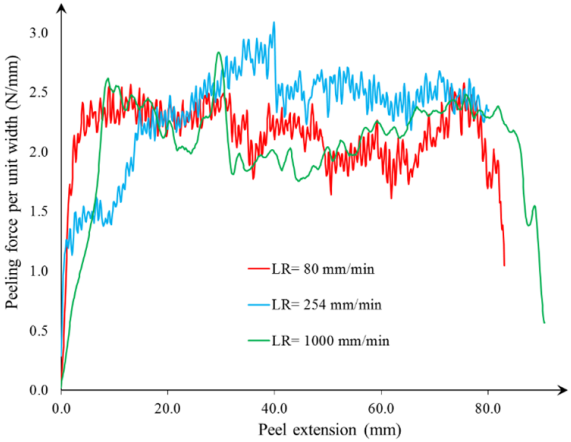

Figure 61: Loading rate effect on the peeling response.

for five different adhesive thicknesses: $t_a = 0.5, 0.8, 1.2, 1.9, 3.0\text{mm}$. For each test, at least three samples have been tested for a total of 150 peeling acquisitions. The flexible strip is removed at a constant rate and the force necessary for the surfaces debonding is measured by the tension in the tape. The tests have been executed with three different loading rate values: $80, 254$ and 1000mm/min to investigate possible effects on the peeling response.

The results for a sample are shown Figure 61 and it can be observed that higher loading rates smooth out the oscillations in the measured peeling force but without effect on the average peeling force values in the steady-state range.

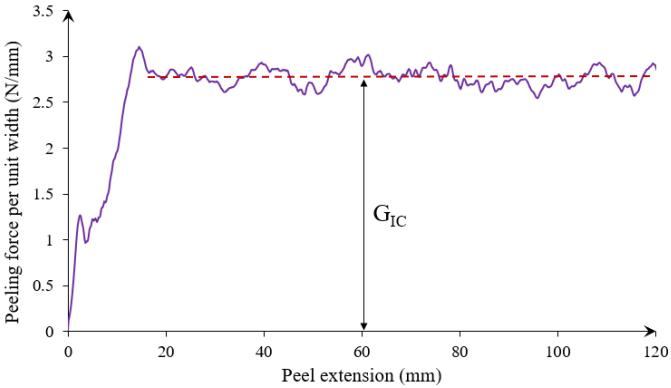

Figure 62: For the 90° peeling test, the plateau of the peeling force corresponds to the adhesive fracture energy for Mode I.

3.3 Experimental results and discussion

The experimental responses have been evaluated in terms of peeling extension, d, and peeling force, F, to assess the effect of roughness and adhesive thickness. Moreover, the failure modes have been analyzed to evaluate the consequences on the peeling force.

When the peeling force reaches the steady-state, its value can be related to the adhesive fracture energy G_C and to the peeling angle θ according to Rivlin equation [102] with the assumption of an inextensible peeling strip:

$$\frac{F}{w} = \frac{G_C}{1 - \cos(\theta)} \tag{3.1}$$

where $\frac{F}{w}$ is the peeling force (F) per unit width (w).

Hence, for the 90° peeling tests the value of the plateau of the peeling force for unit width corresponds directly to the adhesive fracture energy in Mode I, G_{IC}, as in Figure 62. Since the sample surface is divided into the smooth and rough sections, the adhesive fracture energy can be referred to the smooth part or to the rough part as well considering the peeling extension: the last 25mm of peeling extension refers to the adhesive fracture energy for the rough part.

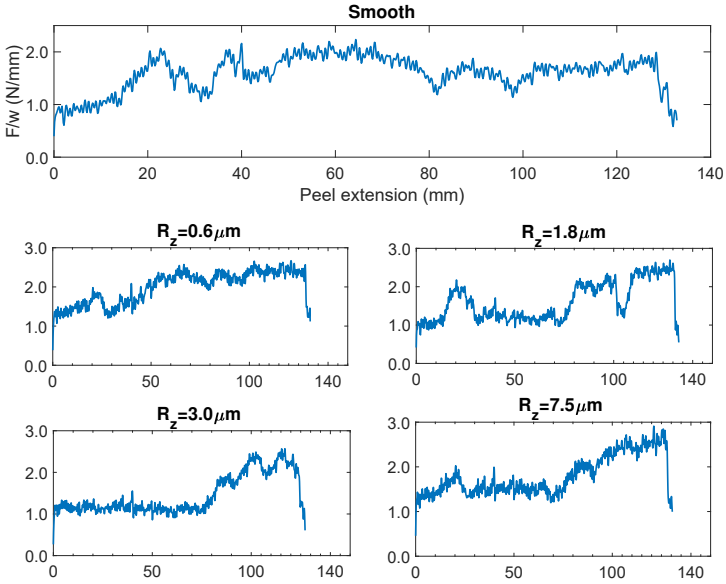

Figure 63: 90° peeling test results for samples having adhesive layer thickness $t_a = 0.5\text{mm}$.

3.3.1 Adhesive thickness and roughness influence

The experimental curves obtained from the 90° peeling test are presented in Figures 63 - 66 limited to a small number of plots, since plotting all the obtained curves would excessively lengthen this Chapter.

The adhesive thickness plays a significant role in the adhesive fracture energy of the joints, immediately visible in Figure 67 which shows the peeling response for samples with smooth substrates and different t_a. The adhesive thickness increase corresponds to the increase of the adhesive fracture energy except for the cases $t_a = 1.2, 1.9\text{mm}$ that have similar plateau values.

It has been noticed that in some cases there is a jump in the peeling force of the rough part compared to the corresponding value of the smooth part. This jump is particularly visible for the thinnest adhesive layers and for the rougher samples, as in Figure 63 for $R_z = 0.7, 1.8\mu\text{m}$,

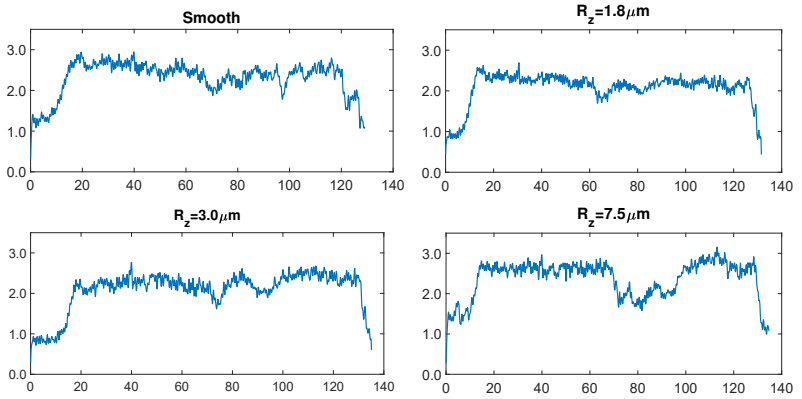

Figure 64: 90° peeling test results for samples having adhesive layer thickness $t_a = 0.8\text{mm}$.

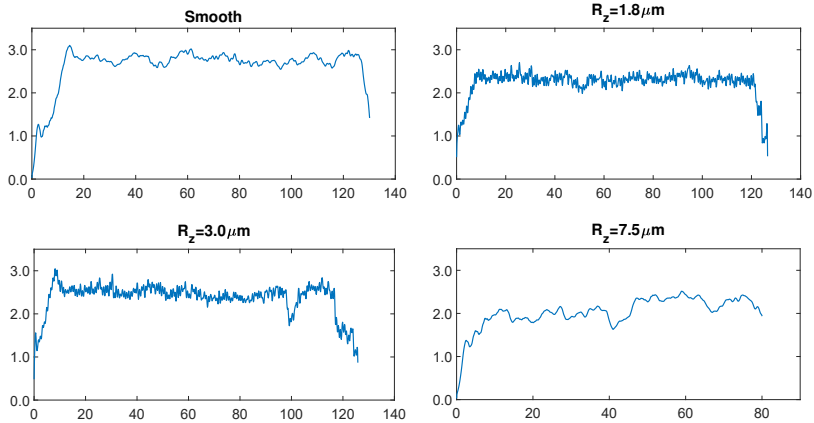

Figure 65: 90° peeling test results for samples having adhesive layer thickness $t_a = 1.2\text{mm}$.

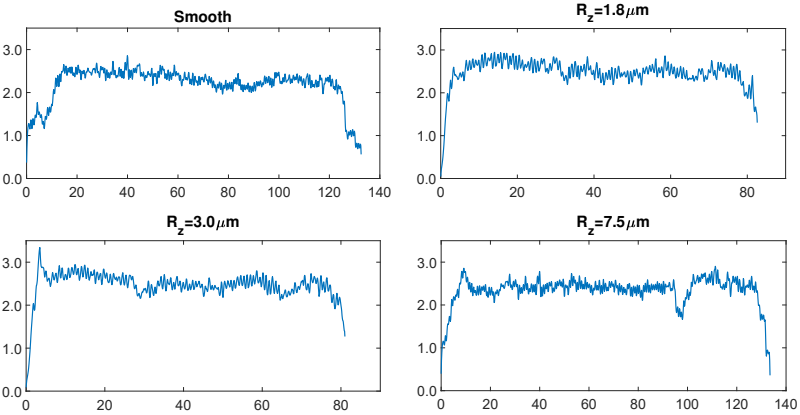

Figure 66: 90° peeling test results for samples having adhesive layer thickness $t_a = 1.9\text{mm}$.

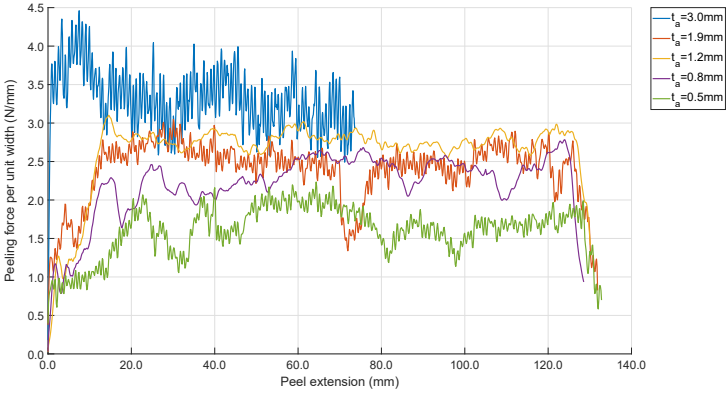

Figure 67: Adhesive thickness influence on the peeling response for the samples with smooth substrates.

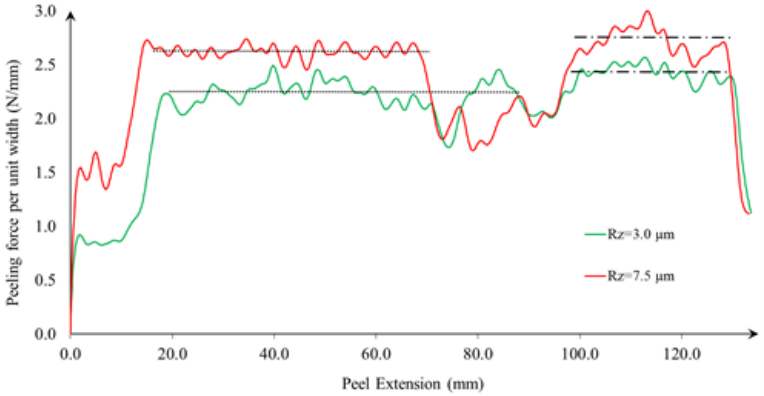

Figure 68: Plateau values of the peeling force referred to the smooth section (dotted line) and the rough section (dash-dotted line) for two samples having $t_a = 0.8\text{mm}$.

and $R_z = 3.0, 7.5\mu\text{m}$, Figure 64 for $R_z = 3.0, 7.5\mu\text{m}$, Figure 65 for $R_z = 7.5\mu\text{m}$, and Figure 66 for $R_z = 7.5\mu\text{m}$. While in other cases, these two peeling force values (for both smooth and rough parts) are almost equal as in Figure 64 for $R_z = 1.8\mu\text{m}$, Figure 65 for $R_z = 0.7, 1.8\mu\text{m}$, and Figure 66 for $R_z = 1.8, 3.0\mu\text{m}$.

These values have been quantitatively compared by considering the average peeling force over the peeling extension for the smooth and the rough sections after removing the drops caused by a change of the failure modes (major details about the failure mechanisms will be explained in the next section). An example of the result of this analysis is shown in Figure 68 regarding the response of two samples with adhesive thickness $t_a = 0.8\text{mm}$ and roughness $R_z = \{3.0, 7.5\mu\text{m}\}$.

The average peeling force, which corresponds to the adhesive fracture energy, has been compared with the properties of the sample: adhesive thickness and root mean square (σ) of the elevations of the statistically representative surface.

It has been observed that the presence of the jump in the peeling force can be related to the adhesive thickness and the r.m.s. roughness elevation. Hence, a dimensionless parameter, α, defined as the ratio between

		Adhesive thickness t_a[mm]				
$R_z[\mu m]$	$\sigma[\mu m]$	0.5	0.8	1.2	1.9	3.0
0.6	1.14	439	702	1053	1667	2632
0.7	2.20	227	363	545	864	1364
1.8	3.25	154	246	369	585	923
3.0	4.03	124	199	298	471	744
7.5	11.36	44	70	106	167	264

Table 8: Values of the dimensionless parameter $\alpha = \frac{t_a}{\sigma}$ for the different scenarios.

the adhesive thicknesses and the root mean square roughness, has been proposed as an indicator for estimating the importance of roughness on the peeling response:

$$\alpha = \frac{t_a}{\sigma} \tag{3.2}$$

The ratio values can be found in Table 8 and the highlighted cells report the cases where the experimental jump of the peeling force has been found. A "critical" value of α equal to 246 can be considered as the threshold above which the roughness effect cannot be appreciated.

The second set of experimental tests have been conducted with a peeling angle equal to 180° and for adhesive layer thickness $t_a = 0.8, 1.2, 1.9\text{mm}$. The experimental curves are presented in Figure 69 as exemplary cases.

For this experimental set-up, the surface roughness does not play a significant role in the adhesion strength. Based on the experimental results, the presence of roughness at the interface does not affect the peeling force, due to the mixed-mode fracture with dominant shear failure mode, characteristic of the 180° peeling test, on the opposite of the 90° peeling experiments where mode I is the dominant failure mode.

3.3.2 Failure mechanisms

The peeling tests have been evaluated also with respect to the failure mechanism, differentiating for each sample between:

- adhesive failure (AF), referring to an interfacial bond failure mode,

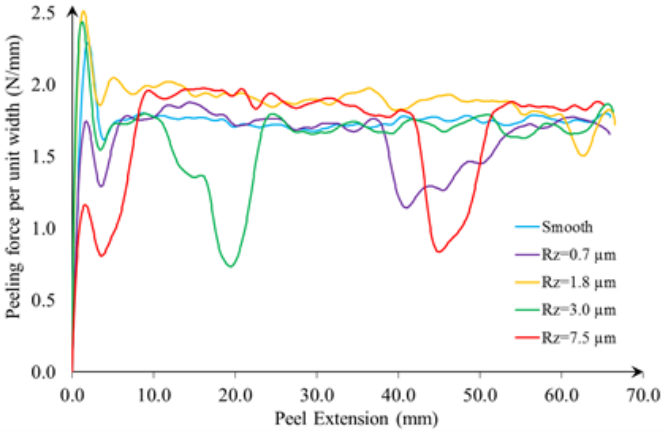

Figure 69: 180° peeling tests results for samples with $t_a = 0.8\text{mm}$ and different substrate roughness.

which may occur at the interface between the adhesive and the adherends (the substrate or the strip);

- cohesive failure (CF), occurring when a crack travels within the finite thickness of the adhesive and, at failure, thin layers of the adhesive remain attached to both adherends.

A sketch of these different scenarios has been shown in the introductory Chapter, Figure 21. Most of the samples point out a mixed-mode failure pattern, hence, it is interesting to evaluate how the peeling response is influenced by the failure mechanism.

To quantitatively assess the percentage of each damage mechanism in a sample, an image processing routine implemented in MATLAB has been used. The routine analyses the optical scans of strips after the peeling, taking advantage of the contrast between the white strip and the black color of the silicone adhesive. In the post-peeling scan, the white color represents an adhesive failure close to the strip (since the white color of the strip is still visible), while the black color requires the analysis of the substrate scan since it is necessary to distinguish between cohesive

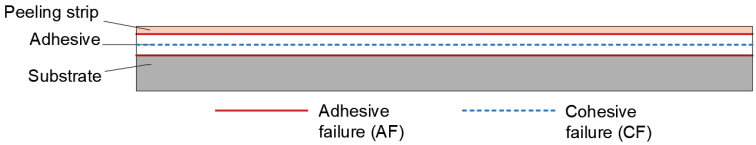

maybe it is just a matter of the numbers in the

Figure 70: Possible failure mechanisms of the sample: adhesive failure (AF) and cohesive failure (CF).

failure and adhesive failure close to the substrate surface (see Figure 70). Four meaningful examples are here reported to show the influence of the failure mechanism on the peeling response.

The Figure 71 shows the images of three samples with $t_a = 1.2\text{mm}$ and smooth substrate after 90° peeling test. Peeling response, strip, and substrate are reported for each case. For all three specimens, the damage pattern starts with an AF mechanism, which corresponds to the first peak load. The case denoted with (a), green curve, shows a crack propagation in CF mechanism corresponding to the second peak load and the steady-state range. The sample (c), red line, moves from a cohesive failure to an adhesive failure close to the substrate in the central part of the specimen, corresponding to a load drop in the force-displacement plot. Moreover, it can be seen that, except for the central drop, the (a) and (c) tests reaches the same steady-state values of peeling force for the same failure mechanism. The same central load drop due to AF failure is visible also in case (b). However, after the initial AF stage, sample (b) shows a mixed AF and CF pattern leading to small load drops in the peeling force also in the other sections and a lower average steady-state.

The next scenario considers the peeling response of 90° peeled samples having an adhesive thickness equal to $t_a = 0.8\text{mm}$ and it is depicted in Figure 72. Sample (a) shows a perfect cohesive failure for the entire specimen. The other 2 samples reveal mixed failure mechanisms including CF and AF close to the substrate. The post-peeling surface is characterized by a ridge pattern, particularly visible in the substrates picture. Analyzing the peeling response, it can be observed that the samples

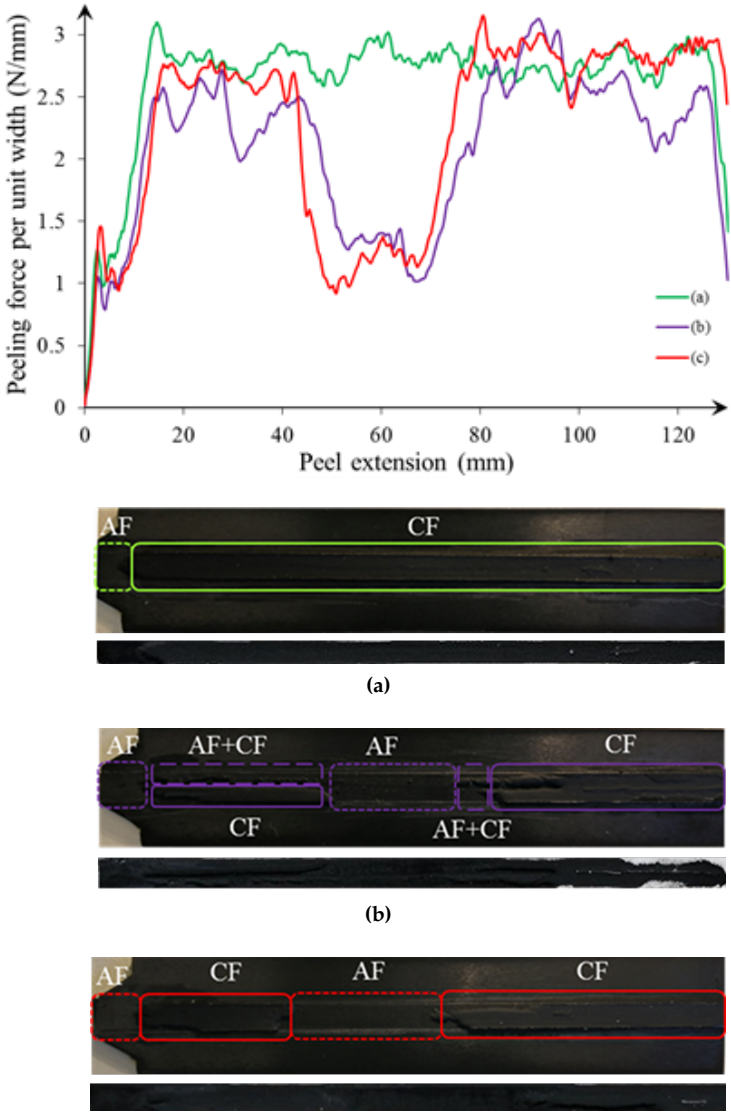

(a)

(b)

(c)

Figure 71: 90°peeling test response and failure mechanisms for three samples with smooth substrate and $t_a = 1.2\text{mm}$.

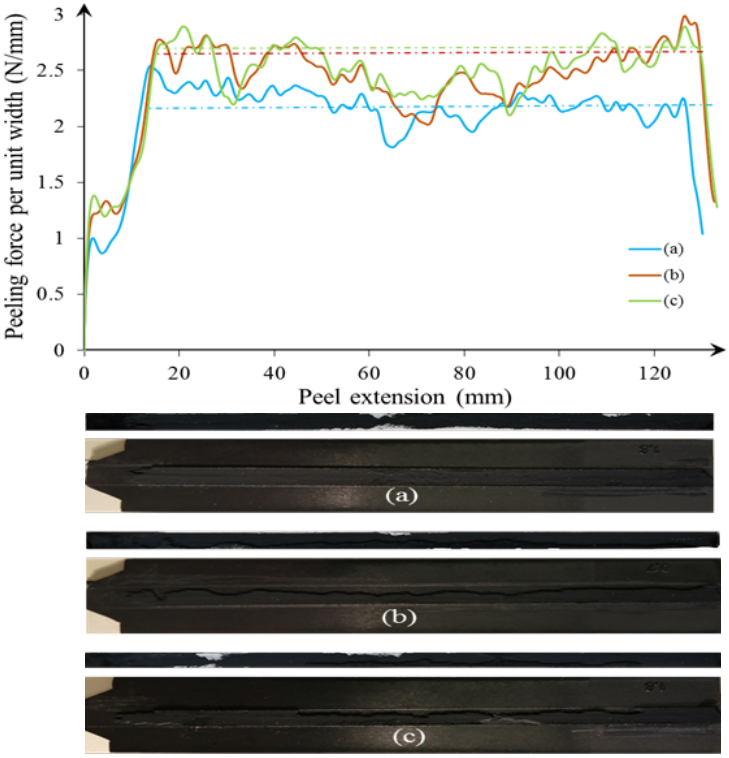

Figure 72: 90°peeling test response and failure mechanisms for three samples with smooth substrate and $t_a = 0.8\text{mm}$.

(b) and (c) show a higher peeling force compared to the case (a), which can be explained considering that, during the crack propagation, there is a larger surface creation in the mixed-mode mechanism (ridge pattern) compared the smooth cohesive failure surface, corresponding to higher energy dissipation.

For the 180° peeling force, in Figure 73, two specimens having adhesive layer thickness $t_a = 1.9\text{mm}$ are compared. The first case, corresponding to the strip on top of the plot and to the red curve, has a percentage of cohesive failure equal to 80%, while, for the lower strip it

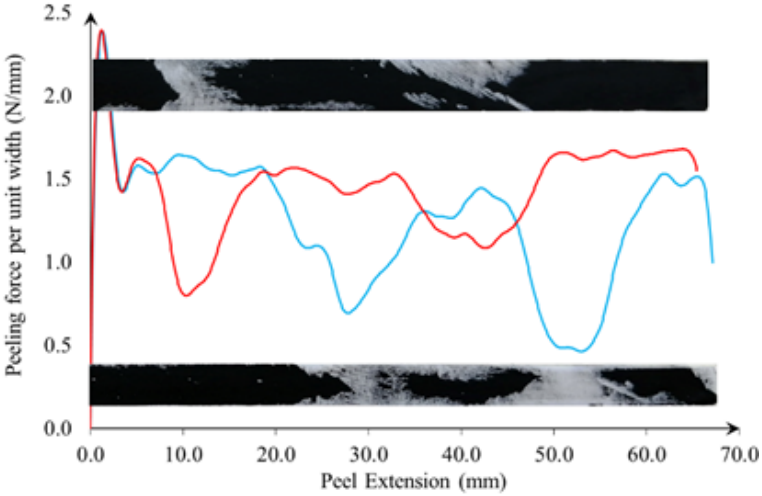

Figure 73: 180°peeling test response and failure mechanisms for two samples with smooth substrates and $t_a = 1.9\text{mm}$.

is equal to 65%. The failure starts with the cohesive failure for both the samples and the peeling force curves initially overlap. The changes in the failure mechanism cause loading drops corresponding to the white area in the post-peeling strips pictures.

The same results can be observed also in the case of post-peeling analysis of samples having $t_a = 0.8\text{mm}$, where the loading drops corresponding to adhesive failure in the sample (a) are clearly visible compared to the peeling response of the sample (b) where the cohesive failure has been found along the entire adhesive bond line (see Figure 74).

3.4 Finite Element Simulations

Starting from the described peeling experiments and considering a starting 2D model under the plane strain assumption of the specimen, the adhesive layer has been modeled through an interface finite element following the cohesive zone model approach.

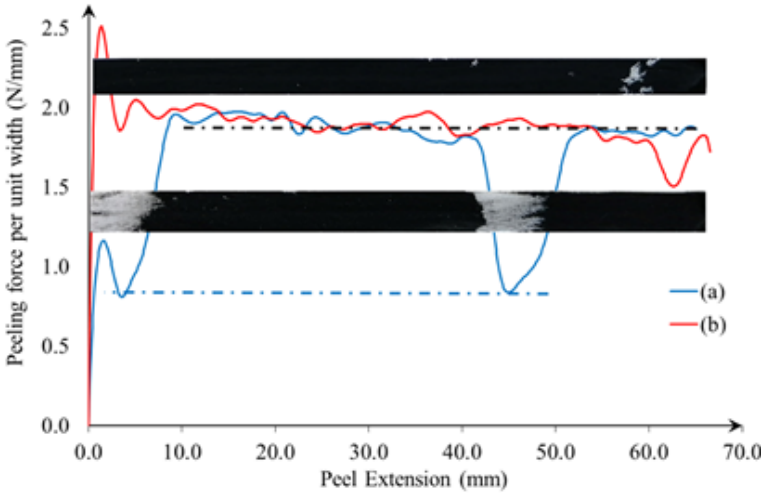

Figure 74: 180°peeling test response and failure mechanisms for two samples with smooth substrates and $t_a = 0.8\text{mm}$.

3.4.1 Interface finite element formulation

The kinematics of the zero-thickness interface finite element follows the same approach seen in Chapter 2 and the framework proposed in [103]. The variational formulation considers two deformable bodies $\Omega_i \in \mathbb{R}^2$ in the undeformed configuration. A displacement field $\mathbf{u}_i = (u_i, v_i)^{\mathrm{T}}$ is introduced for each bodies. As in the previous chapter, the boundary of each solid, $\delta\Omega_i$, is split into the Dirichlet boundary condition, $\delta\Omega_i^{\mathrm{D}}$, Neumann boundary condition, $\delta\Omega_i^{\mathrm{N}}$, and the cohesive interface Γ.

Focusing the attention on the interface between the solids, denoted with Γ, the energy contribution of the interface cohesive traction $\mathbf{T} = (\tau, \sigma)^{\mathrm{T}}$ to the principle of virtual work is given by:

$$\Pi_{\mathbf{int}} = \int_{\Gamma} \mathbf{g}_{\mathrm{loc}}^{\mathrm{T}} \mathbf{T} \mathrm{d}\Gamma \tag{3.3}$$

where $\mathbf{g}_{\mathrm{loc}}$ describes the gap field across the interface represented by the relative displacement field between the two sides of the interface. The notation introduced in this Chapter differs from the previous one be-

cause of a different sign convention attributed to the gap and the traction vector: in the previous Chapter, a positive gap g_n corresponds to positive contact pressure (see the contact conditions in Eq.s 2.1), on the opposite, in the present adhesion problem, a positive normal component of the gap represents the detachment of the interface and corresponds to positive tensile traction σ.

The virtual variation of the equation reads:

$$\delta\Pi_{\mathbf{int}} = \delta\mathbf{u}^{\mathrm{T}} \int_{\Gamma} \left(\frac{\partial \mathbf{g}_{\mathrm{loc}}}{\partial \mathbf{u}} \right)^{\mathrm{T}} \mathbf{T} \mathrm{d}\Gamma \tag{3.4}$$

After a standard discretization process of the interface, for convenience, the element formulation is related to a middle line obtained by averaging the position vectors and the displacements of the two sides of the interface. The position vector of a generic point on the middle line, $\hat{\mathbf{x}}$, can be computed using an averaging operator $\mathbf{M}$:

$$\hat{\mathbf{x}} = \mathbf{M}\mathbf{x} \tag{3.5}$$

The same relation holds for the displacement field.

It is hence possible to define the normal and the tangential vectors at the middle line of the interface, respectively $\mathbf{n}$ and $\mathbf{t}$, which constitute the local coordinate system of the interface element.

Using an isoparametric interpolation, the position vector and the displacement vector can be obtained using an operator $\mathbf{N}$ that collects the standard linear shape functions:

$$\mathbf{x} = \mathbf{N}\bar{\mathbf{x}} \tag{3.6}$$

$$\mathbf{u} = \mathbf{N}\mathbf{d} \tag{3.7}$$

where $\bar{\mathbf{x}}$ and $\mathbf{d}$ denote, respectively, the position vector and the displacement vector of the interface finite element nodes.

As already done in Section 2.3.1, the relative displacements between the nodes couples 1-4 and 2-3, can be obtained using an operator $\mathbf{L}$ and a rotation matrix $\mathbf{R}$:

$$\mathbf{g}_{\mathrm{loc}} = \mathbf{R}\mathbf{N}\mathbf{L}\mathbf{d} \tag{3.8}$$

The partial derivative in Eq. 3.4, in the hypothesis of small displacement, can be approximated as:

$$\frac{\partial \mathbf{g}_{\text{loc}}}{\partial \mathbf{u}} = \mathbf{RNL} \tag{3.9}$$

A Newton-Raphson scheme is adopted to solve the system of equations deriving from the finite element discretization, as in the Eq. 2.10. In the present Chapter formulation, the residual vector and the tangent stiffness matrix read:

$$\mathbf{R}_e^{(k)} = \int_{\Gamma_e^*} \mathbf{L}^{\mathrm{T}}\mathbf{N}^{\mathrm{T}}\mathbf{R}^{\mathrm{T}}\mathbf{T}\,\mathrm{d}\Gamma, \tag{3.10a}$$

$$\mathbf{K}_e^{(k)} = \int_{\Gamma_e^*} \mathbf{L}^{\mathrm{T}}\mathbf{N}^{\mathrm{T}}\mathbf{R}^{\mathrm{T}}\mathbb{C}\mathbf{RNL}\,\mathrm{d}\Gamma, \tag{3.10b}$$

where $\mathbb{C} = \dfrac{\partial \mathbf{T}}{\partial \mathbf{g}_{\text{loc}}}$ is the tangent interface constitutive matrix and it is computed considering:

$$\mathbb{C} = \begin{bmatrix} \dfrac{\partial \tau}{\partial g_t} & \dfrac{\partial \tau}{\partial g_n} \\ \dfrac{\partial \sigma}{\partial g_t} & \dfrac{\partial \sigma}{\partial g_n} \end{bmatrix} \tag{3.11}$$

In the following simulations, only the 90° peeling test has been considered which corresponds to Mode I deformation, consequently the tangent constitutive matrix has been reduced to the contribution in the normal direction:

$$\mathbb{C} = \begin{bmatrix} 0 & 0 \\ 0 & \dfrac{\partial \sigma}{\partial g_n} \end{bmatrix} \tag{3.12}$$

The contact condition corresponding to a negative normal gap is here solved using a standard penalty parameter k_{p} which takes the value of $10000\text{MPa}/\text{mm}$ in the following simulations.

Different interface constitutive laws may be chosen for modeling the interface and computing the tangent stiffness matrix $\mathbb{C}$. In this investigation, the proposed stress-displacement relations are:

- a tension cut-off model, characterized by a critical traction, σ_c and a critical crack opening g_{nc};
- a bilinear model, after the critical traction and opening (σ_c, g_{nc}), a linear descending behavior follows till the critical displacement g_{nu} at the complete decohesion.

In the case of the tension cut-off model, the governing equation at the interface reads:

$$\sigma(g_n) = \begin{cases} k_n g_n & \text{if} \quad 0 \leq g_n \leq g_{nc} \\ 0 & \text{if} \quad g_n > g_{nc} \\ k_p g_n & \text{if} \quad g_n < 0 \end{cases} \tag{3.13}$$

For the bilinear model the governing equation becomes:

$$\sigma = \begin{cases} k_n g_n & \text{if} \quad 0 \leq g_n \leq g_{nc} \\ \sigma_c(g_n)\left(1 - \frac{g_n - g_{nc}}{g_{nu} - g_{nc}}\right) & \text{if} \quad g_{nc} < g_n \leq g_{nu} \\ 0 & \text{if} \quad g_n > g_{nu} \\ k_p g_n & \text{if} \quad g_n < 0 \end{cases} \tag{3.14}$$

The stiffness parameter k_n is proportional to the ratio between the Young's modulus of the adhesive, E_a, and the adhesive layer thickness [95], t_a, and this assumption will be later used to add the influence of roughness to the model. The constitutive laws are depicted in Figure 75.

The area under the curves identifies the associated interface fracture energy which corresponds to the adhesive fracture energy, G_{IC}, already mentioned:

$$G_{\text{IC}} = \frac{1}{2} g_{nc} \sigma_c \qquad \text{(Tension cut-off)} \tag{3.15a}$$

$$G_{\text{IC}} = \frac{1}{2} g_{nu} \sigma_c \qquad \text{(Bilinear)} \tag{3.15b}$$

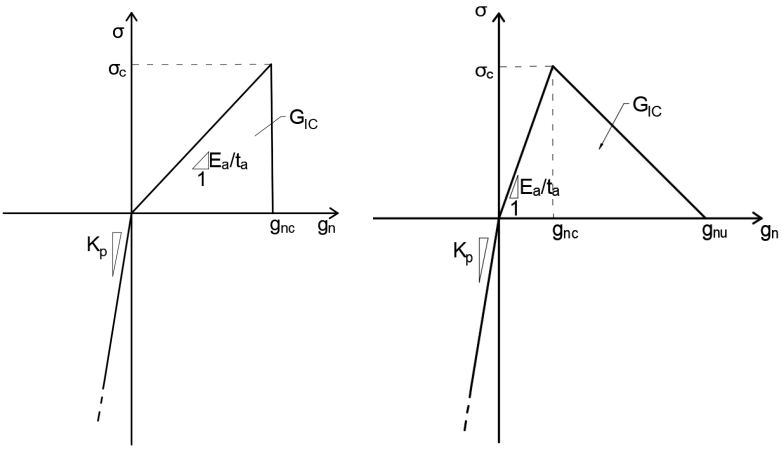

(a) Tension cut-off **(b)** Bilinear

Figure 75: Interface constitutive laws.

When the energy dissipated is equal to the interface fracture energy, the cohesive traction is reduced to zero and new crack surfaces are formed. This approach allows the simulation of the cohesive failure of the adhesive layer, which is modeled as a zero-thickness layer, while the real thickness is considered inside the interface law. Moreover, in the case of the tension cut-off model, for a given stiffness k_n (related to E_a/t_a), it is possible to assign one quantity: the interface fracture energy or the critical tension or the critical opening g_{nc} such that the other two parameters can be computed. For the bilinear model, for a given k_n, two quantities must be assigned to complete the description of the interface law among the parameters G_{IC}, σ_c (or g_{nc}), g_{nu}.

3.4.2 Model of the specimens with smooth substrates

The 90° peeling test has been reproduced through a finite element model which geometry is shown in Figure 76. The mesh and boundary conditions are in Figure 77. The material parameters used for the simula-

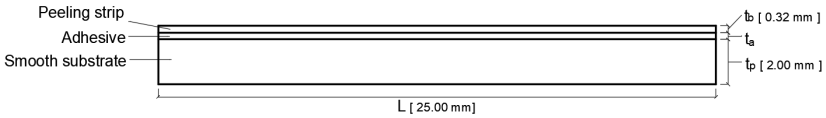

Figure 76: Geometry of the 90° peeling test model for the smooth substrate.

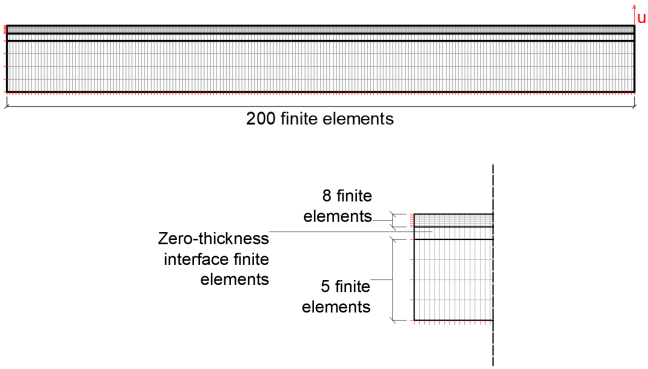

Figure 77: Mesh and boundary conditions for the 90° peeling test model with smooth substrate. Details of the mesh are given in (b).

tion derive from the experimental characterization of the components, see Section 3.2.2. This first model considers a smooth substrate, hence, the same interface constitutive law has been used along the entire interface.

The model has been used to compare the peeling response with the bilinear and the tension cut-off interface laws to the experimental tests. Preliminary results have been obtained considering different adhesive layer thicknesses for fixed $G_{\text{IC}} = 3.2\text{Nmm}$. For the tension cut-off case, the other interface law parameters can be computed considering:

$$g_{nc} = \sqrt{\frac{2G_{\text{IC}}t_a}{E_a}}, \qquad \sigma_c = \frac{E_a g_{nc}}{t_a} \tag{3.16}$$

For the bilinear CZM, another input is necessary aside $G_{\text{IC}} = 3.2\text{N/mm}$: in this simulation, the value of g_{nu} has been given as 3mm. The other

quantities are computed as:

$$\sigma_c = \frac{2G_{\mathrm{IC}}}{g_{nu}}, \qquad g_{nc} = \frac{\sigma_c t_a}{E_a} \tag{3.17}$$

The CZM laws varying t_a for the two cases are depicted in Figure 78.

The model results are shown in Figure 79 for the tension cut-off interface law, and in Figure 80 for the bilinear CZM.

For both cases, the variation of the adhesive layer thickness changes the initial slope of the peeling response, while the peeling force reaches at the steady-state exactly the value of $3.2\mathrm{N/mm}$ which corresponds to the given value of G_{IC}. The increasing value of t_a in the bilinear interface law corresponds to the increase of g_{nc}, and to the consequent increase of the peak load, and of the corresponding imposed displacement in the force-displacement curve.

The comparison between the tension cut-off and the bilinear interface laws results show that the bilinear CZM system provides a peeling response that better reproduces the experimental curves and it will be used for the following simulations.

3.4.3 Zeroth-order approximation model for rough substrate

The second set of simulations aim at reproducing the effect of roughness on the peeling response. This investigation has been carried considering only the samples for which the ratio α is lower than the proposed threshold. The goal of the simulation is to predict the peeling response of the rough interface, knowing the response of the smooth section. In other words, the peeling curves related to the smooth substrate will be used to tune the interface constitutive law variables; these values are then used to predict the peeling force for the rough interface.

The model considers the substrate as nominally 'flat', introducing the effect of roughness in the interface constitutive law. The adhesive interface of the sample is split into two sections where the interface constitutive law uses different parameters for the smooth and the rough section.

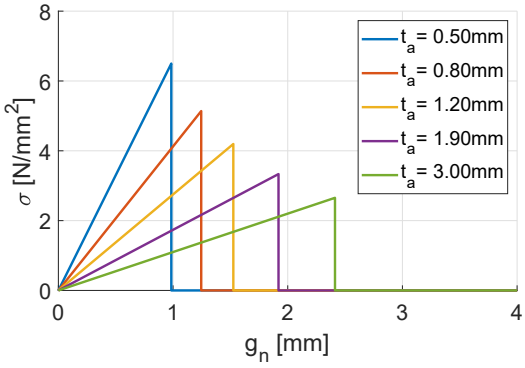

(a) Tension cut-off

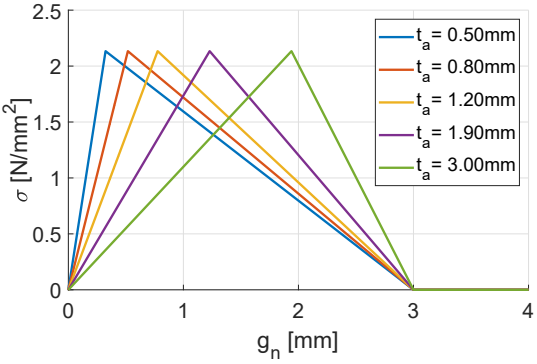

(b) Bilinear

Figure 78: CZM interface laws for different adhesive thicknesses.

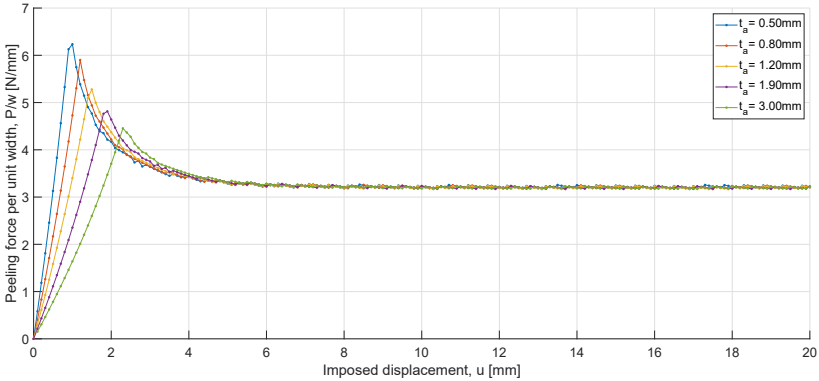

Figure 79: Influence of the adhesive thickness layer with given G_{IC} and tension cut-off interface constitutive law.

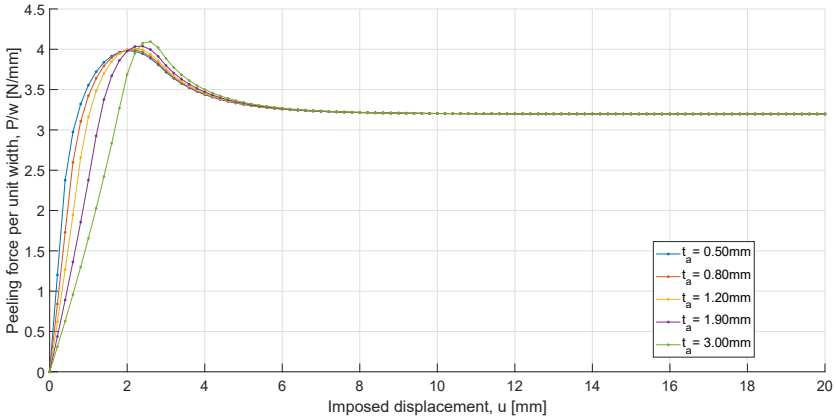

Figure 80: Influence of the adhesive thickness layer with given G_{IC} and bilinear interface constitutive law.

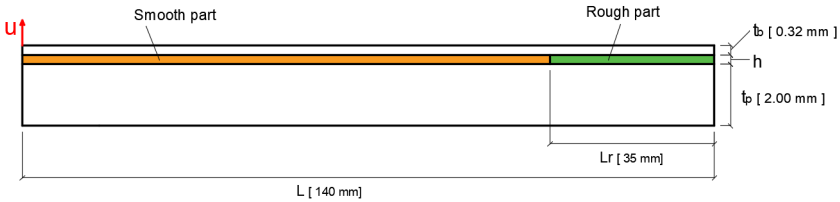

Figure 81: Peeling model with the adhesive interface divided into smooth and rough sections.

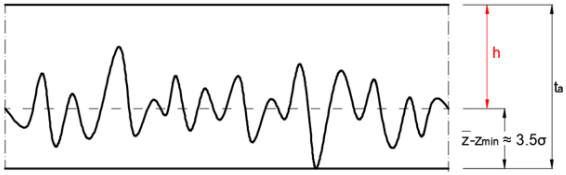

Figure 82: Adhesive thickness reduction due to the presence of roughness at the interface.

A sketch of the geometry of the model is shown in Figure 81, where the two parts that composed the interface are clearly visible. The model is $10\mathrm{mm}$ longer than the real sample to avoid boundary influence on the peeling results when the peeling extension reaches the right edge.

The influence of roughness in the related interface part has been introduced into the model using a so-called "zeroth-order approximation" where the nominal thickness of the adhesive, t_a, has been reduced by an average thickness of the adhesive, h, available considering the average height of the statistically representative rough surface of the substrate. A sketch of the reduction of the adhesive thickness due to the presence of roughness is shown in Figure 82.

In particular, the statistical characterization of the rough surfaces provides the root mean square of the surface elevations as seen in the Section 3.2.1 and given in Table 7. These values can be used to approximate the average height of the surface as $\bar{z} - z_{\min} \approx 3.5\sigma$. The nominal thick-

		Nominal thickness t_a				
R_z (µm)	σ (µm)	0.5 mm	0.8 mm	1.2 mm	1.9 mm	3.0 mm
0.6	1.14	0.4960	0.7960	1.1960	1.8960	2.9960
0.7	2.20	0.4923	0.7923	1.1923	1.8923	2.9923
1.8	3.25	0.4886	0.7886	1.1886	1.8886	2.9886
3.0	4.03	0.4859	0.7859	1.1859	1.8859	2.9859
7.5	11.36	0.4602	0.7602	1.1602	1.8602	2.9602

Table 9: Effective thickness values, h, used in the simulations.

ness of the adhesive can be reduced according to the relation:

$$h = t_a - 3.5\sigma \tag{3.18}$$

where h is called effective thickness. The values of h for each scenarios are in Table 9. The highlighted cells represent the values corresponding to $\alpha < 246$ for the roughness effect can be appreciated.

The experimental results for the smooth part of the sample can be used to tune the parameters of the interface constitutive law to match the experimental curves. For each nominal thickness, the adhesive fracture energy has been evaluated averaging the peeling force per unit width of the different samples since the adhesive thickness influences the steady-state peeling force as shown in Figure 67. Hence, the first part of the analysis focused on retrieving from the model the steady-state value of the peeling force related to the smooth part of the substrate, as in Figure 83.

The same critical traction has been used for all the samples equal to 0.8MPa, while the critical displacements, g_{nc} and g_{nu}, are computed from Eq.s 3.17. The values are in Table 10.

$t_a[\text{mm}]$	$G_{\text{IC,smooth}}[\text{N/mm}]$	$\sigma_{\text{c,smooth}}[\text{MPa}]$	$g_{nc}[\text{mm}]$	$g_{nu}[\text{mm}]$
0.5	2.08	0.8	0.12	5.21
0.8	2.44	0.8	0.19	6.09
1.2	2.20	0.8	0.29	5.50
1.9	2.38	0.8	0.46	5.94

Table 10: Smooth interface parameters used for the bilinear cohesive zone model.

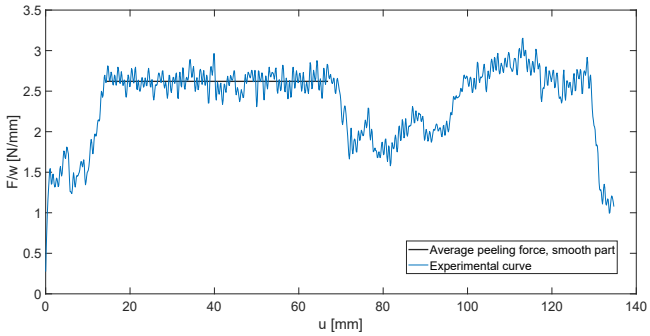

Figure 83: Steady-state value of the peeling force per unit width for the sample with $t_a = 0.8\text{mm}$ and rough substrate with $R_z = 7.5\mu\text{m}$.

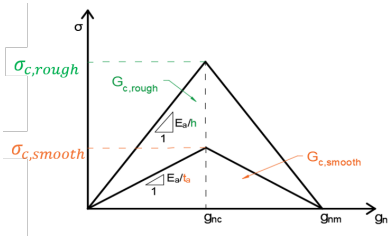

Figure 84: Bilinear interface laws for the rough and the smooth part of the sample.

To predict the peeling response for the rough part, the critical traction $\sigma_{\text{c,rough}}$ is computed using the effective thickness h, knowing the value of g_n and g_{nc} from the smooth interface.

With the proposed assumptions, a sketch of the bilinear constituive equations for the smooth and rough interface is given in Figure 84. All the values used as input in the simulations are reported in Table 11.

The results of the simulations together with the values of G_{IC} for the smooth (input of the model) and the rough part (predicted by the model) are given in Figures 85, 86, 87 and 88.

In these plots, the shaded area represents the range spanned by the experimental curves with the same nominal adhesive thickness, used to

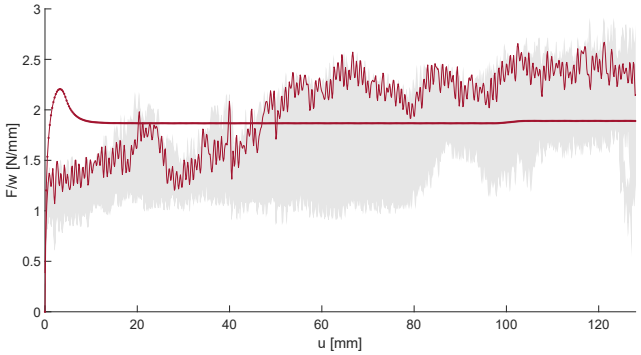

(a) $t_a = 0.5mm - R_z = 0.7\mu\text{m}$

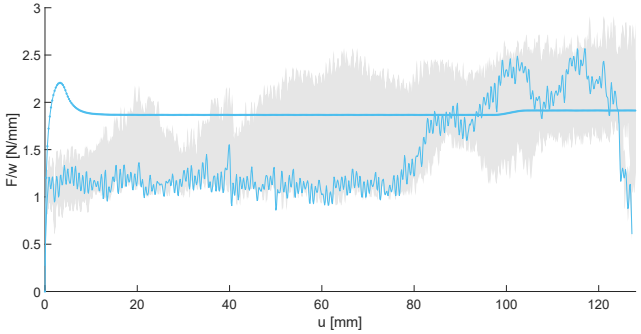

(b) $t_a = 0.5mm - R_z = 1.8\mu\text{m}$

Figure 85: Comparison of the experimental curves related to the nominal adhesive thickness $t_a = 0.5mm$ with the simulations results obtained using the effective thickness h.

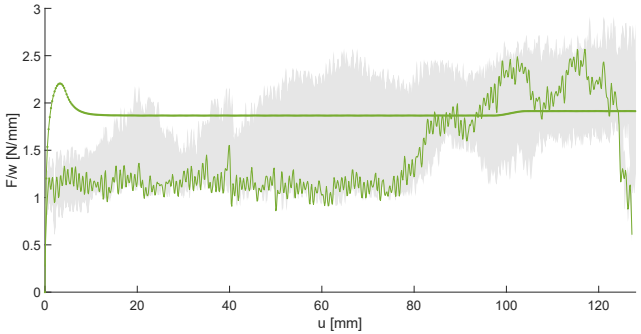

(a) $t_a = 0.5mm - R_z = 3\mu\text{m}$

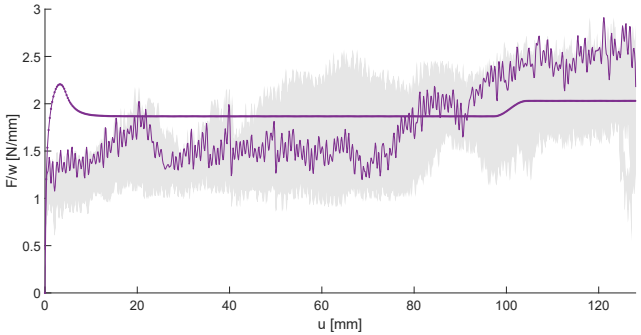

(b) $t_a = 0.5mm - R_z = 7.5\mu\text{m}$

Figure 86: Comparison of the experimental curves related to the nominal adhesive thickness $t_a = 0.5mm$ with the simulations results obtained using the effective thickness h.

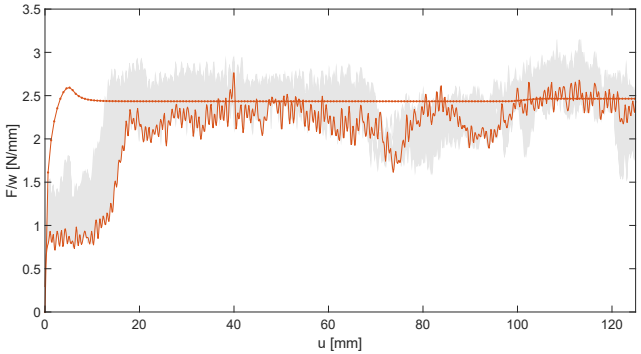

(a) $t_a = 0.8mm - R_z = 3\mu$m

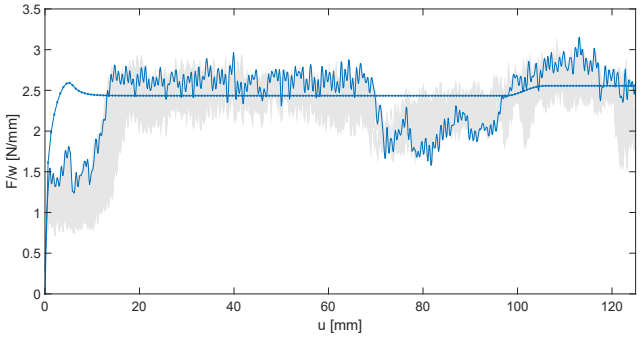

(b) $t_a = 0.8mm - R_z = 7.5\mu$m

Figure 87: Comparison of the experimental curves related to the nominal adhesive thickness $t_a = 0.8$mm with the simulations results obtained using the effective thickness h.

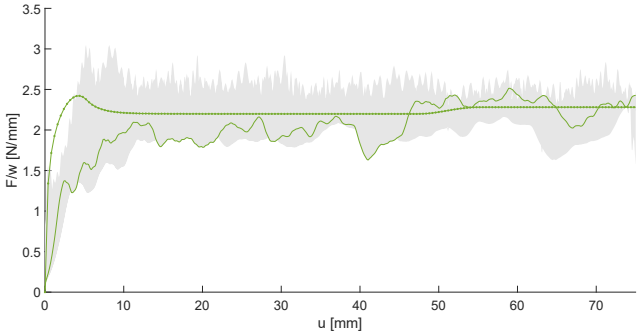

(a) $t_a = 1.2mm - R_z = 7.5\mu\text{m}$

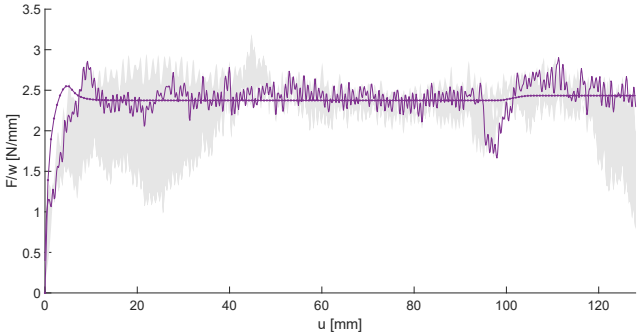

(b) $t_a = 1.9mm - R_z = 7.5\mu\text{m}$

Figure 88: Comparison of the experimental curves related to the nominal adhesive thickness $t_a = 1.2, 1.9mm$ with the simulations results obtained using the effective thickness h.

t_a[mm]	R_z[μm]	h[mm]	$\sigma_{\text{c,smooth}}$[MPa]	g_{nc}[mm]	g_{nu}[mm]
0.5	0.7	0.4923	0.81	0.12	5.21
0.5	1.8	0.4886	0.82	0.12	5.21
0.5	3	0.4859	0.82	0.12	5.21
0.5	7.5	0.4602	0.87	0.12	5.21
0.8	3	0.7859	0.81	0.19	6.09
0.8	7.5	0.7602	0.84	0.19	6.09
1.2	7.5	1.1602	0.83	0.29	5.50
1.9	7.5	1.8602	0.82	0.46	5.94

Table 11: Rough interface parameters used for the bilinear cohesive zone model.

compute the average value of $G_{\text{IC,smooth}}$ for the smooth part of the interface. Moreover, each plot contains the experimental curve considered for the specific R_z value and the peeling response obtained through the simulation. Consequently, the peeling force is the same for the samples having the same nominal thickness, see for example Figure 85 and Figure 86, while the peeling force relating to the rough part of the substrate varies according to R_z. In particular, the simulation results show that the peeling force jump between the smooth and rough sections increases with the increase of R_z and the consequent decrease of h.

Not all the cases are well captured by the model. the thinnest adhesive layer is characterized by a big variability of results already in the smooth range, caused also by crack propagation in adhesive failure mode instead of cohesive failure mode, which cannot be captured by the proposed finite element model, see Figure 85 and 86.

For $t_a = 0.8\text{mm}$ and $R_z = 3\mu\text{m}$, Figure 87, it can be observed that even though the jump in the peeling force is not well captured, the model reproduces the correct steady-state of the experimental curve in the rough part. On the opposite, the case with $t_a = 0.8\text{mm}$ and $R_z = 7.5\mu\text{m}$, Figure 87 show a correct jump in the peeling force but different values of steady-state peeling force for both the smooth and rough part. In these cases, tuning the bilinear constitutive parameters of the smooth part on the specific sample and not on the average behavior, the model results are closer to the experimental curves, see Figure 89. However, this strategy is not physically meaningful since the model uses two different in-

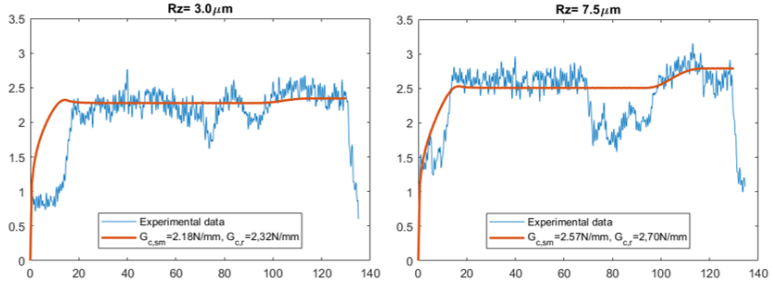

(a) $t_a = 0.8mm - R_z = 3\mu\text{m}$ **(b)** $t_a = 0.8mm - R_z = 7.5\mu\text{m}$

Figure 89: Model results obtained tuning the interface parameters on the single sample instead of using the averaging procedure.

terface constitutive laws even in the smooth region where the samples have the same characteristics (same adhesive thickness and smooth substrate). Moreover, this approach does not show relevant results for the other values of t_a.

Finally, the peeling force jumps predicted by the model are more accurate for thick adhesive layers, $t_a = 1.2, 1.9\text{mm}$, which show less variability in the experimental peeling curves (and narrower shaded area), Figure 88.

The procedure for identifying the cohesive zone model parameters appears hence complex, and it cannot be based on the simple modification of the initial stiffness of the interface law as in the proposed model. The roughness effect allowed us to classify the peeling response and the failure mechanisms experimentally. However, the numerical simulation requires a more complex algorithm to capture the analyzed system's correct mechanical response.

Chapter 4

Simulation of bio-inspired adhesives with mushroom-shaped micro-structures

The industrial sector has shown a growing interest in dry adhesives, especially bio-mimetic adhesives inspired by the natural micro-structures observed on the animals' skin. This Chapter focuses on the simulation of adhesives having mushrooms-shaped patterned surface through the formulation of an interface finite element capable of capturing the attachment and detachment mechanisms without the necessity of modeling in detail the microstructures on the surface. Hence, the proposed interface finite element represents a versatile tool for modeling possible applications of bio-inspired adhesives starting from simple pull-out experimental tests.

The Chapter starts with a short description of the literature contributions on bio-mimetic adhesives in Section 4.1, while Section 4.2 illustrates the experimental investigation that constitutes the basis of the interface model formulation proposed in Section 4.4. The final Section (4.5) delineates the results of the proposed interface finite element.

Nomenclature

α	Tilt angle
T	Nominal traction
g	Displacement gap at interface
g^{u}	Unloading displacement
T^{u}	Unloading traction
T^{ad}	Maximum traction (pull-off force)
g^{ad}	Displacement corresponding to the maximum traction
g^{max}	Critical displacement at the complete decohesion
$\mathbf{P}_1(g)$	Fitting function for the loading phase for a given α
$\mathbf{P}_2(g, g^{\mathrm{u}})$	Fitting function for the unloading increasing phase for a given α
$\mathbf{P}_3(g, g^{\mathrm{u}})$	Fitting function for the unloading decreasing phase for a given α
$\mathbf{g}^{\mathrm{u}}$	Vector containing g^{u} values of the cycles for a given α
$\mathbf{p}$	Vector of the polynomial coefficients
$\mathbf{g}_i$	Vector of g values for the i-th cycle for a given α
n	Number of cycles for the analysed tilt angle
$\mathbf{g}$	Total displacement vector given by concatenation of $\mathbf{g}_i$
$\mathbf{C}$	Matrix form of the powers of $\mathbf{g}$ for the polynomial fitting
$\mathbf{T}_i$	Vector of the traction data T for the i-th cycle for a given α
$\mathbf{T}$	Total traction vector given by concatenation of $\mathbf{T}_i$
$\mathbf{A}$	Inequality constrains displacement matrix
$\mathbf{A}_{\mathrm{eq}}$	Equality constrains displacement matrix
$\mathbf{b}$	Inequality constrains traction vector
$\mathbf{b}_{\mathrm{eq}}$	Equality constrains traction vector
$\mathbf{T}^{\mathrm{u}}$	Vector of the unloading traction values
$\mathbf{g}^{\mathrm{ad}}$	Vector of the adhesion peak displacements
$\mathbf{T}^{\mathrm{ad}}$	Vector of the adhesion peak tractions
$\mathbf{Q}_1(\mathbf{g})$	Fitting function for the adhesion peak traction vector
t	Generic time-step
$\mathbf{g}_{\mathrm{loc}} = (g_n, g_t)^{\mathrm{T}}$	Gap at the interface
g_t	Tangential component of the gap vector
g_n	Normal component of the gap vector
$\bar{\alpha}$	Experimental tilt angles
t	Current time-step
g_{hist}	History variable containing the value of the gap at $t-1$
$g^{\mathrm{u}}_{\mathrm{hist}}$	History variable containing the unloading displacement
$\mathrm{T}_1(g, g^{\mathrm{u}}, \alpha_1)$	Traction value corresponding to the tilt angle α_1
$\mathrm{T}_2(g, g^{\mathrm{u}}, \alpha_2)$	Traction value corresponding to the tilt angle α_1
τ	Tangential component of the traction vector
σ	Normal component of the traction vector
$\mathbb{C}$	Interface tangent stiffness matrix
$\bar{\alpha}_1$ and $\bar{\alpha}_2$	Experimental tilt angles used in the interface finite element routine
E_i and ν_1	Young's modulus and Poisson ratio of the i-th body
u_n and u_t	Normal and tangent components of the unloading displacement

4.1 Model bio-mimetic mushroom-shaped adhesives

As underlined in the introductory Chapter of this thesis, adhesion is a fundamental phenomenon with great importance also in biological systems at different scales: cell adhesion is the process by which cells form contacts with each other, bacterial adhesion allow bacteria to live in close association with surfaces and plants and animals like insects, spiders, and geckos developed complex biological systems of attachment.

This kind of biological attachment device represents a significant source of information for developing novel bio-inspired adhesives. The adhesive properties of these natural surfaces are highly influenced by the micro-structures contact shape, as seen in Section 1.2.3. Next to the more famous micro-structures on the gecko's footpads, the attachment systems of beetles from the family Chrysomelidae have been the inspiration for Mushrooms-Shaped Adhesive Microstructures (MSAMSs) instead of previously used patterned adhesives having cylindrical pillars [104]. While the geckos' attachment system has a hierarchical structure composed of setae and spatulae, the fibrillar surface inspired by the beetles can be easier reproduced for industrial dry adhesives with better results compared to flat surfaces.

Moreover, the adhesive performance of the mushroom-shaped pillars have been compared against the cylindrical flat punch geometry [105], and other tip shapes [106], showing the positive influence of the thin plate at the pillars extremity on the adhesion strength emerged from the experimental research and explained theoretically by the analysis of the pillar detachment.

A close-up of the attachment and detachment of the mushroom-shaped pillars and of the crack propagation is proposed in [107] through compression and shear tests on PVS (polyvinylsiloxane) patterned disks, suggesting that the shear loads can be used to release the contact and easily separate the adhesive from the substrate.

A detailed review of the experimental and theoretical investigations on the micro-pillars has been proposed in [108]. The analyses focus

mainly on the analytical derivation of the stress state at the interface between the pillar and the adhering surface. In the same paper, a FE analysis of the pillar is also introduced to investigate the relation between the pillar's geometrical dimensions and the stress distribution under the plate. The detachment process has also been simulated in [109] testing the frictionless and sticking friction conditions at the contact surface for the mushroom-shape and the flat punch geometry.

The adhesive interface has also been studied through the cohesive zone model in [110] using a Dugdale-Barenblatt model for the normal direction and neglecting the possibility of the interface failure in the tangential direction. A bilinear traction-separation law has been used in [111] to simulate loading and unloading experimental tests on polyurethane fibrils with different plate thicknesses.

Few computational models have been proposed about systems more extensive than the single pillar due to the computational effort required for meshing the complex geometry of a patterned surface. An example can be found in [112] regarding gecko-inspired adhesive pressed against a rigid sphere. A contact formulation including friction, adhesion, and decohesion conditions have been proposed integrating a penalty approach with a bilinear separation law.

A more complex approach has been proposed in [113] simulating the gecko's seta through a 3D multiscale finite element model. Nonlinear finite element beams have been used for the setae branching in multiple spatulae. These latter elements have been modeled at a smaller scale with a detailed FEM. Finally, the adhesive interaction with the surface uses Lennard-Jones' potential for the molecular interaction between the spatula pad and the adhering surface.

The simulation of the MSAMSs adhesive at a scale bigger than the single pillar represents an open issue nowadays. For this reason, the present work aims at reproducing the mushroom patterned adhesive performance without the necessity of a detailed description of the surface through the formulation of a phenomenological interface law that can be used inside a zero-thickness finite element. In this way, computational models of peeling tests and real applications can be easily studied

since only a nominally flat interface will be required.

The starting point of the computational framework is the experimental data acquired during pull-off tests on PVS samples, focusing the attention on the dependence of the adhesion strength on the tilt angle, which is a crucial parameter of the performance of the adhesive, as it will be described in the following Section.

4.2 Experimental investigation

The experimental campaign has been carried on using MSAMS samples produced with polyurethane (PVS), in which elastic modulus is about $3\mathrm{MPa}$. The height of a singular pillar is about $100\mu\mathrm{m}$, while the base diameter is $60\mu\mathrm{m}$ decreasing to $35\mu\mathrm{m}$ at the middle section and having a neck close to the contact plate with a $25\mu\mathrm{m}$ diameter. The contact plate diameter is about $48\mu\mathrm{m}$, and its thickness is $2\mu\mathrm{m}$. The mushroom-shaped pillars are hexagonally packed on the sample's surface, and they have been shown in Figure 24.

The adhesion measurements have been performed on a custom-built apparatus, shown in Figure 90 at a constant velocity of $0.1\mathrm{mm/s}$, composed by a 6-axis positioning table. The samples have been pressed against a glass cylinder with $5\mathrm{mm}$ diameter and later retracted from it, considering a defined tilt angle α. Nine values of the tilt angle have been tested: $0.0°, 0.5°, 1.0°, 1.5°, 2.0°, 2.5°, 3.0°, 3.5°, 4.0°$. For each angle, about 30 cycles of attachment (loading) and detachment (unloading) have been tested using decreasing values of the maximum loading displacement ranging between $-0.80\mathrm{mm}$ up to $-0.1\mathrm{mm}$.

An exemplary force-timestep diagram can be seen in Figure 91 related to the 31 cycles done with $\alpha = 2.5°$. The positive values are recorded during the loading phase when the MSAMS is pressed against the cylinder. During the unloading phase, the minimum peak values represent the force needed to completely detach the adhesive, referred to as pull-off force. The overall behavior shows that the pull-off force is a function of the maximum loading displacement and the tilt angle. At increasing values of loading displacement (corresponding to the increase of loading

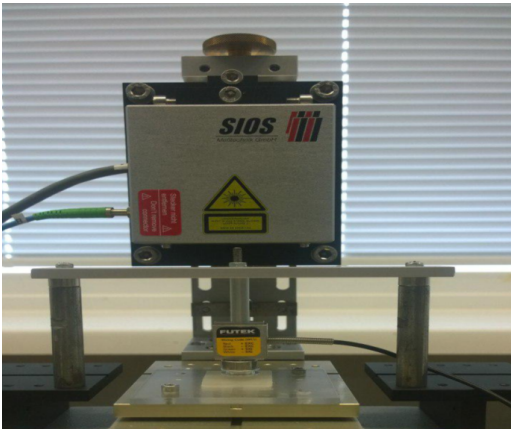

Figure 90: Experimental set-up for adhesion measurements.

force), the pull-off force increases up to a plateau value.

The traction-displacement curve has been obtained for each cycle considering the nominal traction T as the ratio between the force value and the glass cylinder area. The sign convention here adopted agrees with the finite element formulation introduced in Chapter 3, assuming the loading traction as negative and the adhesive traction in the unloading phase positive. The unloading phase can be further divided into (i) an increasing phase up to the maximum traction values corresponding to the pull-off force and (ii) a decreasing phase till the complete detachment of the adhesive. The division in these two steps is required to identify the maximum adhesive traction and to facilitate the fitting procedure, as will be described in the next Section.

The traction-displacement curve obtained with the tilt angle $\alpha = 2.5°$ is depicted in Figure 92 and it is related to the first loading-unloading cycle. Some relevant quantities are shown in the same plot to introduce the notation that will be used in the following paragraphs: (i) the displacement at the end of the loading phase, g^{u} (afterward referred to as unloading displacement), and the corresponding traction values T^{u}, (ii) the maximum traction T^{ad} and the related displacement g^{ad}, and (iii) the critical displacement at the complete adhesive failure $g^{\max}$.

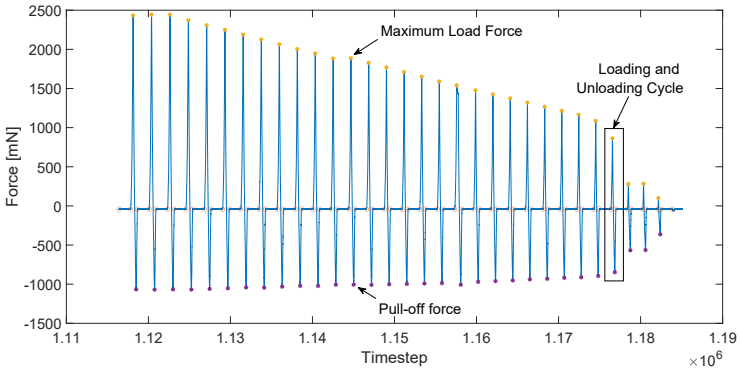

Figure 91: Force-timestep diagram of 31 cycles of loading and unloading with tilt angle $\alpha = 2.5°$.

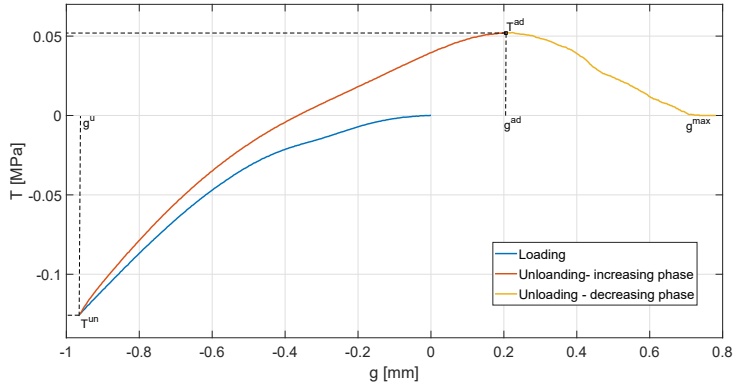

Figure 92: Traction-displacement curve obtained with the tilt angle $\alpha = 2.5°$ with an unloading displacement $\mathbf{g}^{\mathrm{u}} = -0.81\mathrm{mm}$.

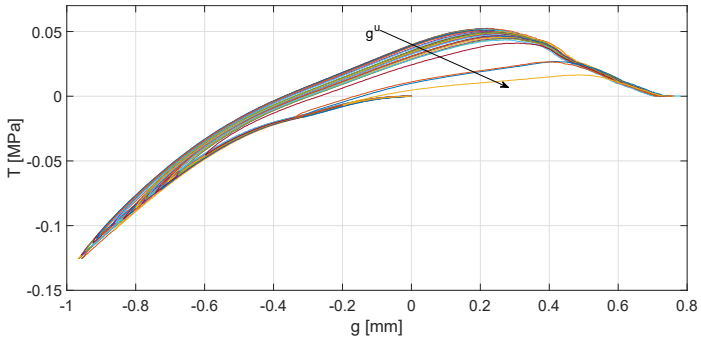

Figure 93: Experimental curves related to the same tilt angle $\alpha = 2.5°$ but with a decreasing unloading displacement g^{u}.

The different cycles related to the same tilt angle have been overlapped in Figure 93 to observe the effect of the unloading displacement g^{u}. The plot shows that for increasing values of tilt angle, the adhesion peak decreases. In the applications, this phenomenon can be exploited to have a rapid detachment of the MSAMSs adhesive by changing the pillar's inclination.

The same procedure has been repeated for each tilt angle and the curves of the first cycle for different tilt angles are shown in Figure 94.

4.3 Development of the interface model

The experimental data collection has been followed by the definition of an interface constitutive model that can reproduce the behavior of the MASAMs adhesive to be used in the zero-thickness interface finite element, already exploited in Chapters 2 and 3.

The experimental investigations show that in general, the traction at the interface depends on the tilt angle α used during the test, on the displacement jump at the interface, g, and on the loading history, since the adhesion pull-off traction depends on the unloading displacement g^{u}.

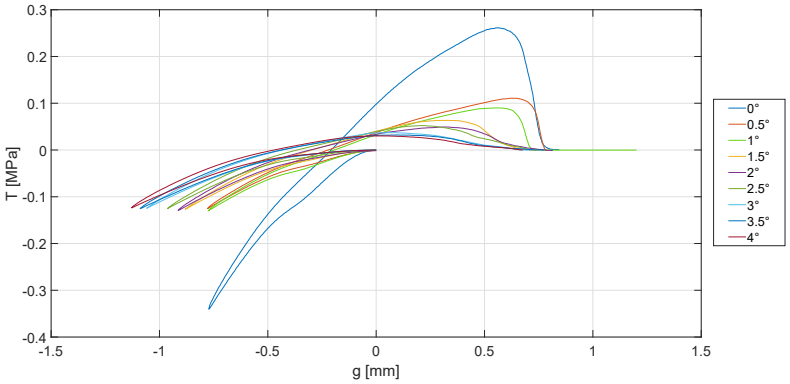

Figure 94: Experimental traction-displacement curves obtained at the first-cycle for different tilt angles.

Hence, the desired constitutive model assumes the form of: $\mathrm{T} = f(\alpha, g, g^{\mathrm{u}})$. The experimental data are firstly used to define a function having the form of $\mathrm{T} = f(g, g^{\mathrm{u}})$ for each tilt angle. Secondly, a linear interpolation of the traction values will be considered to deal with all the values of $\alpha \in [0°, 4°]$. The first step is described in detail in the present Section, while the linear interpolation will be described directly in the next Section together with the interface finite element routine.

For each tilt angle, to relate the imposed displacement to the measured traction, three different functions have been used for the loading phase, $\mathbf{P}_1(g)$, the increasing unloading phase, $\mathbf{P}_2(g, g^{\mathrm{u}})$, and the decreasing unloading phase, $\mathbf{P}_2(g, g^{\mathrm{u}})$.

Polynomial expressions of the gap have been fitted to the experimental data using the linear least-squares solver with linear constraints offered by Matlab (function *lsqlin*[1]) which provides the solution to least-

[1]See `https://it.mathworks.com/help/optim/ug/lsqlin.html`

squares curve fitting problems of the form:

$$\begin{aligned} \min_{\mathbf{p}} \quad & \frac{1}{2}||\mathbf{C}\cdot\mathbf{p}-\mathbf{T}||_2^2 \\ \text{s.t.} \begin{cases} \quad & \mathbf{A}\cdot\mathbf{p}\leq\mathbf{b} \\ \quad & \mathbf{A}_{\text{eq}}\cdot\mathbf{p}=\mathbf{b}_{\text{eq}} \end{cases} \end{aligned} \tag{4.1}$$

where $\mathbf{p}$ is the vector of the polynomial coefficients, $\mathbf{C}$ collects the displacement data in a matrix form according to the degree of the polynomial, and $\mathbf{T}$ collects the traction values in a vector as described in the following paragraphs.

Collecting the displacement data of the i-th cycle in column vector $\mathbf{g}_i$ with $i = 1, ..n$ and n number of cycles for the analysed tilt angle, the total displacement vector $\mathbf{g}$ reads:

$$\mathbf{g} = \begin{Bmatrix} \mathbf{g}_1 \\ \vdots \\ \mathbf{g}_i \\ \vdots \\ \mathbf{g}_n \end{Bmatrix} \tag{4.2}$$

In the same way, $\mathbf{T}$ collects the traction data in the form of a vector, by concatenation of the different cycles:

$$\mathbf{T} = \begin{Bmatrix} \mathbf{T}_1 \\ \vdots \\ \mathbf{T}_i \\ \vdots \\ \mathbf{T}_n \end{Bmatrix} \tag{4.3}$$

where $\mathbf{T}_i$ is the column vector of the traction data corresponding to the i-th cycle.

The matrix $\mathbf{C}$ collects hence the element-wise powers of $\mathbf{g}$. As an

example, in the case of a third order polynomial, $\mathbf{C}$ reads:

$$\mathbf{C} = \begin{bmatrix} \left\{\mathbf{g}\right\}^3 & \left\{\mathbf{g}\right\}^2 & \left\{\mathbf{g}\right\} & \left\{\mathbf{g}\right\}^0 \end{bmatrix} \tag{4.4}$$

The matrix $\mathbf{A}$ and $\mathbf{A}_{\text{eq}}$ are used to enforce constraints on the fitting function. The inequality constraint has been used to impose the monotonic increasing (or decreasing) of the function, while the equality condition binds the curve to pass through given couples of traction-gap values. As for the $\mathbf{C}$ matrix, $\mathbf{A}$ and $\mathbf{A}_{\text{eq}}$ collect the powers of the displacement vector, while $\mathbf{b}$ and $\mathbf{b}_{\text{eq}}$ contain the traction vectors.

The experimental curves' three phases differ for the polynomial order and variables and for the imposed constraints. Depending on which part of the experimental curves is considered in the minimization problem, only a section of the displacement data and the related traction is considered in the vectors $\mathbf{g}$ and $\mathbf{T}$.

As shown in the following paragraphs, it is necessary to also introduce the vector of the unloading displacement $\mathbf{g}^{\text{u}}$ that collects the unloading displacements of all the cycles. Since $\mathbf{g}^{\text{u}}$ must have the same length of $\mathbf{g}$, it is obtained by repeating the value of $\mathbf{g}^{\text{u}}$ of the i-th cycle a number of times equal to the number of elements of $\mathbf{g}_i$. The same procedure has been used for introducing the vector of the unloading traction $\mathbf{T}^{\text{u}}$.

4.3.1 Loading phase

The loading phase is interpolated using a third-degree polynomial expression having general expression:

$$\mathbf{P}_1(\mathbf{g}) = p_3\mathbf{g}^3 + p_2\mathbf{g}^2 + p_1\mathbf{g} + p_0 \tag{4.5}$$

The vector $\mathbf{p}$ in the minimization problem in Eq.(4.1) is hence given by $\{p_3, p_2, p_1, p_0\}^{\text{T}}$. Since the polynomial must assume zero value traction at the initial displacement, the fourth coefficient p_0 is always equal

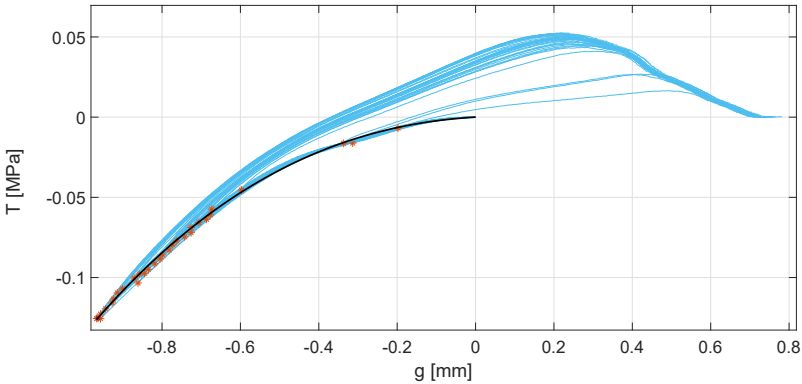

Figure 95: Loading phase interpolation curve (black line) for $\alpha = 2.5°$.

to zero. Moreover, the function is constrained to pass through the unloading traction-displacement couple of the first cycle since it has been observed that this constrain improves the fitting quality (see Figure 95, where the unloading points for all the cycles are highlighted with red asterisks).

As a second constrain, the monotonic increasing of the curve has been enforced by computing the powers of $\mathbf{g}$ related to $\mathbf{P}_1(\mathbf{g})$ in the matrix $\mathbf{A}$ as:

$$\mathbf{A} = -\begin{bmatrix} 3\left\{\mathbf{g}\right\}^2 & 2\left\{\mathbf{g}\right\} & \left\{\mathbf{g}\right\}^0 & \left\{0\right\} \end{bmatrix} \tag{4.6}$$

and $\mathbf{b}$ is a vector of zeros.

The result for $\alpha = 2.5°$ is shown in Figure 95 where the fitting curve is represented by the black line. The constraints are satisfied within the default tolerance of the Matlab function. The coefficient values found for each α are given in the Appendix A.

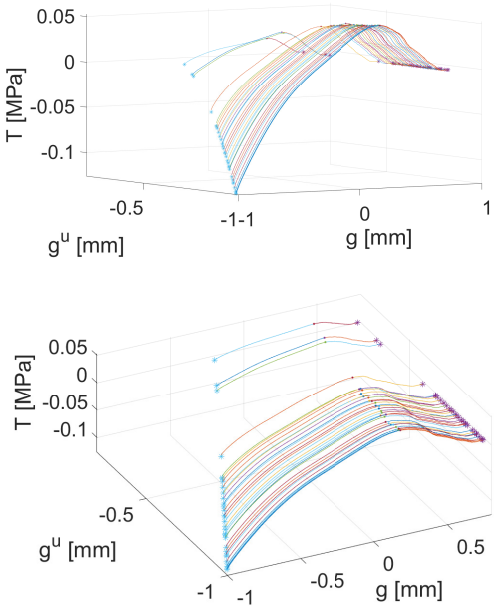

Figure 96: 3D plots of the unloading phase experimental curves for $\alpha = 2.5°$.

4.3.2 Unloading phase

The second step regards the fitting of the unloading phase. The fitting procedure of the unloading phase is complicated by the traction's dependency not only on the gap at the interface but also on the unloading displacement g^{u}. The 3D plot in Figure 96 represents the experimental curves obtained varying g^{u}, which becomes the third axis of the plot. In the same figure, the initial points, the adhesion peaks, and the final points of each curve are highlighted. These values have been collected in the vectors $\mathbf{g}^{\mathrm{u}}, \mathbf{g}^{\mathrm{ad}}$ and $\mathbf{T}^{\mathrm{ad}}$. Two different polynomial functions are used for the increasing and decreasing sections of the curves to achieve a good fitting of the data.

To improve the convergence of the algorithm used for the minimization problem, the traction values at the adhesive peak $\mathbf{T}^{\mathrm{ad}}$ have been

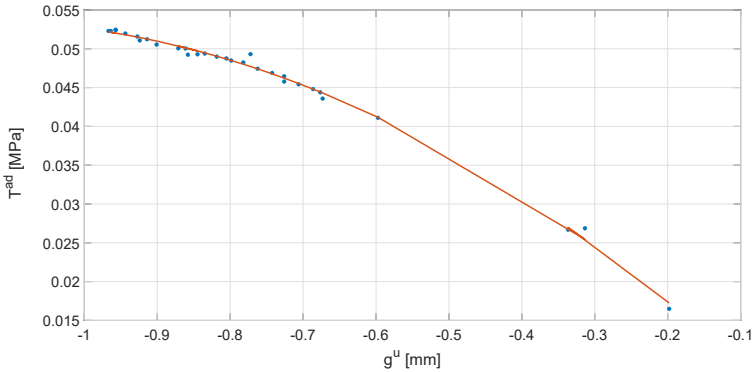

Figure 97: Fitting of the adhesion peak traction $\mathbf{T}^{\text{ad}}$ with respect to the unloading gap $\mathbf{g}^{\text{u}}$ for $\alpha = 2.5°$.

interpolated by a more regular function of the unloading displacement $\mathbf{g}^{\text{u}}$ before being used in the equality conditions. It has been noticed that a second-order polynomial function can reproduce very well the experimental values, see Figure 97. Hence, the fitting function for this case reads:

$$\mathbf{Q}_1(\mathbf{g}) = q_2(\mathbf{g}^{\text{u}})^2 + q_1\mathbf{g}^{\text{u}} + q_0 \tag{4.7}$$

The polynomial coefficients found using Eq.(4.1) without constraints are given in the Appendix A.

Going back to the unloading phase fitting procedure, the chosen functions are polynomials of fifth degree in $\mathbf{g}$ and second degree in $\mathbf{g}^{\text{u}}$ having the following general expression:

$$\begin{aligned}\mathbf{P}_i(\mathbf{g},\mathbf{g}^{\text{u}}) =& p_{00} + p_{10}\mathbf{g} + p_{01}\mathbf{g}^{\text{u}} + p_{20}\mathbf{g}^2 + p_{11}\mathbf{g}\circ\mathbf{g}^{\text{u}} + p_{02}(\mathbf{g}^{\text{u}})^2 + p_{30}\mathbf{g}^3 + \\ & p_{21}\mathbf{g}^2\circ\mathbf{g}^{\text{u}} + p_{12}\mathbf{g}\circ(\mathbf{g}^{\text{u}})^2 + p_{40}\mathbf{g}^4 + p_{31}\mathbf{g}^3\circ\mathbf{g}^{\text{u}} + p_{22}\mathbf{g}^2\circ(\mathbf{g}^{\text{u}})^2 + \\ & p_{50}\mathbf{g}^5 + p_{41}\mathbf{g}^4\circ\mathbf{g} + p_{32}\mathbf{g}^3\circ(\mathbf{g}^{\text{u}})^2\end{aligned} \tag{4.8}$$

where $\circ$ represents the element-wise product, and the index i assumes the value 2 for the increasing phase and 3 for the decreasing phase.

The Eq. (4.1) provides the coefficients vectors for the increasing and the decreasing sections of the unloading phase, specified in the Appendix A

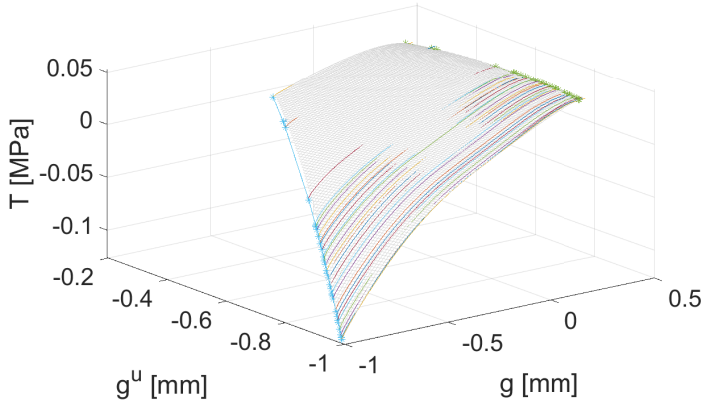

Figure 98: Experimental curves and fitting surface for the increasing section of the unloading phase for $\alpha = 2.5°$.

for each α. The fitting surfaces are in Figure 98 for the increasing section and in Figure 99.

The fifteen coefficients for the increasing phase have been computed using Eq. 4.1 imposing the equality constraints at the unloading points, represented by blue asterisks in Figure 98, and at the adhesion peaks, represented by green asterisks in the same plot.

For the decreasing section, the chosen constraints are the equality condition at the maximum tractions (green asterisks in Figure 99) and the inequality condition for the fitting surface's monotonic behavior, which must decrease towards zero till the critical displacement (purple asterisks in Figure 99). This condition has been computed considering the derivative of $\mathbf{P}_3(\mathbf{g}, \mathbf{g}^u)$ with respect to $\mathbf{g}$.

In both cases, the experimental tractions at the adhesion peaks are substituted by the interpolated values using the polynomial in Eq. (4.7). Finally, the complete interface model for a given angle α assumes the form summarised in Table 13 and the final result is shown in Figure 100 for $\alpha = 2.5°$.

To better compare the obtained surface and the experimental data, the result is shown also in the form of a 2D plot in Figure 101, by fixing

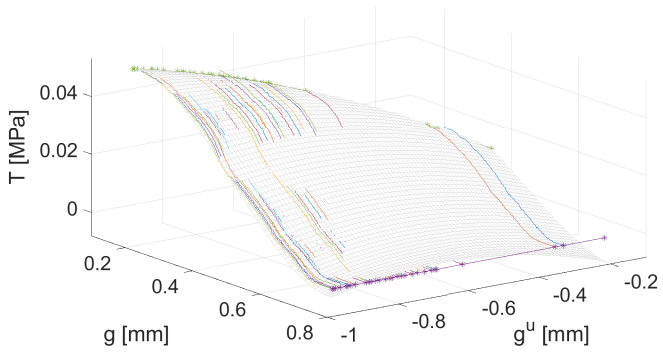

Figure 99: Experimental curves and fitting surface for the decreasing section of the unloading phase for $\alpha = 2.5°$.

Phase	General Form	Intervals	Polynomial order	Number of coefficients
Loading	$\mathbf{T} = P_1(\mathbf{g}, \alpha)$	$\mathbf{g}^{\mathrm{u}} < \mathbf{g} \leq 0$	3^{rd} order in $\mathbf{g}$	4
Increasing Unloading	$\mathbf{T} = P_2(\mathbf{g}, \mathbf{g}^{\mathrm{u}}, \alpha)$	$\mathbf{g}^{\mathrm{u}} \leq \mathbf{g} < \mathbf{g}^{\mathrm{ad}}$	5^{th} order in $\mathbf{g}$ and 2^{nd} order in $\mathbf{g}^{\mathrm{u}}$	15
Decreasing Unloading	$\mathbf{T} = P_3(\mathbf{g}, \mathbf{g}^{\mathrm{u}}, \alpha)$	$\mathbf{g}^{\mathrm{ad}} \leq \mathbf{g} \leq \mathbf{g}^{\mathrm{max}}$	5^{th} order in $\mathbf{g}$ and 2^{nd} order in $\mathbf{g}^{\mathrm{u}}$	15

Table 13: Summary of the different fitting polynomials used for the interface constitutive model.

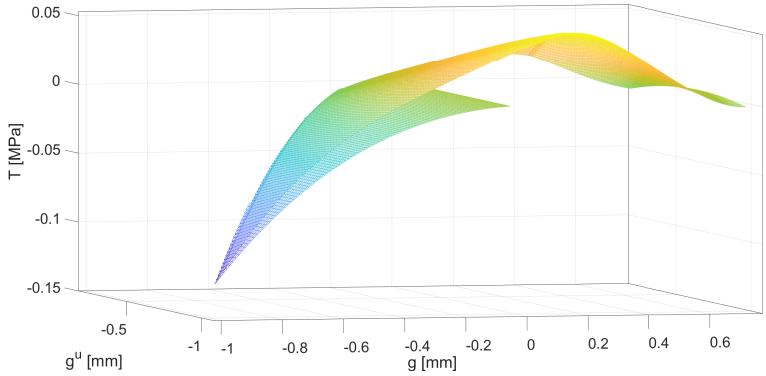

Figure 100: 3D Fitting Surface obtained for $\alpha = 2.5°$.

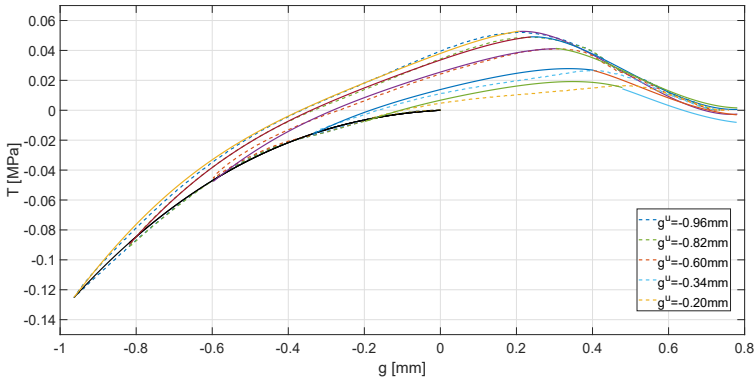

Figure 101: Experimental curves in dashed line are compared with the fitting curves for $\alpha = 2.5°$ and for given values of $\mathbf{g}^{\mathrm{u}}$.

the value of $\mathbf{g}^{\mathrm{u}}$ for each curve.

4.4 Interface Finite Element formulation

The kinematics of the interface finite element follows the same procedure illustrated in Section 3.4.1. Here, the contribution of the interface at the internal virtual work is recalled together with the contribution at the element tangent matrix:

$$\mathbf{R}_e^{(k)} = \int_{\Gamma_e^*} \mathbf{L}^{\mathrm{T}}\mathbf{N}^{\mathrm{T}}\mathbf{R}^{\mathrm{T}}\mathbf{T}\,\mathrm{d}\Gamma, \tag{4.9a}$$

$$\mathbf{K}_e^{(k)} = \int_{\Gamma_e^*} \mathbf{L}^{\mathrm{T}}\mathbf{N}^{\mathrm{T}}\mathbf{R}^{\mathrm{T}}\mathbb{C}\mathbf{R}\mathbf{N}\mathbf{L}\,\mathrm{d}\Gamma, \tag{4.9b}$$

Let us consider a generic time-step t of a quasi-static finite element analysis. The interface finite element routine provides the tangential and normal components of the gap vector, g_t and g_n which allow to compute

the local tilt angle α as:

$$\alpha = \begin{cases} \arctan\left(\left|\dfrac{g_t}{g_n}\right|\right) & \text{if } g_n \neq 0 \\ 90^\circ & \text{if } g_n = 0 \\ 0 & \text{if } g_n = 0 \,\text{and}\, g_t = 0 \end{cases} \tag{4.10}$$

The conditions and the absolute value are necessary to get $\alpha \in [0, 90^\circ]$ since the considered experimental angles are assumed to be always positive, and the results are symmetrical with respect to the central vertical axis.

The local tilt angle is compared with the known experimental angles $\bar{\alpha} = \{0^\circ, 0.5^\circ, 1^\circ, 1.5^\circ, 2^\circ, 2.5^\circ, 3^\circ, 3.5^\circ, 4^\circ\}$, evaluating the interval for which $\alpha \in [\bar{\alpha}_1, \bar{\alpha}_2]$. The notation with $\bar{\square}$ is here introduced to distinguish the quantities obtained through the analysis of the experimental data and the quantities computed during the FE simulation at the element level. In the case of a local tilt angle greater than 4°, the analyzed interval is $[4^\circ,\, 90^\circ]$ and the traction contribution related to the tilt angle 90° is supposed to be equal to zero.

The modulus of the gap vector is needed as well, and it reads:

$$g = \sqrt{g_n^2 + g_t^2} \tag{4.11}$$

The interface law described in the previous Section considers the gap to be negative during the unloading phase, and then it spans from negative to positive values in the unloading phase. For this reason, the gap value used as input in the interface law subroutine must account for the sign as well: the gap g is considered to be negative if $g_n < 0$ and positive if $g_n > 0$.

The interface element subroutine contains the information regarding the experimental critical displacements, $\bar{g}^{\mathrm{u}}$, $\bar{g}^{\mathrm{ad}}$ and $\bar{g}^{\mathrm{max}}$ for each angle $\bar{\alpha}$ to be compared with the simulation gap g. The routine also stores all the polynomial function coefficients and expressions necessary to compute the traction vector according to the gap.

To obtain the correct traction value for a given gap g, it is essential to identify if the interface is in the loading or unloading phase. In the

latter case, it is also necessary to know the unloading displacement g^{u}. For this purpose, two history variables are introduced at each integration point: g_{hist} containing the gap g of the previous timestep $t-1$, and $g^{\mathrm{u}}_{\mathrm{hist}}$ containing the unloading gap g^{u}. While the variable g_{hist} is updated at each timestep, the variable $g^{\mathrm{u}}_{\mathrm{hist}}$ is updated only during the loading phase such that it remains available for the following unloading phase.

With these inputs, the traction values $\mathrm{T}_1(g, g^{\mathrm{u}}, \bar{\alpha}_1)$ and $\mathrm{T}_2(g, g^{\mathrm{u}}, \bar{\alpha}_2)$ are computed selecting the appropriate polynomial expressions according to the intervals in Table 13. The derivative of the traction with respect to g, necessary for the tangent stiffness matrix of the element, is computed using the analytical derivative of the polynomial fitting functions. Subsequently, the traction values are linearly interpolated to obtain the traction T and $\frac{\partial \mathrm{T}}{\partial g}$ for the angle α. The sign of the traction T derives directly from the fitting function.

The final step of the element routine regards the computation of the traction components τ and σ, and the tangent stiffness matrix $\mathbb{C}$. The traction components are evaluated as:

$$\sigma = \mathrm{T}\cos(\alpha) \tag{4.12a}$$

$$\tau = \mathrm{T}\sin(\alpha) \tag{4.12b}$$

The interface tangent stiffness matrix has components:

$$\mathbb{C} = \begin{bmatrix} \dfrac{\partial \tau}{\partial g_t} & \dfrac{\partial \tau}{\partial g_n} \\ \dfrac{\partial \sigma}{\partial g_t} & \dfrac{\partial \sigma}{\partial g_n} \end{bmatrix}, \tag{4.13}$$

Since the polynomial functions allow the direct computation of the derivative of T with respect to the gap g, the stiffness matrix components

have been derived as:

$$\frac{\partial \tau}{\partial g_t} = \frac{\partial (\mathrm{T}\sin(\alpha))}{\partial g_t} = \frac{\partial \mathrm{T}}{\partial g_t}\sin(\alpha) + \mathrm{T}\frac{\partial \sin(\alpha)}{\partial g_t} \tag{4.14a}$$

$$\frac{\partial \tau}{\partial g_n} = \frac{\partial (\mathrm{T}\sin(\alpha))}{\partial g_n} = \frac{\partial \mathrm{T}}{\partial g_n}\sin(\alpha) + \mathrm{T}\frac{\partial \sin(\alpha)}{\partial g_n} \tag{4.14b}$$

$$\frac{\partial \sigma}{\partial g_t} = \frac{\partial (\mathrm{T}\cos(\alpha))}{\partial g_t} = \frac{\partial \mathrm{T}}{\partial g_t}\cos(\alpha) + \mathrm{T}\frac{\partial \cos(\alpha)}{\partial g_t} \tag{4.14c}$$

$$\frac{\partial \sigma}{\partial g_n} = \frac{\partial (\mathrm{T}\cos(\alpha))}{\partial g_n} = \frac{\partial \mathrm{T}}{\partial g_n}\cos(\alpha) + \mathrm{T}\frac{\partial \cos(\alpha)}{\partial g_n} \tag{4.14d}$$

Exploiting the chain rule for the derivation, the equations become:

$$\frac{\partial \mathrm{T}}{\partial g_t} = \frac{\partial \mathrm{T}}{\partial g}\frac{\partial g}{\partial g_t} \tag{4.15a}$$

$$\frac{\partial \mathrm{T}}{\partial g_n} = \frac{\partial \mathrm{T}}{\partial g}\frac{\partial g}{\partial g_n} \tag{4.15b}$$

Moreover, the derivatives of g are computed considering that the gap is obtained through the Eq. 4.11:

$$\frac{\partial g}{\partial g_t} = \frac{\partial (\sqrt{g_t^2 + g_n^2})}{\partial g_t} = \frac{g_t}{\sqrt{g_t^2 + g_n^2}} \tag{4.16a}$$

$$\frac{\partial g}{\partial g_n} = \frac{\partial (\sqrt{g_t^2 + g_n^2})}{\partial g_n} = \frac{g_n}{\sqrt{g_t^2 + g_n^2}} \tag{4.16b}$$

As last step, the chain rule is applied also to obtain the derivative of the trigonometric functions of α with respect to the gap components obtaining:

$$\frac{\partial \sin(\alpha)}{\partial g_t} = \frac{g_n^2}{(g_t^2 + g_n^2)^{\frac{3}{2}}} \tag{4.17a}$$

$$\frac{\partial \sin(\alpha)}{\partial g_n} = \frac{-g_n g_t}{(g_t^2 + g_n^2)^{\frac{3}{2}}} \tag{4.17b}$$

$$\frac{\partial \cos(\alpha)}{\partial g_t} = \frac{-g_n g_t}{(g_t^2 + g_n^2)^{\frac{3}{2}}} \tag{4.17c}$$

$$\frac{\partial \cos(\alpha)}{\partial g_n} = \frac{g_t^2}{(g_t^2 + g_n^2)^{\frac{3}{2}}} \tag{4.17d}$$

The final form of the stiffness matrix components is hence obtained by substituting Eqs. 4.16,4.15 and 4.17 in 4.14:

$$\mathbb{C}_{1,1} = \frac{\partial \mathrm{T}}{\partial g} \frac{g_t}{\sqrt{g_t^2 + g_n^2}} + \mathrm{T} \frac{g_n^2}{(g_t^2 + g_n^2)^{\frac{3}{2}}} \tag{4.18a}$$

$$\mathbb{C}_{1,2} = \frac{\partial \mathrm{T}}{\partial g} \frac{g_n}{\sqrt{g_t^2 + g_n^2}} + \mathrm{T} \frac{-g_n g_t}{(g_t^2 + g_n^2)^{\frac{3}{2}}} \tag{4.18b}$$

$$\mathbb{C}_{2,1} = \frac{\partial \mathrm{T}}{\partial g} \frac{g_t}{\sqrt{g_t^2 + g_n^2}} + \mathrm{T} \frac{-g_n g_t}{(g_t^2 + g_n^2)^{\frac{3}{2}}} \tag{4.18c}$$

$$\mathbb{C}_{2,2} = \frac{\partial \mathrm{T}}{\partial g} \frac{g_n}{\sqrt{g_t^2 + g_n^2}} + \mathrm{T} \frac{g_t^2}{(g_t^2 + g_n^2)^{\frac{3}{2}}} \tag{4.18d}$$

The algorithm of the presented interface finite element is summarised in Algorithms 5, 6 and 7. The Algorithm 5 contains the overall structure of the interface finite element starting from the computation of the local tilt angle α and the gap g to the element residual vector and the stiffness matrix, while Algorithms 6 and 7 focus on the evaluation of the interface traction. In particular Algorithm 6 linearly interpolates the values of T and $\dfrac{\partial \mathrm{T}}{\partial g}$ computed in Algorithm 7 for $\bar{\alpha}_1$ and $\bar{\alpha}_2$.

In the following algorithms, with the aim of shortening the notation, the partial derivatives of a variable $\square$ with respect to the gap g have been written as $\square_{,g}$. Moreover, it can be observed that Algorithm 7 computes the values of traction also in the case of $g < g^{\mathrm{u}}$, but raises a warning since the fitting function might not be accurate for such interval.

Algorithm 5: Interface finite element for MSAMSs

Input : Iteration number inside the Newton-Raphson scheme (k), Nodal coordinates $\mathbf{x}$, Nodal displacement $\mathbf{d}$, Gauss quadrature weights w_{igp}, History variables $\mathcal{H}_{st1}, \mathcal{H}_{st2}$, Vector of $\bar{\boldsymbol{\alpha}}$,

For each $\bar{\alpha}$: unloading displacement $\bar{g}^{\mathrm{u}}$, adhesion peak displacement $\bar{g}^{\mathrm{ad}}$, critical displacement $\bar{g}^{\max}$, parameters of the fitting functions $\mathbf{P}_1(g)$, $\mathbf{Q}_1(g)$, $\mathbf{P}_2(g, g^{\mathrm{u}})$ and $\mathbf{P}_3(g, g^{\mathrm{u}})$, parameters of the derivatives of the fitting functions $\mathbf{P}_{1,g}(g)$, $\mathbf{P}_{2,g}(g, g^{\mathrm{u}})$ and $\mathbf{P}_{3,g}(g, g^{\mathrm{u}})$.

Initialization: Gauss points index igp, $\mathbf{g}_{igp} = [g_{\mathrm{t}}, g_{\mathrm{n}}]^{\mathrm{T}}$, $\mathbf{T}_{igp} = [\tau, \sigma]^{\mathrm{T}}$, $\mathbb{C}$, α, $\bar{\alpha}_1$, $\bar{\alpha}_2$.

for $igp \leftarrow 1$ **to** 2 **do**

- Compute $detJ$, $\mathbf{N}$, $\mathbf{L}$, $\mathbf{R}$
- $\mathbf{g}_{igp} \leftarrow \mathbf{RNLd}$
- $g \leftarrow \mathrm{sign}(g_n)\sqrt{g_t^2 + g_n^2}$
- $g_{hist} \leftarrow \mathcal{H}_{st1,igp}$
- $g^{\mathrm{u}}_{hist} \leftarrow \mathcal{H}_{st2,igp}$
- **if** $g_{\mathrm{n}} == 0$ ***and*** $g_{\mathrm{t}} \neq 0$ **then**
  - $\alpha \leftarrow \pi/2$
- **else**
  - $\alpha \leftarrow \arctan\left(\left|\frac{g_t}{g_n}\right|\right)$
- **end**
- **if** $\alpha < \pi/2$ **then**
  - Computing interval $\bar{\alpha}_1 \leq \alpha \leq \bar{\alpha}_2$
  - Call procedure ***Traction Evaluation***:
  - **begin**
    - **Input :** g, g_{hist}, g^{u}_{hist}, α, $\bar{\alpha}_1$, $\bar{\alpha}_2$, Parameters of the fitting functions and derivatives, $\bar{g}^{\mathrm{u}}(\bar{\alpha})$, $\bar{g}^{\mathrm{ad}}(\bar{\alpha})$, $\bar{g}^{\max}(\bar{\alpha})$
    - See Algorithm 6
    - **Output:** Traction T, derivative $\mathrm{T}_{,g}$
  - **end**
  - $\sigma \leftarrow \mathrm{T}\cos(\alpha)$
  - $\tau \leftarrow \mathrm{T}\sin(\alpha)$
  - Computing $\mathbb{C}$ according to Eq.(4.18)
  - $\mathcal{H}_{st1,igp} \leftarrow g$ (at convergence)
  - $\mathcal{H}_{st2,igp} \leftarrow \min\{g, g^{\mathrm{u}}_{hist}\}$ (at convergence)
- **end**
- $\mathbf{R}_e^{(k)} \leftarrow \mathbf{R}_e^{(k)} + \mathbf{L}^T\mathbf{N}^T\mathbf{R}^T\mathbf{T}_{igp}w_{igp}detJ$
- $\mathbf{K}_e^{(k)} \leftarrow \mathbf{K}_e^{(k)} + \mathbf{L}^T\mathbf{N}^T\mathbf{R}^T\mathbb{C}\mathbf{RNL}w_{igp}detJ$

end

Output: Residual vector $\mathbf{R}_e^{(k)}$, Stiffness Matrix $\mathbf{K}_e^{(k)}$

Algorithm 6: Subroutine computing T and $\mathrm{T}_{,g}$

Input : g, g_{hist}, g^{u}_{hist}, α, $\bar{\alpha}_1$, $\bar{\alpha}_2$, Parameters of the fitting functions and their derivatives, $\bar{g}^{\mathrm{u}}(\bar{\alpha})$, $\bar{g}^{\mathrm{ad}}(\bar{\alpha})$, $\bar{g}^{\max}(\bar{\alpha})$

Initialization: T_1, T_2, $\mathrm{T}_{1,g}$, $\mathrm{T}_{2,g}$

$g^{\mathrm{ad}} \leftarrow \bar{g}^{\mathrm{ad}}(\bar{\alpha}_1)$

$g^{\max} \leftarrow \bar{g}^{\max}(\bar{\alpha}_1)$

$g^{\mathrm{u}} \leftarrow \bar{g}^{\mathrm{u}}(\bar{\alpha}_1)$

Call subroutine with $\bar{\alpha}_j = \bar{\alpha}_1$:

begin

  Input : $\bar{\alpha}_1$, g, g_{hist}, g^{u}_{hist}, Coefficients of the fitting functions and their derivatives, g^{u}, g^{ad}, $g^{\max}$

  See Algorithm 7

  Output: Traction T_1, derivative $\mathrm{T}_{1,g}$

end

$g^{\mathrm{ad}} \leftarrow \bar{g}^{\mathrm{ad}}(\bar{\alpha}_2)$

$g^{\max} \leftarrow \bar{g}^{\max}(\bar{\alpha}_2)$

$g^{\mathrm{u}} \leftarrow \bar{g}^{\mathrm{u}}(\bar{\alpha}_2)$

if $\bar{\alpha}_2 \neq \pi/2$ **then**

  Call subroutine with $\bar{\alpha}_j = \bar{\alpha}_2$:

  begin

    Input : $\bar{\alpha}_2$, g, g_{hist}, g^{u}_{hist}, Coefficients of the fitting functions and their derivatives, g^{u}, g^{ad}, $g^{\max}$

    See Algorithm 7

    Output: Traction T_2, derivative $\mathrm{T}_{2,g}$

  end

else

  $\mathrm{T}_2 \leftarrow 0$

  $\mathrm{T}_{2,g} \leftarrow 0$

end

$$\mathrm{T} \leftarrow \frac{\alpha - \bar{\alpha}_2}{\bar{\alpha}_1 - \bar{\alpha}_2}\mathrm{T}_1 - \frac{\alpha - \bar{\alpha}_2}{\bar{\alpha}_1 - \bar{\alpha}_2}\mathrm{T}_1$$

$$\mathrm{T}_{,g} \leftarrow \frac{\alpha - \bar{\alpha}_2}{\bar{\alpha}_1 - \bar{\alpha}_2}\mathrm{T}_{1,g} - \frac{\alpha - \bar{\alpha}_2}{\bar{\alpha}_1 - \bar{\alpha}_2}\mathrm{T}_{2,g}$$

Output: Traction T, derivative $\mathrm{T}_{,g}$

Algorithm 7: Subroutine T_j and $\mathrm{T}_{j,g}$ for a given $\bar{\alpha}_j$

Input : $\bar{\alpha}_j$, g, g_{hist}, g^{u}_{hist}, Coefficients of the fitting functions and their derivatives, g^{u}, g^{ad}, g^{max}

Initialization: T_j, $\mathrm{T}_{j,g}$

if $g < g^{max}$ **then**

  if $g == 0$ ***and*** $g_{hist} == 0$ **then**

    $\mathrm{T}_j \leftarrow 0$

    $\mathrm{T}_{j,g} \leftarrow 0$

  else if $g < 0$ ***and*** $|g_{hist}| \leq |g|$ **then**

    $\mathrm{T}_j \leftarrow \mathbf{P}_1(g, \bar{\alpha}_1)$

    $\mathrm{T}_{j,g} \leftarrow \mathbf{P}_{1,g}(g, \bar{\alpha}_1)$

    if $g < g^u$ **then**

      Raise a warning: *"Computed quantities might be incorrect since $g < g^u$."*

    end

  else

    if $g \leq g^{ad}$ **then**

      $\mathrm{T}_j \leftarrow \mathbf{P}_2(g, g^{\mathrm{u}}_{\mathrm{hist}}, \bar{\alpha}_1)$

      $\mathrm{T}_{j,g} \leftarrow \mathbf{P}_{2,g}(g, g^{\mathrm{u}}_{\mathrm{hist}}, \bar{\alpha}_1)$

    else

      $\mathrm{T}_j \leftarrow \mathbf{P}_3(g, g^{\mathrm{u}}_{\mathrm{hist}}, \bar{\alpha}_1)$

      $\mathrm{T}_{j,g} \leftarrow \mathbf{P}_{3,g}(g, g^{\mathrm{u}}_{\mathrm{hist}}, \bar{\alpha}_1)$

    end

else

  $\mathrm{T}_j \leftarrow 0$

  $\mathrm{dT}_j \leftarrow 0$

end

Output: Traction T_j, derivative $\mathrm{T}_{j,g}$

4.5 Numerical results

The finite element formulation, coded as a new user element for the FE program FEAP, has been tested using a simple benchmark model to reproduce the experimental results. The model consists of two square blocks meshed with standard 4-node linear finite elements and separated by the novel interface finite element. The geometry and boundary conditions are shown in Figure 102. The two solids have been considered almost rigid compared to the interface and with the same material parameters: Young's moduli $E_1 = E_2 = 1000\mathrm{MPa}$ and Poisson ratios $\nu_1 = \nu_2 = 0.45$, where the subscripts 1 and 2 refers to the lower and upper block respectively.

The simulation is conducted under displacement control imposing vertical and horizontal displacements on the upper edge such that the far-field tilt angle is known and can be compared with the experimental $\bar{\alpha}$. The normal and the tangential components of the reaction force are computed and compared with the experimental curves. As in the experiments, the simulation considers a loading phase by pressing the upper block against the lower one and then an unloading phase until the interface's complete failure. Since the two solids are almost rigid compared to the interface, the tilt angle applied through the displacement components imposed at the upper edge is equal to the local tilt angle.

The results for a tilt angle equal to 2.5° are provided in Figures 103 and 104 and compared with the experimental data and the fitting functions for different values of $\mathbf{g}^{\mathrm{u}}$. As expected, the model reproduces exactly the fitting functions, and it is in excellent agreement with the experimental data.

More complex simulations have been considered to evaluate the method's potentiality, starting from testing the efficiency of the model for tilt angles that have not been tested during the experimental campaign.

The traction-displacement curves for increasing values of α are shown in Figure 105 for for the normal direction and in Figure 106 for the tangential one. The same unloading displacement has been used for all the simulations; however, the normal and tangent components of the un-

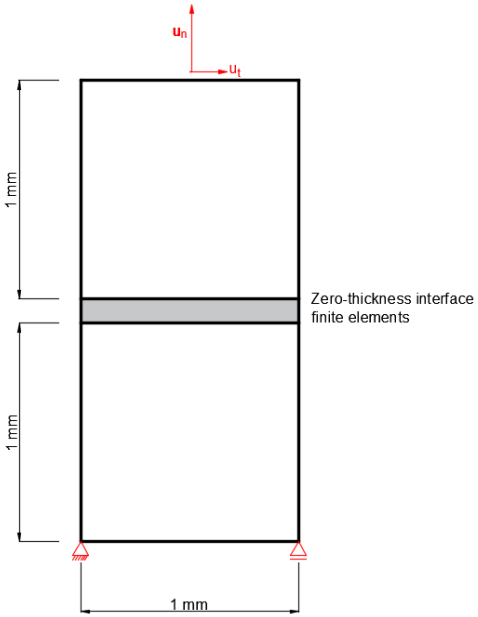

Figure 102: Benchmark test geometry and boundary conditions with one single interface finite element.

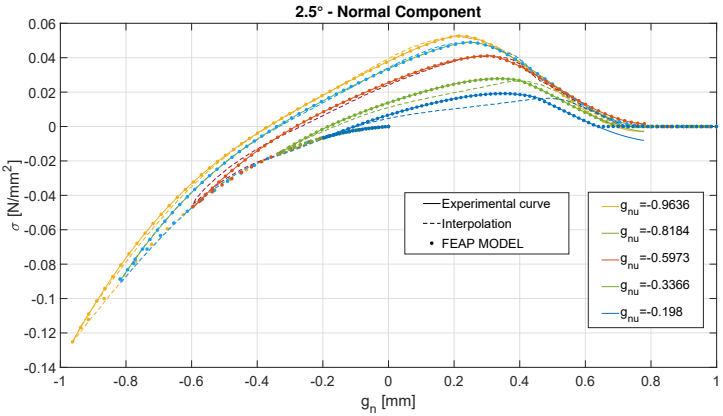

Figure 103: Numerical simulation results for the normal direction compared to experimental and fitting functions for different g^{u} and $\alpha = 2.5°$.

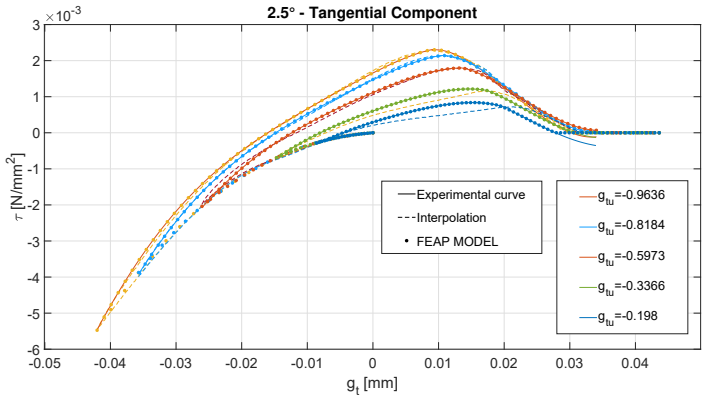

Figure 104: Numerical simulation results for the tangential direction compared to experimental and fitting functions for different g^{u} and $\alpha = 2.5°$.

loading displacements, u_n and u_t are different for the reported curves because of the different tilt angles. The curves with α equal to $\{\, 0.2°, 0.8°, 1.2° \,\}$ have been obtained through linear interpolation of the known experimental angles, reported in the same plot for comparison. The chosen linear interpolation captures the experimental dependence of the traction on the applied tilt angle with good results.

The proposed computational framework can also model a more realistic application of the MSAMSs adhesive, for example, the simulation of a polymeric layer's bond to a glass substrate through the mushroom-shaped adhesive. In fact, the following simulation has been inspired by the use of MSAMSs adhesives to realize adhesive gloves for climbing vertical walls. These applications rely on the tilt angle variation to quickly release the gloves from the wall since the detachment force is strictly connected to the peeling angle. Hence, the proposed formulation must correctly capture the force variation with the tilt angle variation over time.

The finite element model used for this simulation is shown in Figure 107 and consists of a glass substrate layer with Young's Modulus equal to $70\mathrm{GPa}$ and Poisson ratio equal to 0.3, and an upper polymeric layer in ABS (acrylonitrile butadiene styrene) having $E = 3200\mathrm{MPa}$ and

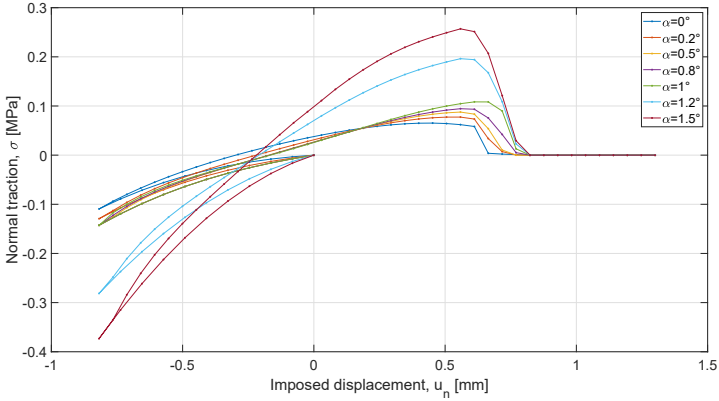

Figure 105: Normal traction-displacement curves for different values of α.

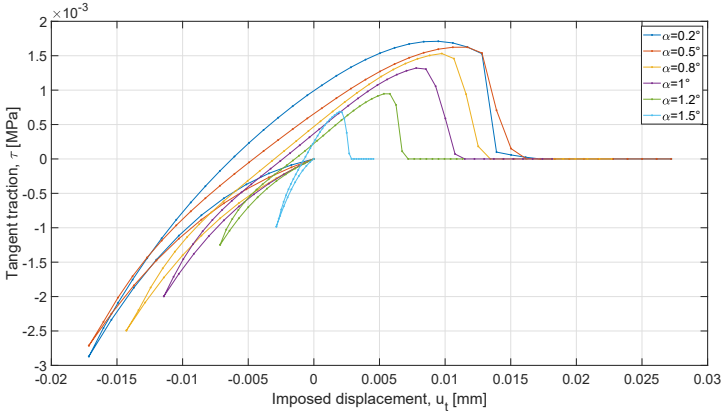

Figure 106: Tangential traction-displacement curves for different values of α.

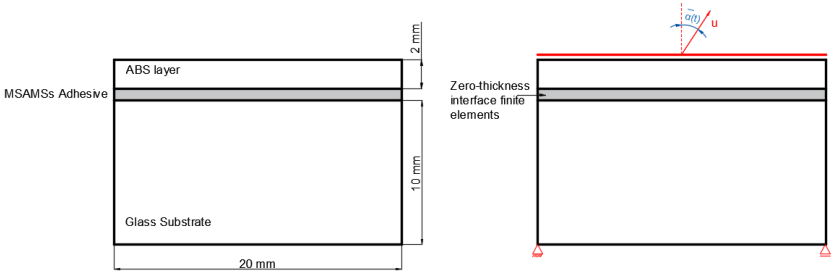

Figure 107: FEM Model for a peeling test of MSAMSs adhesive bonding an ABS layer to a glass substrate.

$\nu = 0.3$. The simulation has been conducted in a quasi-static framework with the far-field $\bar{\alpha}$ depending on the current timestep.

The mesh consists of standard 4-node elements for the two bulk solids having $h = 0.17\text{mm}$ resulting in 120 elements along the interface.

After the loading phase with a constant tilt angle $\alpha = 1°$, the interface has been tested considering firstly an increasing tilt angle and secondly a decreasing behavior. The results have been hence compared with a constant angle peeling. The tilt angle evolution has been controlled by checking the local tilt angle at the interface at the last integration point, as underlined in Figure 108 and it has have been plotted in Figure 109. In this latter plot, it can be noticed that after the loading phase with the local α equal to the constant value $1°$, the blue curve identifies the simulation with the increasing tilt angle, and the red curve represents the decreasing behaviour.

Figure 110 shows the displacement field magnitude of the structure for the case with constant α at different time-steps: the initial configuration in Figure 110(a), the end of the loading phase (b) and the unloading steps (c)-(e).

The simulation results in terms of reaction force vs imposed displacements are shown in Figure 111 and Figure 112 in terms of normal components and tangential components respectively for the simulations with constant tilt angle equal to $1°$ (green curve), and for the increasing (blue curve) and decreasing α (red curve) plotted in Figure 109. As expected,

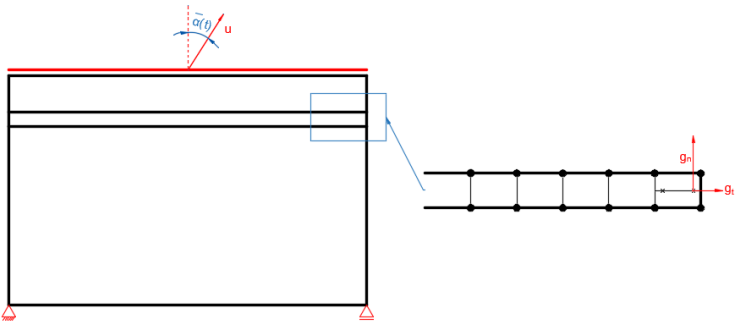

Figure 108: The local tilt angle for an integration point of the interface is obtained as in Eq. (4.10) using the values of g_n and g_t.

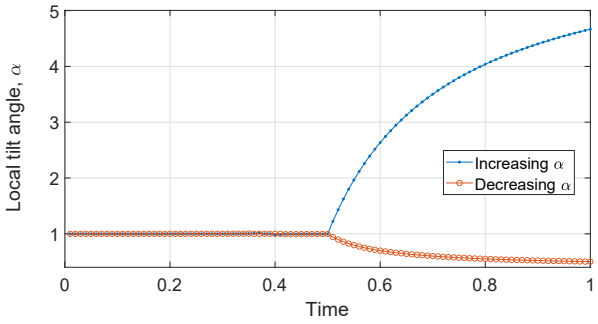

Figure 109: Variation of the local tilt angle α during the peeling tests.

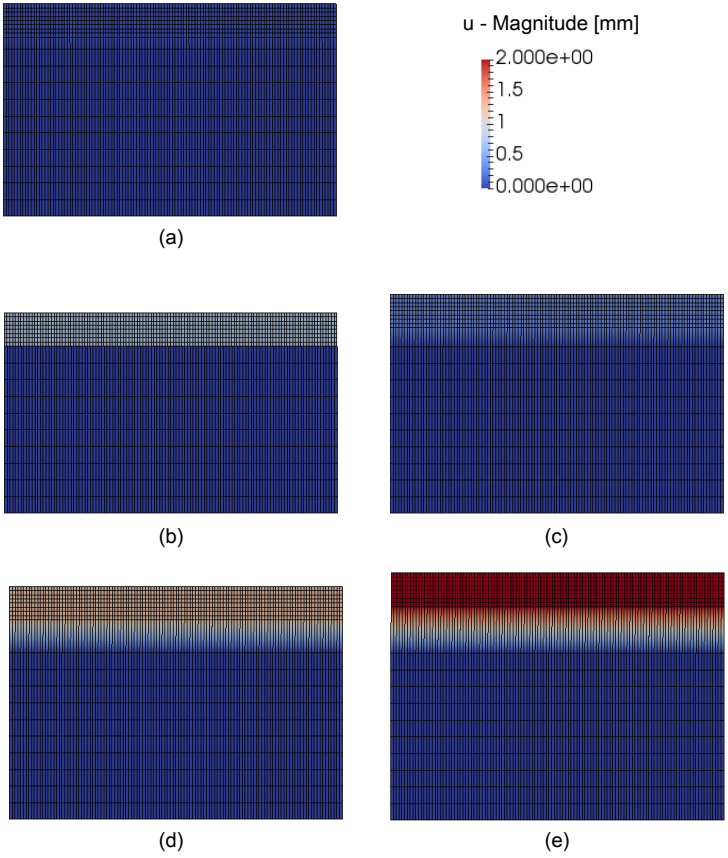

Figure 110: Snapshots of the simulation with $\alpha = 1$ showing the magnitude of the displacement field. The initial configuration is represented in (a), while the following time-steps correspond to the imposed displacement $u = -0.8\text{mm}$ (b), $u = 0.30\text{mm}$ (c), $u = 1.16\text{mm}$ (d), and $u = 2.00\text{mm}$ (e).

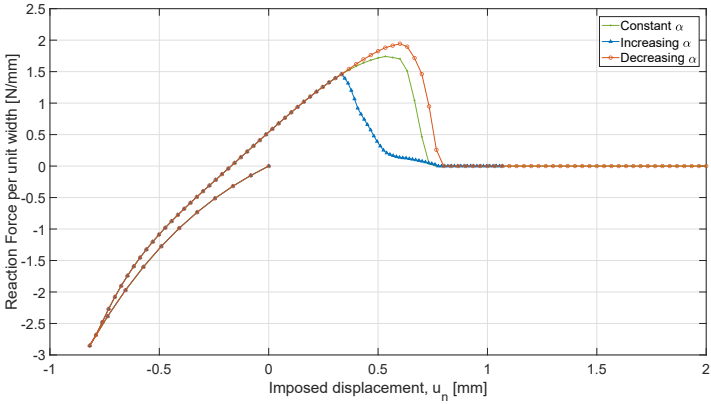

Figure 111: Normal components of the force-displacement curve for the peeling test with α varying during the simulation.

the tangential components increase for decreasing values of the tilt angle; however, the peeling response is mainly dominated by the normal components because of the considered angles' low values.

A better comprehension of the result can be achieved by looking at Figure 113 where the results are plotted in terms of the magnitude of the force and displacement values without the decomposition in normal and tangential directions. It can be observed that the required peeling force decreases for increasing α, corresponding to an easier detachment of the mushroom-shaped adhesive.

Hence, the zero-thickness interface element can be a valuable tool for simulations of industrial applications of mushroom-shaped adhesives without the necessity of expensive computational models involving a detailed discretization of the surface microstructures.

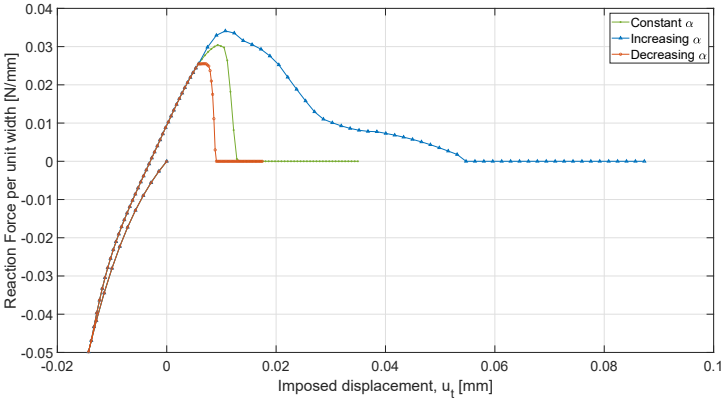

Figure 112: Tangential components of the force-displacement curve for the peeling test with α varying during the simulation.

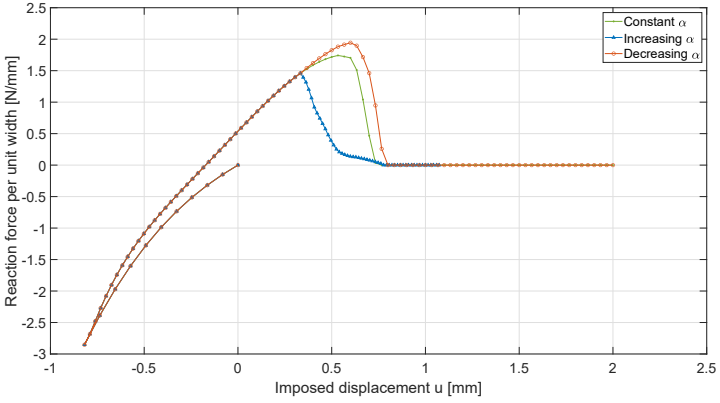

Figure 113: Force-displacement curve for the peeling test with α varying during the simulation.

Chapter 5

A phase-field approach for crack propagation in layered structures with rubber-like materials

In line with previous contents in this Thesis, adhesive joints models often consider the adhesive layer as an interface between the adherends, see references [94, 95]. However, in many applications, the adhesive layer behaves as a bulk layer that can experience large deformations and high-stress states and gives rise to cracks, especially for an adhesive thickness comparable with the thickness of the components. In the latter case, thick adhesive joints belong to the broader range of mechanical joints with layered heterogeneous structures. The simulation of joint failure requires hence a more detailed model, based not only on the interface properties, being the main target of the current Chapter.

Among the applications, in solar energy production devices, most of the silicone-based adhesives show a hyperelastic material behavior as many other rubber-like materials which are characterized by a relatively low elastic modulus and high bulk modulus. Moreover, in many industrial applications, hyperelastic materials are used as substrate for

more rigid components with linear elastic behavior, featuring thin layer-substrate systems. The present chapter aims at formulating a numerical tool for the fracture simulation of structural joints with rubber-like components.

The contents of the present Chapter commence with a short description of the large strain theory quantities used to describe the kinematics of hyperelastic material in Section 5.1. Note that for the sake of brevity, this document exclusively includes the concepts that are required in order to understand the following sections, while other theory details can be found in many continuum mechanics textbooks and treatises, see [114], [115], among many others. The fracture behavior of materials subject to large deformation is described in Section 5.2, introducing the phase-field approach for Fracture Mechanics simulations. The final Section (5.3) exploits this method to evaluate the crack propagation of bi-layered structure with Neo-Hookean material.

Nomenclature

Ω_0	Body domain in the initial configuration
$\mathbf{O}\mathbf{e}_1\mathbf{e}_2\mathbf{e}_3$	Reference system
Ω	Body domain in the current configuration
$\mathbf{X}$	Position vector with respect to the initial configuration
t	Generic time-step
$\mathbf{x}$	Position vector with respect to the current configuration
$\boldsymbol{\varphi}$	Nonlinear deformation map
$\mathbf{u}$	Displacement vector
$\mathbf{F}$	Deformation gradient
J	determinant of $\mathbf{F}$, Jacobian
$\mathbf{H}$	Displacement gradient
$\mathbf{E}$	Green-Lagrangian strain tensor
$\mathbf{I}$	Unit tensor
$\mathbf{C}$	Right Cauchy-Green strain tensor
$\mathbf{b}$	Left Cauchy-Green strain tensor
$\boldsymbol{\varepsilon}$	Linear strain tensor
$\mathcal{C}_0$	Internal cut of the solid in the initial configuration
$\mathcal{C}$	Internal cut of the solid in the current configuration
∂C_0	Boundary of $\mathcal{C}_0$
∂C	Boundary of $\mathcal{C}$
$\mathrm{d}A$	Infinitesimal surface area element in the initial configuration
$\mathrm{d}a$	Infinitesimal surface area element in the current configuration
$\mathbf{t}$	Traction vector in the current configuration
$\mathbf{N}_0$	Normal unit vector in the initial configuration
$\mathbf{n}$	Normal unit vector in the current configuration

Nomenclature

$\boldsymbol{\sigma}$	Cauchy stress tensor
$\mathbf{P}$	First Piola-Kirchhoff stress tensor
$\mathbf{P}_{\mathrm{N}}$	Nominal stress tensor
$\mathbf{S}$	Second Piola-Kirchhoff stress tensor
W	Strain energy function or density
$\mathbb{A}$	First elasticity tensor
$\mathbb{C}^{SE}$	Second elasticity tensor
$\boldsymbol{\delta}$	Kronecker delta
λ and μ	Lamè parameters
β	Material parameter describing the volumetric compressibility
E and ν	Young's Modulus and Poisson ratio
G	Energy released rate per unit of new crack surface
G_c	Critical energy release rate
Γ_0	Crack set in the body domain in the initial configuration
$\partial\Omega_0$	External boundary of the solid in the initial configuration
$\mathbf{u}^*$	Prescribed displacements
$\mathbf{t}^*$	Prescribed surface tractions
$\partial\Omega_0^{\mathrm{D}}$	Dirichlet boundary in the initial configuration
$\partial\Omega_0^{\mathrm{N}}$	Neumann boundary in initial configuration
$\mathbf{b}^*$	Body force per unit mass
$\mathcal{P}$	External potential energy
$\mathcal{E}$	Internal energy of the solid
Π	Total potential energy of the solid
ϕ	Crack phase-field parameter
$g(\phi)$	Energetic degradation function
k_{res}	Residual parameter to avoid numerical instability
$\gamma(\phi;\nabla\phi)$	Crack surface density function
$\alpha(\phi)$	Geometric crack function
ξ	Parameter of the geometric crack function
l_0	Length scale parameter
c_0	Scaling parameter
$\boldsymbol{\sigma}_c$	Material tensile strength
$\delta\mathcal{E}$	First variation of the internal energy
$\delta\Pi$	First variation of the total potential energy
$\mathbf{N}$	Linear shape function matrix of the displacement field
$\delta\bar{\mathbf{u}}$	Nodal displacement values
$\mathbf{J}$	Jacobian of the transformation between global and natural reference system
$\boldsymbol{\xi}$	Nodal coordinates in the natural reference system
$\mathbf{X}$	Nodal coordinates in the global reference system
$\nabla\phi$	Gradient of phase field
$\bar{\phi}$	Nodal phase-field values
$\bar{\mathbf{N}}$	Linear shape function matrix of the phase-field
$\bar{\mathbf{B}}$	Derivatives of the phase-field shape function matrix
$\mathbf{K}^{uu}$	Stiffness matrix of the displacement sub-problem
$\mathbf{K}^{\phi\phi}$	Stiffness matrix of the phase-field sub-problem
$\mathbf{K}^{u\phi}$ and $\mathbf{K}^{\phi u}$	Coupling components of the stiffness matrix
$\delta W(\mathbf{F})$	Virtual energy density
$\mathbf{K}_{ab}^{\mathrm{mat}}$	Material tangent matrix

Nomenclature

$\mathbf{K}_{ab}^{\text{geom}}$	Geometrical tangent matrix
$\delta\mathbf{E}$	Variation of the Green-Lagrange strain energy
$\mathbf{B}_{0a}$	Matrix relating $\delta\mathbf{E}$ and $\delta\bar{\mathbf{u}}$
u	Imposed displacement used in the numerical simulations
t	Upper layer thickness used in the numerical simulations
h	Mesh dimension

5.1 Finite elasticity theory definitions

Consider a solid in its initial state whose domain is denoted by $\Omega_0 \subset \mathbb{R}^3$. This domain is formally described as a set of continuously distributed points (called material points) $P \in \Omega_0$. A point position is identified by the vector $\mathbf{X} = \{X_1, X_2, X_3\}^{\mathrm{T}}$ in $\mathbb{R}^3$ with respect to the origin $\mathbf{O}$. This initial configuration is considered as undeformed and stress-free and it is also identified as the *reference configuration*.

Throughout the deformation process, the solid assumes the so-called *current configuration* occupying the domain denoted by $\Omega \subset \mathbb{R}^3$ at an arbitrary time t, and whose position vectors are identified by the vector $\mathbf{x}(\mathbf{X}, t)$ as in Figure 114. The initial and current configurations are related through the nonlinear deformation map $\boldsymbol{\varphi} : \Omega_0 \times [0, t] \to \mathbb{R}^3$, so that $\mathbf{x} = \boldsymbol{\varphi}(\mathbf{X}, t)$.

Furthermore, it is possible to introduce the displacement vector which describes the motion of the body from the undeformed to the deformed configuration at the time t:

$$\mathbf{u}(\mathbf{X}, t) := \mathbf{x}(\mathbf{X}, t) - \mathbf{X} \tag{5.1}$$

Equivalently, the current position of the material points is given by:

$$\mathbf{x}(\mathbf{X}, t) = \mathbf{X} + \mathbf{u}(\mathbf{X}, t) \tag{5.2}$$

In the quasi-static framework, the time represents only a "pseudo-time" necessary to characterize the state of deformation.

The motion of the body can be described following two approaches which are physically equivalent to each other, but bring to different interpretations and quantity definitions in conjunction with alternative numerical implementations: (i) the Lagrangian or Material description, where

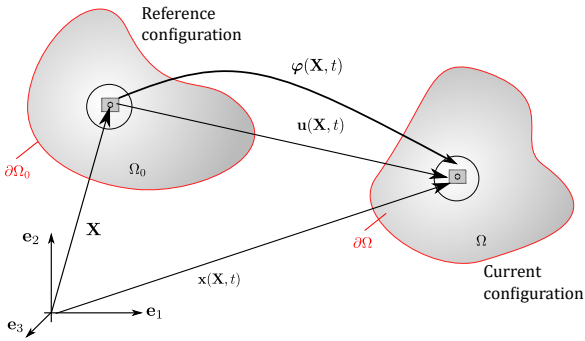

Figure 114: Solid deformation process from the reference configuration to the current one.

the variables and the system equations are formulated with respect to the reference configuration and to the vector $\mathbf{X}$; (ii) the Eulerian or Spatial description, where the current configuration and the vector $\mathbf{x}$ are considered instead. In what follows, the Lagrangian approach is used to describe the deformation of the body, so not all the strain and stress measures are introduced (see [114] and [115] for the additional ones).

The deformation of the body is described using a tensor $\mathbf{F}$, called Deformation Gradient, which relates tangent vectors of initial and current configuration to each other, mapping an infinitesimal line segment $\mathrm{d}\mathbf{X}$ in Ω_0 of the initial state, to a line segment $\mathrm{d}\mathbf{x}$ of the current configuration:

$$\mathbf{F} := \nabla_{\mathbf{X}}(\boldsymbol{\varphi}) = \frac{\partial \boldsymbol{\varphi}}{\partial \mathbf{X}} = \frac{\partial \mathbf{x}}{\partial \mathbf{X}} \;\rightarrow\; \mathbf{F} = \frac{\mathrm{d}\mathbf{x}}{\mathrm{d}\mathbf{X}} \tag{5.3}$$

where $\nabla_{\mathbf{X}}(\cdot)$ is the gradient of $(\cdot)$ with respect to the material configuration. An alternative expression for $\mathbf{F}$ derives from the definition of the displacement vector in (5.1):

$$\mathbf{F} = \frac{\partial(\mathbf{u}+\mathbf{X})}{\partial \mathbf{X}} = \mathbf{I} + \frac{\partial \mathbf{u}}{\partial \mathbf{X}} = \mathbf{I} + \nabla_{\mathbf{X}}(\mathbf{u}) \tag{5.4}$$

with $\mathbf{I}$ representing the unit tensor. Using the tensor $\mathbf{H} = \nabla_{\mathbf{X}}(\mathbf{u})$, called Displacement Gradient, $\mathbf{F}$ can be written also as $\mathbf{F} = \mathbf{I} + \mathbf{H}$.

Particularly relevant is the determinant of $\mathbf{F}$, denoted by J and called Jacobian. The Jacobian expresses the volume variation of the solid during the deformation process. Hence, a deformation process with a negative Jacobian would correspond to a negative volume, which is not physically admissible. In order to keep the consistency of the mapping of the deformation process and preventing negative volume: $J > 0$. Moreover, an incompressible material will have $J = 1$.

5.1.1 Strain tensors

The first strain measure considered is the Green-Lagrangian tensor defined as:

$$\mathbf{E} := \frac{1}{2}(\mathbf{F}^{\mathrm{T}}\mathbf{F} - \mathbf{I}) = \frac{1}{2}(\mathbf{H} + \mathbf{H}^{\mathrm{T}} + \mathbf{H}^{\mathrm{T}}\mathbf{H}) \tag{5.5}$$

The Lagrange strain tensor quantifies the changes in length of a material segment, and angles between pairs of segments in the deformable solid. It can be noticed that the term $\mathbf{H}^{\mathrm{T}}\mathbf{H}$ represent the high order contribution due to the non-linearity of the system. In the geometrically linear theory, this term is neglected and the Green-Lagrangian strain tensor reduces to the linear strain measure $\boldsymbol{\varepsilon} = \frac{1}{2}(\mathbf{H} + \mathbf{H}^{\mathrm{T}})$.

Moreover, the right Cauchy-Green tensor can be defined as well:

$$\mathbf{C} := \mathbf{F}^{\mathrm{T}}\mathbf{F} \tag{5.6}$$

It can be regarded as quantifying the squared length of an infinitesimal segment in the reference configuration. In the same way, the left Cauchy-Green tensor can be defined as:

$$\mathbf{b} := \mathbf{F}\mathbf{F}^{\mathrm{T}} \tag{5.7}$$

and it represents the squared length of an infinitesimal segment in the current configuration.

5.1.2 Stress tensors

The stress measures related to the Lagrangian formulation do not directly correspond to physical stress because, in the case of large strain

theory, the difference between the initial cross-section area and the current one is not negligible so far. Hence, the first introduced stress tensor is the Cauchy stress tensor which is related to the deformed area. Other stress measures will be later defined for the reference configuration.

Consider an internal cut of the solid denoted with $\mathcal{C}_0 \in \Omega_0$ at the reference configuration and with $\mathcal{C}$ at the current state, having boundaries ∂C_0 and ∂C, respectively. According to the Cauchy Lemma, the traction vector $\mathbf{t}$, acting on an infinitesimal surface area element, $\mathrm{d}a$, on $\mathcal{C}$ with normal vector $\mathbf{n}$, can be written as:

$$\mathbf{t} = \boldsymbol{\sigma} \cdot \mathbf{n}, \; t_i = \sigma_{ij} n_j \tag{5.8}$$

where $\boldsymbol{\sigma}$ is the Cauchy stress tensor (or true stress tensor) which can be seen as the internal force per unit deformed area. The component of the stress tensor, σ_{ji}, represents the i-th component of the traction vector acting on a plane with normal in the e_j direction.

According to Nanson's formula [116], the transformation of surface area elements from Ω to Ω_0 is given by:

$$\mathbf{n}\mathrm{d}a = J\mathbf{F}^{-\mathrm{T}} \cdot \mathbf{N}_0 \mathrm{d}A \tag{5.9}$$

where $\mathbf{N}_0$ is the normal vector in the reference configuration of the infinitesimal surface area element $\mathrm{d}A$. This relation allows to introduce the first Piola-Kirchhoff stress tensor, $\mathbf{P}$:

$$\begin{aligned} &\boldsymbol{\sigma}\mathbf{n} \cdot \mathrm{d}a = \boldsymbol{\sigma} J\mathbf{F}^{-\mathrm{T}} \cdot \mathbf{N}_0 \mathrm{d}A = \mathbf{P}\mathbf{N}_0 \mathrm{d}A \\ &\rightarrow \; \mathbf{P} = J\boldsymbol{\sigma} \cdot \mathbf{F}^{-\mathrm{T}} \end{aligned} \tag{5.10}$$

In components, the first Piola-Kirchhoff reads:

$$P_{iI} = J\sigma_{ij} F^{-1}_{Ij} \tag{5.11}$$

where the uppercase indices are reserved to the reference configuration and the lowercase to the current deformed configuration. The first Piola-Kirchhoff stress tensor can be regarded as the internal force per unit undeformed area acting within a solid. Since $\boldsymbol{\sigma}$ is multiplied by $\mathbf{F}$ only from the left, the first Piola-Kirchhoff tensor is related to both the initial and the current configuration. Moreover it is not symmetric and it is

important to distinguish it from the Nominal stress tensor, which is the transpose of the first Piola-Kirchhoff stress, used by many authors and often denoted with $\mathbf{P}$ as well:

$$\mathbf{P}_{\mathrm{N}} = \mathbf{P}^{\mathrm{T}} = J\mathbf{F}^{-1} \cdot \boldsymbol{\sigma} \tag{5.12}$$

With the aim of considering only the reference configuration, the second Piola-Kirchhoff tensor is introduced as:

$$\mathbf{S} = \mathbf{F}^{-1} \cdot \mathbf{P} = J\mathbf{F}^{-1}\boldsymbol{\sigma}\mathbf{F}^{-\mathrm{T}} \tag{5.13}$$

It follows that:

$$\mathbf{P} = \mathbf{F} \cdot \mathbf{S}, \; P_{iI} = F_{iJ}S_{JI} \tag{5.14}$$

No physical meaning can be related to this latter stress tensor but it is used very often because it is symmetric and it is easier to deal with symmetrical stress tensors in the reference configuration.

5.1.3 Constitutive models

Hyperelastic (or Green) materials are defined as elastic materials for which the work is independent from the load path. It is then possible to introduce a stored energy function, called also strain energy function or density, W, such that the stress can be related to the strain:

$$\mathbf{S} = 2\frac{\partial W(\mathbf{C})}{\partial \mathbf{C}} = \frac{\partial W(\mathbf{E})}{\partial \mathbf{E}}, \; S_{IJ} = 2\frac{\partial W}{\partial C_{IJ}} = \frac{\partial W}{\partial E_{IJ}} \tag{5.15}$$

The stored energy potential for the stress can be written as function of the right Cauchy-Green tensor $\mathbf{C}$ or Green-Lagrange strain tensor $\mathbf{E}$. Equivalent expressions can be obtained for different stress tensors, like for the first Piola-Kirchhoff tensor:

$$\mathbf{P} = \mathbf{F}\frac{\partial W(\mathbf{E})}{\partial \mathbf{E}} = \frac{\partial W(\mathbf{F})}{\partial \mathbf{F}} \tag{5.16}$$

In components, the equation reads:

$$P_{iI} = \frac{\partial W(F_{jJ})}{\partial F_{iI}} \tag{5.17}$$

The linearization of the weak form equations of the system, introduced later in Section 5.2, requires the computation of the first elasticity tensor:

$$\mathbb{A}^{(1)} = \frac{\partial^2 W}{\partial \mathbf{F} \partial \mathbf{F}},\ A_{iIjJ} = \frac{\partial^2 W}{\partial F_{iI} \partial F_{jJ}} \tag{5.18}$$

This operator, is used in the Newton-Raphson solution method in fully implicit nonlinear FE schemes. The constitutive material model can be also expressed using the second elasticity tensor or material tangent modulus $\mathbb{C}^{SE}$, which is a forth order tensor and can be derived from the expression:

$$\mathbb{C}^{SE} = 4\frac{\partial^2 W(\mathbf{C})}{\partial \mathbf{C} \partial \mathbf{C}} = \frac{\partial^2 W(\mathbf{E})}{\partial \mathbf{E} \partial \mathbf{E}} = \frac{\partial \mathbf{S}}{\partial \mathbf{E}} \tag{5.19}$$

The relation between the first and the second elasticity tensors is the following [114]:

$$A^{(1)}_{iIjJ} = F_{iN} C^{SE}_{NIMJ} F_{jM} + S_{IJ}\delta_{ij} \tag{5.20}$$

where δ is the Kronecker delta: $\delta_{ij} = 1$ if $i = j$, $\delta_{ij} = 0$ if $i \neq j$.

The numerical simulations presented in this Chapter are developed using hyperelastic material models. Within this context, the simplest material model that extends the linear elastic laws to large displacements is called *Kirchhoff-Saint-Venant*, and it is characterized by the Lamè parameters λ and μ (the latter constant is called also shear modulus).

The response of the material is modeled by the following elastic strain energy potential:

$$W(\mathbf{E}) = \frac{\lambda}{2}[\mathrm{tr}(\mathbf{E})]^2 + \mu \mathrm{tr}(\mathbf{E}^2) \tag{5.21}$$

The second Piola–Kirchhoff stress tensor can be derived from the relation:

$$\mathbf{S} = \frac{\partial W}{\partial \mathbf{E}} = \lambda \mathrm{tr}(\mathbf{E})\mathbf{I} + 2\mu\mathbf{E} \tag{5.22}$$

Finally, the second elasticity tensor reads:

$$\mathbb{C}^{SE} = \lambda \mathbf{I} \otimes \mathbf{I} + 2\mu \mathbf{I}_4 \tag{5.23}$$

The second formulation used in the chapter is the compressible *Neo-Hookean* material model in the form adopted in [117]. The strain energy

function is written in terms of $\mathbf{C}$ as:

$$W(\mathbf{C}) = \frac{\mu}{2}\left[\text{tr}(\mathbf{C}) - 3\right] + \frac{\mu}{\beta}\left[J^{-\beta} - 1\right] \tag{5.24}$$

where $J = det(\mathbf{F})$, μ is the shear modulus and $\beta = 2\nu/(1-2\nu) > 0$ describes a weak volumetric compressibility of the elastic solid through the Poisson ratio ν.

The first Piola-Kirchhoff stress tensor is given by:

$$\mathbf{P} = \mu\left[\mathbf{F} - J^{-\beta}\mathbf{F}^{-\text{T}}\right] \tag{5.25}$$

The first elasticity tensor in component notation can be computed as:

$$A^{(1)}_{iIjJ} = \frac{\partial^2 W}{\partial F_{Ii}\partial F_{Jj}} = \left[\mu\delta_{ij}\delta_{IJ} + \mu\beta J^{-\beta}F^{-1}_{Ii}F^{-1}_{Jj} + \mu J^{-\beta}F^{-1}_{iI}F^{-1}_{jJ}\right] \tag{5.26}$$

5.2 Phase field approach for fracture

5.2.1 Brief State of the Art of phase field method for hyperelastic materials

Modeling of the fracture phenomena is still a relevant challenge in Computational Mechanics and different methods have been proposed so far in the related literature such as the Cohesive Zone Model [103, 118], the eXtended FEM (XFEM) [119], among many others.

The mathematical background of the eXtended FEM is based on the concept of the partition of unity: a set of functions such that the sum of all the function values at a point x is 1 [119]. The shape functions of the standard finite element method satisfy this condition, and the XFEM takes advantage of it by introducing in the approximation space some enrichment functions and extra degrees of freedom able to reproduce the jump in the displacement field caused by the crack [120]. The direction of the crack growth is determined by computing the stress intensity factors at the crack tip, in conjunction with the use of a predefined crack propagation criterion for the determination of the crack advance progression in terms of extent and direction. In general, only the nodes near the

crack are enriched, and a remeshing algorithm is introduced to allow the simulation of the crack propagation in the domain. The splitting algorithm is necessary for the elements containing the crack tip or crossed by the crack, which can become computationally demanding, especially in complex geometries and in 3D simulations, since the method needs a variable number of extra degrees of freedom per node. The method has been widely adopted in the scientific literature, and a review of the state of the art can be found in [121].

Recent developments of the Virtual Element Method (VEM) show the potential of this approach within the field of fracture mechanics. The method was initially proposed in [122, 123], and it represents a generalization of the standard finite element method. The domain is discretized in general polygonal elements, and one key advantage of the method is the flexibility concerning the mesh generation since irregularly shaped elements (even non-convex) can be employed to deal with complex geometries. In brief, the VEM differs from the classical finite elements since it does not require the computation of the interpolation functions in the interior of the elements. Instead, they have an explicit representation only at the boundary of the elements through polynomial functions of order k. For $k = 1$ (known as low-order VEM), the element nodes are placed entirely at the vertices of the polygonal elements, and the shape or basis functions restricted at the element boundaries are linear functions [124].

In general, the VEM relies on the split of the discrete space of test functions into a projected part and a remainder. The projection is required since the approximated displacement field is available only on the boundaries of the element. This approach leads to a rank-deficient stiffness matrix that needs a stabilization term to solve the system. It has been applied to finite elastoplastic deformation in [125], compressible and incompressible hyperelastic materials in [126], contact problems in [127] and to homogenization problems in [128]. Applications to fracture mechanics can be found in [129] and in [130]. In the first work, brittle crack propagation is modeled by computing the crack growth direction and splitting the virtual elements in such directions following the crack

evolution. In [130], the VEM discretization of the bulk has been coupled with 2D interface cohesive elements. The work proposes a tracking algorithm to determine the crack nucleation and evolution and to refine the virtual elements mesh accordingly. Moreover, interface finite elements are introduced in the cutting line along with the evolution of the crack.

In order to simulate crack initiation, crack branching, and crack coalescence for multiple fronts in an efficient and reliable manner, multifield variational formulations (usually denominated *phase field methods*), have been proposed in the last decades with a tremendous impact within the research community. These methods can be envisaged as a particular form the Continuum Damage approaches which use a parameter to describe the solid deterioration and to control the material strength [131].

Phase-field methods are based on Griffith's idea of competition between elastic and fracture energy. According to Griffith's theory for brittle elastic solids [85], when a crack propagates, there's a reduction of the elastic strain energy stored in the body, and, at the same time, the surface energy increases because of the creation of new crack surfaces. Hence a preexisting crack will propagate if the crack growth results in a reduction of the potential energy greater or equal to the increase of surface energy. The energy released rate per unit of new crack surface is referred to as G and the critical value for which the crack propagates is noted with G_c. This value called also fracture toughness, is independent of the geometry of the solid, and it is a material property.

The pioneer works in the direction of a variational approximation of Griffith's energy balance approach have been carried out by Francfort and Marigo [132], Bourdin et al. [133] and Miehe et al. [134]. These authors consider a damage variable as an additional primary unknown of the problem, defining an extra degree of freedom per node in the FE discretization to model brittle fracture phenomena. The additional variable is governed by a Poisson-type partial differential equation to model fracture events.

One of the most appealing aspect of phase-field methods is the fact that any sharp discontinuity represented by the crack can be approximated by a diffuse-interface description of cracks. Correspondingly,

and in line with the developments given in [133, 134], the fracture phenomenon is modeled by two partial differential equations: the stress equilibrium equation, which accounts for the increasing damage of the body, and the evolution equation which describe the energy dissipation and the crack growth.

In the specialized literature, the individual phase-field formulations differ for the approximation of the sharp crack, for the degradation function used to lower the damaged material stiffness, and for the method used to enforce the irreversibility condition (the level of damage can only increase). This approach has been used to describe brittle materials at the beginning, but later they were extended to cohesive [135, 136] or ductile [137, 138] fracture, and to dynamic crack propagation [139, 140].

In [141], advancements of the variational approach to fracture are presented to model complex crack patterns in heterogeneous materials and composite structures. To trigger fracture events in thin-walled structures, solid shells relying on the enhanced assumed strain (EAS) method have been exploited in [142], while interface debonding problems have been treated using discrete cohesive zone model for the interface coupled with phase-field for the bulk [97, 143, 144]. A broader presentation of phase-field approaches can be found in [145].

The phase-field approach have been developed also for virtual elements by Wriggers and coworkers in [146, 124] considering the projection of the displacement and phase fields on to a polynomial space. The results are in line with the ones obtained with second-order triangular finite elements and the technique seems to be promising especially in the case of severe distortion of the elements.

The application of the phase-field method to rubber-like material at large deformation is more challenging compared to the linear elastic brittle fracture at infinitesimal strain because both material and geometric nonlinearities should be considered simultaneously [147]. Moreover, the material nonlinearity is also influenced by the evolution of the damage field.

In the last decade, a phase-field model for rate-independent hyperelastic materials was firstly proposed by Miehe [117]. Mandal and cowork-

ers [148] simulated crack nucleation and propagation in composites materials with polymeric matrix, while Russ et al. [149] propose the simulation of 3D-printed polymeric composites. A phase-field model for a general nonlinear elastic material based on a novel energy decomposition has been proposed by Tang et al. [150].

In [151, 152], a variational formulation based on the phase-field approximation of fracture has been developed to include some specific attributes of elastomers: (i) crack nucleation as consequence of hydrostatic stress concentrations (as near rigid fillers, often used for engineering applications), (ii) total or partial healing of micro-cracks, and (iii) fracture resistance, not as a material property, but depending on the history of fracture and healing.

5.2.2 Motivation for the use of PF methods in adhesive joints

In the light of the previous description of the potential capabilities of PF methods, this technique can be considered as an extraordinary candidate for its application in adhesive joints due to: (i) the complex character of the geometric definition of such joints, (ii) the possible different failure modes within the component (adhesive/cohesive failures), among other aspects. Therefore, this approach is here exploited to simulate the failure of polymeric materials used in many structural joints, both as components or adhesives.

Regarding this topic, the failure phenomena of an adhesive layer considered as bulk material has been studied in [153]. In this contribution the experimental results are compared with FEM simulations relying on the constitutive and fracture mechanical characterization of a silicone adhesive.

The phase field method has been used in [154] to simulate fracture in layered heterogeneous structures analysing the material parameters mismatch and the influences of interface properties. Thin films on compliant substrates have been analysed also in [155] providing a characterization of the different damage patterns according to the mechanical properties

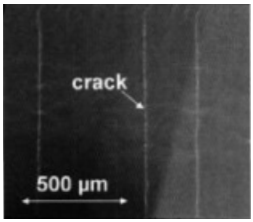

Figure 115: Cracks perpendicular to the stretch direction in a gold stripe on a silicone elastomeric substrate. Adapted from [156].

of the system. With respect to the cited works, the proposed formulation takes into account also the hyperelastic material models of the components.

Interesting applications of the proposed parametric study can be found in the field of flexible electronics where the material properties of the materials needs to be properly tuned to guarantee the deformability of the final device. Several failure modes are observed for thin rigid layer on flexible substrate, consisting in crack propagation through the layers or debonding at the interface. In [156] and [157], metal thin layers on elastomeric substrates of different Young's Modulus have been studied. In these studies, it is possible to observe the formation of subsequent cracks in the metal layer (see Figure 115).

In [158], fracture and debonding of stiff ceramic islands on deformable substrates have been experimentally investigated considering different dimensions and thickness (see Figure 116).

A phase-field finite element for large deformation has been developed and implemented in the commercial FE package Abaqus using the user-defined capability UEL (user element interface) starting from the material model proposed in [117]. The formulation is described in the next Section. The choice of Abaqus in the present Chapter instead of FEAP is motivated by the more advanced pre-processing and post-processing tools offered by the software and by the complexity of the simulations that are the goal of the present framework. FEAP has a limitation of 100000 finite elements for 3D simulations, and the present framework

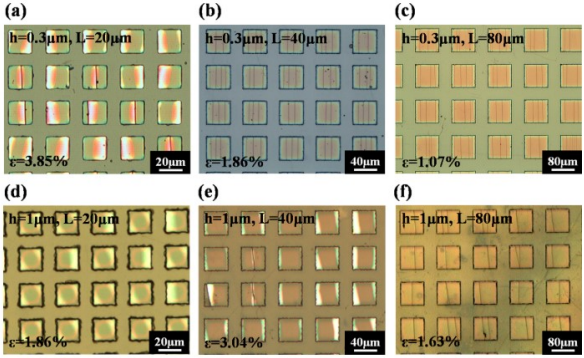

Figure 116: Ceramic islands (size L and thickness h) on PI (polyimide) substrate stretched horizontally. Source [158].

has been coded with the perspective of modeling examples more complex than the one presented in this Chapter. Another advantage is the possibility of an easier technology transfer since Abaqus is widely used in the industrial sector. Moreover, the use of a different software has been the opportunity to enlarge the author's knowledge of finite elements packages. It has to be remarked that the programming language (FORTRAN) and the structure of the user element are the same in both the programs such that the Abaqus user element can be easily transferred to FEAP, if necessary.

With respect to the cited work [117], the proposed formulation does not use the artificial viscous regularization of the above rate-independent formulation of crack propagation in rubbery polymers. The staggered method implemented in the Abaqus user element for the solution of the displacement and phase-field equations requires solving independently the two problems at the same time, using the variables obtained in the previous iteration and stored in appropriate history variables. The resulting algorithm differs from Miehe and Schänzel's implementation where the fracture phase-field problem is solved as a first step and the solution is used for the displacement problem.

5.2.3 Phase field variational formulation for finite deformation

Consider the solid already introduced in section 5.1 but with a crack set $\Gamma_0 \subset \mathbb{R}^{n_{dim}-1}$ as in Figure 117.

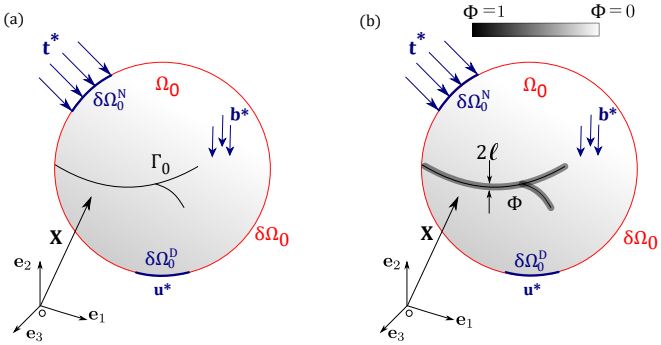

Figure 117: A cracking solid Ω_0 in the reference configuration with sharp crack Γ_0 (a) and its regularization (b).

The external boundary is signified by $\partial\Omega_0$ having $\mathbf{N}_0$ as outward unit normal vector. Moreover, on the external boundary, the prescribed displacements $\mathbf{u}^*$ and surface tractions $\mathbf{t}^*$ are applied on $\partial\Omega_0^{\mathrm{D}}$ and $\partial\Omega_0^{\mathrm{N}}$ respectively, such that $\partial\Omega_0 = \partial\Omega_0^{\mathrm{D}} \cup \partial\Omega_0^{\mathrm{N}}$ and $\partial\Omega_0^{\mathrm{D}} \cap \partial\Omega_0^{\mathrm{N}} = \emptyset$. Let also assume that the domain Ω_0 is subjected to $\mathbf{b}^*$ which denotes a body forces per unit mass.

The external potential energy is:

$$\mathcal{P}(\mathbf{u}) = \int_{\Omega_0} \mathbf{b}^* \cdot \mathbf{u}\, \mathrm{dV} + \int_{\partial\Omega_0^{\mathrm{N}}} \mathbf{t}^* \cdot \mathbf{u}\, \mathrm{dA} \tag{5.27}$$

The internal energy functional of the solid is:

$$\mathcal{E}(\mathbf{u}, \Gamma_0) = \int_{\Omega_0 \setminus \Gamma_0} W(\mathbf{F}) \mathrm{dV} + \int_{\Gamma_0} G_c \mathrm{dA} \tag{5.28}$$

where G_c is the critical energy release rate or fracture toughness of the material. The total energy of the solid is then sum of the two contribution:

$$\Pi(\mathbf{u}, \Gamma_0) = \mathcal{E}(\mathbf{u}, \Gamma_0) + \mathcal{P}(\mathbf{u}) \tag{5.29}$$

The variational approach introduced by Francfort and Marigo [132] evaluates the crack evolution by finding a global minimizer of (5.29) through the introduction of a phase-field approximation. The principal idea of the phase-field formulation is the substitution of the sharp crack with a transition region from undamaged to broken material. The sharp crack is approximated as a band of finite thickness characterized by a crack phase-field parameter $\phi \in [0, 1]$ such that $\phi = 0$ denotes the intact material and $\phi = 1$ represents the cracked one. The crack approximation converges to the sharp crack when the band thickness approaches zero.

The energy contribution from the crack surface, contained in equation (5.28), is obtained through a volumetric approximation:

$$\int_{\Gamma_0} G_c \mathrm{dA} \approx \int_{\Omega_0} G_c \gamma(\phi; \nabla\phi) \mathrm{dV} \tag{5.30}$$

.

Accordingly the strain energy functional is given by:

$$\mathcal{E}(\mathbf{u}; \phi) = \int_{\Omega_0} g(\phi) W(\mathbf{F}) \mathrm{dV} + \int_{\Omega_0} G_c \gamma(\phi; \nabla\phi) \mathrm{dV} \tag{5.31}$$

where $g(\phi)$ is called energetic degradation function and acts to reduce the elastic strength of the material.

There are different choices for the function $g(\phi)$, a more detailed discussion can be found in [145], in this thesis we used the model introduced by Bourdin et al. in [133] and it is referred as AT2 model:

$$g(\phi) = (1 - \phi)^2 \tag{5.32}$$

In order to avoid numerical instabilities at the fully broken state, a parameter $k_{\text{res}} \approx 0$ is used in the expression of $g(\phi)$:

$$g(\phi) = (1 - \phi)^2 + k_{\text{res}} \tag{5.33}$$

In the equation (5.31), $\gamma(\phi; \nabla\phi)$ is the crack surface density function that assumes this generic form:

$$\gamma(\phi, \nabla\phi) = \frac{1}{c_0} \left[\frac{1}{l_0} \alpha(\phi) + l_0 |\nabla\phi|^2 \right] \tag{5.34}$$

where $\alpha(\phi)$ is called geometric crack function, l_0 is the length scale parameter that controls the width of the diffuse crack band (see Figure 117b), and c_0 is called scaling parameter and it computed as:

$$c_0 := 4 \int_0^1 \alpha^{-1/2}(\hat{\phi}) \mathrm{d}\hat{\phi} \tag{5.35}$$

For the AT2 approach $c_0 = 2$.

The length scale parameter l_0 is strictly related to the thickness of the band approximating the sharp crack such that when $l_0 \to 0$, the regularised solution converges to the fracture mechanics solution according to the Γ-convergence theorem [148]. Moreover, in the related literature, in [159, 160] for example, it has been shown that by assigned to l_0 a value related to the material tensile strength, $\boldsymbol{\sigma}_c$, it is possible to predict the nucleation of fracture in the system correctly. These authors established that the length scale is proportional to the Irwin's characteristic length, $\frac{G_c E}{\boldsymbol{\sigma}_c^2}$, by a factor depending on the type of phase model. For the AT2 model, the formula reads:

$$l_0 = \frac{27}{256} \frac{G_c E}{\boldsymbol{\sigma}_c^2} \tag{5.36}$$

This approach has been successfully applied to many experimental results for ceramics, metals, and hard polymers, showing a very good agreement between the numerical and the experimental tests [160] especially for the cases of fracture nucleation from large pre-existing cracks. The Eq. 5.36 has also been used in the numerical simulations presented in this Chapter triggering the crack nucleation with the presence of a notch.

However, using l_0 as a material constant is less effective for the prediction of fracture nucleation in the bulk or from small pre-existing cracks and in the case of almost incompressible materials [161]. Moreover, the mesh size has to be smaller than the length scale parameter to ensure the fracture phenomena' correct prediction. In some cases, the length scale might be too small, leading to an even smaller element dimension and consequently to a computational model too expensive, or it can be too large such that modeling a small scale system. Different approaches

have been proposed to overcome these issues: the phase-field regularized cohesive zone model proposed in [145] (specialized for hyperelastic material in [148]) encodes the tensile strength in the energy degradation function. In contrast, the phase-field approach proposed by [161] considers an external crack driving force to account for the strength of the material.

The geometric crack function $\alpha(\phi)$ determines the distribution of the crack phase field and can be written as:

$$\alpha(\phi) = \xi\phi + (1-\xi)\phi^2 \in [0,1] \qquad \forall\phi \in [0,1] \tag{5.37}$$

with the parameter $\xi \in [0,2]$. The AT2 formulation can be obtained using $\xi = 0$ such that $\alpha = \phi^2$.

In order to find the minimizing couple $(\mathbf{u}, \phi)$, the following variational formulation is considered:

$$\begin{aligned}\delta\mathcal{E} = &\int_{\Omega_0} g(\phi)\frac{\partial W(\mathbf{F})}{\partial \mathbf{F}}\frac{\partial \delta\mathbf{u}}{\partial \mathbf{X}}\mathrm{dV} + \int_{\Omega_0}\frac{\mathrm{d}g(\phi)}{\mathrm{d}\phi}W(\mathbf{F})\delta\phi\mathrm{dV} + \\ &\int_{\Omega_0}\frac{G_c}{c_0 l_0}\frac{\mathrm{d}\alpha(\phi)}{\mathrm{d}\phi}\delta\phi\mathrm{dV} + \int_{\Omega_0}\frac{2G_c l_0}{c_0}\nabla\phi\nabla\delta\phi\mathrm{dV}\end{aligned} \tag{5.38}$$

The total potential first variation with respect to the displacement and phase-field must vanish at a minimum:

$$\delta\Pi(\mathbf{u},\phi) = \delta\mathcal{E} + \delta\mathcal{P} = 0 \tag{5.39}$$

The governing equations in weak form become:

$$\begin{aligned}\int_{\Omega_0} g(\phi)\frac{\partial W(\mathbf{F})}{\partial \mathbf{F}}\frac{\partial \delta\mathbf{u}}{\partial \mathbf{X}}\mathrm{dV} = &\int_{\Omega_0}\mathbf{b}^*\cdot\delta\mathbf{u}\mathrm{dV} + \int_{\partial\Omega_t} t^*\cdot\delta\mathbf{u}\mathrm{dA} + \\ &\int_{\Omega_0}\frac{\mathrm{d}g(\phi)}{\mathrm{d}\phi}W(\mathbf{F})\delta\phi\mathrm{dV} + \\ &\int_{\Omega_0}\frac{G_c}{c_0 l_0}\frac{\mathrm{d}\alpha(\phi)}{\mathrm{d}\phi}\delta\phi\mathrm{dV} + \int_{\Omega_0}\frac{2G_c l_0}{c_0}\Delta\phi\delta\phi\mathrm{dV} = 0\end{aligned} \tag{5.40}$$

The given formulation can be specified for different material models substituting the desired expression for $W(\mathbf{F})$. As stated before, the numerical simulations will be conducted using the expression of the energy

strain potential provided for the Kirchhoff-Saint-Venant and the Neo-Hookean material models in Section 5.1.3. Using the Eq. (5.17), the formulation can be written as:

$$\int_{\Omega_0} g(\phi)\mathbf{P}\frac{\partial \delta \mathbf{u}}{\partial \mathbf{X}}\mathrm{dV} = \int_{\Omega_0} \mathbf{b}^* \cdot \delta\mathbf{u}\mathrm{dV} + \int_{\partial\Omega_t} t^* \cdot \delta\mathbf{u}\mathrm{dA} + \int_{\Omega_0} \frac{\mathrm{d}g(\phi)}{\mathrm{d}\phi} W(\mathbf{F})\delta\phi\mathrm{dV} + \int_{\Omega_0} \frac{G_c}{c_0 l_0}\frac{\mathrm{d}\alpha(\phi)}{\mathrm{d}\phi}\delta\phi\mathrm{dV} + \int_{\Omega_0} \frac{2G_c l_0}{c_0}\Delta\phi\delta\phi\mathrm{dV} = 0 \tag{5.41}$$

5.2.4 Finite element discretization

The finite element discretization is here described for the displacement and the phase-field equations. Using the isoparametric form, the coordinates in the reference configuration are expressed as:

$$\mathbf{X} = \sum_a N_a(\boldsymbol{\xi})\bar{\mathbf{X}}_a = \mathbf{N}(\boldsymbol{\xi})\bar{\mathbf{X}} \tag{5.42}$$

where $\boldsymbol{\xi} = \{\xi_1, \xi_2, \xi_3\}$ are the natural coordinates for each element in the three-dimensional case and $\bar{\mathbf{X}}_a$ are the nodal coordinates where the index a ranges from 1 to the number of nodes in the element (four nodes for 2D and 8 nodes for 3D). Moreover, $\mathbf{N}$ is the standard linear shape function matrix.

The displacement field is interpolated in terms of nodal displacements as:

$$\mathbf{u}(\boldsymbol{\xi}) \approx \sum_a \mathbf{N}_a(\boldsymbol{\xi})\bar{\mathbf{u}}_a = \mathbf{N}(\boldsymbol{\xi})\bar{\mathbf{u}} \tag{5.43}$$

The virtual displacement, that appears in the weak form equations, is approximated using the same shape functions as:

$$\delta\mathbf{u}(\boldsymbol{\xi}) \approx \sum_a \mathbf{N}_a(\boldsymbol{\xi})\delta\bar{\mathbf{u}}_a = \mathbf{N}(\boldsymbol{\xi})\delta\bar{\mathbf{u}} \tag{5.44}$$

The weak form in Eq. (5.41) includes first derivatives of the displacement and of the phase-field. For their discretization, we need to derive firstly the derivatives of the shape functions with respect to X_I,with

$I = 1, 2, 3$ for 3D problems, using the chain rule:

$$\frac{\partial N_a}{\partial X_J} = \frac{\partial N_a}{\partial \xi_I} \frac{\partial \xi_I}{\partial X_J} \tag{5.45}$$

In matrix form, the relation reads:

$$\frac{\partial N_a}{\partial \mathbf{X}} = \mathbf{J}^{-1} \frac{\partial N_a}{\partial \boldsymbol{\xi}} \tag{5.46}$$

where

$$\frac{\partial N_a}{\partial \boldsymbol{\xi}} = \begin{Bmatrix} \dfrac{\partial N_a}{\partial \xi_1} \\ \dfrac{\partial N_a}{\partial \xi_2} \\ \dfrac{\partial N_a}{\partial \xi_3} \end{Bmatrix}, \frac{\partial N_a}{\partial \mathbf{X}} = \begin{Bmatrix} \dfrac{\partial N_a}{\partial X_1} \\ \dfrac{\partial N_a}{\partial X_2} \\ \dfrac{\partial N_a}{\partial X_3} \end{Bmatrix}, \mathbf{J} = \begin{bmatrix} \dfrac{\partial X_1}{\partial \xi_1} & \dfrac{\partial X_2}{\partial \xi_1} & \dfrac{\partial X_3}{\partial \xi_1} \\ \dfrac{\partial X_1}{\partial \xi_2} & \dfrac{\partial X_2}{\partial \xi_2} & \dfrac{\partial X_3}{\partial \xi_2} \\ \dfrac{\partial X_1}{\partial \xi_3} & \dfrac{\partial X_2}{\partial \xi_3} & \dfrac{\partial X_3}{\partial \xi_3} \end{bmatrix} \tag{5.47}$$

in which the $\mathbf{J}$ is the Jacobian transformation between the natural coordinates $\boldsymbol{\xi}$ and the reference system $\mathbf{X}$. The derivatives will be written in the sequel using the notation:

$$\frac{\partial N_a}{\partial X_J} = N_{a,X_J} \equiv N_{a,J} \tag{5.48}$$

The displacement derivatives with respect to the reference system are computed as:

$$\mathbf{u}_{a,J} = \frac{\partial \mathbf{u}_a}{\partial X_J} = \sum_a N_{a,J} \bar{\mathbf{u}}_a \tag{5.49}$$

In order to express the weak form equations, the columns of matrix $\mathbf{B}$ containing the derivatives of the shape functions can be expressed as:

$$\mathbf{B}_a = \begin{bmatrix} N_{a,1} \\ N_{a,2} \\ N_{a,3} \end{bmatrix} \tag{5.50}$$

Similarly, for the phase field ϕ and its gradient $\nabla\phi$ the interpolation in terms of nodal values $\bar{\boldsymbol{\phi}}$ reads:

$$\phi \approx \sum_a \bar{N}_a(\boldsymbol{\xi}) \bar{\phi}_a = \bar{\mathbf{N}} \bar{\boldsymbol{\phi}} \tag{5.51}$$

$$\delta\phi \approx \sum_a \bar{N}_a(\boldsymbol{\xi})\delta\bar{\phi}_a = \bar{\mathbf{N}}\delta\bar{\boldsymbol{\phi}} \tag{5.52}$$

$$\boldsymbol{\nabla}\boldsymbol{\phi} \approx \sum_a \bar{\mathbf{B}}_a(\boldsymbol{\xi})\bar{\phi}_i = \bar{\mathbf{B}}\bar{\boldsymbol{\phi}} \tag{5.53}$$

where the interpolation matrix $\bar{\mathbf{N}}$ and $\bar{\mathbf{B}}$ have components:

$$\bar{N}_a(\boldsymbol{\xi}) = N_a(\boldsymbol{\xi}), \qquad \bar{\mathbf{B}}_a = \begin{bmatrix} \bar{N}_{a,1} \\ \bar{N}_{a,2} \\ \bar{N}_{a,3} \end{bmatrix} \tag{5.54}$$

With the above approximations, the nonlinear equation (5.41) becomes:

$$\delta\Pi_u = (\delta\bar{\mathbf{u}})^{\mathbf{T}} \left(\mathbf{f}^{\text{ext}} - \int_{\Omega_0} \mathbf{B}^{\mathrm{T}} g(\phi)\mathbf{P}\mathrm{dV} \right) = 0 \tag{5.55a}$$

$$\begin{aligned} \delta\Pi_\phi = &(\delta\bar{\phi})^{\mathrm{T}} \int_{\Omega_0} \bar{\mathbf{N}}^{\mathrm{T}} \left(g'(\phi)W(\mathbf{F}) + \frac{G_c}{c_0 l_0}\alpha'(\phi) \right) \mathrm{dV} + \\ &(\delta\bar{\phi})^{\mathrm{T}} \int_{\Omega_0} \frac{2G_c l_0}{c_0} \bar{\mathbf{B}}^{\mathrm{T}}\bar{\mathbf{B}}\bar{\boldsymbol{\phi}}\mathrm{dV} = 0 \end{aligned} \tag{5.55b}$$

The residuals needed in the Newton-Raphson solver for the solution of the finite element problem read:

$$\mathbf{r}_u = \mathbf{f}^{\text{ext}} - \int_{\Omega_0} \mathbf{B}^{\mathrm{T}} g(\phi)\mathbf{P}\mathrm{dV} = 0 \tag{5.56a}$$

$$\mathbf{r}_\phi = \int_{\Omega_0} \left[\bar{\mathbf{N}}^{\mathrm{T}} \left(g'(\phi)W(\mathbf{F}) + \frac{G_c}{c_0 l_0}\alpha'(\phi) \right) + \frac{2G_c l_0}{c_0} \bar{\mathbf{B}}^{\mathrm{T}}\bar{\mathbf{B}}\bar{\boldsymbol{\phi}} \right] \mathrm{dV} = 0 \tag{5.56b}$$

In Eq. (5.56) the external forces are expressed as:

$$\mathbf{f}_a^{\text{ext}} = \int_{\Omega_0} \mathbf{N}_a \mathbf{b}^* \mathrm{dV} + \int_{\partial\Omega_0^{\mathrm{N}}} \mathbf{N}_a \mathbf{t}^* \mathrm{dA} \tag{5.57}$$

and the integral term represents the internal forces:

$$\mathbf{f}_a^{\text{int}} = \int_{\Omega_0} \mathbf{B}^{\mathrm{T}} g(\phi)\mathbf{P}\mathrm{dV} \tag{5.58}$$

A staggered method has been used for the solution of this system of equations, allowing the interaction between displacement and phase-field problems only through history field variables. This method is based on the consideration that the two fields are weakly coupled. For each time step, the current displacement is computed using the phase-field value at the previous step, while the current phase field is calculated based on the energy history.

The weak form of the displacement problem at the time step $n+1$ is formulated as follows:

$$\mathbf{r}_u = \mathbf{f}^{ext} - \int_{\Omega_0} \mathbf{B}^{\mathrm{T}} g(\phi_n) \mathbf{P} \mathrm{dV} = 0 \tag{5.59}$$

This is solved for $\mathbf{u}$, assuming ϕ_n known from the previous time step.

Similarly the phase-field problem is written as:

$$\mathbf{r}_\phi = -\int_{\Omega_0} \left[\bar{\mathbf{N}}^{\mathrm{T}} \left(g'(\phi) \mathcal{H}_{n+1} + \frac{G_c}{c_0 l_0} \alpha'(\phi) \right) + \frac{2 G_c l_0}{c_0} \bar{\mathbf{B}}^{\mathrm{T}} \bar{\mathbf{B}} \bar{\boldsymbol{\phi}} \right] \mathrm{dV} = 0 \tag{5.60}$$

where the potential energy from the displacement problem is replaced by a history variable defined as:

$$\mathcal{H}_0 = 0 \tag{5.61a}$$

$$\mathcal{H}_{n+1} = \max\{W(\mathbf{F}_n), H_n\} \tag{5.61b}$$

In order to use the Newton-Raphson method to solve the system, the linearization of the equations is required, obtaining the following linear system:

$$\begin{bmatrix} \mathbf{K}^{uu} & \mathbf{K}^{u\phi} \\ \mathbf{K}^{u\phi} & \mathbf{K}^{\phi\phi} \end{bmatrix} \begin{bmatrix} \delta \bar{\mathbf{u}} \\ \delta \bar{\phi} \end{bmatrix} = \begin{bmatrix} \mathbf{r}_u \\ \mathbf{r}_\phi \end{bmatrix} \tag{5.62}$$

where $\delta \bar{\mathbf{u}}$ and $\delta \bar{\phi}$ are the new nodal solutions at the time step $n+1$. The coupling matrix $\mathbf{K}^{u\phi}$ and $\mathbf{K}^{\phi u}$ are set to zero in a Jacobi-type staggered solution scheme.

The matrix $\mathbf{K}^{uu}$ can be obtained in terms of first Piola-Kirchhoff stress starting from the virtual energy density $\delta W(\mathbf{F})$ as:

$$\mathrm{d}(\delta W) = \delta F_{i,I} \, \mathrm{d}P_{iI} = \delta F_{i,I} \, \mathbb{A}_{iIjJ} \, \mathrm{d}F_{jJ} \tag{5.63}$$

where $\mathbb{A}_{iIjJ}$ is the first elasticity tensor in Eq. (5.18). The tangent matrix is hence given by [162]:

$$\mathbf{K}_{ab}^{uu} = \int_{\Omega_0} \frac{\partial N_a}{\partial X_I} \mathbb{A}_{iIjJ} \frac{\partial N_b}{\partial X_J} \mathrm{dV} \tag{5.64}$$

Each sub-matrix K_{ab}^{uu} has the size $n_{\text{dofu}} \times n_{\text{dofu}}$ where n_{dofu} is the number of displacement degrees of freedom for each node, and the indices a and b vary from 1 to the number of nodes of the element.

Equivalently, the expression for the tangent matrices can be then split into two different contributions called *material* and *geometrical* tangent matrices and addressed with $\mathbf{K}_{ab}^{\text{mat}}$ and $\mathbf{K}_{ab}^{\text{geom}}$ respectively:

$$\mathbf{K}_{ab}^{uu} = \mathbf{K}_{ab}^{\text{mat}} + \mathbf{K}_{ab}^{\text{geom}} \tag{5.65}$$

The two contribution can be derived considering that $\mathbf{P} = \mathbf{F} \cdot \mathbf{S}$, the Eq. (5.63) can also be expressed as [115]:

$$\mathrm{d}P_{iJ} = F_{iR}\mathrm{d}S_{JR} + S_{JR}\mathrm{d}F_{iR} \tag{5.66}$$

The material stiffness matrix can be derived more easily switching to Voigt notation for the Green strain and the second Piola-Kirchhoff tensors, $\{\mathbf{E}\}$ and $\{\mathbf{S}\}$, and considering the definition of the second elasticity tensor $[\mathbb{C}^{\text{SE}}]$ given in Eq. (5.19).

The material stiffness matrix hence reads:

$$\mathbf{K}_{ab}^{\text{mat}} = \int_{\Omega_0} \mathbf{B}_{0a}^{\text{T}} g(\phi) [\mathbb{C}^{\text{SE}}] \mathbf{B}_{0b} \mathrm{dV} \tag{5.67}$$

where $\mathbf{B}_{0a}$ is used to relate $\delta\{\mathbf{E}\}$ and $\delta\bar{\mathbf{u}}$ as:

$$\delta\mathbf{E} = \mathbf{B}_{0a}\delta\bar{\mathbf{u}}_a \tag{5.68}$$

with:

$$\mathbf{B}_{0a} = \begin{bmatrix} F_{11}N_{a,1} & F_{21}N_{a,1} & F_{31}N_{a,1} \\ F_{12}N_{a,2} & F_{21}N_{a,2} & F_{32}N_{a,2} \\ F_{13}N_{a,3} & F_{23}N_{a,3} & F_{33}N_{a,3} \\ F_{11}N_{a,2} + F_{12}N_{a,1} & F_{21}N_{a,2} + F_{22}N_{a,1} & F_{31}N_{a,2} + F_{32}N_{a,1} \\ F_{12}N_{a,3} + F_{13}N_{a,2} & F_{22}N_{a,3} + F_{23}N_{a,2} & F_{32}N_{a,3} + F_{33}N_{a,2} \\ F_{13}N_{a,1} + F_{11}N_{a,3} & F_{23}N_{a,1} + F_{21}N_{a,3} & F_{33}N_{a,1} + F_{31}N_{a,3} \end{bmatrix} \tag{5.69}$$

The second contribution can be computed as:

$$\mathbf{K}_{ab}^{\text{geom}} = \mathbf{I} \int_{\Omega_0} \frac{\partial N_a}{\partial X_I} g(\phi) S_{IJ} \frac{\partial N_b}{\partial X_J} \mathrm{dV} \tag{5.70}$$

where $\mathbf{I}$ is a unit matrix whose size depends on the dimension of the problem and $\mathbf{S}$ is in matrix form.

Finally, the tangent matrix $\mathbf{K}_{ab}^{uu}$ reads:

$$\mathbf{K}_{ab}^{uu} = \int_{\Omega_0} \mathbf{B}_{0a}^{\mathrm{T}} g(\phi) [\mathbb{C}^{\mathrm{SE}}] \mathbf{B}_{0b} \mathrm{dV} + \mathbf{I} \int_{\Omega_0} \frac{\partial N_a}{\partial X_I} g(\phi) S_{IJ} \frac{\partial N_b}{\partial X_J} \mathrm{dV} \tag{5.71}$$

More details on this derivation are given in [162], while the proposed finite element implementation uses the formula based on the first Piola-Kirchhoff (Eq.s (5.59) and (5.64)).

From the phase-field residual in Eq. (5.60), the tangent matrix $\mathbf{K}^{\phi\phi}$ is computed as:

$$\mathbf{K}^{\phi\phi} = \int_{\Omega_0} \left[\left(g''(\phi) \mathcal{H}_{n+1} + \frac{G_c}{c_0 l_0} \alpha''(\phi) \right) \bar{\mathbf{N}}^{\mathrm{T}} \bar{\mathbf{N}} + \frac{2 G_c l_0}{c_0} \bar{\mathbf{B}}^{\mathrm{T}} \bar{\mathbf{B}} \right] \mathrm{dV} \tag{5.72}$$

The phase-field variable represents an extra degree of freedom for each node, consequently the matrix $\mathbf{K}^{\phi\phi}$ has the size given by the number of nodes: $n_{\text{nodes}} \times n_{\text{nodes}}$.

5.3 Numerical simulations

The described formulation has been tested considering 3D, plane strain, and plane stress cases through benchmark tests taken from the literature using the commercial finite element software Abaqus FEA coding a specific user element subroutine.

The capability of the framework has also been explored for more complex 3D simulations considering thin cylindrical structures.

Subsequently, the computational framework has been used to evaluate structures composed of two different hyperelastic layers with mechanical parameters mismatch. The analyzed materials are typically used in stretchable devices and flexible electronics. These applications usually

involve a polymeric layer to assure a large deformation to the final product together with metallic or ceramic components. The simulations aim at reproducing the crack propagation within these types of structures.

The first example considers a notched 2D plate with two different thin layers. A parametric study on the fracture propagation through the layers has been conducted varying fracture toughness and bulk properties between the joint materials to understand the competition between crack branching and penetration when the crack impinges into the interface represented by the materials discontinuity.

The parametric study is followed by an interesting application with real materials considering a thin linear elastic material layer on top of a hyperelastic one.

5.3.1 2D formulation: penny shaped model

In order to demonstrate the capability of our formulation, a first benchmark test has been compared to results available in [117] for the same problem. We considered a penny-shaped specimen with a pre-existing notch in the center, with geometry and boundary conditions depicted in Figure 118. The test consists in a rectangular plate of 0.4mm height and 2mm height with a central horizontal notch of 0.2mm width and 0.01mm height. A monotonically increasing displacement u has been applied on the upper boundary, while the bottom boundary is fixed.

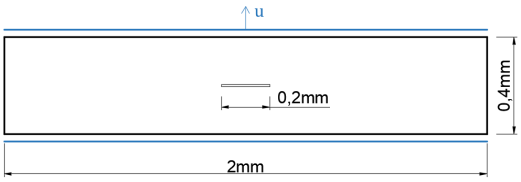

Figure 118: Geometry and boundary conditions of a rectangular plate with a central notch under remote tension u.

The finite element discretization of the plate consists of around 64700 elements (characteristic element length $h = 0.002\text{mm}$ as in [117]), and a

magnification of the mesh in the area close to the central notch is shown in Figure 119.

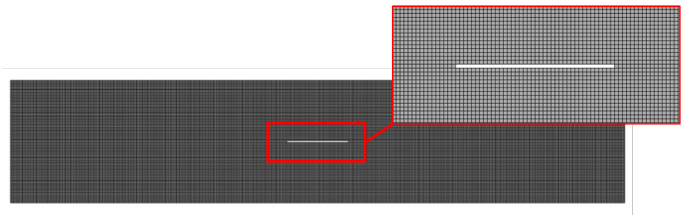

Figure 119: Mesh of the rectangular plate with the central notch.

Following the benchmark test proposed in [117], the plate has shear modulus $\mu = 5\mathrm{N/mm}^2$ and Poisson ratio $\nu = 0.45$ which corresponds to $\beta = 9$. The critical fracture energy is $G_c = 2.4\mathrm{N/mm}$ and the length scale is $l_0 = 0.01\mathrm{mm}$, while the residual parameter k has been set to 1.0×10^{-6} (the same value is used in all the simulations of this chapter).

Different simulations have been performed comparing the result of the 2D plane stress and plane strain assumptions with the solution in [117]. The deformed configurations at different imposed displacements till the complete rupture for plane strain configuration is shown in Figure 120.

The corresponding load-displacement curves are plotted in Figure 121. In this plot, the green and purple curves correspond to the same geometry solved with standard finite elements available in Abaqus: the green curve is obtained with "CPS4" elements for plane strain, and the violet curve with "CPE4" plane stress elements, using the same material parameters for the Neo-Hookean model. They have been juxtaposed to the phase-field elements results (both plane strain, yellow curve, and plane stress, red curve, formulation) to observe that they overlap perfectly when the plate is still undamaged, as expected. The results are in line with the benchmark test taken from [117], verifying the formulation.

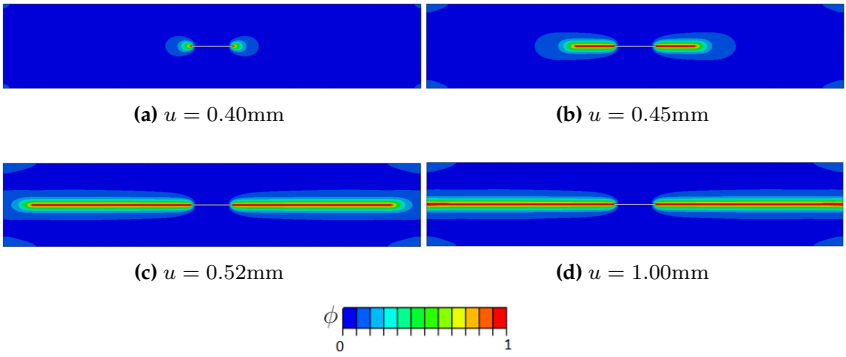

(a) $u = 0.40\text{mm}$ **(b)** $u = 0.45\text{mm}$

(c) $u = 0.52\text{mm}$ **(d)** $u = 1.00\text{mm}$

Figure 120: Phase field evolution during the crack propagation for the rectangular plate under plane strain assumption.

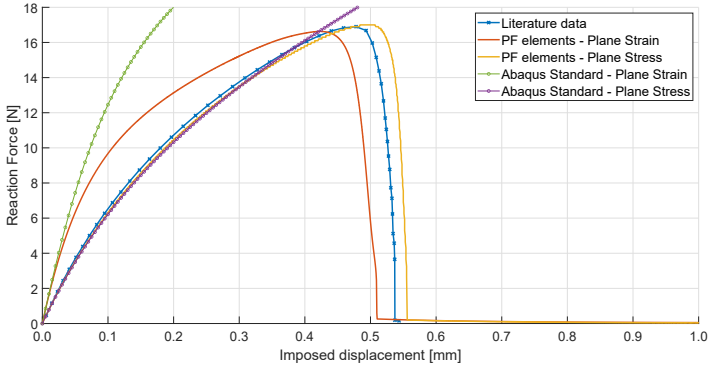

Figure 121: Central notched plate response in terms of imposed displacement vs total reaction force considering plane strain and plane stress hypothesis. Comparison between the present approach and the results obtained in [117]. and using standard Abaqus hyperelastic elements.

5.3.2 3D formulation: thin cylindrical structure

The coded phase-field element with the hyperelastic material model has been used to simulate the crack initiation and propagation in a thin cylinder with a central notch. For saving computational time, only half of a cylinder has been modeled and solved considering symmetrical boundary conditions at the vertical faces and equal applied displacement at the top and bottom face. The simulation considers only half of the cylinder with height equal to 60mm, internal radius equal to 52.5mm and thickness 5mm as shown in 122. The layer has a central notch with dimensions $10\text{mm} \times 1\text{mm}$.

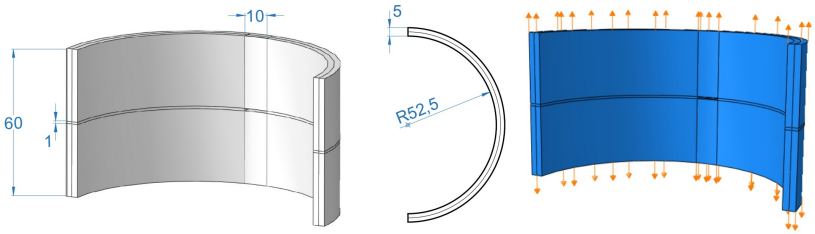

(a) **(b)**

Figure 122: Geometry (a) and boundary conditions (b) for the cylindrical layer. The dimensions are reported in mm.

The material taken into account for the simulation is the polymer PET (Polyethylene terephthalate) which is one of the most common polymers, and it is used for packaging, in the form of containers for food and liquids, as the substrate in solar cells and flexible electronics, and for 3D printing products. Its mechanical properties are shown in Table 15. The length scale parameter $l_0 = 1\text{mm}$ has been computed using E and $\boldsymbol{\sigma}_c$ as given in the table through the Eq. (5.36).

The mesh uses 3D elements with $h = 1\text{mm}$ and it is shown in Figure 123. The requirement of $h \leq l_0$ would require a lower element size, but since the test is here presented only to show the potentiality of the implemented finite element method in a 3D setting, the mesh size has

been chosen to show the crack path in the cylindrical structure within a reasonable computational time for the simulation.

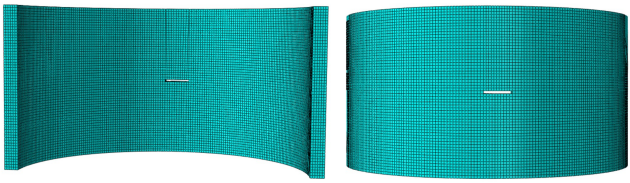

(a) (b)

Figure 123: Mesh of the cylinder.

The crack path is shown in Figure 125, while the structure response in terms of imposed displacement vs reaction force is plotted in Figure 124.

5.3.3 Parametric study on a bilayer joint with parameters mismatch

The analysis proposed in this Section regards a structural joint composed of two layers with different mechanical and geometrical properties. The failure of a joint subject to a tensile test is simulated using the proposed hyperelastic phase-field element. With the aim of understanding which parameters can affect the failure of the joint, a parametric study has been conducted considering: (i) the Young's modulus ratio between the two layers, (ii) the critical fracture energies mismatch, and (iii) the thickness of the joined components.

The geometry of the sample is presented in Figure 126 together with the applied boundary conditions. The current simulation is conducted

Material	**E** [GPa]	ν	λ [GPa]	μ [GPa]	$\mathbf{G_c}$ [N/mm]	$\boldsymbol{\sigma}_c$ MPa	$\mathbf{l_0}$ [mm]
PET	2.80	0.37	2.91	1.02	10.34	55	1.00

Table 15: Mechanical parameters of the polymer PET (Polyethylene terephthalate).

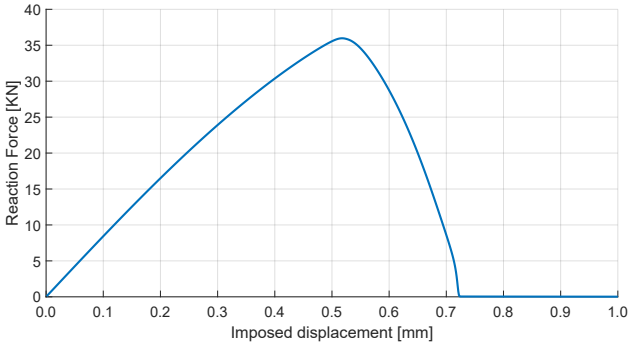

Figure 124: Load-displacement curve for the simulation of the cylindrical polymeric layer.

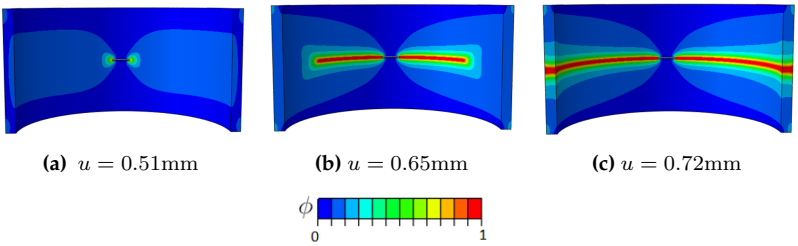

(a) $u = 0.51\text{mm}$ **(b)** $u = 0.65\text{mm}$ **(c)** $u = 0.72\text{mm}$

Figure 125: Crack propagation of the cylindrical layer.

under plane strain assumption. Moreover, in order to keep the consistency in the analysis, the total height of the joint is constant and equal to 10mm, while the ratio between the upper and lower layer thickness may vary. In this latter case, the notch depth varies so that it is always half of the upper layer thickness.

Both the layers are modeled using the Neo-Hookean constitutive model described in Section 5.1. Concerning the mechanical parameters, the lower layer is considered as made from PET, with the material properties reported in the previous Section Table 15. The properties of the upper layer can take different values to assess the impact of the specific parameters for the current study case.

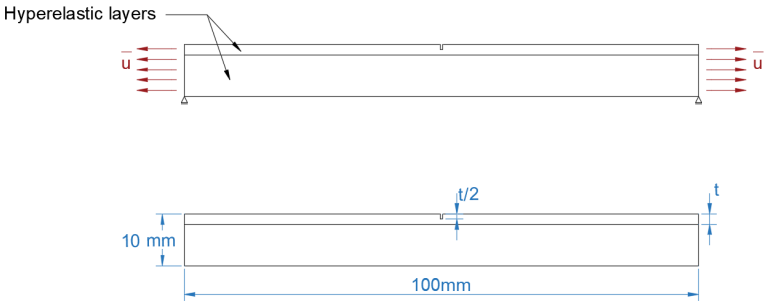

Figure 126: Geometry (a) and boundary conditions (b) of a bilayer rectangular plate with a notch in the top layer. The simulations include thickness $t = 1, 2\text{mm}$.

Regarding the underlying FE discretization and in order to avoid mesh influence on the results, a convergence study has been carried out on the element dimension, choosing $h = \{1.0, 0.5, 0.2, 0.1\}\text{mm}$. The resulting meshes are shown in Figure 127, while the response of the joint is plotted in Figure 128 in terms of imposed displacement and reaction force at the right bounded edge of the plate. It can be noted that the results for $h = 0.2\text{mm}$ and $h = 0.1\text{mm}$ are almost coincident to each other, and the value of $h = 0.2\text{mm}$ has been chosen for the following simulations since it saves computational time with respect to the smaller value.

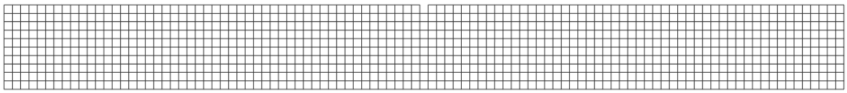

(a) Mesh of the entire plate with $h = 1\text{mm}$.

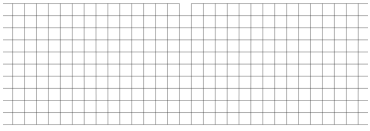

(b) $h = 1\text{mm}$.

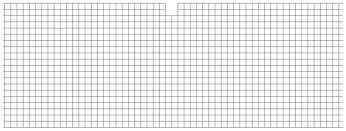

(c) $h = 0.5\text{mm}$.

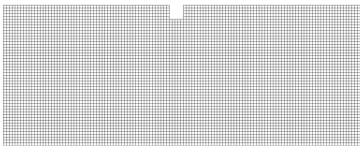

(d) $h = 0.2\text{mm}$.

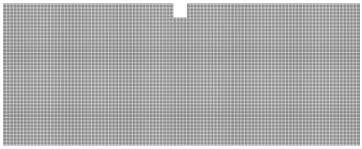

(e) $h = 0.1\text{mm}$.

Figure 127: Different element dimensions used for the mesh convergence study of the bilayer joint.

Young's Modulus influence

The first parameter for the joint analysis is the Young's Modulus ratio between the two layers E_1/E_2, where E_1 and E_2 refer to the upper and lower layers, respectively. The considered range accounts for different order of magnitude from $E_1/E_2 = 0.001$ to $E_1/E_2 = 100$. The study aims to assess how different stiffness values of the upper layer can change the crack initiation and propagation. The analysis is repeated for two different upper layer thickness: $t = \{1.0, 2.0\}\text{mm}$.

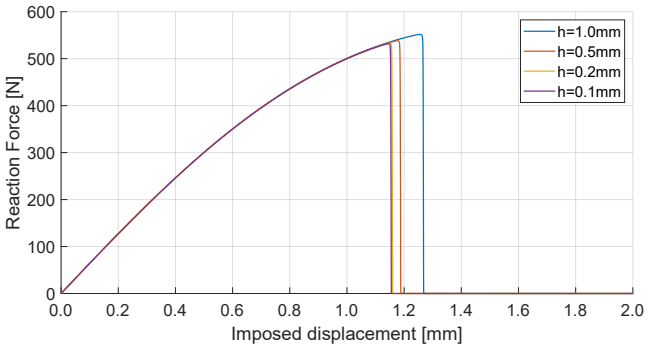

Figure 128: Mesh with different elements dimension.

The imposed displacement - reaction force results are depicted in Figure 129. It can be noticed immediately that a higher Young's modulus ratio corresponds to a smaller prescribed displacement for the failure of the joint for both the upper layer thickness considered. For $E_1/E_2 = 100$, after a sudden drop of the reaction force caused by the propagation of the crack in the upper layer, when the crack arrives at the interface, the reaction force curve shows a second stage due to the propagation of the crack into the lower layer with a lower Young's modulus.

The crack path for the different stiffness ratio are shown starting from Figure 130 to Figure 135, comparing for each case the results for the two values of thickness. Through the analyses of these graphs, it can be observed that the thickness of the layers does not have a strong influence on the predicted crack path. Moreover, the first three cases (Figures 132, 131 and 130) have the upper layer more flexible than the substrate, and despite the presence of the notch, the failure phenomenon starts from the lower layer.

The case in Figure 133 is reported only for comparison, since in this case, the same parameters are used for the upper and lower layer, hence the plate is composed only of one material.

Finally, in Figure 135 and Figure 134, the crack starts from the notch, propagates in the more rigid upper layer till the complete failure when

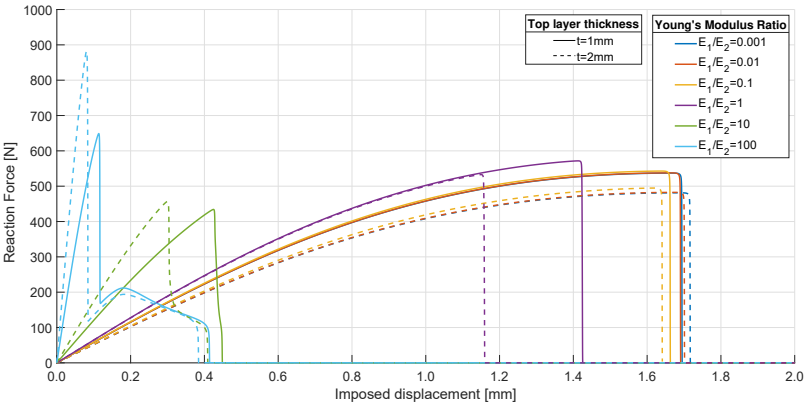

Figure 129: Parametric study on the effect of Young's modulus mismatch in a bilayer structure. For the lower layer, the PET material parameters have been used (see Table 15), varying the top layer thickness and its value of Young's modulus E_1.

the propagation reaches the end of the lower layer.

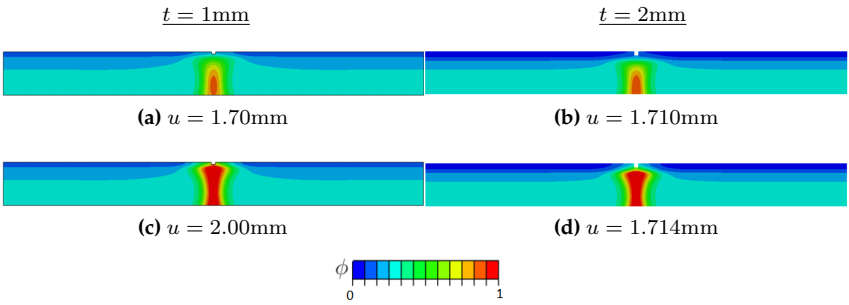

Figure 130: Crack evolution for Young's modulus ratio $E_1/E_2 = 0.001$.

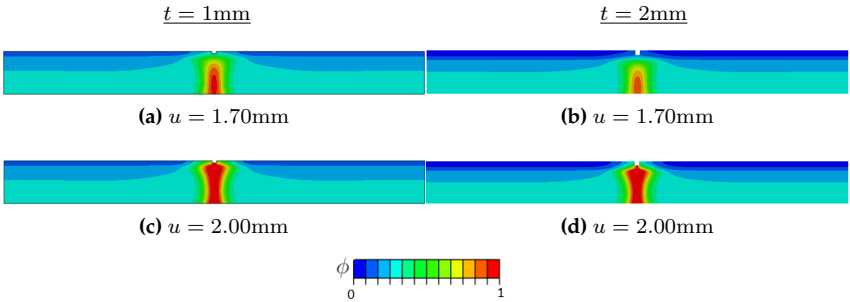

Figure 131: Crack evolution for Young's modulus ratio $E_1/E_2 = 0.01$.

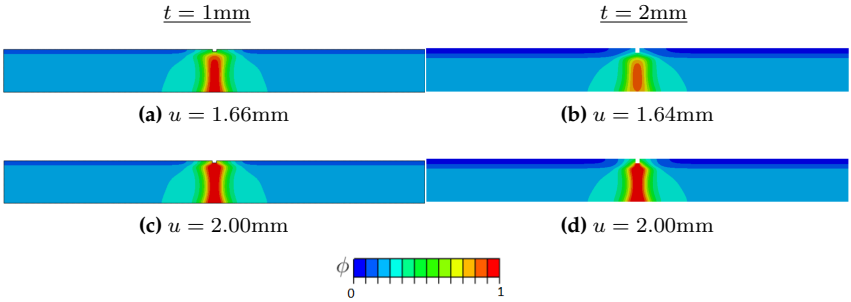

Figure 132: Crack evolution for Young's modulus ratio $E_1/E_2 = 0.1$.

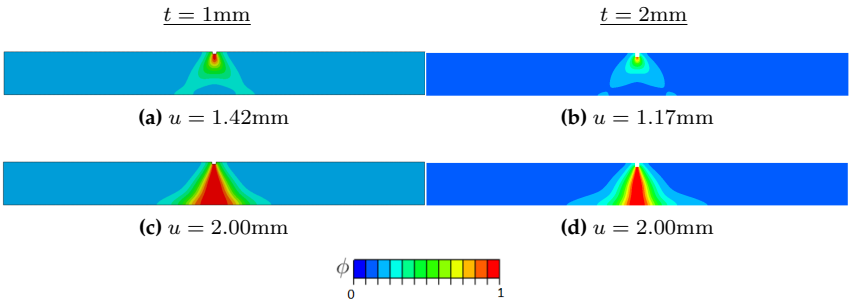

(a) $u = 1.42\text{mm}$ **(b)** $u = 1.17\text{mm}$

(c) $u = 2.00\text{mm}$ **(d)** $u = 2.00\text{mm}$

Figure 133: Crack evolution for Young's modulus ratio $E_1/E_2 = 1$.

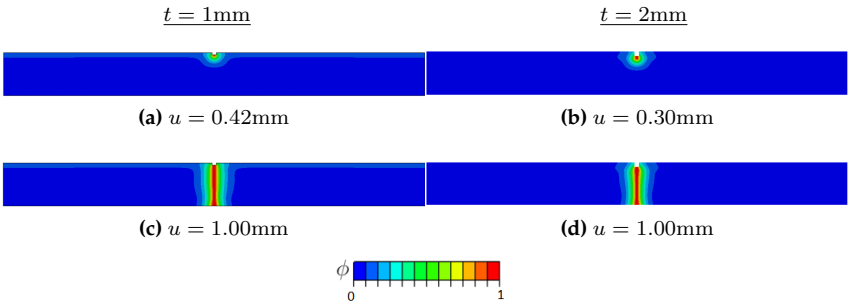

(a) $u = 0.42\text{mm}$ **(b)** $u = 0.30\text{mm}$

(c) $u = 1.00\text{mm}$ **(d)** $u = 1.00\text{mm}$

Figure 134: Crack evolution for Young's modulus ratio $E_1/E_2 = 10$.

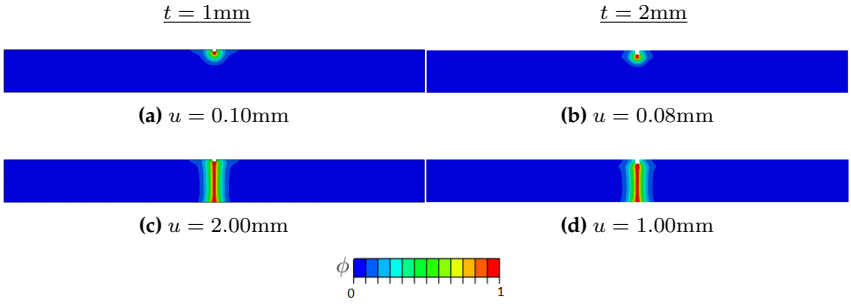

(a) $u = 0.10\text{mm}$ **(b)** $u = 0.08\text{mm}$

(c) $u = 2.00\text{mm}$ **(d)** $u = 1.00\text{mm}$

Figure 135: Crack evolution for Young's modulus ratio $E_1/E_2 = 100$.

Critical fracture energy influence

The models with upper layer thickness $t = 1\text{mm}$ and $t = 2\text{mm}$ have been used to assess the effect of another material parameter: the critical energy fracture G_c, varying the value of the top layer G_{c1} and keeping constant the value of $G_{c2} = 10.34\text{N/mm}$ for the lower layer. The response is shown in Figure 136. The curves have very similar behavior to each other, distinguished only by the prescribed displacement that causes the complete failure of the joint.

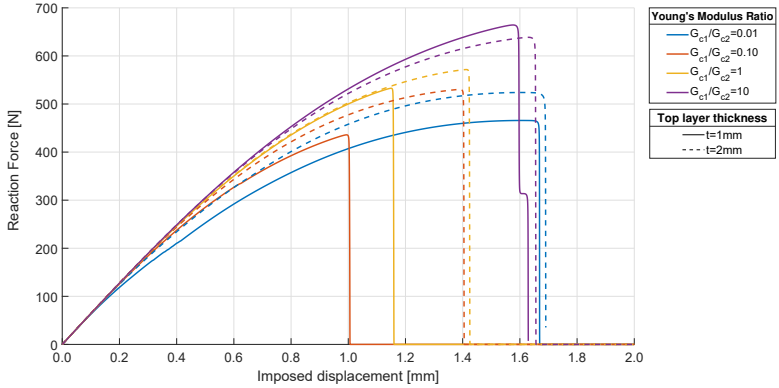

Figure 136: Parametric study on the effect of critical fracture energy mismatch in a bilayer structure. For the lower layer, the PET material parameters have been used (see Table 15), varying the upper layer value of G_{c1}.

However, if the crack path is analysed, it can be seen that the critical fracture energy ratio $G_{c1}/G_{c2} = 0.01$ brings to the failure of the upper layer only, without the propagation of the crack through the joint thickness (see Figures 137 and 138). For $G_{c1}/G_{c2} = 0.1$, the damage firstly develops within the upper layer, and propagates vertically in a second step (see Figure 139). This difference is not visible for $G_{c1}/G_{c2} = 1$ (Figure 140) as expected since the two layer have the same parameters. Finally, for $G_{c1}/G_{c2} = 10$, the crack starts in the lower layer, which has lower G_c, and propagates into the upper layer later (Figure 141). This latter case shows a different crack path for the case with $t = 1\text{mm}$ and

$t = 2\text{mm}$, since in the thicker layer model, two symmetrical cracks developed from the bottom edge, reach the interface and propagate along it towards the central notch in the upper layer.

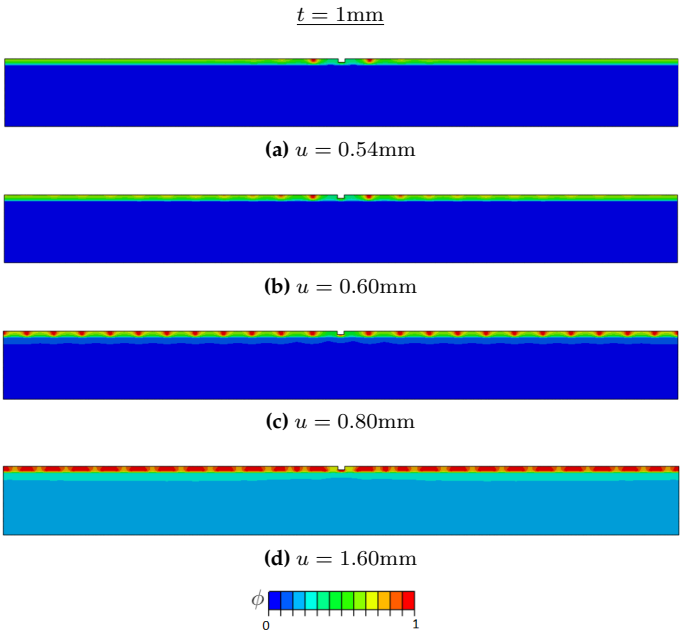

Figure 137: Crack evolution for the fracture energy ratio $G_{c1}/G_{c2} = 0.01$ and upper layer thickness 1mm.

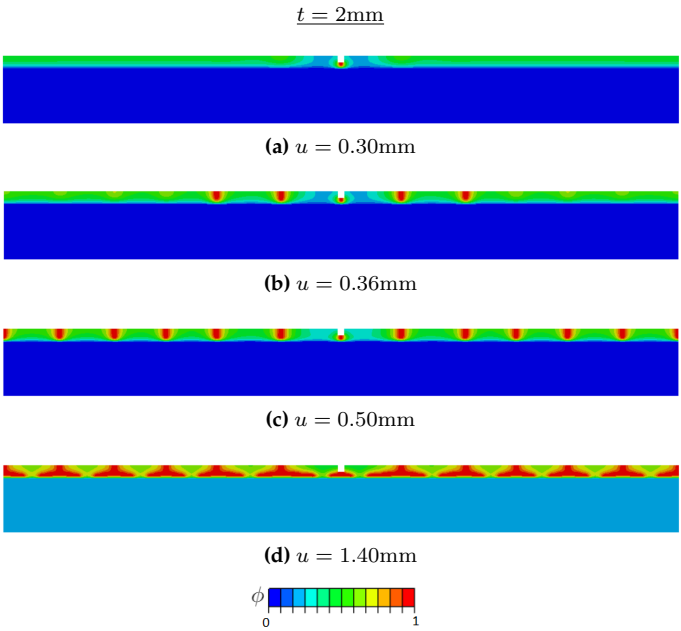

Figure 138: Crack evolution for the fracture energy ratio $G_{c1}/G_{c2} = 0.01$ and upper layer thickness $t = 2\text{mm}$.

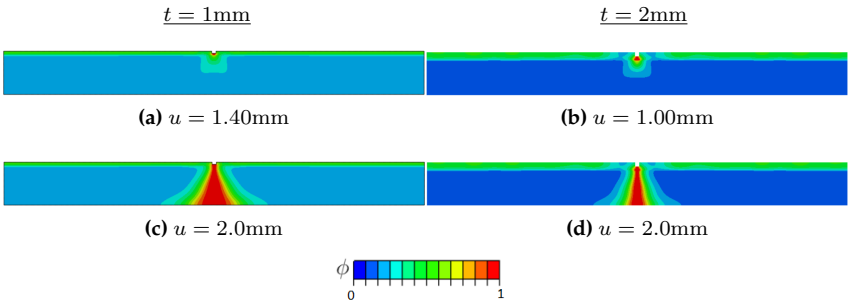

Figure 139: Crack evolution for the fracture energy ratio $G_{c1}/G_{c2} = 0.1$.

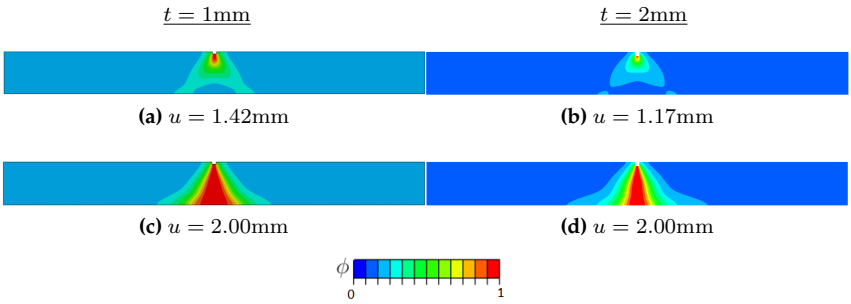

Figure 140: Crack evolution for Young's modulus ratio $G_{c1}/G_{c2} = 1$.

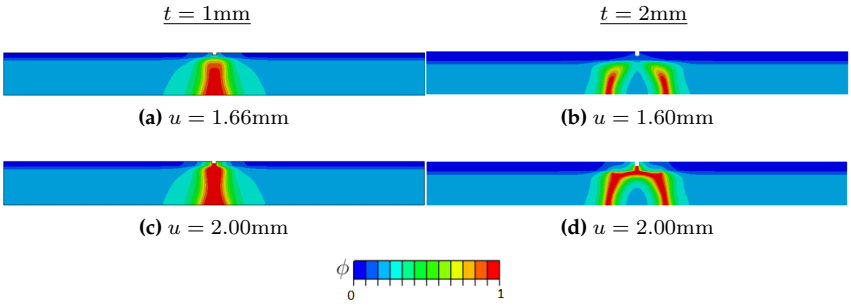

Figure 141: Crack evolution for the fracture energy ratio $G_{c1}/G_{c2} = 10$.

5.3.4 Thin linear elastic layer on hyperelastic substrate

The present Section expands the results obtained in the previous one considering more realistic multi-material joints. In fact, in real applications, the components of structural joints do not differ for only one material parameter at a time, but the mismatch regards all the mechanical properties. Hence, in this Section, the simulations are carried out considering a polymeric substrate joined to other materials with very different properties.

In particular, Table 16 reports the mechanical properties of the considered materials: silicone, aluminium and copper. Very often, in flexible electronics and solar cells application, the PET polymer is coupled to these materials, and it is more flexible than the linear elastic layer.

Material	$\mathbf{E}$ [GPa]	ν	λ [GPa]	μ [GPa]	$\mathbf{G_c}$ [N/mm]	$\boldsymbol{\sigma}_c$ [MPa]	$\mathbf{l_0}$ [mm]
PET (substrate)	2.80	0.37	2.91	1.02	10.34	55	1.00
Aluminium	64	0.33	46.70	24.06	20.00	190	3.73
Copper	120	0.34	95.15	44.78	0.57	222	0.15
Silicone	130	0.16	26.37	56.03	0.04	72	0.1

Table 16: Mechanical properties of linear elastic materials used for the bi-layer plate simulations.

For the simulations carried out under plane strain hypothesis, the upper layer is considered linear elastic using the Kirchhoff-Saint Venant constitutive law. In contrast, the lower layer is modeled as Neo-Hookean material (see 5.1 for the difference between these two constitutive models).

The first application considers the coupling of a silicone layer with a PET substrate, using the geometry and boundary conditions shown in Figure 142. With respect to the previous model, only the materials are different. The mesh size h has been chosen equal to 0.1mm, which in the case of the silicone material also corresponds to the length scale l_0. However, it is usually suggested a value of h smaller than l_0 (in [163] the suggested value is $h \leq 1/2 l_0$) our numerical tests involving hyperelastic materials show that reducing the mesh size leads to a higher distortion

of the elements, especially around the crack path, and arrests the convergence of the simulation.

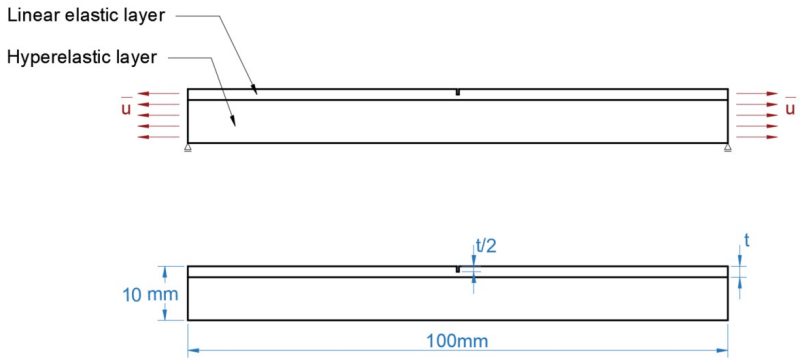

Figure 142: Geometry and boundary conditions for a bilayer joint with linear elastic and hyperelastic components. The simulations consider $t = 1, 2, 3, 4, 5\text{mm}$.

The influence of the upper layer thickness is shown in Figure 143. For each simulation, the crack pattern is depicted through different snapshots in Figures 144, 145 and 146.

For the silicone layer thickness equal to 1mm, the crack starts from the notch and propagates till the interface (Figure 144a), causing a first drop of the load in the force-displacement curve. With the increase of the applied displacement, while the first one propagates horizontally (Figure 144b), new equidistant cracks start from the upper layer in the proximity of the lateral edges, corresponding to other load drops. The phenomenon repeats creating crack pattern composed by equidistant cracks in the upper layer (Figure 144c and 144d) till the complete debonding from the substrate (Figure 144e).

For thicker silicone layers ($t = \{2.0, 3.0, 4.0, 5.0\}\text{mm}$), the crack firstly propagates vertically within the upper layer, causing a first drop in the relative load-displacement curve. At the interface with the polymeric substrate, the crack is deflected and branches horizontally until the sub-

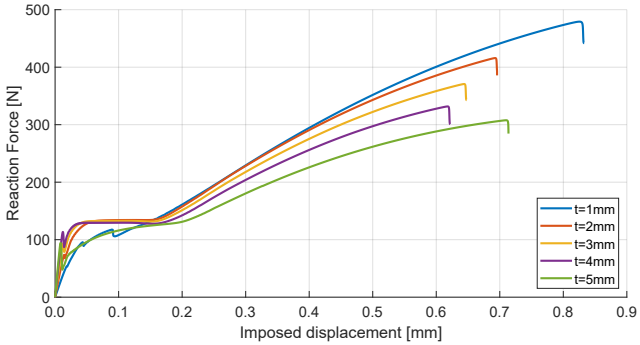

Figure 143: Thickness influence on the response of a bilayer structure composed by a linear elastic silicone layer (top) and a hyperelastic PET layer (bottom).

strate's debonding, without the initiation of a new crack from the upper edge. The phase-field evolution is very similar to each other for all current the simulations, being depicted in Figures 145 and 146.

The second set of simulations compares the results already obtained for the silicone-PET joint with the response of the same polymeric substrate coupled with thin aluminum and copper layers. The displacement-force curves have been plotted in Figure 147 considering the upper layer thickness equal to $t = 1\text{mm}$ and $t = 2\text{mm}$.

The load-displacement curve for the aluminium layer corresponds to a crack propagation that starts from the notch and propagates vertically through the two layers, as shown in Figure 148, for both the upper layer thicknesses 1mm and 1mm. Moreover, it can be noticed that the failure of the aluminium-PET joint shows a discontinuity corresponding to arrival of the crack at the interface in Figures 148a and 148b, before propagating across it as captured in Figures 148c and 148e for $t = 1\text{mm}$ and in Figures 148d and 148f for $t = 2\text{mm}$.

Looking at the copper-PET joint crack evolution for the smaller thickness, the phase-field evolution shows the formation of cracks equidistant from the notch that propagates till the central crack propagates through

$t = 1\text{mm}$

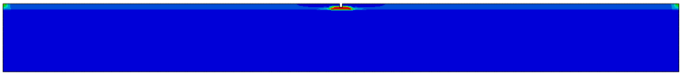

(a) $u = 0.08\text{mm}$

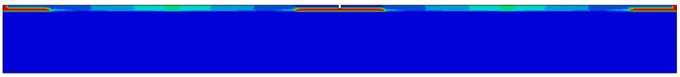

(b) $u = 0.18\text{mm}$

(c) $u = 0.19\text{mm}$

(d) $u = 0.40\text{mm}$

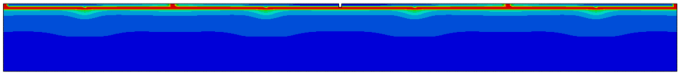

(e) $u = 1.64\text{mm}$

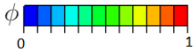

Figure 144: Crack evolution for the joint composed by the PET substrate and silicone layer of thickness $t = 1\text{mm}$.

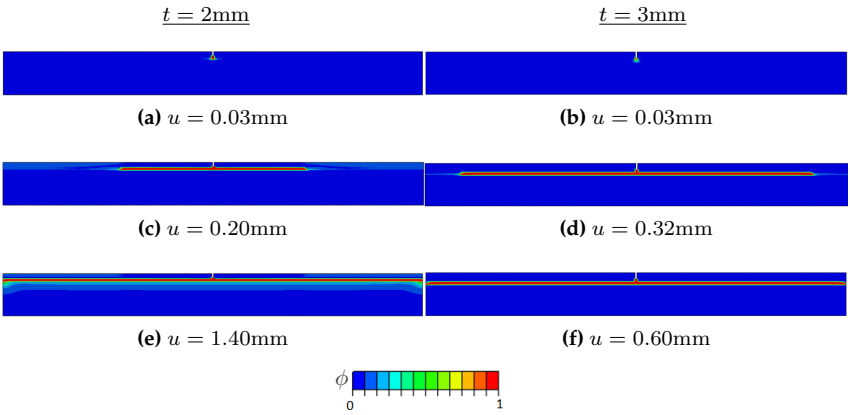

Figure 145: Crack evolution for the joint composed by the PET substrate and silicone layer with $t = \{2.0, 3.0\}$mm.

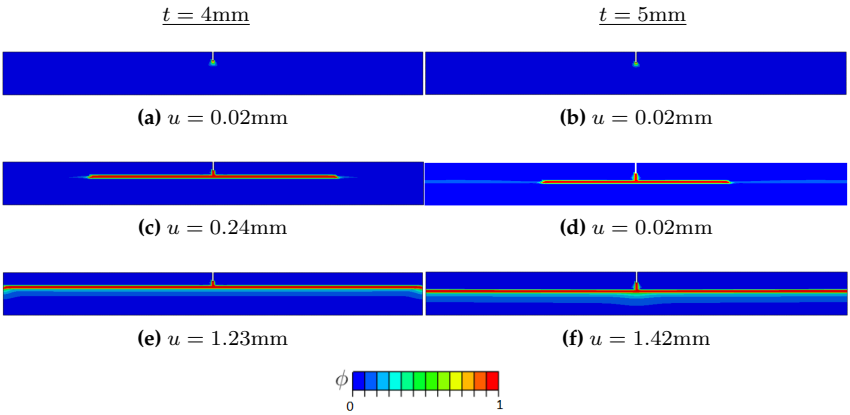

Figure 146: Crack evolution for the joint composed by the PET substrate and silicone layer with $t = \{4.0, 5.0\}$mm.

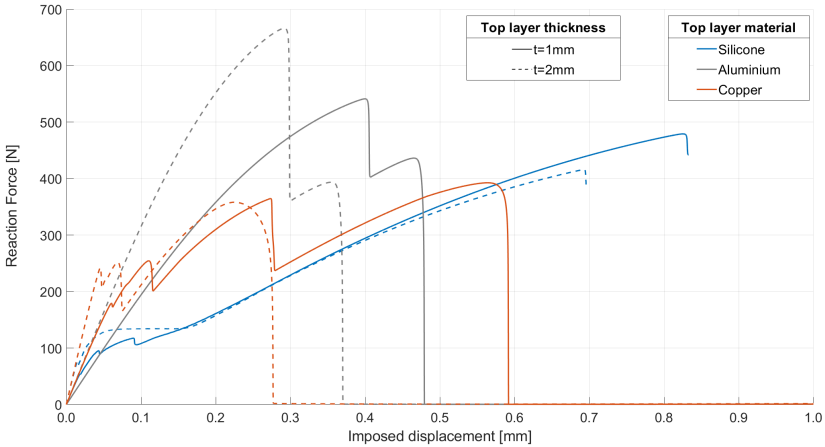

Figure 147: Thickness and material properties influence on the response of a bilayer structure composed by a PET layer (lower layer, hyperelastic) and different linear elastic layers: aluminium, copper and silicon, with different thickness.

.

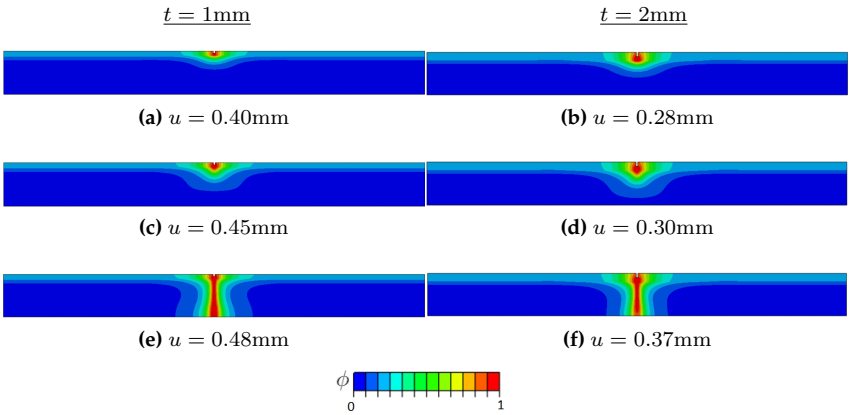

(a) $u = 0.40\text{mm}$ **(b)** $u = 0.28\text{mm}$

(c) $u = 0.45\text{mm}$ **(d)** $u = 0.30\text{mm}$

(e) $u = 0.48\text{mm}$ **(f)** $u = 0.37\text{mm}$

Figure 148: Crack evolution for the bilayer joint with aluminium layer of thickness $t = \{1.0, 2.0\}\text{mm}$.

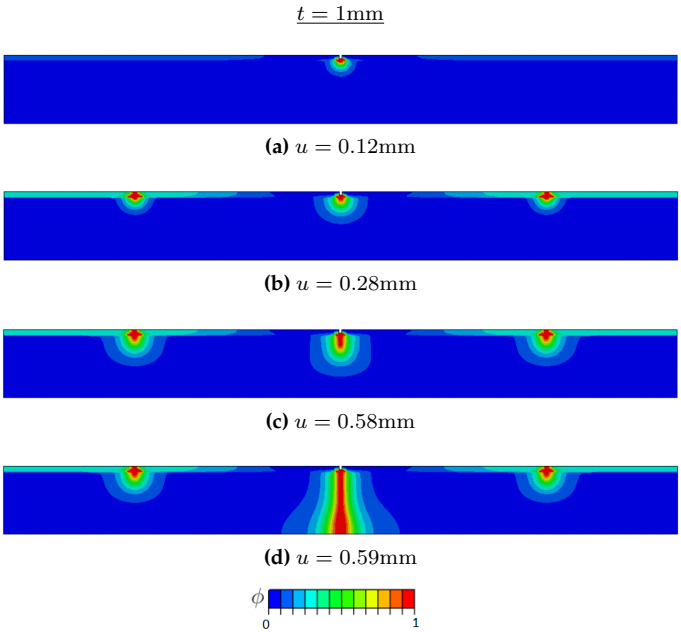

Figure 149: Crack evolution for the plate with copper layer of thickness $t = 1\text{mm}$.

the interface till the complete failure of the joint (see Figure 149). Silicone and copper have Young's modulus of the same order of magnitude, and this is reflected in a similar failure mode at the initial stage. However, the different G_{c1}/G_{c2} ratio, equal to 0.056 for the copper joint and 0.003 for the silicon one, determines the different crack path since the mismatch for the other mechanical parameters do not reach an order of magnitude. The thicker case $t = 2\text{mm}$, depicted in Figure 150, starts with a horizontal crack propagation (as in the corresponding silicone case), but the higher critical energy release rate translates into the propagation of the crack in the PET layer and the failure of the joint.

The described simulations have been developed considering only phase-field elements without coupling with CZM elements at the interface between the two layers, which will be considered for future developments

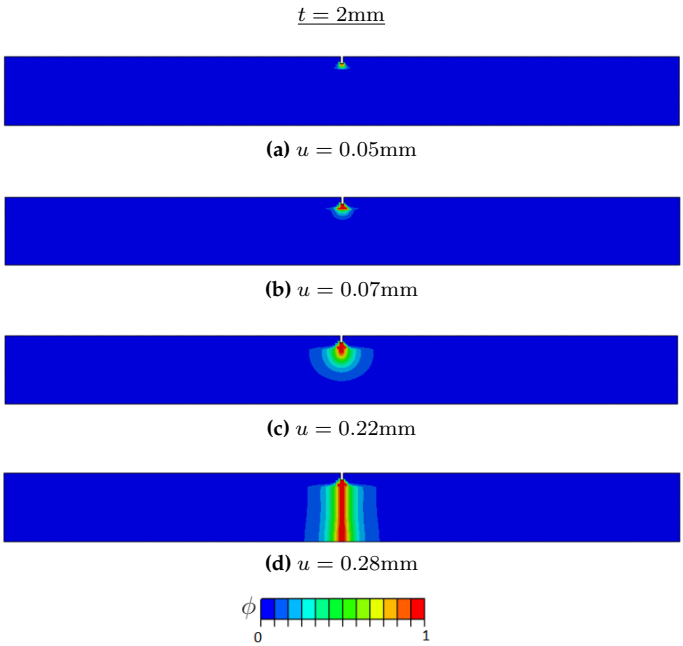

Figure 150: Crack evolution for the plate with copper layer of thickness $t = 2\text{mm}$.

of the topic. As shown in this Section, the crack propagation along the interface is already captured by the present formulation, allowing to analyze the competition between crack penetration and debonding in the layered structure.

Chapter 6

Conclusion and future developments

The research work conducted in this thesis regards the development of new methods to assess the reliability of structural joints, focusing on the performance of adhesive bonded joints and structures with complex interfaces. The morphology of the interface between the bonded components highly influences the overall performance of a structural joint. The industrial sector shows a growing interest in optimized surfaces with a controlled roughness or micro-structures to improve the mechanical features of structures obtained by joining different materials.

The thesis's main results will be presented in the following Sections, together with a brief discussion on possible future developments for each of the topics addressed in the previous Chapters.

6.1 Multi-scale FEM-BEM formulation for rough contact problems: main results and future investigations

The first topic of discussion in this thesis regards the influence of the surface's morphological properties on the stress transfer between compo-

nents directly in contact in the context of computational contact mechanics. While different experimental methods allow the characterization of the surface topography, the computational tools dealing with macro-scale components are not adequate to capture also the influence of roughness which is observed at a much smaller scale: a numerical model of a structural joint taking into account the surface morphology would require both a macro-scale representation of the joints components and an accurate representation of the roughness at the micro-scale and the necessary computational effort for such a model would be very high.

To overcome this issue, the research project proposes a multi-scale approach combining novel interface finite elements to simulate the solids interactions at the macro-scale with the boundary element approach at the micro-scale to simulate the rough contact at the interface. Specifically, assuming a frictionless contact problem, the macro-scale interface is modeled as nominally flat using interface finite elements and storing the information regarding the surface roughness within the element routine. A statistically representative rough surface can be used as input of the model or different surface topography that can be varied with the position along the macro-scale finite element model's contact surface. The interface finite element provides the information regarding the surfaces' separation in terms of relative displacement in the normal direction to a subroutine based on the boundary element method for solving the contact problem at each integration point. The boundary element method provides the homogenized normal contact traction and the normal contact stiffness to the macro-scale interface finite element.

This approach allows the solution of rough contact problems without any assumption on the surface height field's statistical distribution. With respect to a micro-mechanical approach, the computational cost increases because of the necessity to use the BEM algorithm at each integration point. However, possible acceleration strategies have been proposed based on different approximations of the Jacobian used in the iterative solution scheme. Moreover, the possibility of exploiting an off-line solution of the contact problem at the micro-scale. Advantages and disadvantages for each of the three alternatives have been compared and

discussed through benchmark tests.

Aside from extending the framework to 3D simulations and to different contact geometry, the computational framework can be considered for multi-field problems involving friction, thermal conduction, and wear, extracting information on the contact area directly from the microscale. In the case of wear, the rough surface height field could be updated along the simulation according to the wear law.

6.2 Main results and future developments for silicone-based adhesive joints

The role of roughness in adhesive bonded joints has been investigated in Chapter 3. Adhesive technology is used extensively in the aerospace and automotive industry, civil engineering, and everyday objects due to good mechanical performance, total weight reduction, reduced cost, and ease of bonding realization compared to other binding techniques such as bolting, mechanical fastenings, or welding. Hence, it is necessary to introduce new methods to assess the bonding strengths of adhesive joints, especially in complex interfaces, as in the presence of microstructured or rough surfaces.

Roughness influence has been investigated through $90°$ and $180°$ peeling tests on a two-component silicone adhesive used to bond flexible polymeric strips to thermoplastic substrates having specific rough surfaces. The substrates' surface topography was previously acquired through a non-contact profilometer and analyzed to determine the statistically representative surface for each substrate type. The peeling test results have been analyzed in terms of adhesive thickness influence, roughness characteristics, and failure mechanism.

The $90°$ peeling tests show that peeling force increases for increasing thickness values. Moreover, the influence of roughness is visible only for samples having the ratio between the adhesive thickness and the r. m. s. of the statistically representative heights field below a certain threshold that has been proposed as an indicator for adhesive joints design. No relation between the surface topography and the peeling force has been

found for the 180° peeling set-up. Finally, the failure mechanism has been analyzed by acquiring post-peeling images of the substrates and the strips and processing them with a routine implemented in Matlab to differentiate between adhesive and cohesive failure. The experimental results show that the peeling curve has a load drop when the failure mechanism changes from cohesive to adhesive failure and that mixed-mode mechanisms are characterized by a higher peeling force and a ridge pattern on the failure surface, indicating a higher energy dissipation.

The described experimental analyses have been used to formulate a zeroth-thickness interface finite element introducing the interface law dependence on the roughness properties and the adhesive thickness by computing an effective thickness of the adhesive layer. This model has been tested against the experimental curves showing a limited efficiency, especially in the case of the smallest thickness. The identification of the cohesive zone model parameters cannot be based on the simple modification of the interface law's initial stiffness through the effective thickness of the adhesive, as in the proposed model. Although the roughness effect can be used to classify the peeling response and the failure mechanisms experimentally, the computational model requires a more complex algorithm to capture the analyzed system's correct mechanical response.

The proposed model could be enriched by adding other relations between the interface constitutive law and the surface topology to improve the simulation accuracy. A possible strategy could introduce other statistical quantities to describe the sample roughness as the average slope of profiles since an empirical dependence of the peeling force on this statistical parameter has been found in [80] for FRP-concrete joints. A more complex algorithm for the interface parameters identification could be explored as well, for example, adopting a genetic algorithm to compute the adhesive fracture energy at each point of the interface according to the rough surface heights field. Another possible approach is represented by the simulation of the failure mechanisms observed in the peeling tests through the phase-field approach seen in Chapter 5 coupled with the cohesive zone model at the adhesive interfaces to model the crack propagation and the eventual migration from cohesive to adhesive

failure.

6.3 Computational framework for bio-inspired MSAMSs adhesives: conclusions and future applications

Chapter 4 presents a novel computational framework for the simulation of bio-inspired adhesives since the experimental results show the great potentiality of this technology compared to traditional pressure-sensitive adhesives. In particular, bio-mimetic PVS adhesive samples with mushroom-shaped microstructures have been analyzed in pull-off tests. The experimental data have been used to develop an interface finite element model capable of reproducing the adhesive performance without modeling the complex surface in detail.

The first step regards the identification of the dominant parameters affecting the adhesive response in the experimental tests. In line with the literature, the MSAMSs adhesive's pull-off strength depends on the maximum load reached during the loading phase and on the tilt angle with which the test is conducted. This last aspect is relevant for the applications since the detachment from the adhering surface can be sped up by increasing the inclination of the peeling force. The loading and unloading data have been fitted using polynomial surfaces depending on the gap separation between the adhesive surfaces, the unloading gap, and the applied tilt angle. Hence, the functions have been transferred inside the interface finite element routine and decomposed in the normal and tangential directions.

After comparing the experimental results, the proposed framework has been used to reproduce a loading and unloading test of a polymeric layer from a glass substrate with a tilt angle variable during the simulation, aiming at simulating conditions similar to possible industrial applications of the MSAMSs adhesives. The method's potentiality could be further investigated by extending the method to a 3D setting and simulating more complex applications and prototypes exploiting the pat-

terned adhesives technology.

6.4 Conclusions and future developments for the phase-field approach for crack propagation in rubber-like materials

The final Chapter deals with a different perspective on structural joints considering the adhesive layer as bulk material instead of an interface. In many applications, adhesives can experience large deformations, high-stress states, and consequent crack propagation, especially when the adhesive thickness is comparable with components dimensions. In this case, the adhesive layers perform as hyperelastic materials and require the introduction of a different computational approach for simulating the crack initiation and propagation. For this reason, the phase-field approach for fracture has been exploited to simulate the failure of polymeric materials in structural joints.

The phase-field approach has been formulated in the framework of finite elasticity and used to study the effect of material properties mismatch on the crack propagation in bilayer structures. A parametric study has been conducted varying the mechanical and fracture parameters of the layers and considering the effect of the components' thickness. The parameters influence the failure mechanism since the crack path not always starts from the notch and propagates through the layers, but also it can give origin to the failure of the upper layer only with the formation of subsequent and equidistant cracks for low values of upper layer thickness and when the upper layer fracture energy is two order of magnitude lower than the lower layer values. The phase-field method has also been applied to simulate hyperelastic PET substrate coupled with copper, aluminum, and silicone layers, showing very different crack paths.

The analysis can be further developed considering a coupling of the phase-field elements used in the bulk with cohesive zone model elements at the interface for finite elasticity. Although the proposed framework already captures the crack propagation at the interface, the cou-

pling could provide a better insight into the different failure mechanisms. There are different possible interface laws available in the literature that can be used for the coupling with the phase-field parameter. For example, bilinear and cut-off interface laws have been already proposed in [144] and [143]. The coupling with the nonlinear Tvergaard's traction-displacement curve [164] is a matter of ongoing research since it could offer a better convergence of the algorithm. The large deformation of the phase-field finite elements used in the hyperelastic bulk already represents a computational challenge so the treatment of the interface needs particular care. Moreover, the Tvergaard's interface law would provide a gradual degradation of the interface, compared to the cut-off relation. Finally, other possible developments are represented by the extension of the phase-field framework to anisotropic fracture, thermoelasticity, and fatigue fracture.

Appendix A

Polynomial fitting functions coefficients

The present Appendix includes the list of the polynomial function coefficients computed in Chapter 4. Table 17 contains the coefficients for the polynomial curves used for the loading phase, Table 18 the coefficients for the functions approximating the maximum adhesion traction dependence on the unloading displacement. Tables 19 and 20 include the coefficients for the increasing unloading surfaces. Finally, Tables 21 and 22 contain the coefficients for the decreasing unloading surfaces.

$\alpha = 0°$:	$c(1) = 0.0$
	$c(2) = -0.348933027618362$
	$c(3) = 0.171484306567843$
	$c(4) = 0.0$
$\alpha = 0.5°$:	$c(1) = 0.0566085807852187$
	$c(2) = -0.0617142175273165$
	$c(3) = 0.0860113917812453$
	$c(4) = 0.0$
$\alpha = 1°$:	$c(1) = 0.0566085807852187$
	$c(2) = -0.0617142175273165$
	$c(3) = 0.0860113917812453$
	$c(4) = 0.0$
$\alpha = 1.5°$:	$c(1) = 0.0443670546774775$
	$c(2) = -0.0860361564252807$
	$c(3) = 0.0336779154090824$
	$c(4) = 0.0$
$\alpha = 2°$:	$c(1) = 0.0544663676200605$
	$c(2) = -0.0747052966270060$
	$c(3) = 0.0277303528486271$
	$c(4) = 0.0$
$\alpha = 2.5°$:	$c(1) = 0.0348500253533823$
	$c(2) = -0.0871720034176629$
	$c(3) = 0.0137564199947493$
	$c(4) = 0.0$
$\alpha = 3°$:	$c(1) = -0.00469001236727667$
	$c(2) = -0.116048448956937$
	$c(3) = -0.000125731051997244$
	$c(4) = 0.0$
$\alpha = 3.5°$:	$c(1) = -0.000548369895549598$
	$c(2) = -0.110248463203831$
	$c(3) = -0.00428372597255402$
	$c(4) = 0.0$
$\alpha = 4°$:	$c(1) = 0.0189274812352287$
	$c(2) = -0.0749721904841677$
	$c(3) = 0.00132910905674283$
	$c(4) = 0.0$

Table 17: Coefficients for the polynomial fitting function used for the loading phase.

$\alpha = 0°$:	$c(1) = -0.0079$
	$c(2) = 0.5538$
$\alpha = 0.5°$:	$c(1) = -0.0349242927922089$
	$c(2) = 0.618196175304598$
$\alpha = 1°$:	$c(1) = 0.00550090496585975$
	$c(2) = 0.562970086873730$
$\alpha = 1.5°$:	$c(1) = -0.0349242927922089$
	$c(2) = 0.618196175304598$
$\alpha = 2°$:	$c(1) = 0.203506691806733$
	$c(2) = 0.484407234380967$
$\alpha = 2.5°$:	$c(1) = 0.331504364913189$
	$c(2) = 0.508460864027320$
$\alpha = 3°$:	$c(1) = 0.423357568851700$
	$c(2) = 0.499824859526338$
$\alpha = 3.5°$:	$c(1) = 0.404311085739681$
	$c(2) = 0.532681023849793$
$\alpha = 4°$:	$c(1) = 0.414359030950649$
	$c(2) = 0.456188273479555$

Table 18: Coefficients for the polynomial fitting function used for the maximum adhesive traction.

$\alpha = 0°$:	$c(1) = -0.0138755267136547$	$\alpha = 1.5°$:	$c(1) = -0.00682691144175060$
	$c(2) = 0.156247456543133$		$c(2) = 0.0885837973830941$
	$c(3) = -0.244296117516819$		$c(3) = -0.107700762401314$
	$c(4) = -0.588509698891207$		$c(4) = -0.111559621390995$
	$c(5) = -0.727553093566541$		$c(5) = -0.0539021696646330$
	$c(6) = -0.127854320568900$		$c(6) = -0.0648026232654176$
	$c(7) = 0.637909422883284$		$c(7) = -0.207117327620995$
	$c(8) = -1.40880974735903$		$c(8) = 0.129553030093155$
	$c(9) = -0.472232288720151$		$c(9) = -0.0387431908808649$
	$c(10) = -0.307136991635085$		$c(10) = 0.139520733054923$
	$c(11) = 2.38995453288998$		$c(11) = -0.433552021469844$
	$c(12) = -1.09398252471844$		$c(12) = 0.216480624567229$
	$c(13) = 0.464835214155747$		$c(13) = -0.00531605484453032$
	$c(14) = -0.304898491041879$		$c(14) = 0.254243748733964$
	$c(15) = 1.51038686069351$		$c(15) = -0.269466127252665$
$\alpha = 0.5°$:	$c(1) = -0.0357605447831750$	$\alpha = 2°$:	$c(1) = -0.0126376524566409$
	$c(2) = 0.108767101009007$		$c(2) = 0.0458369414353075$
	$c(3) = -0.245676159853886$		$c(3) = -0.0807769872919593$
	$c(4) = -0.217802110138767$		$c(4) = -0.0491003653879599$
	$c(5) = -0.0637913490204055$		$c(5) = -0.0849051156341541$
	$c(6) = -0.208718885598716$		$c(6) = -0.0349541389603931$
	$c(7) = 0.145634823771983$		$c(7) = -0.0717109117559895$
	$c(8) = -0.288485749386917$		$c(8) = 0.137975949869645$
	$c(9) = -0.00203475749085533$		$c(9) = -0.0524653974772843$
	$c(10) = 0.0558357878349223$		$c(10) = 0.162373067369189$
	$c(11) = 0.248481905814094$		$c(11) = -0.306737458096844$
	$c(12) = 0.0134073514674846$		$c(12) = 0.152457647661829$
	$c(13) = 0.0605684865539400$		$c(13) = -0.0572698457569808$
	$c(14) = 0.226434520312288$		$c(14) = 0.348629352980202$
	$c(15) = 0.00783418792403732$		$c(15) = -0.289463457178687$
$\alpha = 1°$:	$c(1) = -0.0306387173116903$	$\alpha = 2.5°$:	$c(1) = -0.00464119961104771$
	$c(2) = 0.133852363252434$		$c(2) = 0.0468116387824264$
	$c(3) = -0.211034927412920$		$c(3) = -0.0606863012553418$
	$c(4) = -0.229072090860856$		$c(4) = -0.0689961801100444$
	$c(5) = -0.0263724724959447$		$c(5) = -0.0560911852341231$
	$c(6) = -0.172056559995526$		$c(6) = -0.0170645894465773$
	$c(7) = 0.0827338627157611$		$c(7) = 0.0997097258359764$
	$c(8) = -0.265209053297762$		$c(8) = -0.0870064320043343$
	$c(9) = 0.000175368645589642$		$c(9) = -0.00894594300584743$
	$c(10) = 0.187373310525139$		$c(10) = -0.139327419284266$
	$c(11) = 0.198648559653793$		$c(11) = 0.212804160081914$
	$c(12) = -0.00227037209582717$		$c(12) = -0.0712121226905289$
	$c(13) = 0.0776241577552187$		$c(13) = -0.132347732694954$
	$c(14) = 0.377273150012847$		$c(14) = 0.192479231068380$
	$c(15) = -0.00207712350014786$		$c(15) = -0.0595892704218405$

Table 19: Coefficients for the polynomial fitting function used for the increasing unloading phase. Part 1.

$\alpha = 3°$:	$c(1) = 0.00251458239770183$
	$c(2) = 0.0268582815060989$
	$c(3) = -0.0203356255928623$
	$c(4) = -0.0875100790324755$
	$c(5) = -0.0254016523601123$
	$c(6) = 0.00973430491368201$
	$c(7) = 0.0798911520709363$
	$c(8) = -0.0681383048758113$
	$c(9) = 0.00388484690179301$
	$c(10) = -0.0468567021464576$
	$c(11) = 0.0869293695876745$
	$c(12) = -0.0312290428658122$
	$c(13) = -0.0171735813476650$
	$c(14) = 0.0278838714516626$
	$c(15) = -0.00873403368615002$
$\alpha = 3.5°$:	$c(1) = -0.000387528896944143$
	$c(2) = 0.0222231491480431$
	$c(3) = -0.0253699789063068$
	$c(4) = -0.120863535261184$
	$c(5) = 0.0175697339788312$
	$c(6) = 0.000598278129633446$
	$c(7) = 0.0668722418267462$
	$c(8) = -0.0904446344587583$
	$c(9) = 0.0366833568091971$
	$c(10) = 0.0599545409983287$
	$c(11) = -0.0872889586302977$
	$c(12) = 0.0354360421630659$
	$c(13) = 0.0649400567403295$
	$c(14) = -0.0943167720272832$
	$c(15) = 0.0313148539599541$
$\alpha = 4°$:	$c(1) = -0.00345026232959323$
	$c(2) = 0.0236036032809484$
	$c(3) = -0.0382205070940479$
	$c(4) = -0.0814533397451027$
	$c(5) = -0.00202886509455055$
	$c(6) = -0.00725361138057823$
	$c(7) = 0.0662072351787638$
	$c(8) = -0.0488994266941352$
	$c(9) = 0.0103500904712445$
	$c(10) = 0.0381786950913424$
	$c(11) = -0.0371887075248087$
	$c(12) = 0.0145652487899819$
	$c(13) = 0.0615404555215095$
	$c(14) = -0.0812011328372074$
	$c(15) = 0.0230862947832793$

Table 20: Coefficients for the polynomial fitting function used for the increasing unloading phase. Part 2.

$\alpha = 0°$:	$c(1) = 105.140406921943$	$\alpha = 1.5°$:	$c(1) = 1.64700874578315$
	$c(2) = -778.176040681610$		$c(2) = -16.5401102807058$
	$c(3) = -0.585570221220716$		$c(3) = 0.769127002791122$
	$c(4) = 2292.06213263112$		$c(4) = 64.2627819836151$
	$c(5) = 42.2599161181913$		$c(5) = -7.15678403467021$
	$c(6) = 22.9315683799871$		$c(6) = 0.0117800739050713$
	$c(7) = -3358.26485825349$		$c(7) = -120.791896077143$
	$c(8) = -194.596410229804$		$c(8) = 19.7407652007014$
	$c(9) = -107.402394749600$		$c(9) = -0.510514417549132$
	$c(10) = 2447.51847791845$		$c(10) = 109.722445477554$
	$c(11) = 290.918720898563$		$c(11) = -22.9543906849532$
	$c(12) = 161.132081757170$		$c(12) = 0.763637587445181$
	$c(13) = -709.837595745579$		$c(13) = -38.6716298480228$
	$c(14) = -140.830466286573$		$c(14) = 9.65724346256964$
	$c(15) = -78.5163965989426$		$c(15) = -0.382247083874124$
$\alpha = 0.5°$:	$c(1) = 181.327095620153$	$\alpha = 2°$:	$c(1) = 0.493482822110671$
	$c(2) = -1362.23643688171$		$c(2) = -5.50682063484540$
	$c(3) = -358.662818671935$		$c(3) = -0.0256010598447480$
	$c(4) = 4056.78600646084$		$c(4) = 23.4412637096195$
	$c(5) = 2038.91365919043$		$c(5) = -0.716781339416994$
	$c(6) = 19.4508958588012$		$c(6) = -0.114579562820626$
	$c(7) = -5987.66491299123$		$c(7) = -47.3557481302639$
	$c(8) = -4329.09079745761$		$c(8) = 2.44200039815629$
	$c(9) = -79.9163417900632$		$c(9) = 0.489399237873247$
	$c(10) = 4381.12592047691$		$c(10) = 45.3164057627585$
	$c(11) = 4064.23358058317$		$c(11) = -3.35252116762305$
	$c(12) = 107.718712954063$		$c(12) = -1.13334282096398$
	$c(13) = -1271.80421033372$		$c(13) = -16.4956201753299$
	$c(14) = -1423.09123123988$		$c(14) = 1.84490361977576$
	$c(15) = -48.1123777934344$		$c(15) = 0.879855312831650$
$\alpha = 1°$:	$c(1) = 225.060666520605$	$\alpha = 2.5°$:	$c(1) = -0.227018984309417$
	$c(2) = -1734.99876760830$		$c(2) = 1.83192767944990$
	$c(3) = -38.0110875102511$		$c(3) = -0.323281266856323$
	$c(4) = 5321.59398859712$		$c(4) = -5.28778445473530$
	$c(5) = 235.147795208501$		$c(5) = 1.54230259306333$
	$c(6) = -2.53541929170946$		$c(6) = -0.0937701274726055$
	$c(7) = -8115.51045732135$		$c(7) = 7.12773177320101$
	$c(8) = -544.167794342736$		$c(8) = -3.51619879675288$
	$c(9) = 12.3508766821054$		$c(9) = 0.309946245687698$
	$c(10) = 6152.56119757218$		$c(10) = -4.74797889852978$
	$c(11) = 553.762330960345$		$c(11) = 3.67868551760612$
	$c(12) = -21.5813279381053$		$c(12) = -0.592202728312768$
	$c(13) = -1855.03728022235$		$c(13) = 1.28745944297607$
	$c(14) = -208.513113089210$		$c(14) = -1.47960322158605$
	$c(15) = 12.6038245588319$		$c(15) = 0.349009385455814$

Table 21: Coefficients for the polynomial fitting function used for the decreasing unloading phase. Part 1.

$\alpha = 3°$:	$c(1) = 0.0174677453507217$
	$c(2) = -0.196596644846134$
	$c(3) = -0.0201640932667409$
	$c(4) = 0.997477268332579$
	$c(5) = -0.295716980326397$
	$c(6) = -0.000864282362649289$
	$c(7) = -2.24971827217910$
	$c(8) = 0.972738525399850$
	$c(9) = -0.106706278721029$
	$c(10) = 2.24701282643363$
	$c(11) = -1.08575931867458$
	$c(12) = 0.117263246395818$
	$c(13) = -0.812872869284320$
	$c(14) = 0.487202572782801$
	$c(15) = 0.0380969643969823$
$\alpha = 3.5°$:	$c(1) = 0.00745885656760642$
	$c(2) = -0.184554218856766$
	$c(3) = -0.0650601961135821$
	$c(4) = 1.55284154588379$
	$c(5) = 0.144635532517333$
	$c(6) = -0.0340462521525089$
	$c(7) = -4.87705563558546$
	$c(8) = -0.149072440821142$
	$c(9) = 0.178691413982253$
	$c(10) = 6.27239417899551$
	$c(11) = -0.221052784508678$
	$c(12) = -0.498533456731706$
	$c(13) = -2.86553617705132$
	$c(14) = 0.286086687607921$
	$c(15) = 0.352753884066751$
$\alpha = 4°$:	$c(1) = 0.0454070306245241$
	$c(2) = -0.327056395697731$
	$c(3) = 0.0328825577465779$
	$c(4) = 1.10810512000707$
	$c(5) = -0.494281958682189$
	$c(6) = 0.0170214767227383$
	$c(7) = -2.06198931833517$
	$c(8) = 1.28313911774286$
	$c(9) = -0.182610857053950$
	$c(10) = 1.89741492937993$
	$c(11) = -1.40911508844308$
	$c(12) = 0.260551426148524$
	$c(13) = -0.693886243736073$
	$c(14) = 0.562098689862091$
	$c(15) = -0.113774975499430$

Table 22: Coefficients for the polynomial fitting function used for the decreasing unloading phase. Part 2.

Bibliography

[1] Romina Lopes Fernandes et al. "From thin to extra-thick adhesive layer thicknesses: Fracture of bonded joints under mode I loading conditions". In: *Engineering Fracture Mechanics* 218 (Sept. 2019), p. 106607. ISSN: 00137944. DOI: 10.1016/j.engfracmech.2019.106607.

[2] "How pure mode I can be obtained in bi-material bonded DCB joints: A longitudinal strain-based criterion". In: *Composites Part B: Engineering* 153 (Nov. 2018), pp. 137–148. ISSN: 13598368. DOI: 10.1016/j.compositesb.2018.07.033.

[3] *File:AAMD-Adhesive-Solutions.pdf*. URL: http://www.unioneses%20adhesivas.com/wp-content/uploads/2014/07/AAMD-Adhesive-Solutions.pdf (visited on 03/16/2021).

[4] Stefan Böhm et al. "Civil construction". In: *Handbook of Adhesion Technology: Second Edition*. Vol. 2-2. Springer International Publishing, May 2018, pp. 1419–1447. ISBN: 9783319554112. DOI: 10.1007/978-3-319-55411-2_49. URL: https://doi.org/10.1007/978-3-319-55411-2_49.

[5] *File:Charlemagne building - August 2008.jpg - Wikimedia Commons*. URL: https://commons.wikimedia.org/wiki/File:Charlemagne%7B%5C_%7Dbuilding%7B%5C_%7D-%7B%5C_%7DAugust%7B%5C_%7D2008.jpg (visited on 03/16/2021).

[6] *File:Crystal Picture*. URL: https://twitter.com/AkuHeinonen/status/1221876191226945540 (visited on 11/24/2020).

[7] *Chris Supranowitz's OPT 307 Final Project*. URL: http://www2.optics.rochester.edu/workgroups/cml/opt307/spr05/chris/ (visited on 03/16/2021).

[8] B. N.J. Persson et al. “On the nature of surface roughness with application to contact mechanics, sealing, rubber friction and adhesion”. In: *Journal of Physics Condensed Matter* 17.1 (2005). ISSN: 09538984. DOI: 10.1088/0953-8984/17/1/R01. eprint: 0502419v1.

[9] J Bico, C Marzolin, and D Quéré. “Pearl drops”. In: *Europhysics Letters (EPL)* 47.2 (July 1999), pp. 220–226. DOI: 10.1209/epl/i1999-00548-y.

[10] *File:Lotus2mq.jpg - Wikimedia Commons*. URL: https://commons.wikimedia.org/wiki/File:Lotus2mq.jpg (visited on 03/16/2021).

[11] W. Barthlott and C. Neinhuis. “Purity of the sacred lotus, or escape from contamination in biological surfaces”. In: *Planta* 202.1 (1997), pp. 1–8. ISSN: 00320935. DOI: 10.1007/s004250050096.

[12] *Confocal Microscopy — Principle & Applications — ibidi*. URL: https://ibidi.com/content/216-confocal-microscopy (visited on 03/16/2021).

[13] American Society of Mechanical Engineers et al. *Surface Texture: Surface Roughness, Waviness and Lay*. American Society of Mechanical Engineers. American Society of Mechanical Engineers, 2010. ISBN: 9780791832622.

[14] Geneva: International Organization for Standardization. *ISO 4287:1997: Geometric Product Specification (GPS). Surface Texture Profile Method: Terms, Definition and Surface Texture Parameters*. 1997.

[15] Geneva: International Organization for Standardization. *ISO 25178:2016: Geometric Product Specifications (GPS)— Surface texture: Areal*. 2016.

[16] Semiconductor Equipment & Materials Institute. *SEMI MF1811:2016: Guide for Estimating the Power Spectral Density Function and Related Finish Parameters from Surface Profile Data*. 2016.

[17] *Surface Texture Parameters Handbook Download*. URL: https://www.zygoserver.com/?/mailer/SurfaceTextureParametersHandbook.htm (visited on 03/16/2021).

[18] Enrico Gnecco and Ernst Meyer, eds. *Fundamentals of Friction and Wear*. Springer Berlin Heidelberg, 2007. ISBN: 978-3-540-36806-9. DOI: 10.1007/978-3-540-36807-6. URL: http://link.springer.com/10.1007/978-3-540-36807-6.

[19] Bharat Bhushan. “Surface roughness analysis and measurement techniques”. In: *Modern Tribology Handbook: Volume One: Principles of Tribology*. CRC Press, Dec. 2000. Chap. 2, pp. 49–119. ISBN: 9780849377877. DOI: 10.1201/9780849377877.ch2.

[20] A. Majumdar and B. Bhushan. “Role of fractal geometry in roughness characterization and contact mechanics of surfaces”. In: *Journal of Tribology* 112.2 (1990), pp. 205–216. ISSN: 15288897. DOI: 10.1115/1.2920243.

[21] Benoît Mandelbrot. *The Fractal Geometry of Nature*. W. H. Freeman and Co., 1982. ISBN: 0-7167-1186-9.

[22] M. Borri-Brunetto, A. Carpinteri, and B. Chiaia. “Scaling phenomena due to fractal contact in concrete and rock fractures”. In: *International Journal of Fracture* 95.1/4 (1999), pp. 221–238. ISSN: 03769429. DOI: 10.1023/A:1018656403170.

[23] *File:Wiki df figure.png - Wikimedia Commons*. URL: https://commons.wikimedia.org/wiki/File:Wiki%7B%5C_%7Ddf%7B%5C_%7Dfigure.png (visited on 03/16/2021).

[24] “A multivariate Weierstrass–Mandelbrot function”. In: *Proceedings of the Royal Society of London. A. Mathematical and Physical Sciences* 400.1819 (Aug. 1985), pp. 331–350. ISSN: 2053-9169. DOI: 10.1098/rspa.1985.0083.

[25] Jiunn Jong Wu. “Characterization of fractal surfaces”. In: *Wear* 239.1 (Apr. 2000), pp. 36–47. ISSN: 00431648. DOI: 10.1016/S0043-1648(99)00362-2.

[26] *Landscape generation using midpoint displacement — Bites of code*. URL: https://bitesofcode.wordpress.com/2016/12/23/landscape-generation-using-midpoint-displacement/ (visited on 03/16/2021).

[27] Alain Fournier, Don Fussell, and Loren Carpenter. “Computer Rendering of Stochastic Models”. In: *Commun. ACM* 25.6 (June 1982), pp. 371–384. ISSN: 0001-0782. DOI: 10.1145/358523.358553. URL: https://doi.org/10.1145/358523.358553.

[28] H.O. Peitgen, D. Saupe, and M.F. Barnsley. *The Science of fractal images*. Springer-Verlag, 1988. ISBN: 9780387966083.

[29] *Midpoint Displacement Antimatroid, The*. URL: https://antimatroid.wordpress.com%20/tag/midpoint-displacement/ (visited on 03/16/2021).

[30] M Paggi and JR Barber. “Contact conductance of rough surfaces composed of modified RMD patches”. In: *International Journal of Heat and Mass Transfer* 54 (2011), pp. 4664–4672. DOI: 10.1016/j.ijheatmasstransfer.2011.06.011.

[31] Paul Peter Anthony Mazza et al. “A new Palaeolithic discovery: tar-hafted stone tools in a European Mid-Pleistocene bone-bearing bed”. In: *Journal of Archaeological Science* 33.9 (2006), pp. 1310–1318. ISSN: 0305-4403. DOI: https://doi.org/10.1016/j.jas.2006.01.006.

[32] Martine Regert. “Investigation of prehistoric glues by gas chromatography—mass spectrometry”. In: *Journal of separation science* 27 (Feb. 2004), pp. 244–54. DOI: 10.1002/jssc.200301608.

[33] Gerd Habenicht. “From Adhesive to Adhesive Layer”. In: *Applied Adhesive Bonding*. Weinheim, Germany: Wiley-VCH Verlag GmbH & Co. KGaA, Dec. 2008, pp. 13–22. DOI: 10.1002/9783527626458.ch3. URL: http://doi.wiley.com/10.1002/9783527626458.ch3.

[34] *A microscopic photo of a post it note being pulled apart : interestingasfuck — Micro photography, Microscopic, Macro and micro*. URL: https://www.pinterest.es/pin/681450987357197433/ (visited on 03/16/2021).

[35] Lars Heepe and Stanislav N Gorb. “Biologically inspired mushroom-shaped adhesive microstructures”. In: *Annual Review of Materials Research* 44 (2014), pp. 173–203. ISSN: 15317331. DOI: 10.1146/annurev-matsci-062910-100458.

[36] *PU Casting Resin. Styling, Modelling and Tooling Boards. Epoxy Tooling Boards. Rapid Prototyping. Paste Materials. Adhesives. Gel Coats. - PDF Free Download*. URL: https://docplayer.net/103183293-Pu-casting-resin-styling-modelling-and-tooling-boards-epoxy-tooling-boards-rapid-prototyping-paste-materials-adhesives-gel-coats.html (visited on 03/16/2021).

[37] C. C. White et al. “Advances in structural silicone adhesives”. In: *Advances in Structural Adhesive Bonding*. Elsevier Inc., Jan. 2010. Chap. 4. DOI: 10.1533/9781845698058.1.66.

[38] Eduardo W. V. Chaves. “Hyperelasticity”. In: 2013, pp. 423–464. DOI: 10.1007/978-94-007-5986-2_9.

[39] M. Mooney. "A theory of large elastic deformation". In: *Journal of Applied Physics* 11.9 (Sept. 1940), pp. 582–592. ISSN: 00218979. DOI: 10.1063/1.1712836. URL: http://aip.scitation.org/doi/10.1063/1.1712836.

[40] R. W. Ogden. "Large deformation isotropic elasticity – on the correlation of theory and experiment for incompressible rubberlike solids". In: *Proceedings of the Royal Society of London. A. Mathematical and Physical Sciences* 326.1567 (Feb. 1972), pp. 565–584. ISSN: 2053-9169. DOI: 10.1098/rspa.1972.0026.

[41] Ellen M. Arruda and Mary C. Boyce. "A three-dimensional constitutive model for the large stretch behavior of rubber elastic materials". In: *Journal of the Mechanics and Physics of Solids* 41.2 (Feb. 1993), pp. 389–412. ISSN: 00225096. DOI: 10.1016/0022-5096(93)90013-6.

[42] Yves Staudt, Christoph Odenbreit, and Jens Schneider. "Failure behaviour of silicone adhesive in bonded connections with simple geometry". In: *International Journal of Adhesion and Adhesives* 82 (Apr. 2018), pp. 126–138. ISSN: 01437496. DOI: 10.1016/j.ijadhadh.2017.12.015.

[43] M D Banea and L F M Da Silva. "Adhesively bonded joints in composite materials: an overview". In: (2009). DOI: 10.1243/14644207JMDA219.

[44] Hadi Izadi, Katherine M E Stewart, and Alexander Penlidis. "Role of contact electrification and electrostatic interactions in gecko adhesion". In: *J. R. Soc. Interface* (2014). DOI: 10.1098/rsif.2014.0371.

[45] W R Hansen and K Autumn. "Evidence for self-cleaning in gecko setae". In: *Proceedings of the National Academy of Sciences of the United States of America* 102.2 (2005), pp. 385–389. ISSN: 00278424. DOI: 10.1073/pnas.0408304102.

[46] *File:adhesive-hands-gecko-reptile*. URL: https://www.shutterstock.com/it/image-photo/adhesive-hands-gecko-reptile-below-144157456?id=144157456%7B%5C&%7Dsrc=id (visited on 11/24/2020).

[47] Stanislav N. Gorb and Michael Varenberg. “Mushroom-shaped geometry of contact elements in biological adhesive systems”. In: *Journal of Adhesion Science and Technology* 21.12-13 (Oct. 2007), pp. 1175–1183. ISSN: 01694243. DOI: 10.1163/156856107782328317. URL: https://www.tandfonline.com/doi/abs/10.1163/156856107782328317.

[48] Michael P. Murphy et al. “Waalbot II: Adhesion Recovery and Improved Performance of a Climbing Robot using Fibrillar Adhesives”. In: *The International Journal of Robotics Research* 30.1 (Jan. 2011). ISSN: 0278-3649. DOI: 10.1177/0278364910382862.

[49] Moon Kyu Kwak, Hoon Eui Jeong, and Kahp Y. Suh. “Rational design and enhanced biocompatibility of a dry adhesive medical skin patch”. In: *Advanced Materials* 23.34 (Sept. 2011), pp. 3949–3953. ISSN: 09359648. DOI: 10.1002/adma.201101694.

[50] F.P. Bowden and D. Tabor. “The Friction and Lubrication of Solids”. In: (1950).

[51] J. A. Greenwood and J. B. P. Williamson. “Contact of nominally flat surfaces”. In: *Proceedings of the Royal Society of London. Series A. Mathematical and Physical Sciences* 295.1442 (Dec. 1966), pp. 300–319. ISSN: 2053-9169. DOI: 10.1098/rspa.1966.0242.

[52] K. L. Johnson. *Contact Mechanics*. Cambridge University Press, 1985. ISBN: 9781139171731. DOI: 10.1017/CBO9781139171731.

[53] B. N. J. Persson. *Sliding Friction*. NanoScience and Technology. 2000. ISBN: 9783642086526. DOI: 10.1007/978-3-662-04283-0.

[54] V. L. Popov. *Contact mechanics and friction: Physical principles and applications*. Springer Berlin Heidelberg, 2010, pp. 1–362. ISBN: 978364 2108020. DOI: 10.1007/978-3-642-10803-7.

[55] M. Ciavarella, V. Delfine, and G. Demelio. “A ”re-vitalized” Greenwood and Williamson model of elastic contact between fractal surfaces”. In: *Journal of the Mechanics and Physics of Solids* 54.12 (2006), pp. 2569–2591. ISSN: 00225096. DOI: 10.1016/j.jmps.2006.05.006.

[56] M. Ciavarella, J. A. Greenwood, and M. Paggi. “Inclusion of ”interaction” in the Greenwood and Williamson contact theory”. In: *Wear* 265.5-6 (2008), pp. 729–734. ISSN: 00431648. DOI: 10.1016/j.wear.2008.01.019.

[57] J. R. Barber. *Contact Mechanics*. Vol. 250. Solid Mechanics and Its Applications. 2018. ISBN: 9783319709383. DOI: 10.1007/978-3-319-70939-0.

[58] C. A. Brebbia and J. Dominguez. "Boundary element methods for potential problems". In: *Applied Mathematical Modelling* 1.7 (Dec. 1977), pp. 372–378. ISSN: 0307904X. DOI: 10.1016/0307-904X(77)90046-4.

[59] T. Andersson and B. G. Allan-Persson. "Boundary element method applied to two-dimensional contact problems". In: *Progress in Boundary Element Methods* 2 (1983), pp. 136–157. DOI: 10.1007/978-1-4757-6300-3_5.

[60] A. Bemporad and M. Paggi. "Optimization algorithms for the solution of the frictionless normal contact between rough surfaces". In: *International Journal of Solids and Structures* 69–70 (2015), pp. 94–105.

[61] J Leroux, B Fulleringer, and D Nélias. "Contact analysis in presence of spherical inhomogeneities within a half-space". In: *International Journal of Solids and Structures* 47 (2010), pp. 3034–3049. DOI: 10.1016/j.ijsolstr.2010.07.006.

[62] C. Putignano, G. Carbone, and D. Dini. "Mechanics of rough contacts in elastic and viscoelastic thin layers". In: *International Journal of Solids and Structures* 69-70 (2015), pp. 507–517. DOI: 10.1016/j.ijsolstr.2015.04.034.

[63] M. Paggi and J. Reinoso. "A variational approach with embedded roughness for adhesive contact problems". In: *Mechanics of Advanced Materials and Structures* (2018). DOI: 10.1080/15376494.2018.1525454.

[64] L. Pei et al. "Finite element modeling of elasto-plastic contact between rough surfaces". In: *Journal of the Mechanics and Physics of Solids* 53 (2005), pp. 2385–2409. DOI: 10.1016/j.jmps.2005.06.008.

[65] J. Reinelt and P. Wriggers. "Multi-scale approach for frictional contact of elastomers on rough rigid surfaces". In: *Computer Methods in Applied Mechanics and Engineering* 198 (2009), pp. 1996–2008. ISSN: 16137736. DOI: 10.1007/978-3-642-10657-6_3.

[66] G. Zavarise et al. “Real contact mechanisms and finite element formulation–a coupled thermomechanical approach”. In: *International Journal for Numerical Methods in Engineering* 35 (1992), pp. 767–785.

[67] A. Sapora and M. Paggi. “A coupled cohesive zone model for transient analysis of thermoelastic interface debonding”. In: *Computational Mechanics* 53 (2014), pp. 845–857. DOI: 10.1007/s00466-013-0934-8.

[68] P. Lenarda, A. Gizzi, and M. Paggi. “A modeling framework for electro-mechanical interaction between excitable deformable cells”. In: *European Journal of Mechanics - A/Solids* 72 (2018), pp. 374–392.

[69] S Hyun et al. “Finite-element analysis of contact between elastic self-affine surfaces”. In: *Phys. Rev. E* 70 (2004), p. 026117. DOI: 10.1103/PhysRevE.70.026117.

[70] J. F. Molinari and M. Ortiz. “Three-dimensional adaptive meshing by subdivision and edge-collapse in finite-deformation dynamic-plasticity problems with application to adiabatic shear banding”. In: *International Journal for Numerical Methods in Engineering* 53.5 (2002), pp. 1101–1126. ISSN: 00295981. DOI: 10.1002/nme.325.

[71] Marco Paggi, Alberto Bemporad, and José Reinoso. “Computational Methods for Contact Problems with Roughness”. In: *Modeling and Simulation of Tribological Problems in Technology*. Ed. by Marco Paggi and David Hills. Cham: Springer International Publishing, 2020, pp. 131–178. ISBN: 978-3-030-20377-1. DOI: 10.1007/978-3-030-20377-1_4. URL: https://doi.org/10.1007/978-3-030-20377-1_4.

[72] J. R. Barber. “Bounds on the electrical resistance between contacting elastic rough bodies”. In: *Proceedings of the Royal Society of London A* 459 (2003), pp. 53–66. DOI: 10.1098/rspa.2002.1038.

[73] J. R. Barber. *Elasticity*. Springer, Dordrecht, 3rd Edition, 2010.

[74] M. Nakamura. “Constriction Resistance Of Conducting Spots In An Electric Contact Surface”. In: *WIT Transactions on Modelling and Simulation* 3 (1993), p. 10. DOI: 10.2495/BT930121.

[75] H. D. Conway and K. A. Farnham. “The relationship between load and penetration for a rigid, flat-ended punch of arbitrary cross section”. In: *International Journal of Engineering Science* 6.9 (1968), pp. 489–496. ISSN: 0020-7225. DOI: 10.1016/0020-7225(68)90001-3.

[76] R.L. Fernandes, M.F.S.F. de Moura, and R.D.F. Moreira. “Effect of moisture on pure mode I and II fracture behaviour of composite bonded joints”. In: *International Journal of Adhesion and Adhesives* 68 (July 2016), pp. 30–38. ISSN: 0143-7496. DOI: 10.1016/J.IJADHADH.2016.01.010. URL: https://biblioproxy.cnr.it:2114/science/article/pii/S0143749616300033.

[77] O.R. Patil, A. Ameli, and N.V. Datla. “Predicting environmental degradation of adhesive joints using a cohesive zone finite element model based on accelerated fracture tests”. In: *International Journal of Adhesion and Adhesives* 76 (July 2017), pp. 54–60. ISSN: 0143-7496. DOI: 10.1016/J.IJADHADH.2017.02.007. URL: https://biblioproxy.cnr.it:2114/science/article/pii/S0143749617300258.

[78] Tae Min Cho et al. “Effect of surface roughness on the adhesive strength of the heat-resistant adhesive RTV88”. In: *Journal of Adhesion Science and Technology* 23.15 (Sept. 2009), pp. 1875–1882. ISSN: 01694243. DOI: 10.1163/016942409X12508517390671. URL: https://www.tandfonline.com/doi/abs/10.1163/016942409X12508517390671.

[79] S. Azari, M. Papini, and J. K. Spelt. “Effect of surface roughness on the performance of adhesive joints under static and cyclic loading”. In: *Journal of Adhesion* 86.7 (July 2010), pp. 742–764. ISSN: 00218464. DOI: 10.1080/00218464.2010.482430. URL: https://www.tandfonline.com/doi/abs/10.1080/00218464.2010.482430.

[80] Ivano Iovinella, Andrea Prota, and Claudio Mazzotti. “Influence of surface roughness on the bond of FRP laminates to concrete”. In: *Construction and Building Materials* 40 (2013), pp. 533–542. ISSN: 09500618. DOI: 10.1016/j.conbuildmat.2012.09.112. URL: http://dx.doi.org/10.1016/j.conbuildmat.2012.09.112.

[81] Faisal M. Mukhtar and Rayhan M. Faysal. "A review of test methods for studying the FRP-concrete interfacial bond behavior". In: *Construction and Building Materials* 169 (Apr. 2018), pp. 877–887. ISSN: 09500618. DOI: 10.1016/j.conbuildmat.2018.02.163. URL: https://linkinghub.elsevier.com/retrieve/pii/S0950061818304124.

[82] D.R. Moore. "An Introduction to the Special Issue on Peel Testing". In: *International Journal of Adhesion and Adhesives* 28.4-5 (June 2008), pp. 153–157. ISSN: 01437496. DOI: 10.1016/j.ijadhadh.2007.01.001. URL: https://linkinghub.elsevier.com/retrieve/pii/S0143749607000607.

[83] J. J. Bikerman. "Theory of Peeling through a Hookean Solid". In: *Journal of Applied Physics* 28.12 (Dec. 1957), pp. 1484–1485. ISSN: 0021-8979. DOI: 10.1063/1.1722682. URL: http://aip.scitation.org/doi/10.1063/1.1722682.

[84] K Kendall. "The adhesion and surface energy of elastic solids". In: *Journal of Physics D: Applied Physics* 4.8 (Aug. 1971), p. 320. ISSN: 00223727. DOI: 10.1088/0022-3727/4/8/320. URL: http://stacks.iop.org/0022-3727/4/i=8/a=320?key=crossref.8140dfc34535dc8742c55c6d927903c0.

[85] A. A. Griffith. "The Phenomena of Rupture and Flow in Solids". In: *Philosophical Transactions of the Royal Society A: Mathematical, Physical and Engineering Sciences* 221.582-593 (Jan. 1921), pp. 163–198. ISSN: 1364-503X. DOI: 10.1098/rsta.1921.0006. URL: http://rsta.royalsocietypublishing.org/cgi/doi/10.1098/rsta.1921.0006.

[86] J. G. Williams. "End corrections for orthotropic DCB specimens". In: *Composites Science and Technology* 35.4 (Jan. 1989), pp. 367–376. DOI: 10.1016/0266-3538(89)90058-4. URL: https://biblioproxy.cnr.it:2114/science/article/pii/0266353889900584.

[87] J. G. Williams. "Root rotation and plastic work effects in the peel test". In: *The Journal of Adhesion* 41.1-4 (1993), pp. 225–239. ISSN: 15455823. DOI: 10.1080/00218469308026564.

[88] *The peeling of flexible laminates*. Tech. rep. 1994, pp. 45–70. URL: https://biblioproxy.cnr.it:2280/content/pdf/10.1007%7B%5C%%7D2FBF00012635.pdf.

[89] L. F. Kawashita, D. R. Moore, and J. G. Williams. “Protocols for the measurement of adhesive fracture toughness by peel tests”. In: *Journal of Adhesion* 82.10 (2006), pp. 973–995. ISSN: 00218464. DOI: 10.1080/00218460600876142.

[90] M. D. Thouless and H. M. Jensen. “Elastic fracture mechanics of the peel-test geometry”. In: *The Journal of Adhesion* 38.3-4 (1992), pp. 185–197. ISSN: 15455823. DOI: 10.1080/00218469208030454.

[91] Zhigang Suo and John W. Hutchinson. “Steady-state cracking in brittle substrates beneath adherent films”. In: *International Journal of Solids and Structures* 25.11 (Jan. 1989), pp. 1337–1353. ISSN: 00207683. DOI: 10.1016/0020-7683(89)90096-6.

[92] “Finite element multibody simulation of a breathing crack in a rotor with a cohesive zone model”. In: *ISRN Mechanical Engineering* 2013 (2013). ISSN: 20905122. DOI: 10.1155/2013/249035.

[93] C.T. Sun and Z.H. Jin. “Cohesive Zone Model”. In: *Fracture Mechanics* (Jan. 2012), pp. 227–246. DOI: 10.1016/B978-0-12-385001-0.00009-2. URL: https://www.sciencedirect.com/science/article/pii/B9780123850010000092.

[94] Ted Diehl. “On using a penalty-based cohesive-zone finite element approach, Part I: Elastic solution benchmarks”. In: *International Journal of Adhesion and Adhesives* 28.4-5 (2008), pp. 237–255. ISSN: 01437496. DOI: 10.1016/j.ijadhadh.2007.06.003.

[95] J.G. Williams and H. Hadavinia. “Analytical solutions for cohesive zone models”. In: *Journal of the Mechanics and Physics of Solids* 50.4 (Apr. 2002), pp. 809–825. ISSN: 00225096. DOI: 10.1016/S0022-5096(01)00095-3. URL: https://linkinghub.elsevier.com/retrieve/pii/S0022509601000953.

[96] Marco Paggi and Peter Wriggers. “A nonlocal cohesive zone model for finite thickness interfaces - Part I: Mathematical formulation and validation with molecular dynamics”. In: *Computational Materials Science* 50.5 (2011), pp. 1625–1633. ISSN: 09270256. DOI: 10.1016/j.commatsci.2010.12.024.

[97] M. Paggi and J. Reinoso. “Revisiting the problem of a crack impinging on an interface: A modeling framework for the interaction between the phase field approach for brittle fracture and the interface cohesive zone model”. In: *Computer Methods in Applied Mechanics and Engineering* 321 (2017), pp. 145–172. ISSN: 00457825.

DOI: 10.1016/j.cma.2017.04.004. arXiv: 1702.01102. URL: http://dx.doi.org/10.1016/j.cma.2017.04.004.

[98] Gregorio Mariggiò et al. "Peeling of thick adhesive interfaces: The role of dynamics and geometrical nonlinearity". In: *Mechanics Research Communications* 94 (2018), pp. 21–27. ISSN: 00936413. DOI: 10.1016/j.mechrescom.2018.08.018.

[99] M. Corrado and M. Paggi. "Nonlinear fracture dynamics of laminates with finite thickness adhesives". In: *Mechanics of Materials* 80.PB (2015), pp. 183–192. ISSN: 01676636. DOI: 10.1016/j.mechmat.2014.07.012. URL: http://dx.doi.org/10.1016/j.mechmat.2014.07.012.

[100] Laura De Lorenzis and Giorgio Zavarise. "Modeling of mixed-mode debonding in the peel test applied to superficial reinforcements". In: *International Journal of Solids and Structures* 45.20 (Oct. 2008), pp. 5419–5436. ISSN: 0020-7683. DOI: 10.1016/J.IJSOLSTR.2008.05.024. URL: https://www.sciencedirect.com/science/article/pii/S0020768308002369?via%7B%5C%%7D3Dihub.

[101] S. Marfia and E. Sacco. "Numerical techniques for the analysis of crack propagation in cohesive materials". In: *International Journal for Numerical Methods in Engineering* 57.11 (July 2003), pp. 1577–1602. ISSN: 0029-5981. DOI: 10.1002/nme.732. URL: http://doi.wiley.com/10.1002/nme.732.

[102] John A. Williams and James J. Kauzlarich. "The influence of peel angle on the mechanics of peeling flexible adherends with arbitrary load-extension characteristics". In: *Tribology International* 38.11-12 SPEC. ISS. (Nov. 2005), pp. 951–958. ISSN: 0301679X. DOI: 10.1016/j.triboint.2005.07.024.

[103] J. Reinoso and M. Paggi. "A consistent interface element formulation for geometrical and material nonlinearities". In: *Computational Mechanics* 54.6 (2014), pp. 1569–1581. ISSN: 01787675. DOI: 10.1007/s00466-014-1077-2. arXiv: arXiv:1507.05168v1.

[104] S Gorb et al. "Biomimetic mushroom-shaped fibrillar adhesive microstructure". In: *Journal of The Royal Society Interface* 4.13 (Apr. 2007), pp. 271–275. ISSN: 1742-5689. DOI: 10.1098/rsif.2006.0164.

[105] Giuseppe Carbone, Elena Pierro, and Stanislav N. Gorb. "Origin of the superior adhesive performance of mushroom-shaped microstructured surfaces". In: *Soft Matter* 7.12 (June 2011), p. 5545. ISSN: 1744-683X. DOI: 10.1039/c0sm01482f. URL: www.rsc.org/softmatter%20http://xlink.rsc.org/?DOI=c0sm01482f.

[106] Aránzazu del Campo, Christian Greiner, and Eduard Arzt. "Contact Shape Controls Adhesion of Bioinspired Fibrillar Surfaces". In: *Langmuir* 23.20 (Sept. 2007), pp. 10235–10243. ISSN: 0743-7463. DOI: 10.1021/la7010502.

[107] M. Varenberg and S. Gorb. "Close-up of mushroom-shaped fibrillar adhesive microstructure: contact element behaviour". In: *Journal of The Royal Society Interface* 5.24 (July 2008), pp. 785–789. ISSN: 1742-5689. DOI: 10.1098/rsif.2007.1201.

[108] Giuseppe Carbone and Elena Pierro. "A review of adhesion mechanisms of mushroom-shaped microstructured adhesives". In: *Meccanica* 48.8 (Oct. 2013), pp. 1819–1833. ISSN: 00256455. DOI: 10.1007/s11012-013-9724-9. URL: https://link.springer.com/article/10.1007/s11012-013-9724-9.

[109] A.V. Spuskanyuk et al. "The effect of shape on the adhesion of fibrillar surfaces". In: *Acta Biomaterialia* 4.6 (Nov. 2008), pp. 1669–1676. ISSN: 17427061. DOI: 10.1016/j.actbio.2008.05.026.

[110] Tian Tang, Chung-Yuen Hui, and Nicholas J. Glassmaker. "Can a fibrillar interface be stronger and tougher than a non-fibrillar one?" In: *Journal of The Royal Society Interface* 2.5 (Dec. 2005), pp. 505–516. ISSN: 1742-5689. DOI: 10.1098/rsif.2005.0070.

[111] Xuan Zhang et al. "A Design Strategy for Mushroom-Shaped Microfibrils With Optimized Dry Adhesion: Experiments and Finite Element Analyses". In: *Journal of Applied Mechanics* 88.3 (Mar. 2021). ISSN: 0021-8936. DOI: 10.1115/1.4049183. URL: https://asmedigitalcollection.asme.org/appliedmechanics/article/doi/10.1115/1.4049183/1091682/A-Design-Strategy-for-Mushroom-Shaped-Microfibrils.

[112] D Skondras-Giousios, N E Karkalos, and A P Markopoulos. "Finite element simulation of friction and adhesion attributed contact of bio-inspired gecko-mimetic PDMS micro-flaps with SiO 2 spherical surface". In: *Bioinspiration & Biomimetics* 15.6 (Sept.

2020), p. 066004. ISSN: 1748-3190. DOI: 10.1088/1748-3190/ab983e.

[113] Roger A. Sauer. "Multiscale modelling and simulation of the deformation and adhesion of a single gecko seta". In: *Computer Methods in Biomechanics and Biomedical Engineering* 12.6 (2009), pp. 627–640. ISSN: 10255842. DOI: 10.1080/10255840902802917.

[114] T. Belytschko et al. *Nonlinear Finite Elements for Continua and Structures*. Wiley, 2013. ISBN: 9781118700082. URL: https://books.google.it/books?id=e%5C_w8AgAAQBAJ.

[115] Peter Wriggers. *Nonlinear finite element methods*. Springer Berlin Heidelberg, 2008, pp. 1–559. ISBN: 9783540710004. DOI: 10.1007/978-3-540-71001-1.

[116] R Ogden. *Non-linear elastic deformations*. Ed. by E. Horwood ; and Halsted Press. Chichester ;New York: E. Horwood ;;Halsted Press, 1984. ISBN: 9780853122739.

[117] Christian Miehe and Lisa Marie Schänzel. "Phase field modeling of fracture in rubbery polymers. Part I: Finite elasticity coupled with brittle failure". In: *Journal of the Mechanics and Physics of Solids* 65.1 (2014), pp. 93–113. ISSN: 00225096. DOI: 10.1016/j.jmps.2013.06.007.

[118] Pietro Cornetti et al. "An analytical cohesive crack modeling approach to the edge debonding failure of FRP-plated beams". In: *International Journal of Solids and Structures* 53 (2015), pp. 92–106. ISSN: 00207683. DOI: 10.1016/j.ijsolstr.2014.10.017. URL: http://dx.doi.org/10.1016/j.ijsolstr.2014.10.017.

[119] Nicolas Moës, John Dolbow, and Ted Belytschko. "A finite element method for crack growth without remeshing". In: *International Journal for Numerical Methods in Engineering* 46.1 (Sept. 1999), pp. 131–150. ISSN: 00295981. DOI: 10.1002/(SICI)1097-0207(19990910)46:1<131::AID-NME726>3.0.CO;2-J.

[120] T. Belytschko and T. Black. "Elastic crack growth in finite elements with minimal remeshing". In: *International Journal for Numerical Methods in Engineering* 45.5 (1999), pp. 601–620. DOI: https://doi.org/10.1002/(SICI)1097-0207(19990620)45:5<601::AID-NME598>3.0.CO;2-S.

[121] Abdelaziz Yazid, Nabbou Abdelkader, and Hamouine Abdelmadjid. "A state-of-the-art review of the X-FEM for computational fracture mechanics". In: *Applied Mathematical Modelling* 33.12 (2009), pp. 4269–4282. ISSN: 0307904X. DOI: 10.1016/j.apm.2009.02.010. URL: http://dx.doi.org/10.1016/j.apm.2009.02.010.

[122] L. Beirão Da Veiga, F. Brezzi, and L.D. Marini. "Virtual elements for linear elasticity problems". In: *SIAM Journal on Numerical Analysis* 51.2 (2013). cited By 252, pp. 794–812. DOI: 10.1137/120874746.

[123] L. Beirão Da Veiga et al. "Basic principles of virtual element methods". In: *Mathematical Models and Methods in Applied Sciences* 23.01 (Jan. 2013). ISSN: 0218-2025. DOI: 10.1142/S0218202512500492.

[124] Fadi Aldakheel, Blaž Hudobivnik, and Peter Wriggers. "Virtual element formulation for phase-field modeling of ductile fracture". In: *International Journal for Multiscale Computational Engineering* 17.2 (2019). DOI: 10.1615//IntJMultCompEng.2018026804.

[125] P Wriggers and B Hudobivnik. "A low order virtual element formulation for finite elasto-plastic deformations". In: *Comput. Methods Appl. Mech. Engrg* 327 (2017), pp. 459–477. DOI: 10.1016/j.cma.2017.08.053.

[126] P Wriggers et al. "Efficient virtual element formulations for compressible and incompressible finite deformations". In: *Computational Mechanics* 60 (2017), pp. 253–268. DOI: 10.1007/s00466-017-1405-4.

[127] P Wriggers, · W T Rust, and · B D Reddy. "A virtual element method for contact". In: *Computational Mechanics* 58 (2016), pp. 1039–1050. DOI: 10.1007/s00466-016-1331-x.

[128] Edoardo Artioli, Sonia Marfia, and Elio Sacco. "Virtual element technique for computational homogenization problems". In: *AIMETA 2017 - Proceedings of the 23rd Conference of the Italian Association of Theoretical and Applied Mechanics* 2.September (2017), pp. 1686–1698.

[129] Ali Hussein et al. "A computational framework for brittle crack-propagation based on efficient virtual element method". In: *Finite Elements in Analysis and Design* 159 (2019), pp. 15–32. DOI: 10.1016/j.finel.2019.03.001.

[130] E. Artioli, S. Marfia, and E. Sacco. "VEM-based tracking algorithm for cohesive/frictional 2D fracture". In: *Computer Methods in Applied Mechanics and Engineering* 365.March (2020), p. 112956. ISSN: 00457825. DOI: 10.1016/j.cma.2020.112956. URL: https://doi.org/10.1016/j.cma.2020.112956.

[131] H. A. F. A. Santos and V. V. Silberschmidt. "Finite Element Modelling of 2D Brittle Fracture: The Phase-Field Approach". In: *Mechanics of Advanced Materials: Analysis of Properties and Performance*. Ed. by Vadim V. Silberschmidt and Valery P. Matveenko. Cham: Springer International Publishing, 2015, pp. 1–21. ISBN: 978-3-319-17118-0. DOI: 10.1007/978-3-319-17118-0_1. URL: https://doi.org/10.1007/978-3-319-17118-0_1.

[132] G. A. Francfort and J.-J. Marigo. "Revisiting brittle fracture as an energy minimization problem". In: *Journal of the Mechanics and Physics of Solids* 46.8 (Aug. 1998), pp. 1319–1342. ISSN: 0022-5096. DOI: 10.1016/S0022-5096(98)00034-9. URL: https://www.sciencedirect.com/science/article/pii/S0022509698000349.

[133] B. Bourdin, G.A. Francfort, and J-J. Marigo. "Numerical experiments in revisited brittle fracture". In: *Journal of the Mechanics and Physics of Solids* 48.4 (Apr. 2000), pp. 797–826. ISSN: 00225096. DOI: 10.1016/S0022-5096(99)00028-9.

[134] Christian Miehe, Martina Hofacker, and Fabian Welschinger. "A phase field model for rate-independent crack propagation: Robust algorithmic implementation based on operator splits". In: *Computer Methods in Applied Mechanics and Engineering* 199 (2010), pp. 2765–2778. DOI: 10.1016/j.cma.2010.04.011. URL: http://www.crm.sns.it/media/course/3060/miehe+hofacker+welschinger10.pdf.

[135] F. Freddi and F. Iurlano. "Numerical insight of a variational smeared approach to cohesive fracture". In: *Journal of the Mechanics and Physics of Solids* 98 (2017), pp. 156–171. ISSN: 0022-5096. DOI: https://doi.org/10.1016/j.jmps.2016.09.003. URL: http://www.sciencedirect.com/science/article/pii/S0022509616304860.

[136] Renè de Borst and Clemens V. Verhoosel. "A phase-field model for cohesive fracture". In: *INTERNATIONAL JOURNAL FOR NU-*

MERICALMETHODS IN ENGINEERING March (2010), pp. 1885–1891. ISSN: 0743-1619. DOI: 10.1002/nme. arXiv: 1010.1724.

[137] Michael J. Borden et al. "A phase-field formulation for fracture in ductile materials: Finite deformation balance law derivation, plastic degradation, and stress triaxiality effects". In: *Computer Methods in Applied Mechanics and Engineering* 312 (Dec. 2016), pp. 130–166. ISSN: 00457825. DOI: 10.1016/j.cma.2016.09.005.

[138] M. Ambati, T. Gerasimov, and L. De Lorenzis. "Phase-field modeling of ductile fracture". In: *Computational Mechanics* 55.5 (May 2015), pp. 1017–1040. ISSN: 01787675. DOI: 10.1007/s00466-015-1151-4. URL: https://link.springer.com/article/10.1007/s00466-015-1151-4.

[139] Blaise Bourdin, Christopher J. Larsen, and Casey L. Richardson. "A time-discrete model for dynamic fracture based on crack regularization". In: *International Journal of Fracture* 168.2 (Apr. 2011), pp. 133–143. ISSN: 03769429. DOI: 10.1007/s10704-010-9562-x. URL: https://link.springer.com/%20article/10.1007/s10704-010-9562-x.

[140] Michael J. Borden et al. "A phase-field description of dynamic brittle fracture". In: *Computer Methods in Applied Mechanics and Engineering* 217-220 (Apr. 2012), pp. 77–95. ISSN: 00457825. DOI: 10.1016/j.cma.2012.01.008.

[141] V. Carollo et al. "Recent advancements on the phase field approach to brittle fracture for heterogeneous materials and structures". In: *Advanced Modeling and Simulation in Engineering Sciences* 5.1 (Dec. 2018), p. 8. ISSN: 2213-7467. DOI: 10.1186/s40323-018-0102-y. URL: https://amses-journal.springeropen.com/articles/10.1186/s40323-018-0102-y.

[142] J. Reinoso, M. Paggi, and C. Linder. "Phase field modeling of brittle fracture for enhanced assumed strain shells at large deformations: formulation and finite element implementation". In: *Computational Mechanics* 59.6 (2017). ISSN: 01787675. DOI: 10.1007/s00466-017-1386-3.

[143] V. Carollo, J. Reinoso, and M. Paggi. "A 3D finite strain model for intralayer and interlayer crack simulation coupling the phase field approach and cohesive zone model". In: *Composite Structures* 182 (2017), pp. 636–651. ISSN: 02638223. DOI: 10.1016/j.comps

truct.2017.08.095. URL: http://dx.doi.org/10.1016/j.compstruct.2017.08.095%20https://doi.org/10.1016/j.compstruct.2017.08.095.

[144] A. Quintanas-Corominas et al. "A phase field approach enhanced with a cohesive zone model for modeling delamination induced by matrix cracking". In: *Computer Methods in Applied Mechanics and Engineering* 358 (Jan. 2020), p. 112618. ISSN: 00457825. DOI: 10.1016/j.cma.2019.112618.

[145] Jian-Ying Wu et al. "Phase-field modelling of fracture". In: *Advances in Applied Mechanics* 53 (2020).

[146] Fadi Aldakheel et al. "Phase-field modeling of brittle fracture using an efficient virtual element scheme". In: *Computer Methods in Applied Mechanics and Engineering* 341 (Nov. 2018), pp. 443–466. ISSN: 00457825. DOI: 10.1016/j.cma.2018.07.008.

[147] Fan Peng et al. "Phase field simulation for fracture behavior of hyperelastic material at large deformation based on edge-based smoothed finite element method". In: *Engineering Fracture Mechanics* 238 (2020). ISSN: 00137944. DOI: 10.1016/j.engfracmech.2020.107233.

[148] Tushar Kanti Mandal, Vinh Phu Nguyen, and Jian Ying Wu. "A length scale insensitive anisotropic phase field fracture model for hyperelastic composites". In: *International Journal of Mechanical Sciences* 188.April (2020). ISSN: 00207403. DOI: 10.1016/j.ijmecsci.2020.105941.

[149] Jonathan Russ et al. "Rupture of 3D-printed hyperelastic composites: experiments and phase field fracture modeling". In: *Journal of the Mechanics and Physics of Solids* (Apr. 2020), p. 103941. ISSN: 00225096. DOI: 10.1016/j.jmps.2020.103941.

[150] Shan Tang et al. "Phase field modeling of fracture in nonlinearly elastic solids via energy decomposition". In: *Computer Methods in Applied Mechanics and Engineering* 347 (Apr. 2019), pp. 477–494. ISSN: 00457825. DOI: 10.1016/j.cma.2018.12.035.

[151] Heng Chi et al. "A variational formulation with rigid-body constraints for finite elasticity: theory, finite element implementation, and applications". In: 57 (2016), pp. 325–338. DOI: 10.1007/s00466-015-1234-2.

[152] Aditya Kumar, Gilles A Francfort, and Oscar Lopez-Pamies. "Fracture and healing of elastomers: A phase-transition theory and numerical implementation". In: *Journal of the Mechanics and Physics of Solids journal homepage* 112 (2018), pp. 523–551. DOI: 10.1016/j.jmps.2018.01.003. URL: www.elsevier.com/locate/jmps.

[153] P. L. Rosendahl et al. "Nonlinear elastic finite fracture mechanics: Modeling mixed-mode crack nucleation in structural glazing silicone sealants". In: *Materials and Design* 182 (2019), p. 108057. ISSN: 18734197. DOI: 10.1016/j.matdes.2019.108057. URL: https://doi.org/10.1016/j.matdes.2019.108057.

[154] Thanh Tung Nguyen, Danièle Waldmann, and Tinh Quoc Bui. "Role of interfacial transition zone in phase field modeling of fracture in layered heterogeneous structures". In: *Journal of Computational Physics* 386 (June 2019), pp. 585–610. ISSN: 10902716. DOI: 10.1016/j.jcp.2019.02.022.

[155] T. Guillén-Hernández, J. Reinoso, and M. Paggi. "Fracture analysis of thin films on compliant substrates: A numerical study using the phase field approach of fracture". In: *International Journal of Pressure Vessels and Piping* 175.May (2019), p. 103913. ISSN: 03080161. DOI: 10.1016/j.ijpvp.2019.05.008. URL: https://doi.org/10.1016/j.ijpvp.2019.05.008.

[156] Teng Li et al. "Stretchability of thin metal films on elastomer substrates". In: *Applied Physics Letters* 85.16 (Oct. 2004), pp. 3435–3437. ISSN: 00036951. DOI: 10.1063/1.1806275. URL: http://aip.scitation.org/doi/10.1063/1.1806275.

[157] Teng Li, Zhao Zhang, and Benoit Michaux. "Competing failure mechanisms of thin metal films on polymer substrates under tension". In: *Theoretical and Applied Mechanics Letters* 1 (2011), p. 41002. DOI: 10.1063/2.1104102.

[158] Jeong Yun Sun et al. "Debonding and fracture of ceramic islands on polymer substrates". In: *Journal of Applied Physics* 111.1 (2012), p. 103519. ISSN: 00218979. DOI: 10.1063/1.3673805.

[159] Hanen Amor, Jean-Jacques Marigo, and Corrado Maurini. "Regularized formulation of the variational brittle fracture with unilateral contact: Numerical experiments". In: *Journal of the Mechanics and Physics of Solids* 57.8 (Aug. 2009), pp. 1209–1229. ISSN: 00225096. DOI: 10.1016/j.jmps.2009.04.011.

[160] E. Tanné et al. “Crack nucleation in variational phase-field models of brittle fracture”. In: *Journal of the Mechanics and Physics of Solids* 110 (Jan. 2018), pp. 80–99. ISSN: 00225096. DOI: 10.1016/j.jmps.2017.09.006. URL: https://linkinghub.elsevier.com/%20retrieve/pii/S0022509617306543.

[161] Aditya Kumar and Oscar Lopez-Pamies. “The phase-field approach to self-healable fracture of elastomers: A model accounting for fracture nucleation at large, with application to a class of conspicuous experiments”. In: *Theoretical and Applied Fracture Mechanics* 107 (June 2020). ISSN: 01678442. DOI: 10.1016/j.tafmec.2020.102550. URL: https://doi.org/10.1016/j.tafmec.2020.102550.

[162] O. C. Zienkiewicz, R. L. Taylor, and David Fox. *The Finite Element Method for Solid and Structural Mechanics: Seventh Edition*. Elsevier Ltd, 2013, pp. 1–624. ISBN: 9781856176347. DOI: 10.1016/C2009-0-26332-X.

[163] C. Miehe, F. Welschinger, and M. Hofacker. “Thermodynamically consistent phase-fieldmodels of fracture: Variational principles and multi-field FE implementations”. In: *International Journal for Numerical Methods in Engineering* 83.10 (Sept. 2010), pp. 1273–1311. ISSN: 00295981. DOI: 10.1002/nme.2861. URL: http://doi.wiley.com/10.1002/nme.2861.

[164] Viggo Tvergaard. “Fibre debonding and breakage in a whisker-reinforced metal”. In: *Materials Science and Engineering A* 190.1-2 (1995), pp. 215–222. ISSN: 09215093. DOI: 10.1016/0921-5093(95)80005-0.